

Mesoporous CHA and MFI zeolite catalysts for methanol conversion reactions

Citation for published version (APA):

Wu, L. (2014). *Mesoporous CHA and MFI zeolite catalysts for methanol conversion reactions*. [Phd Thesis 1 (Research TU/e / Graduation TU/e), Chemical Engineering and Chemistry]. Technische Universiteit Eindhoven. <https://doi.org/10.6100/IR762548>

DOI:

[10.6100/IR762548](https://doi.org/10.6100/IR762548)

Document status and date:

Published: 01/01/2014

Document Version:

Publisher's PDF, also known as Version of Record (includes final page, issue and volume numbers)

Please check the document version of this publication:

- A submitted manuscript is the version of the article upon submission and before peer-review. There can be important differences between the submitted version and the official published version of record. People interested in the research are advised to contact the author for the final version of the publication, or visit the DOI to the publisher's website.
- The final author version and the galley proof are versions of the publication after peer review.
- The final published version features the final layout of the paper including the volume, issue and page numbers.

[Link to publication](#)

General rights

Copyright and moral rights for the publications made accessible in the public portal are retained by the authors and/or other copyright owners and it is a condition of accessing publications that users recognise and abide by the legal requirements associated with these rights.

- Users may download and print one copy of any publication from the public portal for the purpose of private study or research.
- You may not further distribute the material or use it for any profit-making activity or commercial gain
- You may freely distribute the URL identifying the publication in the public portal.

If the publication is distributed under the terms of Article 25fa of the Dutch Copyright Act, indicated by the "Taverne" license above, please follow below link for the End User Agreement:

www.tue.nl/taverne

Take down policy

If you believe that this document breaches copyright please contact us at:

openaccess@tue.nl

providing details and we will investigate your claim.

Mesoporous CHA and MFI Zeolite Catalysts for Methanol Conversion Reactions

PROEFSCHRIFT

ter verkrijging van de graad van doctor aan de
Technische Universiteit Eindhoven, op gezag van de
rector magnificus, prof.dr.ir. C.J. van Duijn, voor een
commissie aangewezen door het College voor
Promoties in het openbaar te verdedigen
op woensdag 8 januari 2014 om 16.00 uur

door

Leilei Wu

geboren te Rizhao, China

Dit proefschrift is goedgekeurd door de promotoren:

prof.dr.ir. E.J.M. Hensen

Copromotor:

dr. P.C.M.M. Magusin

Dedicated to my husband and parents

A catalogue record is available from the Eindhoven University of Technology Library

ISBN: 978-90-386-3531-6

The work described in this thesis has been carried out at the Schuit Institute of Catalysis, Laboratory of Inorganic Materials Chemistry, Eindhoven University of Technology, The Netherlands. This research is supported by the Dutch Technology Foundation STW, under Vidi grant 07969, which is part of the Netherlands Organisation for Scientific Research (NWO), and which is partly funded by the Ministry of Economic Affairs.

Cover design: Leilei Wu and Paul Verspaget (Verspaget&Bruinink)

Copyright © 2014 by Leilei Wu

Table of contents

Chapter 1	<i>Introduction</i>	1
Chapter 2	<i>Synthesis and Characterization of Mesoporous SSZ-13 Zeolite by a Dual Templating Method</i>	19
Chapter 3	<i>Catalytic Performance of Mesoporous SSZ-13 Zeolite in the Methanol-to-Olefins Reaction</i>	43
Chapter 4	<i>Mesoporous SAPO-34 and high-silica SSZ-13 Zeolites as Catalysts for the Methanol-to-Olefins Reaction</i>	63
Chapter 5	<i>Acidic Properties of Nanolayered ZSM-5 Zeolites</i>	85
Chapter 6	<i>Synthesis and Catalytic Properties of Nanolayered ZSM-5 Zeolite with a Si/Al ratio of 20</i>	135
Summary		163
Acknowledgements		169
List of publications		173
Curriculum Vitae		175

Chapter 1

Introduction

1.1 Catalysis

The best-known application of catalysis to the general audience is the catalytic converter in gasoline cars. It was invented by Houdry, who also pioneered catalytic cracking of oil fractions, and was introduced in the US markets following the Clean Air Act in the 1970's. The use of the three-way catalyst for abatement of unwanted emissions of noxious gases from gasoline cars and related catalysts for clean-up of other exhaust streams from combustion processes has had a major positive impact on the well-being of humankind. Besides being pivotal in environmental pollution control, catalysts are the work horses of the chemical industry. The global turnover of the chemical industry is 1800 billion USD. Compared to this, the turnover of the catalyst manufacturing industry of 13 billion USD appears very modest. Catalysts are used in nearly 90% of all chemical processes and are important to the production of about 80% of all chemicals. This efficiency of catalysts derives from the intrinsic nature of the catalytic cycle, namely that many reactant molecules can be converted to desirable products on the same catalytic site before deactivation occurs (Fig. 1.1).

The phenomenon of catalysis was first recognized around 1816 by Davy when he observed that the combustion of coal gas with oxygen is accelerated by a glowing platinum wire. This example of heterogeneous catalytic oxidation was put to use in the miner's safety lamp. Berzelius coined the name "catalysis" around 1835 to indicate that it involves a 'chemical event that changes the composition of a mixture'. Besides a chemical driving force, he concluded that a reaction occurred by catalytic contact. From these ideas the definition of a catalyst evolved into the contemporary one: a catalyst is a material that will increase the rate of a particular reaction without itself being consumed in the process. Catalysts were already used much earlier, of course, as a tool to carry out reactions, for instance in

fermentation processes (wine, beer, cheese) and the production of sulfuric acid. The field of catalysis developed rapidly at the end of the nineteenth century when the influence of metals and oxides on the decomposition of several organic compounds was studied more intensively. Fundamental understanding of catalysis commenced with the work of scientists such as Ostwald, Faraday, Van 't Hoff, Arrhenius, Sabatier, Langmuir, Taylor and Rideal among others [1, 2] and references therein]. It allowed more systematic, scientifically based research and led to the first large-scale industrial catalytic process in 1909, the continuous synthesis of ammonia from nitrogen and hydrogen (Haber-Bosch process). This process is one of the most studied catalytic reactions and it acts as the prototype reaction that has been used to develop many key concepts in the field [3].

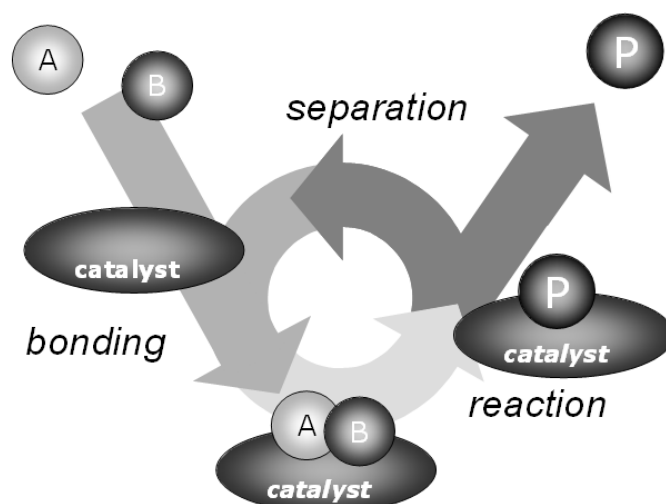


Figure 1.1: All catalytic reactions proceeds through a cycle involving binding of reactants with the catalyst, reactions of the adsorbed reactants into products and desorption of the products, thus recycling the initial state. A good catalyst lowers the overall reaction barrier from reactants to products and may also direct the reaction on the potential energy towards desirable products [1].

Industrial catalysis has always been closely connected with changes in society and especially with the ever increasing need for energy. Initially, society depended on biomass for energy, but the larger amounts of energy required during industrialization led to the large-scale use of coal. After the Second World War petroleum oil became the dominant feedstock next to the continued use of coal. Modern oil refineries are very complex chemical plants in which virtually every drop of oil is used or converted into transportation fuels and

other chemical intermediates and products. In refineries, many catalytic processes are being employed, the largest one being fluid catalytic cracking involving zeolites as solid acids. Natural gas has been becoming more important in the last decade as a source of energy and recently also for production of fuels and chemicals. The most likely technology to upgrade natural gas to these products is Fischer-Tropsch synthesis following the conversion of natural gas to synthesis gas by steam reforming. In the foreseeable future, biorenewable energy resources will undoubtedly become more important again to counter the negative effects of carbon dioxide emissions associated with the use of fossil fuels and also to decrease our dependence on non-renewable feedstock [4-6]. The geopolitical situation has always had and will continue to have its impact on these feedstock issues. For instance, to decrease its dependence on import of crude oil China is heavily investing in coal conversion technology, again with syngas as a platform for conversion to fuels and chemicals.

1.2 Zeolites

Zeolites are microporous crystalline aluminosilicates consisting of a regular frameworks of oxygen tetrahedra occupied by aluminium and silicon cations combined with group IA and IIA elements (e.g. sodium, potassium, calcium and magnesium) to compensate for the negative framework charge induced by the substitution of Si^{4+} by Al^{3+} . Although the preparation of levynite was already reported in 1862 [7], it was the work of Barrer and Milton in the late 1940's and early 1950's that ultimately led to the preparation of synthetic zeolites on a commercial scale [8, 9]. The discovery of faujasites led to the replacement of amorphous solid acids in catalytic cracking applications by strong solid acids. A further important discovery was the use of organic ammonium cations as templates or structure-directing agents to direct zeolite formation. By use of organic cations zeolite Beta (BEA) and ZSM-5 (MFI) were discovered in 1967 and 1972, respectively. Thereafter, numerous frameworks and zeolites have been discovered. The synthesis of novel zeolite frameworks is being increasingly supported by insights into the way zeolites are formed with important contributions from both experimental and computational studies [10]. Currently, more than 200 different zeolite structures are known with the number rising each year. Nowadays, the

worldwide consumption of synthetic zeolites is estimated about 1.7-2 million metric tons, with consumption of natural zeolites being around 2.5 million metric tons [11-13]. The major applications of zeolites comprise detergents, adsorbents, desiccants and catalysis. The main applications of zeolites as catalysts in industry involve fluidized catalyst cracking, hydrocracking, hydroisomerization, aromatics alkylation, reforming, xylene isomerization and dewaxing [14].

1.3 Zeolites as porous solid acid catalysts

The presence of $[\text{AlO}_4]$ tetrahedra in the $[\text{SiO}_4]$ framework causes a net negative charge. This charge is usually compensated by loosely fixed cations (e.g., Na^+ , K^+ , Ca^{2+} and Mg^{2+}). When a proton is used instead, a strong solid Brønsted acidic material is resulting. The high acidity of these sites in zeolites is generally attributed to the rigid structure of the crystalline framework. This prohibits relaxation of the structure around the proton upon interaction with bases. Next to these strong Brønsted acidic sites, zeolites usually contain weakly acidic silanols on defect sites and on the edges of the crystalline framework.

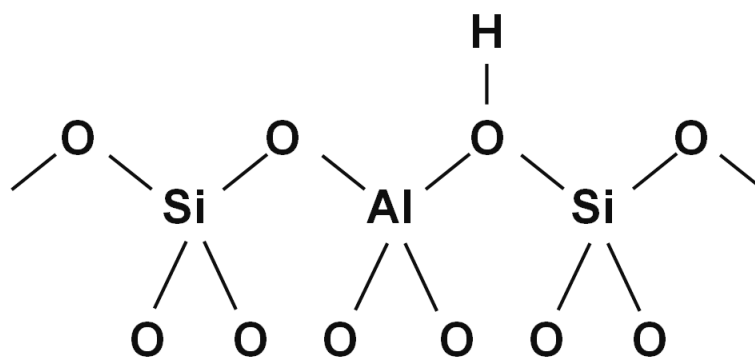


Figure 1.2: Schematic representation of a strong Brønsted acidic site in aluminosilicates.

The total acidity of a zeolite therefore has to be regarded as the product of the total number of acidic sites and their intrinsic acidity. The intrinsic acidity of the sites is determined by the local structure around the acidic site. A tetrahedral aluminium in the next nearest neighbor tetrahedron decreases the intrinsic acidity of the acidic site [15]. Accordingly, the intrinsic acidity of the acid site increases by dilution of the framework Al

atoms. This is very well demonstrated in the case of zeolite faujasite, commonly used as cracking catalyst, whose Si/Al of 2.5 directly after hydrothermal synthesis needs to be increased to values above 5 to render the individual protons strongly acidic.

With an estimated value of 55% based on the yearly world consumption [16], catalysis is one of the major applications of zeolites. Of the more than 200 zeolite structures known, less than 20 are used in commercial processes. By far the largest application of zeolites as catalysts is in the field of petrochemical industry. The major application of zeolites in refineries is fluid catalytic cracking (FCC), where generally silica-enriched forms of zeolite Y (FAU) are used [17]. Other catalytic reactions involving zeolites include reforming, hydrocracking and chemical synthesis. One of the major challenges in the FCC process covers the cracking of heavy molecules. Typical bottom-end fraction molecules have an average carbon number of 25-35 giving them a dynamic molecular size of 12-20 Å. Using the simple model proposed by Spry and Sawyer [18], it can be estimated that the pores size needed is 10-20 times larger than the molecules, meaning that a material with its channels and cages in the mesopore range (2-50 nm) is needed for optimal diffusion. This implies that larger molecules cannot enter the pores of the current generation of zeolites, although they might be cracked on the external surface of the zeolite crystals. Nowadays, FCC catalysts consist of a mixture of components such as faujasite and ZSM-5 zeolite, often combined in an amorphous silica-alumina matrix. Amorphous silica-alumina provides acidic functionalities in meso- and macropores. A drawback is their low acidity, which is to be attributed to the low density of bridging hydroxyl groups [19]. Accordingly, there have been made significant efforts in the last decades to develop porous solid acids which combine larger micropores or interconnected pores of different dimensions with high acidity.

Although zeolites constitute a class of catalysts with very good shape selectivity due to their very high surface areas and an ordered network of micropores of molecular dimensions (typically 0.25–1 nm), their unique microporous structure often results in severe diffusion limitations [20]. Diffusion limitations lead to restricted access of reactants to the active sites and, accordingly, to lower overall reaction rates. In order to overcome this problem, many approaches have been proposed and explored. It is worthwhile to note that despite many efforts no commercial applications have been reported yet, although in some cases successful

trial tests have been performed [21].

A common approach to increase the rate of mass transport involves synthesis of zeolite frameworks with pores larger than faujasite zeolite [22-27]. Such acid porous solids would also be able to convert reactants whose dimensions are too large to enter the pores of current acid zeolites. This is a very active research field. Most of these zeolites based on low-framework density structures such as VPI-5 [22], UTD-1 [28] and ECR-34 [29] suffer from poor hydrothermal stability, low acidity and unidirectional pore systems. Recently, wide-pore zeolites with multidirectional channels have been reported, e.g. ITQ-15 [30], ITQ-21 [31], and ITQ-33 [23], further proving the “promise of emptiness” [32]. This field also includes the synthesis of materials with compositions deviant from the conventional combination of oxygen-occupied tetrahedra of Si and Al [33]. Stability of these novel wide-pore materials is usually so low that the structure is not retained during template removal. Another approach is to decrease the size of the primary zeolite crystals to nanoscale dimensions [34, 35], which meets challenges in terms of product collection and lack of generality of the approach.

Ordered mesoporous silica materials have been explored very extensively for acid-catalysis purposes. However, it is by now well accepted that such X-ray amorphous materials as MCM-41 [36] and SBA-15 [37, 38] modified by Al lack the atomic ordering to bring about high Brønsted acidity [39]. Another drawback is the relatively low hydrothermal stability.

Hierarchical (or mesoporous) zeolites integrate different levels of porosity in one zeolite enabling them to fulfill the complementary tasks of catalyzing chemical reactions on their micropore surface and fast transport of reactants and products in their interconnected larger pores. The shorter diffusion paths and resulting improved intracrystalline transport enhances their effectiveness. The generation of mesoporosity in zeolite crystals has become a very promising approach in the last decade. Industrially, this approach is practiced on a large scale in the steam-calcination process to prepare highly acidic stabilized faujasite-based cracking zeolites. Steaming results in the extraction of Al from the framework, necessary to increase the intrinsic acidity of protons, and simultaneously generates significant mesoporosity [40-43]. There is little control over mesoporosity and, typically, the size of the microporous

domains remains fairly large. Another example of a top-down approach (*i.e.*, modifying the textural properties of a prepared zeolite) is to generate porosity by removing framework Si instead of Al through base leaching. Although the possibilities to introduce mesoporosity are limited with respect to the stability of the starting zeolite [44-46], the method is versatile and can be scaled up.

There has also been substantial interest in bottom-up approaches, which is the one-pot synthesis of zeolites having a network of pores covering sizes from micro- up to meso-dimensions. Several methods have been explored to induce mesoporosity during the zeolite framework formation. A typical strategy has been to combine a mesoporegen (e.g., cetyltrimethylammonium bromide (CTAB) used for MCM-41 synthesis) with the structure directing agent for zeolite growth. Usually, this approach results in microporous zeolite with little mesoporosity or predominantly mesoporous silica or, at best, physical mixtures of the two materials because of the mismatch of conditions for their synthesis. Such hybrid materials show little benefit for catalysis [47, 48]. An approach to overcome the separation of the mesoporegen from the growing zeolite phase is to increase their interaction. For instance, Xiao and co-workers used cationic polymers [49, 50]. The group of Ryoo covalently attached the mesoporegen to the crystallizing zeolite phase [51] resulting in very well-integrated mesoporosity in ZSM-5. This approach has also been used successfully in the synthesis of mesoporous FAU-type zeolite X [52]. The use of organosilanes such as $[(\text{CH}_3\text{O})_3\text{SiC}_3\text{H}_6\text{N}(\text{CH}_3)_2\text{C}_n\text{H}_{2n+1}]\text{Cl}$ has been widely explored because of the generality of the approach [53-60].

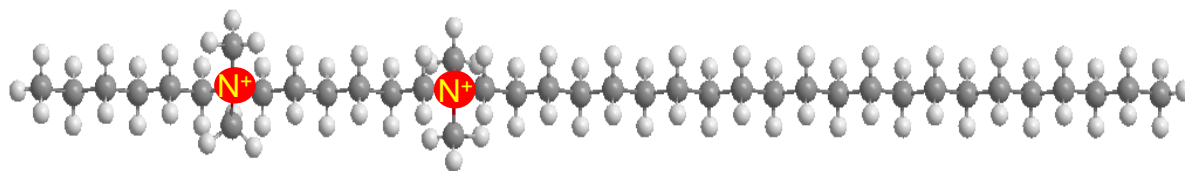


Figure 1.3: Diquaternary ammonium-type surfactant used to direct formation of nanolayered by Ryoo and co-workers [90].

Ryoo's group discovered that the use of diquatery ammonium-type surfactant, e.g. $\text{C}_{22}\text{H}_{45}\text{-N}^+(\text{CH}_3)_2\text{-C}_6\text{H}_{12}\text{-N}^+(\text{CH}_3)_2\text{-C}_6\text{H}_{13}]\text{Br}_2$ (Fig. 1.4) can direct the formation of nanolayered ZSM-5 zeolite [90]. The presence of two quaternary ammonium groups is able

Table 1.1: Summary of the various methods of formation of micro-mesoporous structured zeolites [54].

Method	Template/support	Structure/morphology	Framework/chemical composition of porous materials	Ref.
Hard templating	Nanocarbon	Cave-like mesoporosity	ZSM-5, MTW, MEL, TS-1	[61-64]
	Carbon nanotubes/nanofibers		Silicalite-1, ZSM-5	[40, 65, 66]
	CMK-3		ZSM-5	[67-70]
	Large pore mesoporous carbons	Cave-like mesoporosity	Silicalite-1	[71]
	Carbon aerogels		ZSM-5, Y,	[72, 73]
	Organic aerogels		Silicalite-1, NaA	[74-77]
	CaCO ₃		Silicalite-1	[78]
	Starch-derived bread		ZSM-5	[79]
3Dom carbon	3D ordered mesopores	Silicalite-1, BEA, LTA, FAU, LTL	[80, 81]	
Soft templating	Hydrophilic cationic polymers (PDADMAC)		Beta, ZSM-5, NaX	[82-84]
	Amphiphilic organosilane	Tunable mesoporosity	MFI, LTA, AIPO ₄ -n, SOD	[51, 57-60]
	Silylated polyethylenimine polymer		MFI	[85]
	Polyvinyl butyral (PVB)		Beta, ZSM-11	[86]
	CTAB		MFI, Y, SOD	[87-89]
	Diquaternary ammonium-type surfactant	Lamellar single-unit-cell nanosheets	MFI	[90, 91]
	Dual-porogenic surfactant	Hexagonally ordered mesopores	MFI	[92]

to direct zeolite formation, whilst the hydrophobic tail limits the growth of the zeolite in the *b*-direction. This has led to a significant number of follow-up work focusing on the pillaring of stacked ZSM-5 nanolayers [91], the synthesis of mesoporous BEA zeolite [93] and other templates that combine moieties that direct zeolite formation and mesoporegens [92, 94-96]. These ultrathin zeolites have shown their promise in the methanol-to-hydrocarbons reaction [90] and oxidation of benzene to phenol with nitrous oxide [97].

1.4 Methanol conversion reactions

Mobil were the first to synthesize ZSM-5 zeolite in the early 1970s and explore its unique catalytic properties. Spurred by the two oil crises in this decade, significant research efforts were undertaken towards conversion of methanol to fuels [98]. This led to bench- and pilot-scale demonstration of the methanol-to-gasoline (MTG) process and culminated in its commercialization in New Zealand in 1985 [99]. A 14500 bpd plant using natural gas as a feed was built, which produced intermediate methanol, which was then dehydrated over a weakly acidic catalyst into a mixture of methanol, dimethyl ether and water. This mixture was then converted into a product mixture containing more than 80 % higher hydrocarbons. A significant issue is to temperature control due to the high exothermicity of the involved reactions. The methanol conversion reaction proceeds to light olefins, heavier olefins, aromatics and coke in a sequential reaction scheme (Fig. 1.4). Because of the slow built-up of coke deposits on HZSM-5, intermittent catalyst regeneration was necessary. Driven by low crude oil prices in the latter part of the 20th century, the MTG section of the New Zealand plant was shut down.

Increasing oil prices, fast development of countries like China and geopolitical reasons have led to renewed interest in the conversion of methanol to fuels and chemicals. The syngas feedstock to manufacture methanol can be produced from crude oil, natural gas as well as coal. The main process for converting coal to syngas is gasification and this can also be employed to use biomass as a renewable feedstock for methanol production in the future. The many aspects of methanol and its potential impact on the chemical and fuels industry and broader on our future economy have been highlighted by Olah [101, 102]. In a strive to be

less dependent from oil imports, China has commercialized the methanol-to-olefins (MTO) process with several plants currently under construction. The discovery of Union Carbide that HSAPO-34 can convert methanol with high selectivity to light olefins has been at the base of these developments. This has also led to several demonstration units [103]. In another embodiment, low-acidic HZSM-5 is used to convert methanol with high selectivity to propylene (methanol-to-propylene, MTP) [104].

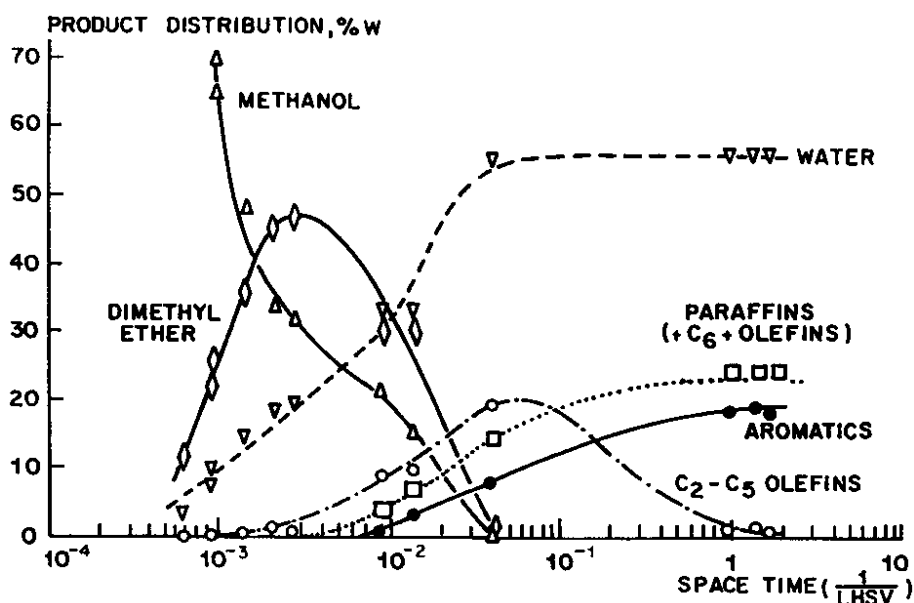


Figure 1.4: Product yields in the methanol conversion reaction over a HZSM-5 zeolite as a function of the space time [100].

The catalytic performance from methanol conversion significantly depends on the shape-selective and acidic properties of the microporous materials employed [103]. Mechanistically, there have been many proposals to explain the formation of hydrocarbons from methanol conversion in zeolites, which have been recently reviewed by Olsbye et al. [103]. An important realization about the mechanism has been that it occurs through a hydrocarbon pool [105, 106]. This pool contains mainly methylated aromatics and these are the key intermediates in mechanisms involving paring and side-chain methylation (Fig. 1.5).

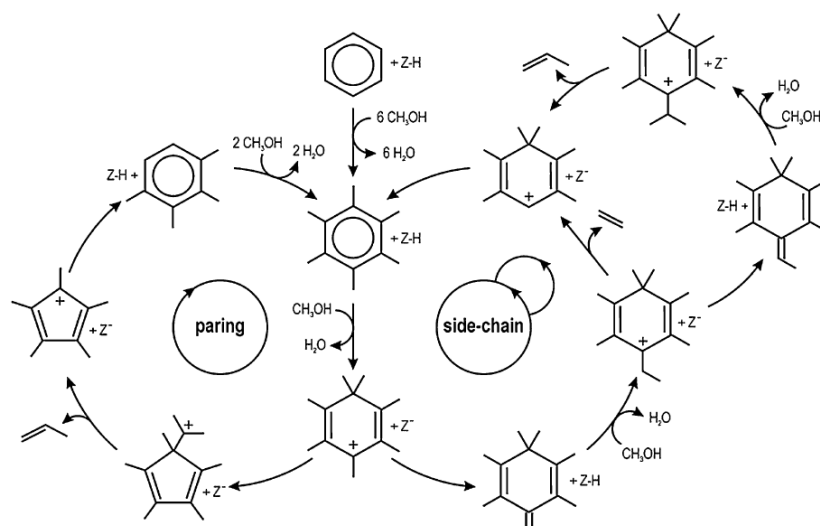


Figure 1.5: Paring and side-chain mechanisms for ethylene and propylene formation involving methylated benzenes as organocatalytic reaction intermediates (reproduced from Lesthaeghe et al. [107]).

Whilst most MTH (methanol-to-hydrocarbons) research had focused on HSAPO-34 until about a decade ago, it was more recently realized that also alkenes may be part of the hydrocarbon reaction intermediates that will give rise to formation of hydrocarbons from methanol [108, 109]. Thus, the dual-cycle concept has been introduced for medium-pore zeolites such as HZSM-5 (Fig. 1.6).

A major disadvantage of carrying out MTH reactions over zeolites is the formation of carbonaceous residue that slowly deactivates the zeolite surface. The rate of deactivation appears to depend on the zeolite topology, the acidity and the reaction conditions. For instance, it has been found that HZSM-5 cokes at a slower rate than HSAPO-34, likely of the smaller size of the intersections of HZSM-5 compared to the large cavities of the CHA structure. The location of coke that deactivates the catalyst has not been resolved yet with some proposing that external coke is responsible for activity loss in case of HZSM-5, whereas internal blocking of micropores of CHA is the cause of the more rapid deactivation of HSAPO-34 [103]. Also, the strength and density of the acid sites has a strong influence on the rate of deactivation. HSSZ-13, the more acidic aluminosilicate counterpart of the silico-aluminophosphate, deactivates faster than HSAPO-34 under similar conditions. At lower temperature, the deactivation rate is expectedly lower; Bleken et al. observed that at

low temperature the total methanol conversion capacity of HSSZ-13 was higher than that of HSAPO-34 [110]. A higher density of Brønsted acid sites results in faster deactivation, presumably because of increased probability of consecutive reactions of the products that will ultimately give rise to coke [111]. In accordance with this, Ryoo and co-workers have found that the rate of coke formation is significantly lower for nanolayered HZSM-5 zeolite [51], although these authors attributed higher catalyst stability mainly to the presence of mesopores that can cope better with large coke deposits.

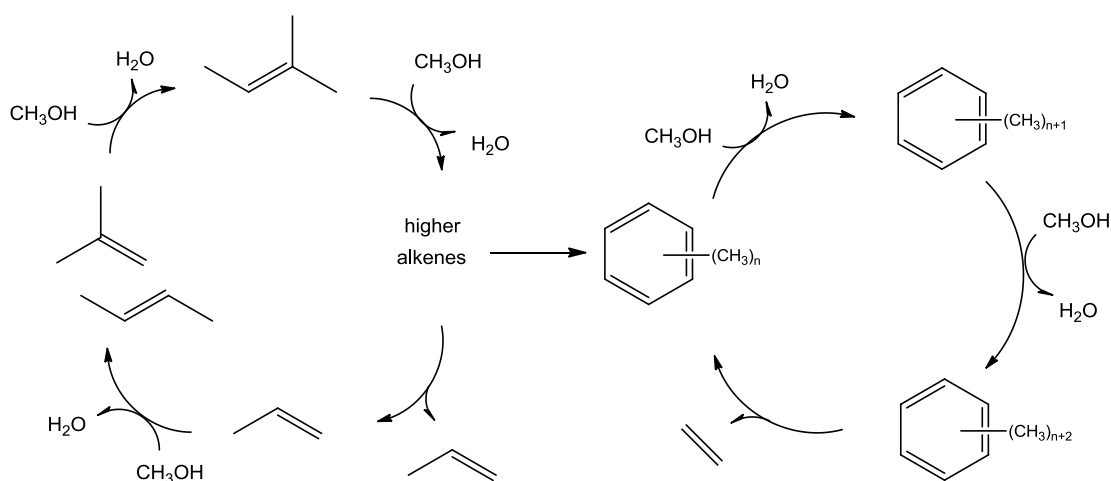


Figure 1.6: Dual-cycle concept proposed for HZSM-5, involving the polymethylated benzene reaction intermediates (right) as well as higher alkene reaction intermediates that crack into lighter olefins, part of which are methylated to higher olefins.

1.4 Scope of thesis

Methanol is a promising platform molecule, which can be produced from a wide range of fossil and renewable feedstocks via synthesis gas. It is poised to become an important intermediate in the production of chemicals and it can also be used as a fuel. There exist a large number of possible applications of zeolites in the transformation of methanol to chemicals and fuels. The main aim of this thesis is to explore the use of hierarchical zeolites to improve the performance of acidic zeolites for methanol conversion reactions.

Chapter 2 describes results of a study of the design, synthesis and characterization of hierarchical SSZ-13 zeolites. Computational modeling provided input for the design of a mesopore, whose action was such that it acted as a crystal growth inhibitor for chabazite zeolite. By tailoring the mesopore structure and its amount in the synthesis gel, it was

shown for the first time how a small template molecule acting to direct the zeolite structure formation and an amphiphilic mesoporegen cooperated in the formation of a truly hierarchical zeolite. The acidic and catalytic properties for the methanol-to-olefins reaction of a range of hierarchical SSZ-13 zeolites are reported in chapter 3. This chapter also discloses the main deactivation mechanism of these zeolites.

Chapter 4 explores a number of approaches to further increase the stability of chabazite zeolite. Firstly, it is attempted to prepare hierarchical SSZ-13 zeolites using the mesoporegens developed in chapter 2 and 3 but with a higher Si/Al ratio. A related approach is the use of an organosilane to interrupt the crystal growth. Finally, attempts were made to silylate the external surface as it was reported in chapter 3 that coke deactivation predominantly occurs on the external surface. Another line of work explored in chapter is mesopore generation in SAPO-34.

Chapter 5 provides an in-depth study of unilamellar and multilamellar HZSM-5 zeolites with a Si/Al ratio between 30 and 50. By variation of the number of quaternary ammonium ions in the template attempts were made to tailor the thickness of nanolayered ZSM-5 zeolites. The effect of these modifications on the location and nature of Al species in framework and extraframework positions was investigated in detail. This led to pronounced acidity differences. The catalytic performance of these hierarchical zeolite materials in the methanol-to-hydrocarbons reaction was correlated to their textural and acidic properties.

Chapter 6 explores the synthesis of nanolayered HZSM-5 zeolites with relatively low Si/Al ratio. The predominant work in this field relates to nanolayered HZSM-5 with a Si/Al > 30, which is not always desirable for catalytic applications. From computational modeling it was inferred that an inherent problem might be the size of the amphiphilic template, in particular the size of the end group. Shortening the end group led to a much better fit of the template in nanolayered zeolites. The synthesis of nanolayered HZSM-5 with a Si/Al ratio of 20 was further optimized towards high crystallinity and high Brønsted acidity.

References

- [1] I. Chorkendorff, and J.W. Niemantsverdriet. 2003. *Concepts of Modern Catalysis and Kinetics*. WILEY-VCH, Weinheim.
- [2] J.N. Armor, *Catal. Today* 163 (2011) 3-9.
- [3] M. Boudart, *Top. Catal.* 1 (1994) 405-414.
- [4] G.W. Huber, S. Iborra, and A. Corma, *Chem. Rev.* 106 (2006) 4044-4098.
- [5] D.M. Alonso, J.Q. Bond, and J.A. Dumesic, *Green Chemistry* 12 (2010) 1493-1513.
- [6] S. Zinoviev, F. Muller-Langer, P. Das, N. Bertero, P. Fornasiero, M. Kaltschmitt, G. Centi, and S. Miertus, *ChemSusChem* 3 (2010) 1106-1133.
- [7] H. De St. Claire Deville, *Comptes. Rendus Acad. Sci.* 54 (1862) 324-327.
- [8] R.M. Barrer, *J. Chem. Soc.* (1948) 127-132.
- [9] R.M. Barrer, L. Hinds, and E.A. White, *J. Chem. Soc.* (1953) 1466-1475.
- [10] C.S. Cundy, and P.A. Cox, *Microporous Mesoporous Mater.* 82 (2005) 1-78.
- [11] G. Bellussi. 2004. Zeolite catalysts for the production of chemical commodities: BTX derivatives. In *Stud. Surf. Sci. Catal.*, E. van Steen, I.M. Claeys, and L.H. Callanan, editors. Elsevier. 53-65.
- [12] T. Maesen, 2007. Chapter 1 In *Stud. Surf. Sci. Catal.*, J. Cejka, H. van Bekkum, A. Corma, and F. Schüth, editors. Elsevier. 1-12.
- [13] B. Yilmaz, and U. Muller, *Top. Catal.* 52 (2009) 888-895.
- [14] S. Bahatia. 1990. In *Zeolite catalysis: Principles and applications*. CRC Press.
- [15] L.A. Pine, P.J. Maher, and W.A. Wachter, *J. Catal.* 85 (1984) 466-476.
- [16] E.M. Flanigen, R.W. Broach, and S.T. Wilson. 2010. *Zeolites in Industrial Separation and Catalysis*. S. Kulprathipanja, editor. Wiley-VCH, 1-26.
- [17] W. Vermeiren, and J.P. Gilson, *Top. Catal.* 52 (2009) 1131-1161.
- [18] J.C. Spry, and W.H. Sawyer. 1975. Configuration Diffusion Effects in Catalytic Demetallation of Petroleum Feedstocks. In 68th Annual AIChE Meeting. Preprint Paper No. 30c, Los Angeles.
- [19] E.J.M. Hensen, D.G. Poduval, V. Degirmenci, D. Ligthart, W.B. Chen, F. Mauge, M.S. Rigutto, and J.A.R. van Veen, *J. Phys. Chem. C* 116 (2012) 21416-21429.
- [20] J. Perez-Ramirez, C.H. Christensen, K. Egeblad, C.H. Christensen, and J.C. Groen, *Chem. Soc. Rev.* 37 (2008) 2530-2542.
- [21] J. Garcia-Martinez, K. Li, and G. Krishnaiah, *Chem. Commun.* 48 (2012) 11841-11843.
- [22] M.E. Davis, C. Saldarriaga, C. Montes, J. Garces, and C. Crowder, *Nature* 331 (1988) 698-699.
- [23] A. Corma, M.J. Diaz-Cabanas, J.L. Jorda, C. Martinez, and M. Moliner, *Nature* 443 (2006) 842-845.
- [24] J.L. Sun, C. Bonneau, A. Cantin, A. Corma, M.J. Diaz-Cabanas, M. Moliner, D.L.

- Zhang, M.R. Li, and X.D. Zou, *Nature* 458 (2009) 1154-U1190.
- [25] A. Corma, M.J. Diaz-Cabanas, J. Jiang, M. Afeworki, D.L. Dorset, S.L. Soled, and K.G. Strohmaier, *PNAS* 107 (2010) 13997-14002.
- [26] J.X. Jiang, J.L. Jorda, J.H. Yu, L.A. Baumes, E. Mugnaioli, M.J. Diaz-Cabanas, U. Kolb, and A. Corma, *Science* 333 (2011) 1131-1134.
- [27] R. Martinez-Franco, M. Moliner, Y.F. Yun, J.L. Sun, W. Wan, X.D. Zou, and A. Corma, *PNAS* 110 (2013) 3749-3754.
- [28] C.C. Freyhardt, M. Tsapatsis, R.F. Lobo, K.J. Balkus, and M.E. Davis, *Nature* 381 (1996) 295-298.
- [29] K.G. Strohmaier, and D.E.W. Vaughan, *J. Am. Chem. Soc.* 125 (2003) 16035-16039.
- [30] A. Corma, M.J. Diaz-Cabanas, F. Rey, S. Nicolououlas, and K. Boulahya, *Chem. Commun.* (2004) 1356-1357.
- [31] A. Corma, M. Diaz-Cabanas, J. Martinez-Triguero, F. Rey, and J. Rius, *Nature* 418 (2002) 514-517.
- [32] R.F. Lobo, *Nature* 443 (2006) 757-758.
- [33] C.H. Lin, R.K. Chiang, and K.H. Lii, *J. Am. Chem. Soc.* 131 (2009) 2068-+.
- [34] B.J. Schoeman, J. Sterte, and J.E. Otterstedt, *J. Chem. Soc. - Chem. Commun.* (1993) 994-995.
- [35] L. Tosheva, and V.P. Valtchev, *Chem. Mater.* 17 (2005) 2494-2513.
- [36] C.T. Kresge, M.E. Leonowicz, W.J. Roth, J.C. Vartuli, and J.S. Beck, *Nature* 359 (1992) 710-712.
- [37] D.Y. Zhao, J.L. Feng, Q.S. Huo, N. Melosh, G.H. Fredrickson, B.F. Chmelka, and G.D. Stucky, *Science* 279 (1998) 548-552.
- [38] D.Y. Zhao, Q.S. Huo, J.L. Feng, B.F. Chmelka, and G.D. Stucky, *J. Am. Chem. Soc.* 120 (1998) 6024-6036.
- [39] A.J.J. Koekkoek, H.C. Xin, Q.H. Yang, C. Li, and E.J.M. Hensen, *Microporous Mesoporous Mater.* 145 (2011) 172-181.
- [40] I. Schmidt, A. Boisen, E. Gustavsson, K. Stahl, S. Pehrson, S. Dahl, A. Carlsson, and C.J.H. Jacobsen, *Chem. Mater.* 13 (2001) 4416-4418.
- [41] A.H. Janssen, A.J. Koster, and K.P. de Jong, *Angew. Chem. Int. Ed.* 40 (2001) 1102-1104.
- [42] Y.S. Tao, H. Kanoh, L. Abrams, and K. Kaneko, *Chem. Rev.* 106 (2006) 896-910.
- [43] S. van Donk, A.H. Janssen, J.H. Bitter, and K.P. de Jong, *Catal. Rev. Sci. Eng.*, 45 (2003) 297-319.
- [44] J. Perez-Ramirez, C.H. Christensen, K. Egeblad, and J.C. Groen, *Chem. Soc. Rev.* 37 (2008) 2530-2542.
- [45] J.C. Groen, L.A.A. Peffer, J.A. Moulijn, and J. Perez-Ramirez, *Chem. Eur. J.* 11 (2005) 4983-4994.
- [46] J.C. Groen, W.D. Zhu, S. Brouwer, S.J. Huynink, F. Kapteijn, J.A. Moulijn, and J.

- Perez-Ramirez, J. Am. Chem. Soc. 129 (2007) 355-360.
- [47] A. Karlsson, M. Stocker, and R. Schmidt, *Microporous Mesoporous Mater.* 27 (1999) 181-192.
- [48] L.M. Huang, W.P. Guo, P. Deng, Z.Y. Xue, and Q.Z. Li, *J. Phys. Chem. B* 104 (2000) 2817-2823.
- [49] F.J. Liu, T. Willhammar, L. Wang, L.F. Zhu, Q. Sun, X.J. Meng, W. Carrillo-Cabrera, X.D. Zou, and F.S. Xiao, *J. Am. Chem. Soc.* 134 (2012) 4557-4560.
- [50] F.S. Xiao, L.F. Wang, C.Y. Yin, K.F. Lin, Y. Di, J.X. Li, R.R. Xu, D.S. Su, R. Schlogl, T. Yokoi, and T. Tatsumi, *Angew. Chem. Int. Ed.* 45 (2006) 3090-3093.
- [51] M. Choi, H.S. Cho, R. Srivastava, C. Venkatesan, D.H. Choi, and R. Ryoo, *Nat. Mater.* 5 (2006) 718-723.
- [52] A. Inayat, I. Knoke, E. Spiecker, and W. Schwieger, *Angew. Chem. Int. Ed.* 51 (2012) 1962-1965.
- [53] H.C. Xin, A. Koekkoek, Q.H. Yang, R. van Santen, C. Li, and E.J.M. Hensen, *Chem. Commun.* (2009) 7590-7592.
- [54] L.-H. Chen, X.-Y. Li, J.C. Rooke, Y.-H. Zhang, X.-Y. Yang, Y. Tang, F.-S. Xiao, and B.-L. Su, *J. Mater. Chem.* 22 (2012) 17381-17403.
- [55] A.J.J. Koekkoek, C.H.L. Tempelman, V. Degirmenci, M.L. Guo, Z.C. Feng, C. Li, and E.J.M. Hensen, *Catal. Today* 168 (2011) 96-111.
- [56] A.J.J. Koekkoek, V. Degirmenci, and E.J.M. Hensen, *J. Mater. Chem.* 21 (2011) 9279-9289.
- [57] M. Choi, R. Srivastava, and R. Ryoo, *Chem. Commun.* (2006) 4380-4382.
- [58] R. Srivastava, M. Choi, and R. Ryoo, *Chem. Commun.* (2006) 4489-4491.
- [59] G.V. Shanbhag, M. Choi, J. Kim, and R. Ryoo, *J. Catal.* 264 (2009) 88-92.
- [60] K. Cho, H.S. Cho, L.-C. de M enorval, and R. Ryoo, *Chem. Mater.* 21 (2009) 5664-5673.
- [61] C.J.H. Jacobsen, C. Madsen, J. Houzvicka, I. Schmidt, and A. Carlsson, *J. Am. Chem. Soc.* 122 (2000) 7116-7117.
- [62] X. Wei, and P.G. Smirniotis, *Microporous Mesoporous Mater.* 89 (2006) 170-178.
- [63] M. Kustova, P. Hasselriis, and C. Christensen, *Catal. Lett.* 96 (2004) 205-211.
- [64] H.C. Xin, J. Zhao, S.T. Xu, J.P. Li, W.P. Zhang, X.W. Guo, E.J.M. Hensen, Q.H. Yang, and C. Li, *J. Phys. Chem. C* 114 (2010) 6553-6559.
- [65] A. Boisen, I. Schmidt, A. Carlsson, S. Dahl, M. Brorson, and C.J.H. Jacobsen, *Chem. Commun.* (2003) 958-959.
- [66] A.H. Janssen, I. Schmidt, C.J.H. Jacobsen, A.J. Koster, and K.P. de Jong, *Microporous Mesoporous Mater.* 65 (2003) 59-75.
- [67] Z.X. Yang, Y.D. Xia, and R. Mokaya, *Adv. Mater.* 16 (2004) 727-732.
- [68] S.I. Cho, S.D. Choi, J.H. Kim, and G.J. Kim, *Adv. Funct. Mater.* 14 (2004) 49-54.
- [69] A. Sakthivel, S.-J. Huang, W.-H. Chen, Z.-H. Lan, K.-H. Chen, T.-W. Kim, R. Ryoo,

- A.S.T. Chiang, and S.-B. Liu, *Chem. Mater.* 16 (2004) 3168-3175.
- [70] C. Sun, J. Du, J. Liu, Y. Yang, N. Ren, W. Shen, H. Xu, and Y. Tang, *Chem. Commun.* 46 (2010) 2671-2673.
- [71] H. Li, Y. Sakamoto, Z. Liu, T. Ohsuna, O. Terasaki, M. Thommes, and S. Che, *Microporous Mesoporous Mater.* 106 (2007) 174-179.
- [72] Y. Tao, H. Kanoh, and K. Kaneko, *J. Am. Chem. Soc.* 125 (2003) 6044-6045.
- [73] Y. Tao, H. Kanoh, and K. Kaneko, *J. Phys. Chem. B* 107 (2003) 10974-10976.
- [74] Y. Tao, H. Kanoh, and K. Kaneko, *Langmuir* 21 (2004) 504-507.
- [75] W.-C. Li, A.-H. Lu, R. Palkovits, W. Schmidt, B. Spliethoff, and F. Schüth, *J. Am. Chem. Soc.* 127 (2005) 12595-12600.
- [76] Y. Kang, W. Shan, J. Wu, Y. Zhang, X. Wang, W. Yang, and Y. Tang, *Chem. Mater.* 18 (2006) 1861-1866.
- [77] Y. Shi, X. Li, J. Hu, J. Lu, Y. Ma, Y. Zhang, and Y. Tang, *J. Mater. Chem.* 21 (2011) 16223-16230.
- [78] H. Zhu, Z. Liu, Y. Wang, D. Kong, X. Yuan, and Z. Xie, *Chem. Mater.* 20 (2007) 1134-1139.
- [79] L. Wang, C. Yin, Z. Shan, S. Liu, Y. Du, and F.-S. Xiao, *Colloids Surf., A* 340 (2009) 126-130.
- [80] W. Fan, M.A. Snyder, S. Kumar, P.S. Lee, W.C. Yoo, A.V. McCormick, R.L. Penn, A. Stein, and M. Tsapatsis, *Nat. Mater.* 7 (2008) 984-991.
- [81] H. Chen, J. Wydra, X. Zhang, P.-S. Lee, Z. Wang, W. Fan, and M. Tsapatsis, *J. Am. Chem. Soc.* 133 (2011) 12390-12393.
- [82] F.-S. Xiao, L. Wang, C. Yin, K. Lin, Y. Di, J. Li, R. Xu, D.S. Su, R. Schlögl, T. Yokoi, and T. Tatsumi, *Angewandte Chemie* 118 (2006) 3162-3165.
- [83] L. Wang, Z. Zhang, C. Yin, Z. Shan, and F.-S. Xiao, *Microporous Mesoporous Mater.* 131 (2010) 58-67.
- [84] S. Liu, X. Cao, L. Li, C. Li, Y. Ji, and F.-S. Xiao, *Colloids Surf., A* 318 (2008) 269-274.
- [85] H. Wang, and T.J. Pinnavaia, *Angew. Chem. Int. Ed.* 45 (2006) 7603-7606.
- [86] H.B. Zhu, Z.C. Liu, D.J. Kong, Y.D. Wang, and Z.K. Xie, *J. Phys. Chem. C* 112 (2008) 17257-17264.
- [87] J. Zhao, Z. Hua, Z. Liu, Y. Li, L. Guo, W. Bu, X. Cui, M. Ruan, H. Chen, and J. Shi, *Chem. Commun.* (2009) 7578-7580.
- [88] M.B. Yue, L.B. Sun, T.T. Zhuang, X. Dong, Y. Chun, and J.H. Zhu, *J. Mater. Chem.* 18 (2008) 2044-2050.
- [89] F.N. Gu, F. Wei, J.Y. Yang, N. Lin, W.G. Lin, Y. Wang, and J.H. Zhu, *Chem. Mater.* 22 (2010) 2442-2450.
- [90] M. Choi, K. Na, J. Kim, Y. Sakamoto, O. Terasaki, and R. Ryoo, *Nature* 461 (2009) 246-250.
- [91] K. Na, M. Choi, W. Park, Y. Sakamoto, O. Terasaki, and R. Ryoo, *J. Am. Chem. Soc.*

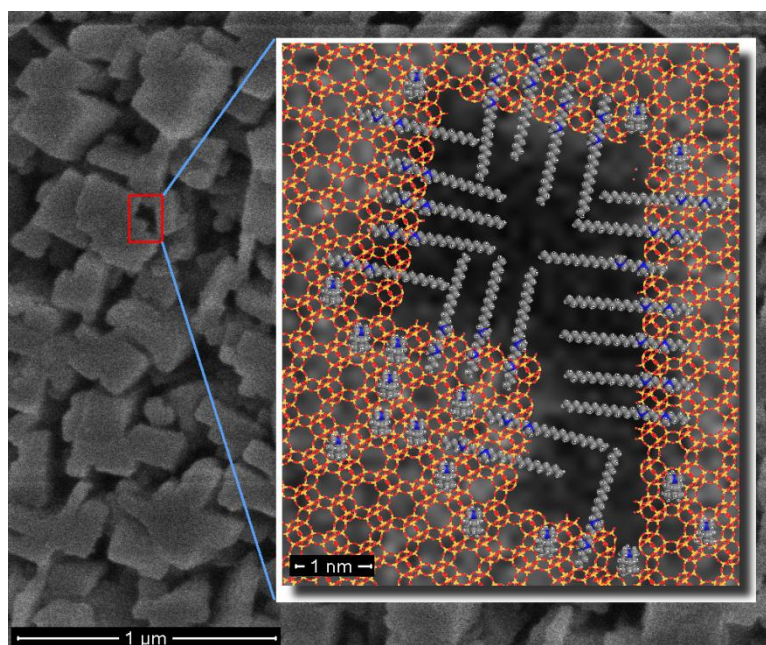
- 132 (2010) 4169-4177.
- [92] K. Na, C. Jo, J. Kim, K. Cho, J. Jung, Y. Seo, R.J. Messinger, B.F. Chmelka, and R. Ryoo, *Science* 333 (2011) 328-332.
- [93] M. Choi, K. Na, and R. Ryoo, *Chem. Commun.* (2009) 2845-2847.
- [94] K. Na, M. Choi, and R. Ryoo, *J. Mater. Chem.* 19 (2009) 6713-6719.
- [95] K. Na, W. Park, Y. Seo, and R. Ryoo, *Chem. Mater.* 23 (2011) 1273-1279.
- [96] W. Park, D. Yu, K. Na, K.E. Jelfs, B. Slater, Y. Sakamoto, and R. Ryoo, *Chem. Mater.* 23 (2011) 5131-5137.
- [97] A.J.J. Koekkoek, W. Kim, V. Degirmenci, H. Xin, R. Ryoo, and E.J.M. Hensen, *J. Catal.* 299 (2013) 81-89.
- [98] C.D. Chang, *Cat. Rev. - Sci. Eng.* 25 (1983) 1-118.
- [99] C.D. Chang, *Catal. Today* 13 (1992) 103-111.
- [100] C.D. Chang, *Cat. Rev. - Sci. Eng.* 26 (1984) 323-345.
- [101] G.A. Olah, *Angew. Chem. Int. Ed.* 44 (2005) 2636-2639.
- [102] G.A. Olah, A. Goepfert, and G.K.S. Prakash. 2006. *Beyond Oil and Gas: The Methanol Economy*. Wiley-VCH.
- [103] U. Olsbye, S. Svelle, M. Bjorgen, P. Beato, T.V.W. Janssens, F. Joensen, S. Bordiga, and K.P. Lillerud, *Angew. Chem. Int. Ed.* 51 (2012) 5810-5831.
- [104] H. Koempel, and W. Liebner, in: F.B. Noronha, M. Schmal, and E.F. Sousa Aguiar, (Eds.), *Natural Gas Conversion VIII, Proceedings of the 8th Natural Gas Conversion Symposium*. 261-267.
- [105] I.M. Dahl, and S. Kolboe, *J. Catal.* 149 (1994) 458-464.
- [106] I.M. Dahl, and S. Kolboe, *J. Catal.* 161 (1996) 304-309.
- [107] D. Lesthaeghe, A. Horre, M. Waroquier, G.B. Marin, and V. Van Speybroeck, *Chem. Eur. J.* 15 (2009) 10803-10808.
- [108] S. Svelle, F. Joensen, J. Nerlov, U. Olsbye, K.P. Lillerud, S. Kolboe, and M. Bjorgen, *J. Am. Chem. Soc.* 128 (2006) 14770-14771.
- [109] M. Bjorgen, S. Svelle, F. Joensen, J. Nerlov, S. Kolboe, F. Bonino, L. Palumbo, S. Bordiga, and U. Olsbye, *J. Catal.* 249 (2007) 195-207.
- [110] F. Bleken, M. Bjorgen, L. Palumbo, S. Bordiga, S. Svelle, K.P. Lillerud, and U. Olsbye, *Top. Catal.* 52 (2009) 218-228.
- [111] M. Guisnet, L. Costa, and F.R. Ribeiro, *J. Mol. Catal. A: Chem.* 305 (2009) 69-83.

Chapter 2

Synthesis and Characterization of Mesoporous SSZ-13 Zeolite by a Dual Templating Method

Summary

Hierarchical SSZ-13 zeolites were synthesized by combining N,N,N-trimethyl-1-adamantan ammonium hydroxide (TMAOH) as the structure-directing agent for chabazite formation with mono- and diquaternary ammonium-type and organoilane mesoporogens and extensively characterized for their structural and textural properties. Mesoporous SSZ-13 zeolites can be synthesized in one step by combining TMAOH and the diquaternary ammonium-type surfactant $C_{22-4-4}Br_2$, which induces considerable mesoporosity without impeding zeolite microporosity. The mesopore volume increases with the mesoporegen/SDA ratio.



2.1 Introduction

Zeolites are microporous crystalline aluminosilicates, which are widely used in the petrochemical industry for acid-catalyzed reactions. The strong Brønsted acidity of zeolites resides in tetrahedral Al^{3+} substitutions in the microporous SiO_2 framework, their combination giving rise to size- and shape-selective acid catalysis. Zeolites are usually synthesized in the form of relatively large crystals, which may lead to mass transport limitations during catalytic reactions. Many synthesis strategies, therefore, deal with improving the accessibility of zeolites either by increasing the size of the micropores [1] or by decreasing the size of the crystalline zeolite domains. The former is especially relevant for the (hydro) conversion of heavy feedstocks. Often, however, relatively small pores are essential to achieve desired activity and selectivity in reactions with hydrocarbons. In such case, the diffusion lengths can be decreased either by synthesizing nanocrystals [2] or by introducing substantial mesoporosity in zeolite crystals during their hydrothermal synthesis step or by post-synthesis treatments [3,4]. Earlier, many attempts have been made to combine structure directing agents (SDAs) for zeolite growth with surfactants usually employed to synthesize ordered mesoporous silicas. At best, this approach resulted in intimate mixtures of small zeolite crystals and amorphous mesoporous silica, however, with little benefit for catalysis [5,6]. The problem can be overcome by the use of cationic polymers [7,8] or by using surfactants that are covalently attached to the crystallizing zeolite phase [9,10].

Several papers review the various methods to synthesize hierarchical zeolites, either by bottom-up approaches or by post-synthesis treatment of zeolites [11-14]. Of the latter type of approaches, desilication has been attempted to improve the catalytic performance of H-SSZ-13, however, without benefit for the methanol-to-olefins (MTO) reaction [15]. SSZ-13 is a zeolite with the chabazite (CHA) topology containing large cavities of 9.4 Å interconnected by small 8 membered ring pore openings with a size of 3.8 Å. In its silicoaluminophosphate form (SAPO-34) it is the preferred catalyst for the MTO process, which is an important step in the conversion of synthesis gas into polymer-grade olefins from methanol [16]. In this process, the presence of mesopores helps to decrease the negative effects of coke deposition, which renders large parts of the zeolite crystal inaccessible.

Herein, we report the first successful direct synthesis of a highly crystalline zeolite by the self-organization of an aluminosilicate framework around two templates, one to generate the microporous framework, the other to introduce mesoporosity.

2.2 Experimental

2.2.1 Synthesis of materials

Synthesis of templates

$C_{22-6-6}Br_2$: The surfactant $(C_{22}H_{45}-N^+(CH_3)_2-C_6H_{12}-N^+(CH_3)_2-C_6H_{13})Br_2$ was synthesized according to literature [17]. Firstly, 4.1 g (0.01 mol) 1-bromodocosane (Aldrich, 96 %) was dissolved in 50 ml toluene and added dropwise into a mixture of 17.2 g (0.1 mol) N, N, N', N'-tetramethyl-1,6-hexanediamine (Aldrich, 99 %) and 50 ml acetonitrile. The mixture was stirred for 3 h at room temperature and then overnight at 70 °C under reflux. After cooling to room temperature, the solution was kept in a refrigerator at 4 °C for 1 h. Afterwards, it was filtered and washed with diethyl ether. Finally, the resulting solid was dried in a vacuum oven at 50 °C. The product was $[C_{22}H_{45}-N^+(CH_3)_2-C_6H_{12}-N(CH_3)_2]Br$. Secondly, 5.6 g (0.01 mol) $[C_{22}H_{45}-N^+(CH_3)_2-C_6H_{12}-N(CH_3)_2]Br$ and 2.8 g (0.02 mol) 1-bromohexane (Aldrich, 98 %) were dissolved in 100 ml acetonitrile and 10 ml ethanol and kept at 70 °C under reflux overnight. After cooling to room temperature, it was kept in a refrigerator at 4 °C for 1 h the solid product was filtered, washed with diethyl ether and dried in a vacuum oven at 50 °C. The final product was $(C_{22}H_{45}-N^+(CH_3)_2-C_6H_{12}-N^+(CH_3)_2-C_6H_{13})Br_2$ (denoted as $C_{22-6-6}Br_2$).

$C_{22-4-4}Br_2$: The surfactant $(C_{22}H_{45}-N^+(CH_3)_2-C_4H_8-N^+(CH_3)_2-C_4H_9)Br_2$ was synthesized in a similar manner as $C_{22-6-6}Br_2$. Firstly, 4.1 g (0.01 mol) 1-bromodocosane (Aldrich, 96 %) was dissolved in 20 ml toluene and added dropwise into the 20 ml solution of 10.3 g (0.07 mol) N, N, N', N'-tetramethyl-1,4-butanediamine (Aldrich, 98 %) in acetonitrile. The resulting solution was stirred for 3 h at room temperature and then mixed at 70 °C under reflux overnight. After cooling to room temperature, the solution was kept in a refrigerator at 4 °C for 1 h, filtered and washed with diethyl ether. The resulting solid was dried in a vacuum oven at room temperature. The product was $(C_{22}H_{45}-N^+(CH_3)_2-C_4H_8-N(CH_3)_2)Br$. Secondly, 3.7 g (0.007 mol) $(C_{22}H_{45}-N^+(CH_3)_2-C_4H_8-N(CH_3)_2)Br$ and 1.96 g (0.014 mol) 1-bromobutane (Aldrich, 98 %) were dissolved in 110 ml of acetonitrile and then stirred in a reflux condenser at 70 °C overnight. Next, the solid product was quenched in refrigerator at 4 °C for 1 h, filtered, washed with diethyl ether and dried in a vacuum oven at room temperature. The resulting product was $(C_{22}H_{45}-N^+(CH_3)_2-C_4H_8-N^+(CH_3)_2-C_4H_9)Br_2$ (denoted as $C_{22-4-4}Br_2$).

$C_{22-4}Br$: The surfactant $(C_{22}H_{45}-N^+(CH_3)_2-C_4H_9)Br$ was synthesized in a single step. 8.2 g (0.02 mol) 1-bromodocosane (Aldrich, 96 %) was dissolved in 40 ml toluene and added drop wise into 4.04 g (0.04 mol) of N,N-dimethylbutylamine (Sigma-Aldrich, 99%) under

vigorous stirring. This mixture was refluxed at 70 °C for 24 h. The solid product was kept in refrigerator at 4 °C for 1 h, filtered and washed with cold diethyl ether and finally dried in a vacuum oven at 50 °C. The resulting product was $(C_{22}H_{45}-N^+(CH_3)_2-C_4H_9)Br$ (denoted as $C_{22-4}Br$).

TMAOH: TMAOH template was synthesized according to literature [18].

Synthesis of zeolites

SSZ-13: Conventional SSZ-13 was synthesized according to a literature procedure [19]. 2 g of a 1 M NaOH solution, 4 g 0.5 M N,N,N-trimethyl-1-adamantanammonium hydroxide (TMAOH) and 2.0 g deionized water were mixed together. 0.05 g aluminum hydroxide (Sigma Aldrich) was added to this solution under vigorous stirring. After 30 min, 0.6 g fumed silica (Sigma) was added. The resulting mixture was stirred at room temperature to obtain a homogeneous gel with the composition 10 TMAOH : 10 Na₂O : 3 Al₂O₃ : 100 SiO₂ : 4400 H₂O, which was then transferred into a Teflon-lined autoclave and kept in oven at 160 °C for 4 days. Afterwards, the solid material was recovered by filtration. Finally, the catalyst was calcined at 550 °C for 10 h in static air. The proton form of the zeolite was obtained by triple ion exchange of the calcined zeolite with 1 M NH₄NO₃ at 70 °C for 2 h followed by calcination in static air at 550 °C for 4 h.

SSZ-13(C_{22-4-4}): Mesoporous SSZ-13 zeolites were synthesized by combining $C_{22-4-4}Br_2$ and TMAOH as templates. A series of syntheses was done by varying the $C_{22-4-4}Br_2$ /TMAOH molar ratio between 0.06 and 1.5 (Table 2.1) for the starting molar gel composition x TMAOH : y $C_{22-4-4}Br_2$: 10 Na₂O : 3 Al₂O₃ : 100 SiO₂ : 5000 H₂O. The initial gel was subjected to crystallization in a Teflon-lined stainless-steel autoclave at 160°C for 6 days. After the crystallization, the solid product was collected by filtration, washed with deionized water, and dried at 110 °C. The catalysts were finally calcined at 550 °C for 10 h in static air. The proton forms of the zeolites were obtained by triple ion exchange of the calcined form with 1 M NH₄NO₃ at 70 °C and calcination at 550 °C for 4 h in static air. The final samples are denoted as SSZ-13(C_{22-4-4} , n), where n refers to $C_{22-4-4}Br_2$ /TMAOH molar ratio in the synthesis gel.

SSZ-13(C_{22-6-6}): Mesoporous SSZ-13 catalyst was synthesized by using $C_{22-6-6}Br_2$ and TMAOH as templates. The synthesis procedure was the same as of C_{22-CHA} as explained above. The synthesis gel composition was: 10 TMAOH : 5 $C_{22-6-6}Br_2$: 10 Na₂O : 3 Al₂O₃ : 100 SiO₂ : 5000 H₂O, and the product was denoted as SSZ-13(C_{22-6-6} , n) where n refers to $C_{22-6-6}Br_2$ /TMAOH molar ratio in the synthesis gel.

Table 2.1: Molar compositions of synthesis gels and hydrothermal synthesis conditions for the preparation of SSZ-13 zeolites.

Zeolite	C ₂₂₋₄₋₄ Br ₂	TMAOH	TPOAC	SiO ₂	Al(OH) ₃	NaOH	H ₂ O	T _{synthesis} (°C)	t _{synthesis} (days)
SSZ-13	0	20	0	100	60	20	4400	150	4
SSZ-13(C ₂₂₋₄₋₄ , 0.06)	1	18	0	100	60	20	5000	150	6
SSZ-13 (C ₂₂₋₄₋₄ , 0.17)	2.5	15	0	100	60	20	5000	150	6
SSZ-13 (C ₂₂₋₄₋₄ , 0.50)	5	10	0	100	60	20	5000	150	6
SSZ-13 (C ₂₂₋₄₋₄ , 1.50)	7.5	5	0	100	60	20	5000	150	6
SSZ-13 (C ₂₂₋₄₋₄ , ∞)	10	0	0	100	60	20	5000	150	6
SSZ-13 (C ₂₂₋₄ , 1)	10	10	0	100	60	20	5000	150	6
SSZ-13 (C ₂₂₋₆₋₆ , 0.5)	5	10	0	100	60	20	5000	150	6
SSZ-13 (TPOAC, 0.04)	0	20	4	100	60	20	4400	150	6
SSZ-13 (TPOAC, 0.08)	0	20	8	100	60	20	4400	150	6

SSZ-13(TPOAC): Mesoporous SSZ-13 zeolites were also synthesized by using octadecyl-(3-trimethoxysilylpropyl)-ammonium chloride (TPOAC, ABCR) as a mesopore-directing organosilane surfactant. A series of synthesis experiments were carried out by varying the amount of TPOAC in the synthesis gel. The gel molar composition was x TPOAC: 20 TMAOH : 10 Na₂O : 3 Al₂O₃ : 100 SiO₂ : 4400 H₂O with x being either 4 or 8. The mixture was stirred further at room temperature until a homogeneous gel was obtained. The resulting gel was transferred into a Teflon-lined stainless steel autoclave and kept at 160 °C for 6 days. Thereafter, the solid material was recovered by filtration. The catalysts were finally calcined at 550 °C for 10 h in static air. The proton forms of the zeolites were obtained by triple ion exchange of the calcined form with 1 M NH₄NO₃ at 70 °C and calcination at 550 °C for 4 h in static air. The catalysts are denoted as SSZ-13(TPOAC, n), where n represents the molar TPOAC/Si ratio in the synthesis gel.

2.2.2 Physicochemical properties

Basic characterization

X-ray diffraction patterns were recorded on a Bruker D4 Endeavor diffractometer using Cu K α radiation in the 2θ range of 5-60 °. Elemental analyses were carried out by ICP-OES (Spectro Ciros CCD ICP optical emission spectrometer with axial plasma viewing). To extract the metals, the catalysts were dissolved in 1.5 ml of an acid mixture of HF/HNO₃/H₂O. Argon adsorption experiments were determined at 87.6 K on a Micromeritics ASAP 2020 instrument in static mode. The samples were outgassed at 400 °C for 8 h prior to the sorption measurements. The Langmuir adsorption isotherm model was used to determine the total surface area (S_L) in the p/p_0 range between 0.05-0.20. The mesopore volume (V_{meso}) and mesopore size distribution was calculated from the adsorption branch of the isotherm by the Barrett-Joyner-Halenda (BJH) method. The micropore volume was determined by the t -plot method (thickness range 0.34-0.40 nm). The micropore diameter was calculated by the NLDFT model. Use was made of the model for cylindrical pores for argon on oxides at 87 K. No use was made of regularization. In order to test the hydrothermal stability of the catalysts, first 0.1 g of catalyst was placed in an autoclave together with 25 mL of water. Next, the autoclave was kept at 160 °C in oven for 5 days. In a separate experiment the sample was kept under similar conditions for 15 days. Afterwards, the zeolites were dried at 110 °C in ambient atmosphere and XRD spectra were recorded.

Electron microscopy

Scanning electron microscopy (SEM) images were performed on a FEI Quanta 3D-FEG dual-beam microscope. The catalysts were coated with gold prior to measurements. Transmission electron microscopy (TEM) pictures were taken on a FEI Tecnai 20 at 200 kV. The catalysts were suspended in ethanol and dispersed over a carbon coated holey Cu grid with a film prior to measurements.

Vibrational spectroscopy

UV Raman spectra were recorded with a Jobin-Yvon T64000 triple stage spectrograph with spectral resolution of 2 cm^{-1} operating in double subtractive mode. The laser line at 325 nm of a Kimmon He-Cd laser was used as exciting source. The power of the laser on the sample was 4 mW.

NMR spectroscopy

Nuclear Magnetic Resonance (NMR) spectra were recorded on a Bruker DMX-500 NMR spectrometer. For ^{29}Si Magic Angle Spinning (MAS) NMR measurement, a standard Bruker MAS probehead was used with rotor diameter of 4 mm, at a spinning rate of 10 kHz. TMA was employed as an external reference for the chemical shift. Two-dimensional $^{29}\text{Si}\{^1\text{H}\}$ heteronuclear correlation (HETCOR) NMR spectra were recorded with a rectangular contact pulse of 3 ms with carefully matched amplitudes on both channels. Tetramethylsilane (TMS) was employed as an external reference for the chemical shift for ^1H and ^{29}Si NMR.

2.3 Results and Discussion

2.3.1 Design of the template

Table 2.2. Interaction of candidate quaternary ammonium templates with all-silica chabazite framework.^a

Mesoporegen	C ₂₂₋₄₋₄	C ₂₂₋₄₋₄	C ₂₂₋₆₋₆	C ₂₂₋₄
Configuration ^b	I	II	I	II
$\Delta E_{\text{framework-template}}$	-247	-242	-242	-155
$\Delta E_{\text{framework destabilization}}$	+28	+28	+39	+28

^a All energies in kJ/mol; ^b Configuration I: one quaternary ammonium center at the surface, II: quaternary ammonium center(s) below surface.

To guide the design of the mesoporegen we carried out a computational study to determine the best fit of three candidate surfactants, $\text{C}_{22}\text{H}_{45}\text{-N}^+(\text{CH}_3)_2\text{-(CH}_2)_4\text{-N}^+(\text{CH}_3)_2\text{-C}_4\text{H}_9$ (C₂₂₋₄₋₄),

($C_{22}H_{45}-N^+(CH_3)_2-(CH_2)_6-N^+(CH_3)_2-C_6H_{13}$) (C_{22-6-6}) and $C_{22}H_{45}-N^+(CH_3)_2-C_4H_9$ (C_{22-4}) in the growing CHA framework. The first one was chosen because tetraethylammonium is a known SDA for CHA [22]. By linking two such moieties with a hydrophobic tail, we expect significantly interactions with SSZ-13 in analogy with the C_{22-6-6} for ZSM-5 [17]. A further comparison is made with C_{22-4} to establish the effect of a single quaternary ammonium head group. We employ classical Molecular Dynamics (MD) simulations because it allows efficient sampling of phase space and takes into account van der Waals interactions in contrast to DFT [23]. The all-silica CHA model contained $2 \times 4 \times 3$ unit cells with one surface terminated by silanol groups. In all cases, the zeolite contained TMAd cations and one mesoporegen. The template-framework interaction and framework destabilization energies are given in Table 2.2.

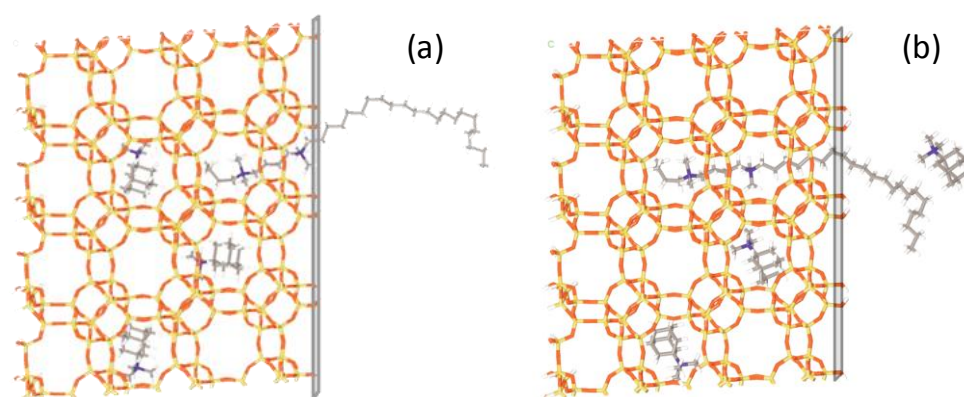


Figure 2.1: Snapshot of a MD simulation of a $C_{22-4.4}$ cation interacting with the CHA framework in the presence of 3 TMAd cations, corresponding to configuration I (a), with its two ammonium centers in the large cavities (configuration II) and the hydrophobic tail sticking out at the zeolite surface (b) (red: oxygen; yellow: silicon, gray: carbon, white: hydrogen; blue: nitrogen). The gray plane indicates the terminating zeolite surface.

Fig. 2.1a shows the preferred configuration (I) of $C_{22-4.4}$ in SSZ-13 with one quaternary ammonium center in the cavity below the surface and the other one at the surface. The interaction energy (-247 kJ/mol) is higher than that of TMAd in SSZ-13 (-163 kJ/mol). This configuration is preferred over configuration II with both quaternary ammonium centers in the cavities below the surface (Fig. 2.1b), because the interaction energy (-242 kJ/mol) is lower than the configuration in which two TMAd templates occupy these cavities (-326 kJ/mol). Note that in this case one TMAd cation is placed outside the framework (Fig. 2.1b). C_{22-6-6} adopts a similar configuration I, but the terminal hexyl fragment is folded back in the large cavity, likely because of the repulsion with the TMAd in the adjacent cavity (Fig. 2.2a). This leads to stronger framework destabilization compared to $C_{22-4.4}$. With C_{22-4} in configuration I the template became detached from the zeolite surface (Fig. 2.2b). In

configuration II, the framework-template interaction energy is below that of TMA₂OH. Based on these results, we predicted C₂₂₋₄₋₄Br₂ to be the preferred mesoporegen.

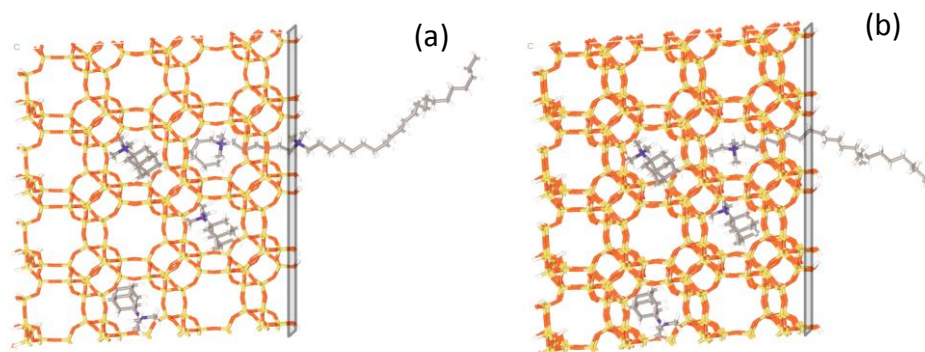


Figure 2.2: The C₂₂₋₆₋₆ template in configuration I showing the folding of the terminating hexyl chain back into the cavity leading to increased destabilization of the zeolite framework (a), and the C₂₂₋₄ template in the CHA model with its ammonium center in the large cavity below the surface (configuration II) and the hydrophobic tail sticking out at the zeolite surface (b).

2.3.2 Structure and morphology

The XRD patterns of the as-synthesized zeolites are shown in Fig. 2.3 (for XRD patterns of calcined zeolites, see Fig. 2.4). The SSZ-13(C₂₂₋₄₋₄) zeolites prepared at C₂₂₋₄₋₄Br₂/TMA₂OH ratios between 0.06 and 1.5 exhibit the typical XRD patterns of zeolites with the chabazite (CHA) framework topology. The patterns are similar to the one of SSZ-13 prepared with only TMA₂OH as structure-directing agent (Fig. 2.3a). The absence of a broad peak around 23 ° in these patterns indicates that none of these zeolites contains a substantial fraction of amorphous silica (Fig. 2.3). This is in line with the high crystallinities computed from the XRD patterns (indicated in Fig. 2.3). SSZ-13(C₂₂₋₄₋₄, ∞) prepared without the structure-directing agent (SDA) TMA₂OH in the synthesis gel is completely amorphous (Fig. 2.3f). The XRD patterns of the SSZ-13(TPOAC) samples (Figs. 2.3i and 1j) are also very similar to that of SSZ-13 with the exception that the pattern of SSZ-13(TPOAC, 0.08) contains additional diffraction peaks around 8, 8.9, 23.9 and 24.4 °. These peaks point to the presence of ZSM-5 as a competing phase. It implies that too high a TPOAC/TMA₂OH ratio will lead to the formation of ZSM-5 as an impurity. TPOAC has been previously used to introduce mesoporosity in ZSM-5 crystals [20]. Koekkoek et al. have shown that the use of TPOAC can also lead to the formation of small ZSM-5 zeolite fragments in a predominantly amorphous silica material [21]. It was also attempted to employ C₂₂₋₆₋₆Br₂, used before to synthesize nanostructured ZSM-5 [17], as a mesoporegen in an otherwise identical synthesis of SSZ-13. In this case, we also obtained SSZ-13 (Fig. 2.3h), but the crystallinity was much

lower (68%) as compared to the materials prepared in the presence of $C_{22-4-4}Br_2$ and TMAOH. When only one quaternary ammonium ion was present in the co-template ($C_{22-4}Br$), the resulting materials were completely amorphous (Fig. 2.3g). The XRD patterns of the calcined zeolites and the crystallinities derived thereof (Fig. 2.4) are very similar. To verify their stability, calcined SSZ-13 and SSZ-13(C_{22-4-4} , 0.17) were subjected to hydrothermal treatment in an autoclave at 160 °C for 5 and 15 days. The XRD patterns (Fig. 2.5) evidence that the zeolites are stable under these conditions: the peak intensities are similar to those of their parent zeolites and no line broadening was observed.

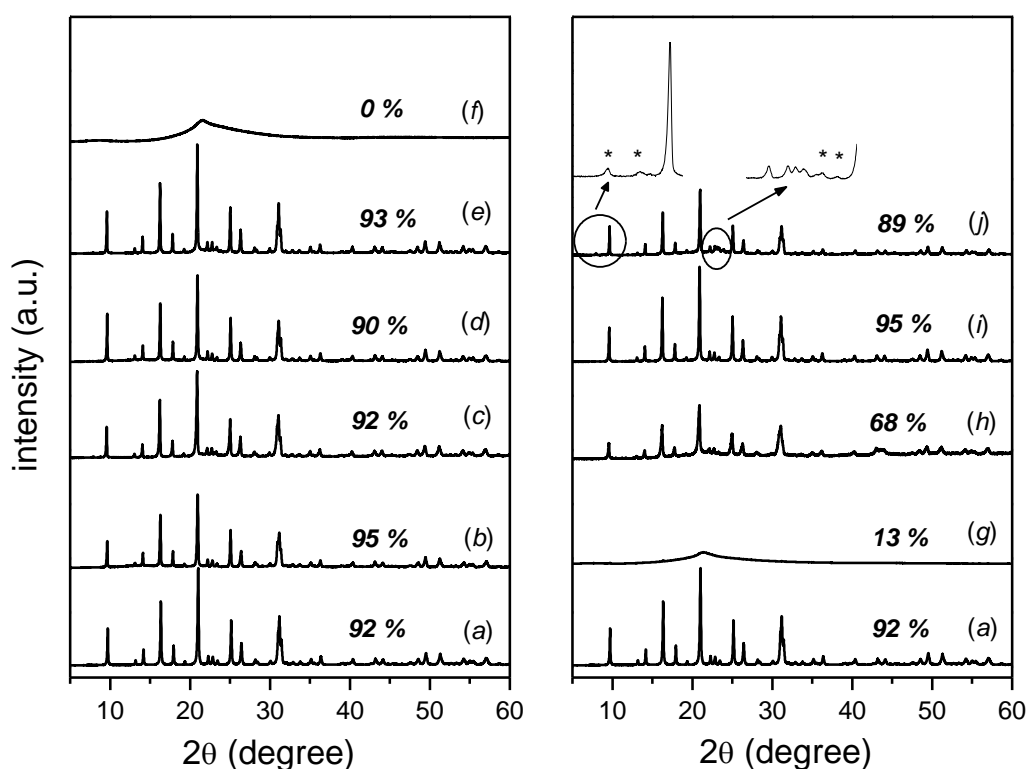


Figure 2.3: XRD patterns of as-synthesized (a) conventional SSZ-13, (b) SSZ-13(C_{22-4-4} , 0.06), (c) SSZ-13(C_{22-4-4} , 0.17), (d) SSZ-13(C_{22-4-4} , 0.50), (e) SSZ-13(C_{22-4-4} , 1.50), (f) SSZ-13(C_{22-4-4} , ∞), (g) SSZ-13(C_{22-4} , 1), (h) SSZ-13(C_{22-6-6} , 0.50), (i) SSZ-13(TPOAC, 0.04) and (j) SSZ-13(TPOAC, 0.08). The asterisk indicates the peaks belonging to the MFI structure and italic numbers indicate the crystallinities of zeolites determined by TOPAS software.

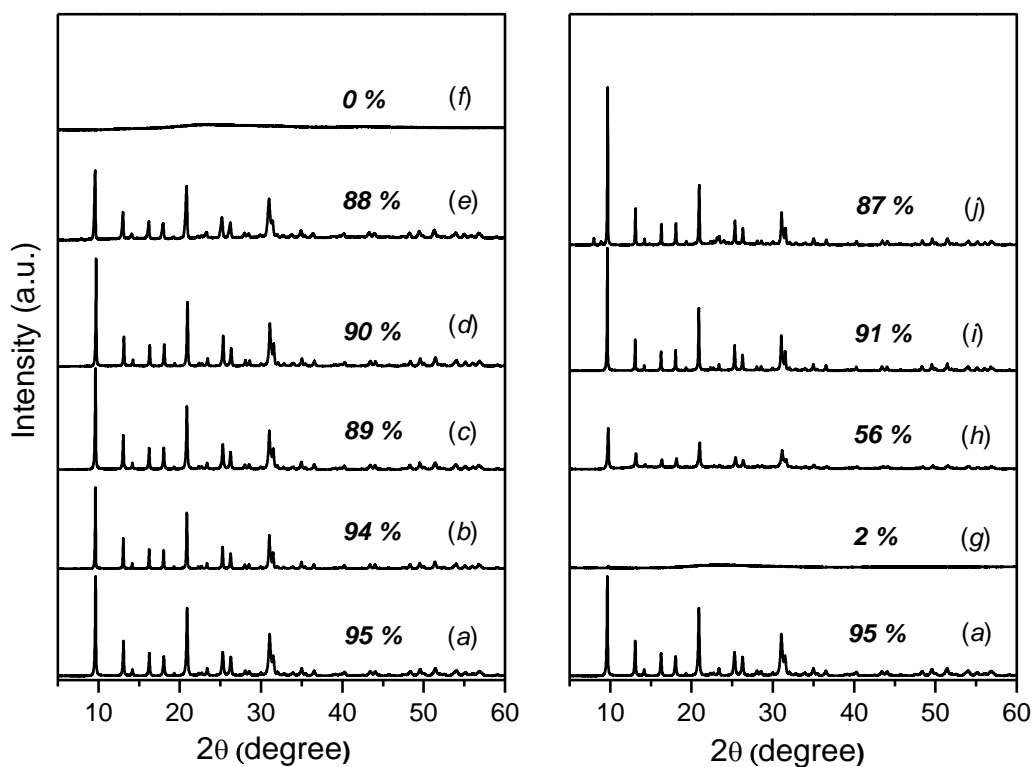


Figure 2.4: XRD patterns of calcined (a) conventional SSZ-13, (b) SSZ-13($C_{22-4,4}$, 0.06), (c) SSZ-1 ($C_{22-4,4}$, 0.17), (d) SSZ-13($C_{22-4,4}$, 0.50), (e) SSZ-13($C_{22-4,4}$, 1.50), (f) SSZ-13 ($C_{22-4,4}$, -4-4), (g) SSZ-1 $_{22,4}$, 1), (h) SSZ-13($C_{22-6,6}$, 0.50), (i) SSZ-13(TPOAC, 0.04) and (j) SSZ-13(TPOAC, 0.08). Italic numbers indicate the crystallinities of zeolites determined by TOPAS software.

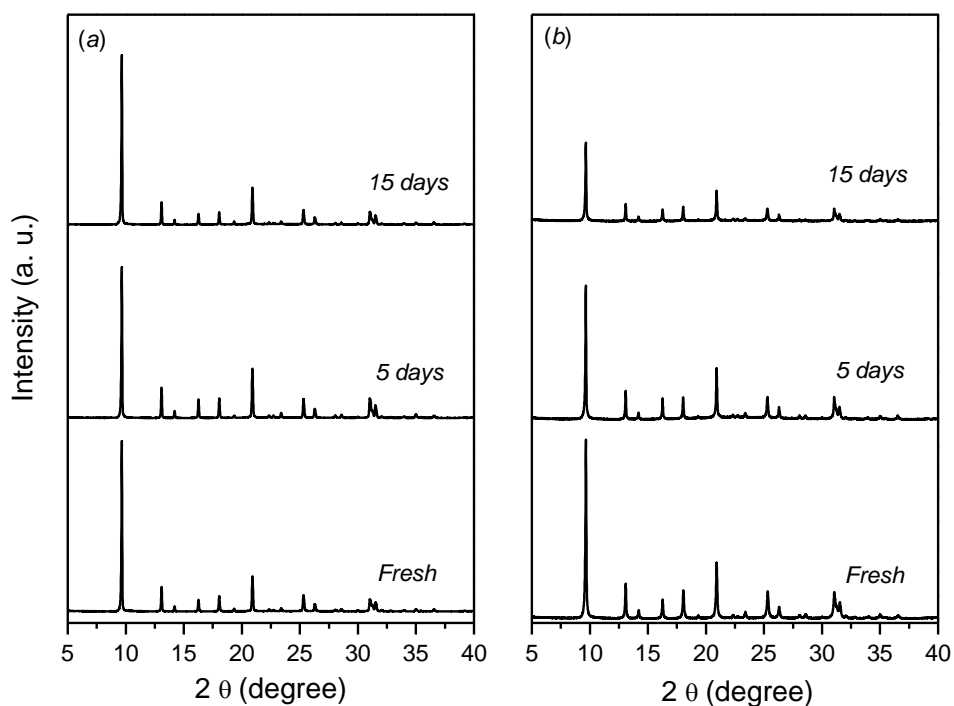


Figure 2.5. XRD patterns of (a) conventional SSZ-13 and (b) mesoporous SSZ-13($C_{22-4,4}$, 0.17) zeolites before and after hydrothermal treatment for 5 and 15 days.

Fig. 2.6 shows the UV Raman spectra of the calcined zeolites. The spectrum of SSZ-13 contains two intense bands at 330 cm^{-1} and 476 cm^{-1} and two weaker ones at 800 cm^{-1} and 1200 cm^{-1} . The intense band centered around 476 cm^{-1} is assigned to the $\nu_s(\text{T-O-T})$ mode (with T being Si or Al) of CHA zeolite [24]. This band is typical for zeolite frameworks consisting of a combination of four-membered and six- or eight-membered rings [25]. The peak observed at 330 cm^{-1} is assigned to the T-O-T vibration mode of the six-membered rings of CHA zeolite. The weak and broad bands at 800 cm^{-1} and 1200 cm^{-1} are typical symmetric and non-symmetric Si-O vibration modes of zeolites [26]. With the exception of amorphous SSZ-13(C_{22-4-4} , ∞), the UV Raman spectra of SSZ-13(C_{22-4-4}) zeolites contain similar bands as that of SSZ-13. This also holds for the SSZ-13(TPOAC) zeolites. The spectrum of SSZ-13(TPOAC, 0.08) contains an additional broad band at 370 cm^{-1} (Fig. 2.6g), which is the $\nu_s(\text{T-O-T})$ mode of the five-membered rings in MFI zeolite [26], confirming the XRD result that this sample contains a small amount of ZSM-5.

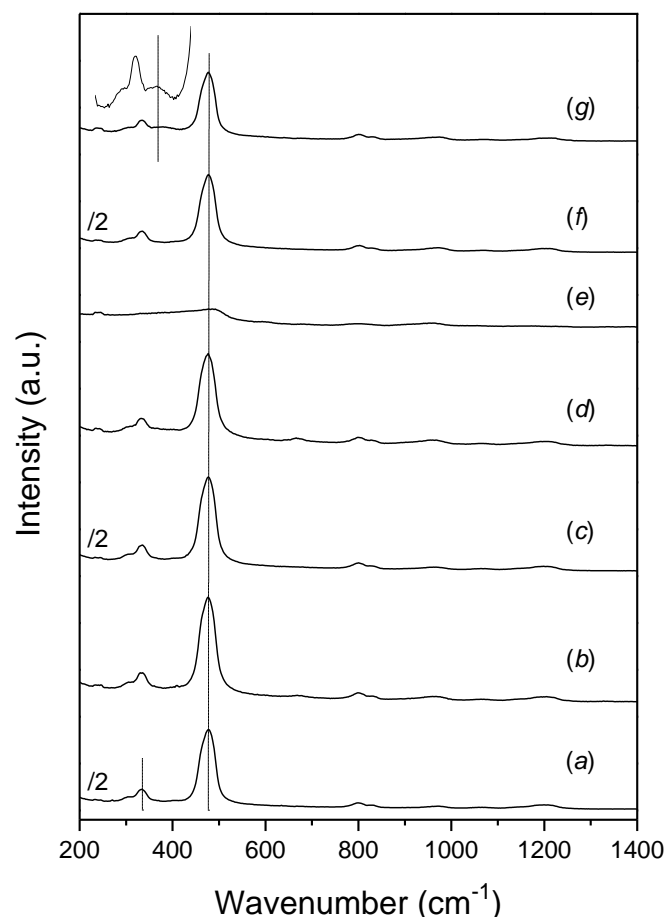


Figure 2.6: UV Raman spectra of (a) conventional SSZ-13, (b) SSZ-13(C_{22-4-4} , 0.17), (c) SSZ-13(C_{22-4-4} , 0.50), (d) SSZ-13(C_{22-4-4} , 1.50), (e) SSZ-13(C_{22-4-4} , ∞), (f) SSZ-13(TPOAC, 0.04) and (g) SSZ-13(TPOAC, 0.08).

Fig. 2.7 shows representative electron micrographs of the SSZ-13 zeolites. SSZ-13

zeolite consists of large cube-shaped crystals with sizes in the range of 10-20 μm . The particles of the zeolites prepared with $\text{C}_{22-4-4}\text{Br}_2/\text{TMAOH}$ have similar sizes as the crystallites in conventional SSZ-13 with the exception of SSZ-13(C_{22-6-6} , 0.06). Whereas conventional SSZ-13 consists of large single crystals, it is clear that the presence of $\text{C}_{22-4-4}\text{Br}_2$ in the synthesis gel leads to particles that appear as a three-dimensional assembly of smaller crystals. At the scale of the SEM images macropores are visible. The morphology changes with increasing $\text{C}_{22-4-4}\text{Br}_2/\text{TMAOH}$ ratio. At lower ratios the nanocrystal are aligned, whereas they become increasingly randomly oriented with increasing $\text{C}_{22-4-4}\text{Br}_2/\text{TMAOH}$ ratio. An exception is SSZ-13(C_{22-4-4} , 0.06), which appears as an assembly of agglomerated larger crystals. Some of the particles seem to be intergrown and to not contain macropores (Fig. 2.7b) while some have intracrystalline voids (Fig. 2.7h). SSZ-13(C_{22-4-4} , ∞) consists of very small particles with a very broad size distribution. A selection of representative transmission electron microscopy (TEM) images is also given in Fig. 2.7. These show that the zeolites synthesized in the presence of $\text{C}_{22-4-4}\text{Br}_2$ consist of very small crystals below 50 nm. Accordingly, it is inferred that the additional porosity is not restricted to the macrorange as the SEM images suggest, but extends down into the mesorange. The primary particles of amorphous SSZ-13(C_{22-4-4} , ∞) have sizes between 40 and 200 nm and contain mesopores with a size of about 4-5 nm. Fig. 2.8 shows electron micrographs of SSZ-13(TPOAC), SSZ-13(C_{22-6-6} , 0.50) and SSZ-13(C_{22-4} , 1.0). The morphologies of SSZ-13(TPOAC) zeolites are similar to that of SSZ-13(C_{22-4-4}) zeolites shown in Fig. 2.8. The cubic structure is less pronounced, some amorphous material is seen and the nanocrystalline areas seem to be less interconnected. SEM shows that SSZ-13(C_{22-6-6} , 0.50) is a rather disordered material, which on the nanoscale (TEM) consists of cubic-shaped crystals smaller than 50 nm and an amorphous silica-alumina phase containing disordered mesopores. TEM shows that SSZ-13(C_{22-4} , 1.0) is mainly amorphous.

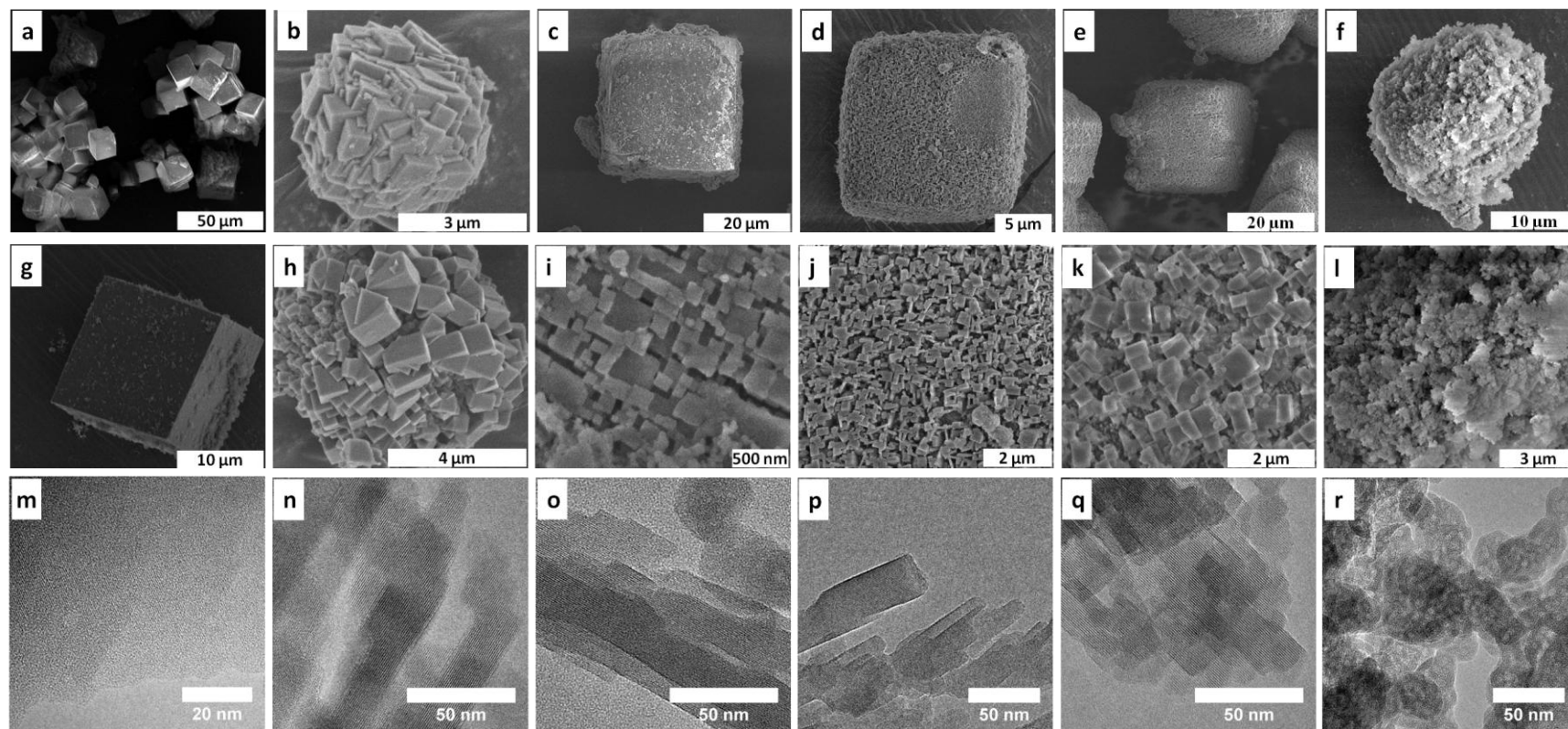


Figure 2.7: SEM images of (a, g) conventional SSZ-13, (b, h) SSZ-13(C₂₂₋₄₋₄, 0.06), (c, i) SSZ-13(C₂₂₋₄₋₄, 0.17), (d, j) SSZ-13(C₂₂₋₄₋₄, 0.50), (e, k) SSZ-13(C₂₂₋₄₋₄, 1.50) and (f, l) SSZ-13(C₂₂₋₄₋₄, ∞) and TEM images of (m) conventional SSZ-13, (n) SSZ-13(C₂₂₋₄₋₄, 0.06), (o) SSZ-13(C₂₂₋₄₋₄, 0.17), (p) SSZ-13(C₂₂₋₄₋₄, 0.50), (q) SSZ-13(C₂₂₋₄₋₄, 1.50) and (r) SSZ-13(C₂₂₋₄₋₄, ∞).

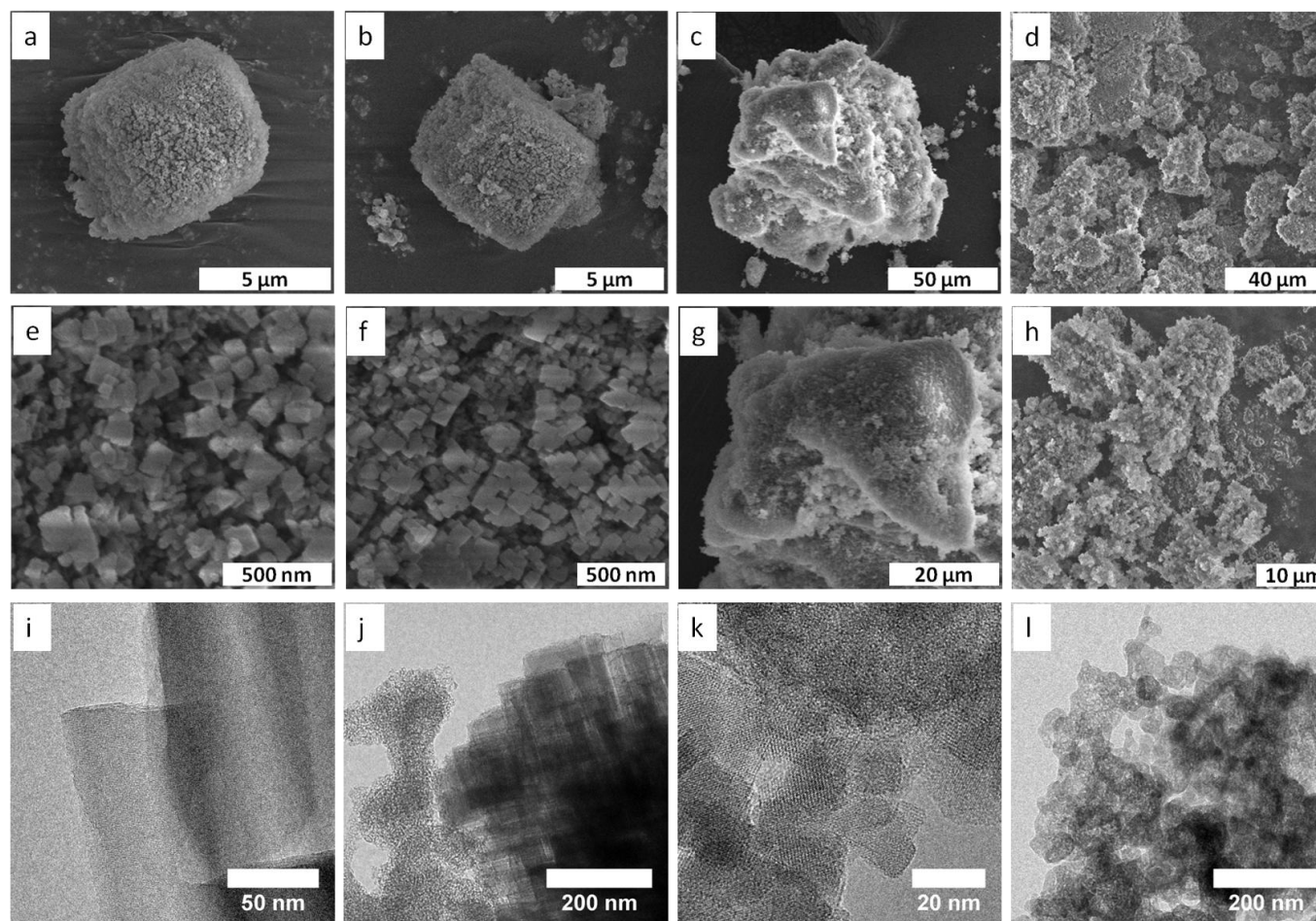


Figure 2.8: SEM images of (a, e) SSZ-13(TPOAC, 0.04), (b, f) SSZ-13(TPOAC, 0.08), (c, g) SSZ-13(C₂₂₋₆₋₆, 0.50) and (d, h) SSZ-13(C₂₂₋₄, 1) and TEM images of (i) SSZ-13(TPOAC, 0.04), (j) SSZ-13(TPOAC, 0.08), (k) SSZ-13(C₂₂₋₆₋₆, 0.50) and (l) SSZ-13(C₂₂₋₄, 1).

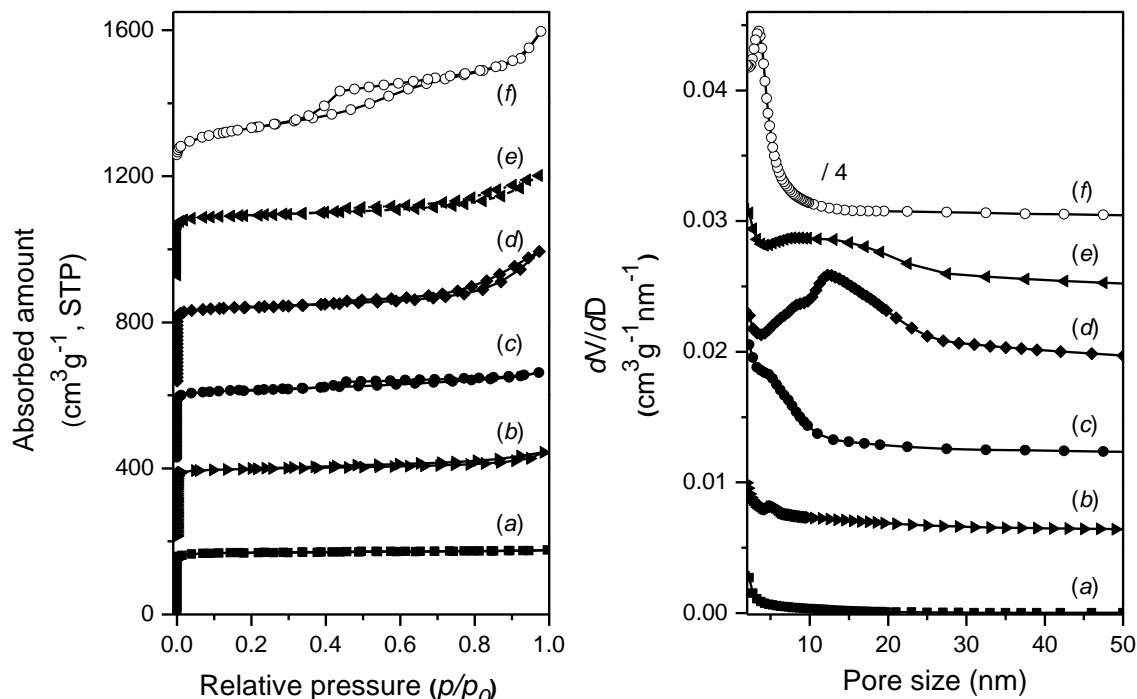


Figure 2.9: (left) Ar physisorption isotherms and (right) pore size distributions of (a) conventional SSZ-13, (b) SSZ-13(C_{22-4-4} , 0.06), (c) SSZ-13(C_{22-4-4} , 0.17), (d) SSZ-13(C_{22-4-4} , 0.50), (e) SSZ-13(C_{22-4-4} , 1.50), (f) SSZ-13(C_{22-4-4} , ∞). The isotherms and the pore size distributions were vertically offset by equal intervals.

Ar adsorption/desorption isotherms and BJH pore size distributions of the calcined zeolites are given in Figs. 2.9 and 2.10. The textural properties derived thereof are summarized in Table 2.3. The isotherm of conventional SSZ-13 is of type I, which is characteristic of microporous materials. The SSZ-13 zeolites prepared with mesopore-directing agents, on the other hand, have the typical type IV isotherms of mesoporous materials. The zeolites with a relative low $C_{22-4-4}Br_2/TMAOH$ ratio have a H4 hysteresis loop. This points to the presence of slit-like mesopores, which can be understood as the mesopore voids between the cubic nanocrystals (e.g., Figs. 2.7o and 3p). The amorphous end member of this series prepared without TMAOH has a H2 hysteresis loop indicative of a disordered mesoporous material. The pore size distribution (PSD) of SSZ-13 shows a single maximum below 2 nm. An NLDFT analysis of the isotherm data points to a micropore diameter of 0.45 nm. The SSZ-13(C_{22-4-4}) zeolites have a relatively broad PSD with the maximum in the mesorange shifting from 5 to 15 nm with increasing $C_{22-4-4}Br_2/TMAOH$ ratio. Fig. 2.10 shows the physisorption isotherms and PSDs of SSZ-13(TPOAC), SSZ-13(C_{22-6-6} , 0.50) and SSZ-13(C_{22-4} , 1). The TPOAC co-templated zeolites have adsorption isotherms typical for disordered mesoporous materials, the mesopore

volume of SSZ-13(TPOAC, 0.08) being larger than that of SSZ-13(TPOAC, 0.04). The isotherm of SSZ-13(C₂₂₋₆₋₆, 0.50) is typical of a material containing micropores and mesopores. In contrast, SSZ-13(C₂₂₋₄, 1) does not contain micropores. The PSDs of these latter two zeolites are quite narrow with maxima at 3 and 5 nm, respectively, resembling those of ordered mesoporous silica.

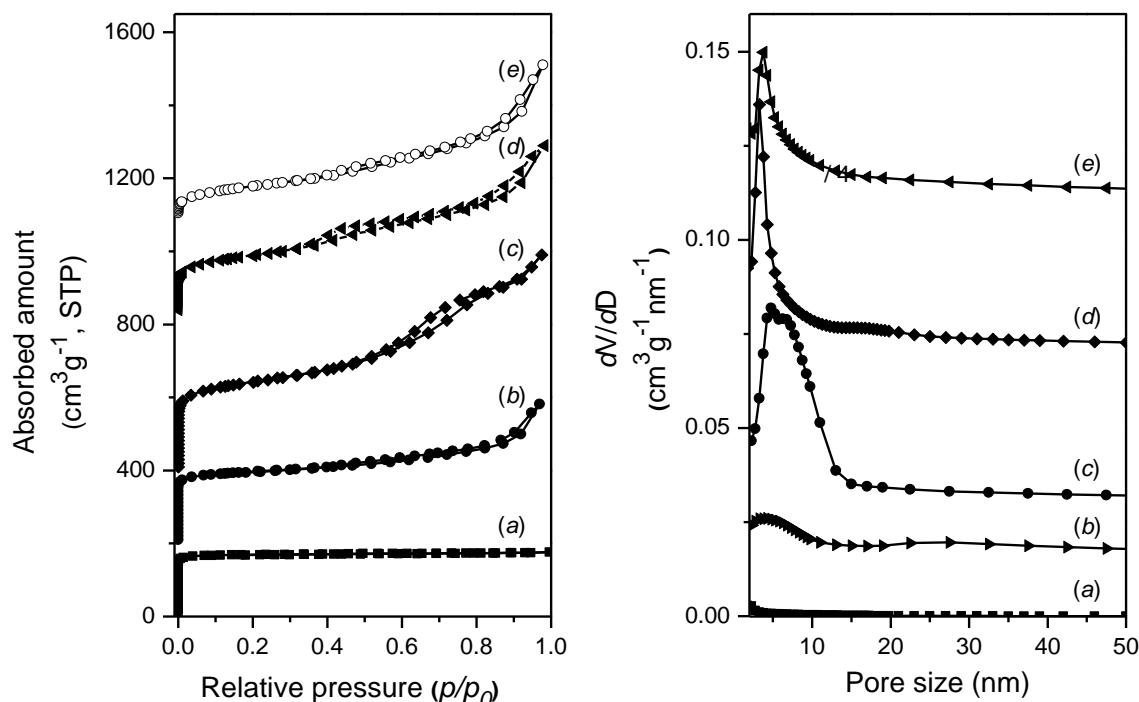


Figure 2.10: (left) Ar adsorption isotherms and (right) pore size distributions of (a) conventional SSZ-13, (b) SSZ-13(TPOAC, 0.04), (c) SSZ-13(TPOAC, 0.08), (d) SSZ-13(C₂₂₋₄, 1) and (e) SSZ-13(C₂₂₋₆₋₆, 0.50). The isotherms of SSZ-13(TPOAC) were vertically offset by equal intervals of 200 cm³ g⁻¹; those of SSZ-13(C₂₂₋₄, 1.0) and SSZ-13(C₂₂₋₆₋₆, 0.50) by equal intervals of 300 cm³ g⁻¹. The pore size distribution curves of SSZ-13(TPOAC) were vertically offset by equal intervals of 0.015 cm³·g⁻¹·nm⁻¹, those of SSZ-13(C₂₂₋₄, 1.0) and SSZ-13(C₂₂₋₆₋₆, 0.50) by equal intervals of 0.04 cm³·g⁻¹·nm⁻¹.

Application of the BET equation to the physisorption data of the hierarchical zeolites proved unsuccessful (negative C values), which is consistent with earlier reports [27, 28]. The total surface area and pore volume of SSZ-13 are 651 m²·g⁻¹ and 0.22 cm³·g⁻¹, respectively (Table 2.3). Its mesopore volume is very small (< 0.1 cm³·g⁻¹). Except for SSZ-13(C₂₂₋₄₋₄, ∞) with a surface area of 386 m²·g⁻¹, all of the mesoporous SSZ-13 zeolites have higher surface areas than conventional SSZ-13. The highest surface area and mesopore volume among the C₂₂₋₄₋₄Br₂ co-templated samples (815 m²·g⁻¹) are for SSZ-13(C₂₂₋₄₋₄, 0.50). SSZ-13(TPOAC, 0.08) has the highest surface area (879 m²·g⁻¹). In contrast to the negligible mesopore volume for SSZ-13, the SSZ-13(C₂₂₋₄₋₄) zeolites have substantial mesopore volumes in the range

0.06-0.34 $\text{cm}^3 \cdot \text{g}^{-1}$. The mesopore volume increases with the $\text{C}_{22-4-4}\text{Br}_2/\text{TMAOH}$ ratio. SSZ-13(C_{22-4-4} , ∞) has the highest mesopore and total pore volume. However, in line with its amorphous nature it does not contain micropores. In spite of the substantial mesopore volumes, the micropore volumes of the SSZ-13(C_{22-4-4}) zeolites are very comparable to that of conventional SSZ-13. Finally, Table 2.3 shows that SSZ-13(C_{22-4} , 1) does not contain any micropores but a substantial amount of mesopores. SSZ-13(C_{22-6-6} , 0.5) combines a micropore volume, which is half of the micropore volume of the SSZ-13(C_{22-4-4}) zeolites, with a high mesopore volume, consistent with its partial crystallinity.

Table 2.3: Textural properties of the calcined SSZ-13 zeolites determined by Ar physisorption.

Zeolite	S_L^a ($\text{m}^2 \cdot \text{g}^{-1}$)	V_{tot}^b ($\text{cm}^3 \cdot \text{g}^{-1}$)	V_{meso}^c ($\text{cm}^3 \cdot \text{g}^{-1}$)	V_{micro}^d ($\text{cm}^3 \cdot \text{g}^{-1}$)
SSZ-13	651	0.22	0.01	0.18
SSZ-13(C_{22-4-4} , 0.06)	724	0.30	0.06	0.22
SSZ-13(C_{22-4-4} , 0.17)	749	0.31	0.07	0.19
SSZ-13(C_{22-4-4} , 0.50)	815	0.46	0.21	0.21
SSZ-13(C_{22-4-4} , 1.50)	673	0.36	0.17	0.16
SSZ-13(C_{22-4-4} , ∞)	386 (279 ^e)	0.44	0.34	0.07
SSZ-13(C_{22-4} , 1)	327	0.53	0.48	0
SSZ-13(C_{22-6-6} , 0.5)	719	0.62	0.45	0.10
SSZ-13(TPOAC, 0.04)	765	0.49	0.27	0.17
SSZ-13(TPOAC, 0.08)	879	0.71	0.53	0.11

^a S_L is the Langmuir surface area obtained in the relative pressure range (p/p_0) of 0.05-0.20; ^b V_{tot} is the total pore volume at $p/p_0 = 0.97$; ^c V_{meso} is the mesopore volume calculated from BJH method; ^d V_{micro} is the micropore volume calculated from t -plot method; ^e BET surface area.

The results discussed above suggest that the C_{22-4-4} template has sufficient interaction with the growing SSZ-13 crystals to introduce substantial mesoporosity in the final zeolite. 2D $^{29}\text{Si}\{^1\text{H}\}$ HETCOR NMR was employed to study the template-silicate interactions of the as-synthesized zeolites. This technique correlates the ^{29}Si and ^1H NMR resonances of ^{29}Si and ^1H nuclear spins that are close (< 1 nm) in the template-aluminosilicate structure [29-31]. Fig. 2.11 show 2D $^{29}\text{Si}\{^1\text{H}\}$ HETCOR NMR spectra of as-synthesized conventional SSZ-13, SSZ-13(C_{22-4-4} , 0.50) and SSZ-13(C_{22-4-4} , ∞). Independently measured direct-excitation ^1H MAS NMR spectra are also shown (Fig. 2.11b). These spectra are composed of proton resonances from TMAH or C_{22-4-4} species. Three partly resolved signals can be recognized: one due to nitrogen-bonded methyl (TMAH) and methylene (C_{22-4-4}) moieties at 3 ppm, one

due to methylene and methine moieties in TMAd at 2 ppm, and one associated with methyl and methylene moieties in the C₂₂ tail of C₂₂₋₄₋₄ at 1 ppm. In comparison, the ¹H NMR projection and sections from the 2D HETCOR NMR data of SSZ-13 (Fig. 2.11c-f, bottom left panel) can be regarded as a broadened version of the direct-excitation spectrum. The broad lineshapes correspond to the “envelope” containing the narrow direct-excitation signals. The cause of this broadening is the hindered mobility of embedded template molecules and, especially, their trimethylammonium moieties inside the aluminosilicate frame. This result implies that TMAd is embedded in the pores of SSZ-13 zeolite. The ¹H NMR projection and sections from the 2D HETCOR NMR data of SSZ-13(C₂₂₋₄₋₄, 0.50) (Fig. 2.11c-f; top panel) are very similar to those shown for TMAdOH and therefore indicate that both TMAd and the quaternary ammonium headgroups of C₂₂₋₄₋₄ are close to the silicon-containing zeolite framework. The very weak correlation peak at 1 ppm arises from the tailgroup H atoms in the C₂₂₋₄₋₄ surfactant indicates that the hydrophobic tailgroup is mobile and relatively distant from the Si atoms in SSZ-13(C₂₂₋₄₋₄, 0.5). This agrees with the preferred location of the headgroup of C₂₂₋₄₋₄ in the zeolite framework as predicted by computational modeling. The correlated signals of proton and silicon are observed to be very weak in the spectra of SSZ-13(C₂₂₋₄₋₄, ∞) (Fig. 2.11, bottom right panel). Relatively speaking, the strongest correlation is that of the headgroups protons with Q⁴ silicon, which is consistent with the formation of ordered mesoporous silica-alumina. It can be argued that the template-silicate interactions are similar to those known in the synthesis of M41S materials [32, 33] in accordance with the XRD, TEM and physisorption results.

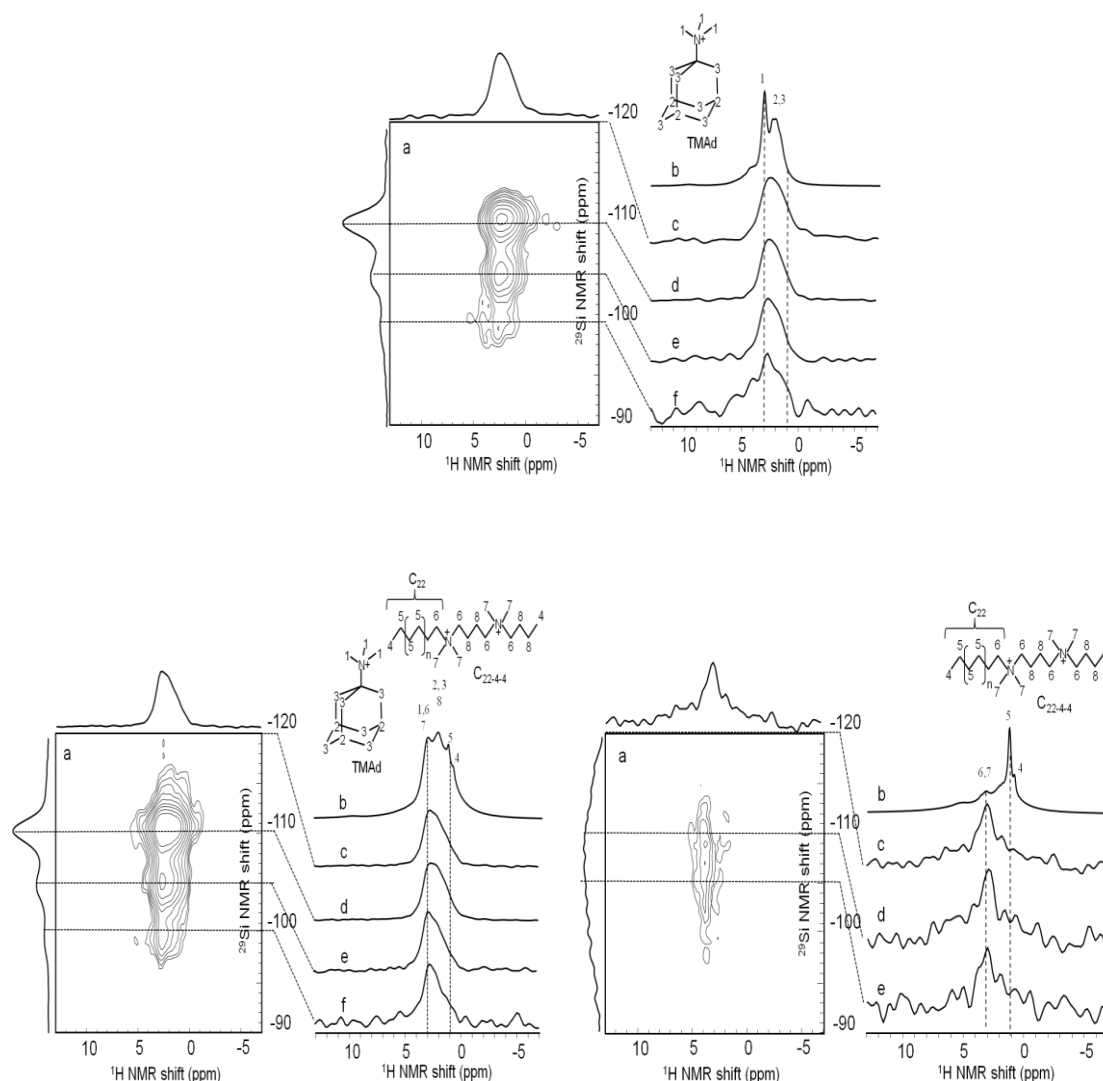


Figure 2.11: 2D $^{29}\text{Si}\{^1\text{H}\}$ HETCOR NMR of (top panel) as-synthesized SSZ-13(C_{22-6-6} , 0.50), (bottom left panel) as-synthesized conventional SSZ-13 and (bottom right panel) as-synthesized SSZ-13(C_{22-4-4} , ∞): (a) 2D $^{29}\text{Si}\{^1\text{H}\}$ HETCOR NMR spectrum with the (^{29}Si NMR) direct frequency axis in vertical direction and ^1H and ^{29}Si NMR projections along the horizontal and vertical axis, respectively; (b) ^1H MAS NMR spectrum indicated above the spectrum; (c) ^1H NMR project from the 2D HETCOR spectrum indicating the cumulative lineshape of all the proton close to silicon atoms, in general; (d-f) ^1H NMR cross-sections from the 2D HETCOR spectrum at ^{29}Si NMR shifts -110, -105 and -100 ppm, assigned to $\text{Q}^4(\text{OAl})$, $\text{Q}^4(1\text{Al})$ and $\text{Q}^3(\text{OAl})$ silicon atoms with respective coordination $\text{Si}(\text{OSi})_4$, $\text{Si}(\text{OSi})_3(\text{OAl})$, $\text{Si}(\text{OSi})_3(\text{OH})$ in the zeolite framework.

2.4 Conclusions

In summary, a set of hierarchical SSZ-13 zeolites was prepared by combining N,N,N-trimethyl-1-adamantan ammonium hydroxide (TMAOH) as a structure-directing agent (SDA) with several mesoporogens ($\text{C}_{22-4-4}\text{Br}_2$, C_{22-4}Br , $\text{C}_{22-6-6}\text{Br}_2$ and TPOAC). Predictive design of templates remains a grand challenge [24]. In our case, computational modeling aided in the design of the mesoporogen, which interacts strongly enough with the

growing zeolite framework and competes with the SDA so that the growth of the zeolite crystal is interrupted. This approach presents a generally applicable strategy for the synthesis of hierarchical zeolites, because it requires only replacing a small part of the conventional SDA by a usually more expensive mesoporegen. This is an advantage over approaches involving the single use of an expensive template, which combines zeolite directing and mesoporegen functions [35].

The resulting zeolites were extensively characterized for their structural and textural properties. The mesoporosity of these zeolites depends on the mesoporegen/SDA ratio, higher ratios leading to more interconnected mesopores. The formation of a highly interconnected network of micro- and mesopores is the result of the inhibition of the growth of the SSZ-13 crystals by inclusion of the C_{22-4-4}^{2+} template.

References

- [1] A. Corma, M.J. Díaz-Cabaña, J. Martínez-Triguero, F. Rey and J. Rius, *Nature* 2002, 418, 514.
- [2] D.P. Serrano, J. Aguado, J.M. Escola, J.M. Rodriguez and A. Peral, *J. Mater. Chem.* 2008, 18, 4210.
- [3] J. Pérez-Ramírez, C.H. Christensen, K. Egeblad, C.H. Christensen and J.C. Groen, *Chem. Soc. Rev.* 2008, 37, 2530.
- [4] R. Chal, C. Gerardin, M. Bulut and S. van Donk, *ChemCatChem* 2011, 3, 67.
- [5] A. Karlsson, M. Stocker and R. Schmidt, *Microporous Mesoporous Mater.* 1999, 27, 181.
- [6] L.M. Huang, W.P. Guo, P. Deng, Z.Y. Xue and Q.Z. Li, *J. Phys. Chem. B* 2000, 104, 2817.
- [7] F. Liu, T. Willhammar, L. Wang, L. Zhu, Q. Sun, X. J. Meng, W. Carrillo-Cabrera, X. Zou, and F.-S. Xiao, *J. Am. Chem. Soc.* 2012, 134, 4557.
- [8] F.-S. Xiao, L. Wang, C. Yin, K. Lin, Y. Di, J. Li, R. Xu, D. S. Su, R. Schlgl, T. Yokoi, and T. Tatsumi, *Angew. Chem. Int. Ed.* 2006, 45, 3090.
- [9] M. Choi, H.S. Cho, R. Srivastava, C. Venkatesan, D.-H. Choi and R. Ryoo, *Nat. Mater.* 2006, 5, 718.
- [10] A. Inayat, I. Knoke, E. Spiecker, W. Schwieger, *Angew. Chem. Int. Ed.* 2012, 51, 1962.
- [11] L.H. Chen, X.Y. Li, J.C. Rooke, Y.H. Zhang, X.Y. Yang, Y. Tang, F.S. Xiao, B.L. Su, *J. Mater. Chem.* 22 (2012) 17381.
- [12] R. Chal, C. Gerardin, M. Bulut, S. van Donk, *ChemCatChem.* 3 (2011) 67.
- [13] K. Egeblad, C.H. Christensen, M. Kustova, C.H. Christensen, *Chem. Mater.* 20 (2008) 946.
- [14] J. Pérez-Ramírez, C.H. Christensen, K. Egeblad, C.H. Christensen, J.C. Groen, *Chem. Soc. Rev.* 37 (2008) 2530.
- [15] L. Sommer, D. Mores, S. Svelle, M. Stöker, B.M. Weckhuysen, U. Olsbye, *Microporous Mesoporous Mater.* 132 (2010) 384.
- [16] Keil, F.J. *Microporous Mesoporous Mater.* 1999, 19, 49.
- [17] M. Choi, K. Na, J. Kim, Y. Sakamoto, O. Terasaki, R. Ryoo, *Nature* 461 (2009) 246.
- [18] S.I. Zones, US Patent (1985) 4544538.
- [19] L.-T. Yuen, S.I. Zone in H. Robson (Ed.), *Verified Syntheses of Zeolitic Materials*, 2nd revised ed., Elsevier Science B.V., Amsterdam, 2001, pp. 126.
- [20] M. Choi, H.S. Cho, R. Srivastava, C. Venkatesan, D.H. Choi, R. Ryoo, *Nature Mater.* 5 (2006) 718.
- [21] A.J.J. Koekkoek, C.H.L. Tempelman, V. Degirmenci, M.L. Guo, Z.C. Feng, C. Li, E.J.M. Hensen, *Catal. Today* 168 (2011) 96.
- [22] B.M. Lok, C.A. Messina, R.L. Patton, R.T. Gajek, T.R. Cannan and E.M. Flanigen, US Patent 1984, 4440871.
- [23] B. Smit and T. L. M. Maesen, *Nature* 2008, 451, 671.
- [24] P.K. Dutta, D.C. Shieh, M. Puri, *Zeolites* 8 (1988) 306.
- [25] P.K. Dutta, K.M. Rao, J.Y. Park, *J. Phys. Chem.* 95 (1991) 6654.

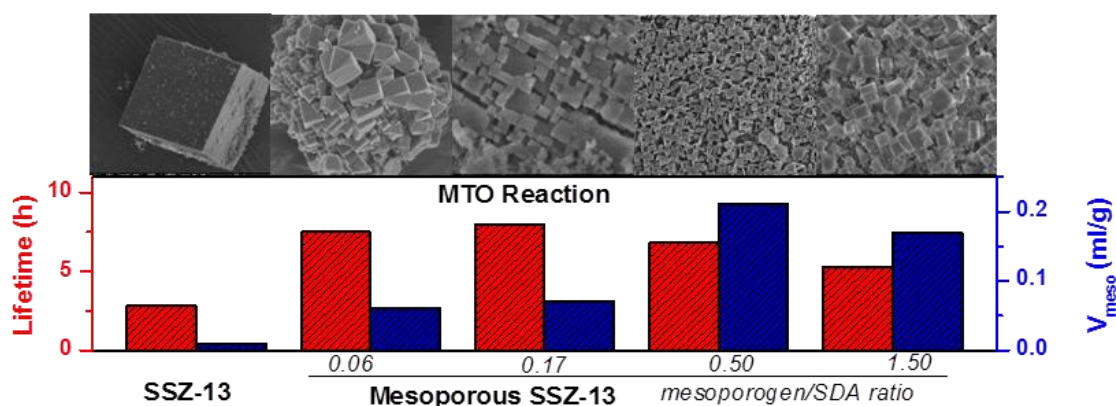
-
- [26] P.K. Dutta, M. Puri, *J. Phys. Chem.* 91 (1987) 4329.
- [27] O. Šolcová, L. Matějová, P. Topka, Z. Musilová and P. Schneider, *J. Porous Mater.* 18 (2011) 557.
- [28] P. Schneider, *Appl. Catal. A: Gen.* 129 (1995) 157.
- [29] M.T. Janicke, C.C. Landry, S.C. Christiansen, D. Kumar, G.D. Stucky, B.F. Chmelka, *J. Am. Chem. Soc.* 120 (1998) 6940.
- [30] K. Na, C. Jo, J. Kim, K. Cho, J. Jung, Y. Seo, R.J. Messinger, B.F. Chmelka, R. Ryoo, *Science* 333 (2011) 328.
- [31] P.C.M.M. Magusin, V.E. Zorin, A. Aerts, C.J.Y. Houssin, A.L. Yakovlev, C.E.A. Kirschhock, J.A. Martens, R.A. Van Santen, *J. Phys. Chem. B* 109 (2005) 22767.
- [32] C.T. Kresge, M.E. Leonowicz, W.J. Roth, J.C. Vartuli, J.S. Beck, *Nature* 359 (1992) 710.
- [33] N. Baccile, G. Laurent, C. Bonhomme, P. Innocenzi, F. Babonneau, *Chem. Mat.* 19 (2007) 1343.
- [34] Lewis, D. W., Catlow, C. R. A., Thomas, J. M., Willock, D. J. & Hutchings, G. J., *Nature* 1996, 382, 604-606; S.M. Woodley and R. Catlow, *Nature Materials* 2008, 7, 937.
- [35] L.T. Yuen, S.I. Zones, T.V. Harris, E.J. Gallegos and A. Auroux, *Microporous Mater.* 1994, 2, 105.

Chapter 3

Catalytic Performance of Mesoporous SSZ-13 Zeolite in the Methanol-to-Olefins Reaction

Summary

The acidic and catalytic properties of the hierarchical SSZ-13 zeolites, synthesized by using N,N,N-trimethyl-1-adamantan ammonium hydroxide (TMAOH) with mono- and diquaternary ammonium-type and organoiline mesoporegens, have been extensively characterized. The hierarchical zeolites exhibit similar Brønsted acidity as SSZ-13, and display increased lifetime in packed-bed MTO experiments than conventional SSZ-13 at similar light olefins yield. The increased lifetime is due to better utilization of the micropore space. With increasing mesoporosity the micropore space is used more efficiently, but also the rate of coke formation at the crystal periphery increases. Accordingly, the most stable zeolite is obtained at a relatively low $C_{22-44}Br_2/SDA$ ratio. These zeolite catalysts can be regenerated without substantial loss of activity.



3.1 Introduction

The methanol-to-olefins (MTO) reaction has attracted widespread attention in the last decades as a potential route for the production of polymer-grade light olefins from methanol [1, 2]. Methanol can be obtained from syngas derived from carbon-containing feedstocks such as coal [3], natural gas [4] and biomass [5, 6]. In UOP's MTO process, zeolite catalysts are employed to convert methanol to a mixture of C₂-C₄ olefins. The technology has recently been commercialized using a H-SAPO-34 zeolite in a fluidized bed catalytic reactor and catalyst regeneration by air calcination [7, 8]. Currently, this process provides profit opportunities because of the low feedstock costs of coal. Ethylene and propylene are obtained at high selectivity and are the primary building blocks for the polymer industry. There is increasing demand for propylene due to significant growth in the markets of polypropylene, acrylonitrile and propylene oxide [9, 10]. A related process under development is the conversion of methanol to propylene (MTP) by Lurgi for which a ZSM-5 zeolite is used. In the past, the methanol-to-gasoline (MTG) process using ZSM-5 zeolite has been developed by Mobil.

The proposal that a hydrocarbon pool is involved in the formation of the olefins by Dahl and Kolboe [11-13] led to a breakthrough in the mechanistic understanding of the methanol conversion reaction in zeolites. Many works focus on the reaction mechanism underlying the MTO reaction with recent emphasis on the occurrence of an alkene mechanism competing with the hydrocarbon pool mechanism, depending on the zeolite topology [7, 14]. In the preferred industrial H-SAPO-34 catalyst, it is thought that the methylated benzene species are the organic reaction intermediates producing ethylene and propylene with high selectivity [15, 16]. These reaction intermediates reside in the large chabazite cages ($7.3 \times 12 \text{ \AA}$), which are connected by eight-membered ring pore openings ($3.8 \times 3.8 \text{ \AA}$). The current generation of MTO catalysts deactivate due to formation of carbonaceous deposits [17-19]. The aluminosilicate analogue of SAPO-34 is SSZ-13, whose synthesis was first reported by Zones and co-workers [20]. H-SAPO-34 is preferred over its aluminosilicate counterpart H-SSZ-13 because of a lower rate of catalyst deactivation due to weaker acidity of the bridging hydroxyl groups in the silicoaluminophosphate [21]. A drawback of the use of H-SAPO-34 is that a higher reaction temperature is required [22]. Accordingly, improving catalyst longevity of H-SSZ-13 may open possibilities to operate the industrial process at significantly lower temperature. Hitherto, creating sufficient mesoporosity in SSZ-13 zeolite to improve its useful lifetime in the MTO reaction has not been successful [23].

There is an increasing body of evidence that deactivation of zeolites due to the deposition of carbonaceous deposits can be countered by the introduction of mesoporosity in the microporous crystals. An additional effect of the more accessible zeolite crystals is the improved transport rates of molecules to and away from the reaction centers, which may increase the overall reaction rate [24-26]. In the case of the oxidation of benzene to phenol with nitrous oxide catalyzed by Fe/ZSM-5, it has been argued that blocking of the micropores at the perimeter of the zeolite crystals will quickly render large part of the micropore space inaccessible. The introduction of a substantial amount of mesopores within the microporous crystals results in a much better utilization of the micropore space, thus improving catalyst longevity. It is easily seen that such effects may also improve the lifetime of MTO catalysts, because deactivation is caused by deposition of carbonaceous deposits [27-29]. A recent report shows that these deposits are mainly formed at the external surface of the zeolite crystals [30].

Several papers review the various methods to synthesize hierarchical zeolites, either by bottom-up approaches or by post-synthesis treatment of zeolites [26, 31-33]. Of the latter type of approaches, desilication has been attempted to improve the catalytic performance of H-SSZ-13 [23]. Desilicated H-SSZ-13 had a shorter lifetime than the H-SSZ-13 parent zeolite in the MTO reaction despite the development of substantial mesoporosity. In contrast, desilication of H-ZSM-5 improved catalyst lifetime. Nanostructured H-ZSM-5 synthesized by use of $[\text{C}_{22}\text{H}_{45}\text{-N}^+(\text{CH}_3)_2\text{-C}_6\text{H}_{12}\text{-N}^+(\text{CH}_3)_2\text{-C}_6\text{H}_{13}]^{2+}$ as the single template has been shown to improve the catalyst lifetime in the methanol conversion reaction [35]. Detailed characterization suggested that the shorter lifetime of desilicated H-SSZ-13 is caused by a decrease of the micropore volume and the Brønsted acid sites.

We have reported about the synthesis of mesoporous SSZ-13 in a single step by combining N,N,N-trimethyl-1-adamantanammonium hydroxide (TMAdOH) as the SDA and several mesoporogens ($[\text{C}_{22}\text{H}_{45}\text{-N}^+(\text{CH}_3)_2\text{-C}_4\text{H}_8\text{-N}^+(\text{CH}_3)_2\text{-C}_4\text{H}_9]\text{Br}_2$ ($\text{C}_{22-4-4}\text{Br}_2$), $[\text{C}_{22}\text{H}_{45}\text{-N}^+(\text{CH}_3)_2\text{-C}_6\text{H}_{12}\text{-N}^+(\text{CH}_3)_2\text{-C}_6\text{H}_{13}]\text{Br}_2$ ($\text{C}_{22-6-6}\text{Br}_2$) and octadecyl-(3-trimethoxysilylpropyl)-ammonium chloride (TPOAC)) in chapter 2. In this chapter, the acidity of the SSZ-13 zeolites is investigated by a combination of ICP, ^{27}Al MAS NMR, ^1H MAS NMR, ^{31}P MAS NMR of adsorbed trimethylphosphine and CO_{ads} IR spectroscopy. These zeolites are tested for their catalytic activity in the MTO reaction.

3.2 Experimental

3.2.1 Zeolite catalyst preparation

Hierarchical SSZ-13 and conventional SSZ-13 were prepared according to the experimental details described in chapter 2.

As shown in Table 2.1 of chapter 2, the samples synthesized by $C_{22-4-4}Br_2$ were denoted as SSZ-13(C_{22-4-4} , n), where n refers to $C_{22-4-4}Br_2$ /TMAdOH molar ratio in the synthesis gel. The sample synthesized by $C_{22-6-6}Br_2$ was denoted as SSZ-13(C_{22-6-6} , n) where n refers to $C_{22-6-6}Br_2$ /TMAdOH molar ratio in the synthesis gel. The samples synthesized by TPOAC were denoted as SSZ-13(TPOAC, n), where n represents the molar TPOAC/Si ratio in the synthesis gel.

3.2.2 Physicochemical properties

Basic characterization

Argon adsorption experiments were determined at 87.6 K on a Micromeritics ASAP 2020 instrument in static mode. The samples were outgassed at 400 °C for 8 h prior to the sorption measurements. The Langmuir adsorption isotherm model was used to determine the total surface area (S_L) in the p/p_0 range between 0.05-0.20. The mesopore volume (V_{meso}) and mesopore size distribution was calculated from the adsorption branch of the isotherm by the Barrett-Joyner-Halenda (BJH) method. The micropore volume was determined by the t -plot method (thickness range 0.34-0.40 nm). The micropore diameter was calculated by the NLDFT model. Use was made of the model for cylindrical pores for argon on oxides at 87 K. No use was made of regularization.

Vibrational spectroscopy

FTIR spectra of CO adsorbed to the zeolite samples were recorded in the range of 4000-400 cm^{-1} by a Bruker IFS 113v instrument. The spectra were acquired at a 2 cm^{-1} resolution and averaged over 20 scans. The samples were prepared as thin self-supporting wafers of 5-10 mg/cm^2 and placed inside a controlled environment infrared transmission cell, capable of heating and cooling, gas dosing and evacuation. Prior to CO adsorption, the catalyst wafer was heated to 550 °C at a rate of 2 °C/min in an oxygen atmosphere. Subsequently, the cell was outgassed at the final temperature until the residual pressure was below 5×10^{-5} mbar. The sample was then cooled to 77 K. CO was introduced into the sample cell via a sample loop (5 μL) connected to a Valco six-port valve.

NMR spectroscopy

Nuclear Magnetic Resonance (NMR) spectra were recorded on a Bruker DMX-500 NMR spectrometer. For the ^{27}Al Magic Angle Spinning (MAS) NMR, a standard Bruker MAS probehead was used with rotor diameter of 2.5 mm, at a spinning rate of 20 kHz. The ^{27}Al chemical shift is referred to a saturated $\text{Al}(\text{NO}_3)_3$ solution.

For ^1H MAS NMR measurements the zeolites were first subjected to a dehydration procedure. A known amount of sample was placed in special glass tube suitable for NMR (Wilmad Glass Company) [37]. This tube was connected to a vacuum line. The zeolite was activated at a temperature of 450 °C at a pressure lower than 10^{-5} mbar for 6 h. After evacuation, the cylindrical glass tubes containing the samples were cooled to room temperature and sealed off by a flame torch. The sealing was done symmetrically by rotating the sample tube in a machine tool. The sealed glass tubes containing the activated samples were placed into a 4 mm MAS NMR rotor made of zirconia. Details of this special preparation of NMR samples suitable for MAS are described, for instance, in Refs. [38] and [39]. A standard Bruker MAS probehead was used at a spinning rate of 6 kHz. ^{31}P MAS NMR measurements were performed after adsorption of trimethylphosphine (TMP). An amount of zeolite was first dehydrated similar to the procedure for ^1H NMR. After cooling to room temperature the vacuum line is closed and TMP was introduced at a pressure of 8 mbar. After 0.5 h, the sample tube was sealed off and placed in a 4 mm MAS rotor. The spinning rate for these measurements was 6 kHz. The ^{31}P chemical shift is with respect to phosphoric acid (H_3PO_4).

3.2.3 Catalytic activity measurements

Catalytic activity measurements were carried out in a quartz tubular fixed-bed reactor. Firstly, the zeolites were pressed, crushed and sieved in a particle size fraction between 250 and 500 μm . Secondly, 50 mg of the shaped catalyst was placed in a quartz tube (inner diameter 4 mm) between two quartz-wool plugs. Prior to the reaction, the catalyst was activated at 550 °C in artificial air (30 ml/min) for 2 h. The methanol-to-olefins reaction was performed at 350 °C. Methanol (Merck, 99%) was introduced to the reactor by flowing He through a saturator kept at -17 °C with the flow rate 30 ml/min. The WHSV was kept at 0.8 $\text{g}\cdot\text{g}^{-1}\cdot\text{h}^{-1}$ and the effluent was analyzed online by gas chromatography (Compact GC Interscience equipped with TCD and FID detectors with RT-Q-Bond and $\text{Al}_2\text{O}_3/\text{KCl}$ columns). In regeneration experiments, the methanol flow was stopped after 24 h of reaction and the catalyst was heated to 550 °C in artificial air (30 ml/min). After regeneration at

550 °C for 5 h, the reactor is cooled to 350 °C in He (30 ml/min) and a consecutive reaction was started by introducing methanol into the He flow.

The amount of coke deposited during the reaction was determined by temperature programmed oxidation (TPO) experiments. The spent catalysts (used in the MTO reaction for 48 h) were exposed to a flow of 6 vol. % O₂ in He at a total flow rate of 100 ml/min. The temperature was increased from room temperature to 850 °C at a rate of 5 °C/min. The amount of CO₂ was quantified by a Balzers mass-spectrometer. The CO₂ (m/e = 44) signal was calibrated by the thermal decomposition of a known amount of NaHCO₃. The coke deposited during MTO on SSZ-13 and SSZ-13(C₂₂₋₄₋₄, 0.17) was also measured by thermogravimetric analysis (TGA) on TGA/DSC 1 STAR system of Mettler Toledo. The temperature was increase to 850 °C at a rate of 5 °C/min under flowing air (50 ml/min).

3.3 Results and Discussion

3.3.1 Acidity of the zeolites

Table 3.1: Silicon to aluminum molar ratios, the fraction of tetrahedral Al obtained by deconvolution of ²⁷Al MAS NMR spectra and the estimated concentration of Brønsted acid sites of the calcined SSZ-13 zeolites.

Zeolite	Si/Al ^a	Al ^{IV,b} (%)	c _{BAS} ^c (mmol.g ⁻¹)
SSZ-13	19	88	0.73
SSZ-13(C ₂₂₋₄₋₄ , 0.06)	19	89	0.74
SSZ-13(C ₂₂₋₄₋₄ , 0.17)	18	86	0.75
SSZ-13(C ₂₂₋₄₋₄ , 0.50)	17	89	0.82
SSZ-13(C ₂₂₋₄₋₄ , 1.50)	19	84	0.70
SSZ-13(C ₂₂₋₄₋₄ , ∞)	21	61	n.d. ^d
SSZ-13(TPOAC, 0.04)	23	81	0.56
SSZ-13(TPOAC, 0.08)	28	77	0.44

^a Determined by ICP elemental analysis; ^b Fraction of tetrahedral Al coordination; ^c concentration computed by multiplying the fraction of tetrahedral Al by the Al concentration determined from elemental analysis; ^d not determined (due to amorphous nature of sample).

An essential prerequisite for the use of zeolites as catalysts in the MTO reaction is the presence of strong Brønsted acid sites (BAS), which arise from the substitution of framework Si⁴⁺ sites by Al³⁺ [40]. The Si/Al ratios of the set of SSZ-13 zeolites are listed in Table 3.1. Conventional SSZ-13 has a Si/Al ratio of 19. The Si/Al ratios of SSZ-13(C₂₂₋₄₋₄) zeolites are close to this value and vary between 17 and 21. ²⁷Al MAS NMR spectra of the zeolites are shown in Fig. 8. In most of the calcined zeolites the Al atoms are predominantly in tetrahedral coordination (Al^{IV}) as evidenced by the sharp resonance band at 59 ppm. The

additional broad band(s) around 0 ppm is related to extraframework Al in octahedral coordination (Al^{VI}). Deconvolution of the ^{27}Al MAS NMR spectra shows that 88 % of the aluminum is in tetrahedral coordination in SSZ-13 (Table 3.1). Similar values (84-89 % Al^{IV}) are obtained for SSZ-13(C_{22-4-4}) zeolites. SSZ-13 ($\text{C}_{22-4-4}, \infty$) has a similar Si/Al ratio as the SSZ-13(C_{22-4-4}) zeolites, but a much larger fraction of Al is in octahedral coordination (39 %) and the tetrahedral Al sites are much less defined as follows from the broadness of the Al^{IV} signal. The SSZ-13(TPOAC) zeolites have slightly higher Si/Al ratios than the C_{22-4-4} templated ones. The ^{27}Al NMR spectra of SSZ-13(TPOAC) evidence that the introduction of Al in the CHA framework is less straightforward than in the $\text{C}_{22-4-4}\text{Br}_2$ templated samples. Not only is the fraction of tetrahedral Al lower but also the total Al content. The BAS concentrations of the SSZ-13(C_{22-4-4}) zeolites vary only slightly and are similar to that of SSZ-13. The two SSZ-13(TPOAC) zeolites contain much less BAS.

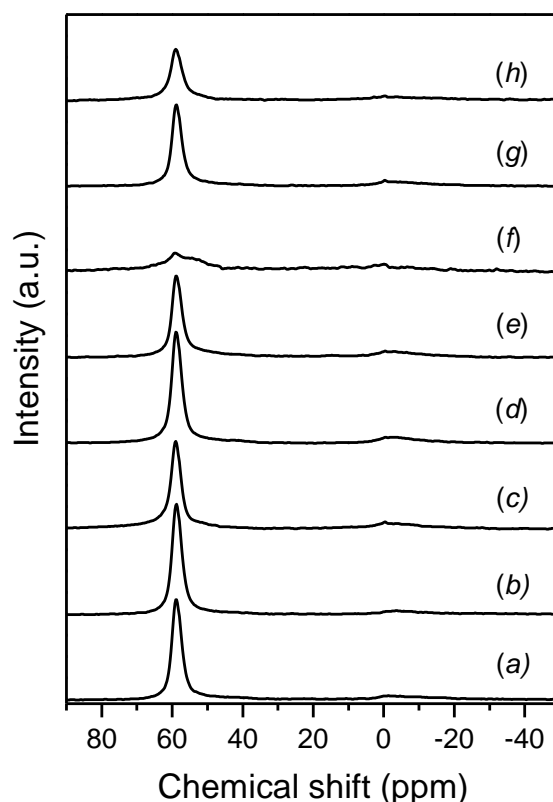


Figure 3.1: ^{27}Al MAS NMR spectra of (a) conventional SSZ-13, (b) SSZ-13(C_{22-4-4} , 0.06), (c) SSZ-13(C_{22-4-4} , 0.17), (d) SSZ-13(C_{22-4-4} , 0.50), (e) SSZ-13(C_{22-4-4} , 1.50), (f) SSZ-13(C_{22-4-4} , ∞), (g) SSZ-13(TPOAC, 0.04) and (h) SSZ-13(TPOAC, 0.08). The spectra were normalized by the weight of the catalysts.

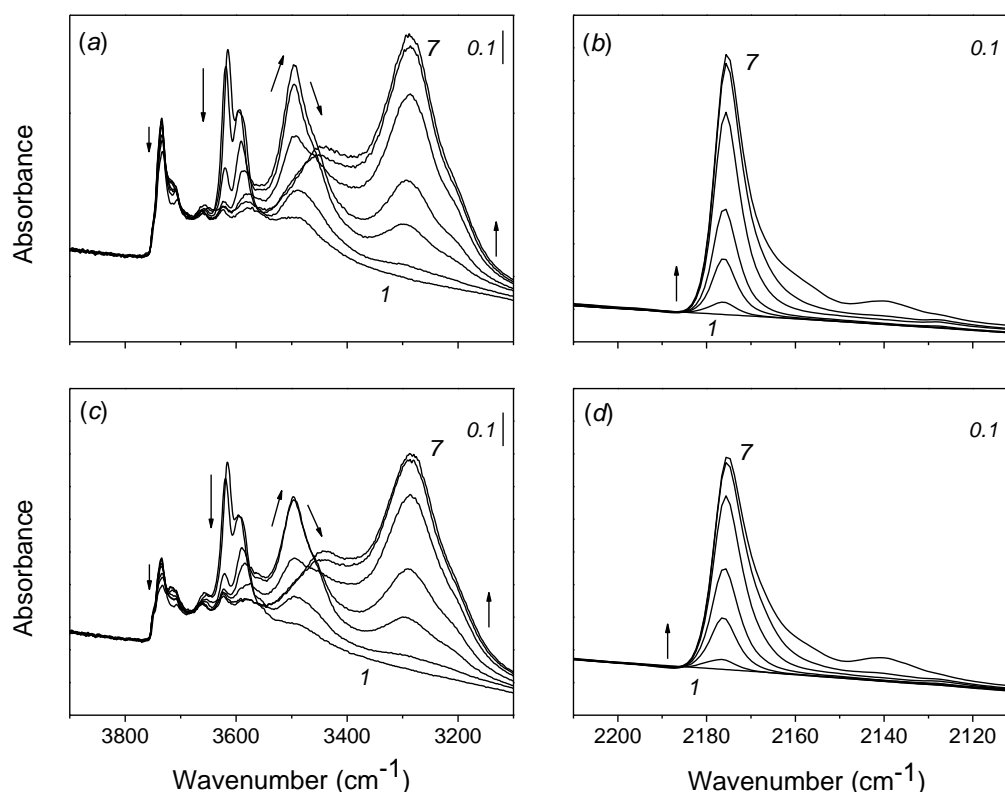


Figure 3.2: FTIR spectra of CO adsorbed on (a, b) conventional SSZ-13 and (c, d) SSZ-13(C₂₂₋₄₋₄, 0.50) at 80 K: (a, c) OH stretching region and (b, d) CO stretching region. Line 1 represents the dehydrated zeolite before CO adsorption, lines 2-7 at increasing CO coverage of 0.55, 0.85, 1.20, 1.85, 2.85, 3.85 μmol . Arrows indicate the increasing and decreasing peak intensities as CO coverage increases.

FTIR spectroscopy of adsorbed CO (CO_{ads} FTIR) is a routine characterization technique for zeolite acidity [22, 41-43]. Interactions between CO and the various hydroxyl groups lead to changes in the intensities and stretching frequencies of adsorbed CO and the hydroxyl group. A higher frequency shift of the hydroxyl group correlates to higher acidity. The CO_{ads} IR spectra of SSZ-13 and SSZ-13(C₂₂₋₄₋₄, 0.50) are given in Fig. 3.2. The spectra of SSZ-13 reveal the presence of isolated silanol bands at 3735 cm^{-1} with a shoulder at 3710 cm^{-1} . The shoulder is due to hydrogen-bonded silanol groups. SSZ-13 contains two distinct families of Brønsted acid sites, which give rise to peaks at high frequency (HF, 3614 cm^{-1}) and low frequency (LF, 3592 cm^{-1}) bands [22, 42, 43]. Perturbation by CO results in the decrease of these two bands. In particular, the HF band decreases more significantly at low CO coverage. At the same time, a sharp peak appears at 3494 cm^{-1} . Another peak is observed at 3290 cm^{-1} with a shoulder at 3210 cm^{-1} (Fig. 3.2a and c, traces 1-4). A further increase of the CO coverage leads to the appearance of a new component around 3450 cm^{-1} and the decrease of the intensity of the 3494 cm^{-1} band concomitant with an increase of the one at 3290 cm^{-1} . The shoulder around 3210 cm^{-1} disappears (Fig. 3.2a and c, traces 5-7). The band at 3490 cm^{-1}

and the shoulder at 3210 cm^{-1} have not yet been reported for SSZ-13. The reason is the much higher CO coverage employed in earlier studies [22,42,43]. Indeed, those spectra in literature are similar to our IR spectra at high CO coverage. A tentative explanation for the presence of two types of BAS might be the slightly different frequencies due to the sites located in the large cages and the smaller pores of the CHA structure. At high CO coverage, condensation of CO in the pores will lead to the averaging of the adsorption complexes, especially because of the close proximity of the two sites, so that a single broad band at 3290 cm^{-1} develops. The 3450 cm^{-1} band corresponds to the perturbed weakly acidic silanol groups. From the similar strong red shift of the HF BAS corresponds to $\Delta\nu(\text{OH}) = -320\text{ cm}^{-1}$ for SSZ-13 and SSZ-13(C_{22-44} , 0.50), we infer that both materials contain similar strong BAS. The CO stretching regions is characterized by a band at 2175 cm^{-1} with a shoulder at 2160 cm^{-1} and, at higher CO coverage, a broad band at 2140 cm^{-1} . The presence of strong BAS induces the highest blue shift of the stretch of adsorbed CO. The shoulder at 2160 cm^{-1} is due to the weakly acidic silanol groups and the band around 2143 cm^{-1} is the vibration of liquid CO.

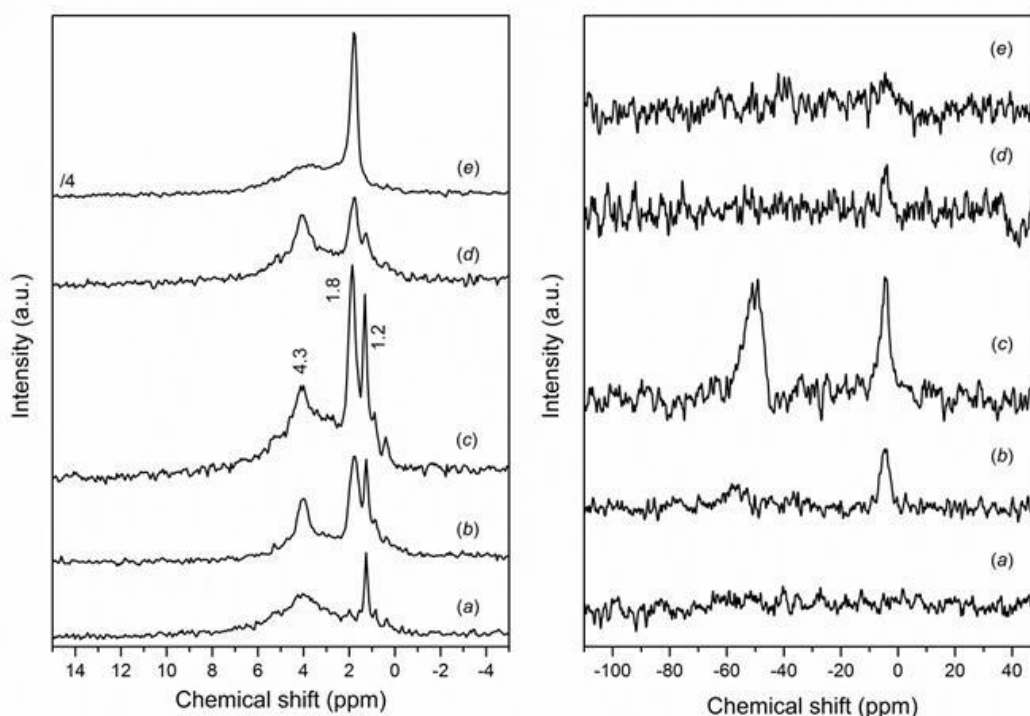


Figure 3.3: (left) ^1H MAS NMR spectra of dehydrated (a) conventional SSZ-13, (b) SSZ-13(C_{22-44} , 0.17), (c) SSZ-13(C_{22-44} , 0.50), (d) SSZ-13(C_{22-44} , 1.50), (e) SSZ-13(C_{22-44} , ∞). The spectra were normalized by the weight of the catalysts. The ppm scale is with respect to liquid tetramethylsilane.

Figure 3.4: (right) ^{31}P MAS NMR spectra of TMP adsorbed on (a) conventional SSZ-13, (b) SSZ-13(C_{22-44} , 0.17), (c) SSZ-13(C_{22-44} , 0.50), (d) SSZ-13(C_{22-44} , 1.50) and (e) SSZ-13 (C_{22-44} , ∞). The spectra are weight-normalized and the scale is with respect to H_3PO_4 .

Fig. 3.3 displays ^1H MAS NMR spectra of several SSZ-13 zeolites. The peak at 1.2 ppm

is assigned to isolated silanol groups, the one at 1.8 ppm to geminal silanol groups and the one at 4.3 ppm to BAS [44-46]. The ^1H MAS NMR spectrum of SSZ-13 (Fig. 3.3a) is dominated by bands due to isolated silanol groups and BAS. The spectra of the SSZ-13(C_{22-4-4}) zeolites exhibit an additional peak at 1.8 ppm due to geminal silanol groups. With increasing $\text{C}_{22-4-4}\text{Br}_2/\text{TMAOH}$ ratio the peak at 1.8 ppm becomes more intense due to an increase of silanol groups. This trend points to a more defective zeolite structure. The alternative interpretation that the intensity trend of the 1.8 ppm peak is due to an increasing contribution of an amorphous phase does not cohere with the XRD results. The peak at 1.8 ppm is the most intense in the spectrum of SSZ-13($\text{C}_{22-4-4}, \infty$) and, notably, the peak due to isolated silanol groups at 1.2 ppm is not observed in this sample (Fig. 3.3e). Besides, there is no clear peak at 4.3 ppm in this sample. The spectrum resembles that of reported spectra for SBA-15 and MCM-41 [45]. The broad feature at lower field is most likely due to hydroxyl groups in typical aluminum hydroxides and oxides [47].

Table 3.2: Amount of trimethylphosphine (TMP) adsorbed on SSZ-13 and SSZ-13 (C_{22-4-4}) zeolites determined by ^{31}P MAS NMR spectra (TMP adsorption done at room temperature at a TMP pressure of 8 mbar for 0.5 h).

Zeolite	TMP adsorbed (mmol g^{-1})
SSZ-13	0
SSZ-13($\text{C}_{22-4-4}, 0.17$)	0.015
SSZ-13($\text{C}_{22-4-4}, 0.50$)	0.023
SSZ-13($\text{C}_{22-4-4}, 1.50$)	0.002
SSZ-13($\text{C}_{22-4-4}, \infty$)	0

^{31}P NMR of adsorbed TMP was employed to probe the presence of BAS in the pores larger than the micropores of SSZ-13 (Fig. 3.4). Trimethylphosphine (TMP) is a weakly basic molecule, which has been extensively used to probe strong BAS in zeolites [46, 48, 49]. Its kinetic diameter (0.55 nm) is significantly larger than the size of the pore openings of SSZ-13 (0.38 nm). Following TMP adsorption on SSZ-13, the ^{31}P NMR spectrum did not contain any signal of TMP (Fig. 3.4a), indicating that the number of BAS accessible to TMP is negligible. The corresponding spectrum of SSZ-13($\text{C}_{22-4-4}, 0.50$), however, exhibits two peaks at -4.5 and -58.2 ppm (Fig. 3.4c). The signal at -58.2 ppm is due to physisorbed TMP, while the one at -4.5 ppm can be assigned to TMP adsorbed on BAS [48]. The spectrum of SSZ-13($\text{C}_{22-4-4}, 1.50$) is qualitatively similar for SSZ-13($\text{C}_{22-4-4}, 0.17$) but with lower intensities. Finally, the

spectrum of TMP adsorbed on SSZ-13(C_{22-4-4}, ∞) does not show any signal. Quantification of the ^{31}P MAS NMR spectra shows an increasing amount of BAS in larger pores with increasing $C_{22-4-4}\text{Br}_2/\text{TMAOH}$ ratio (Table 3.2), commensurate with the increasing mesopore volume. Expectedly, this trend does not hold for the SSZ-13(C_{22-4-4}, ∞) material, because it does not contain strong BAS at all.

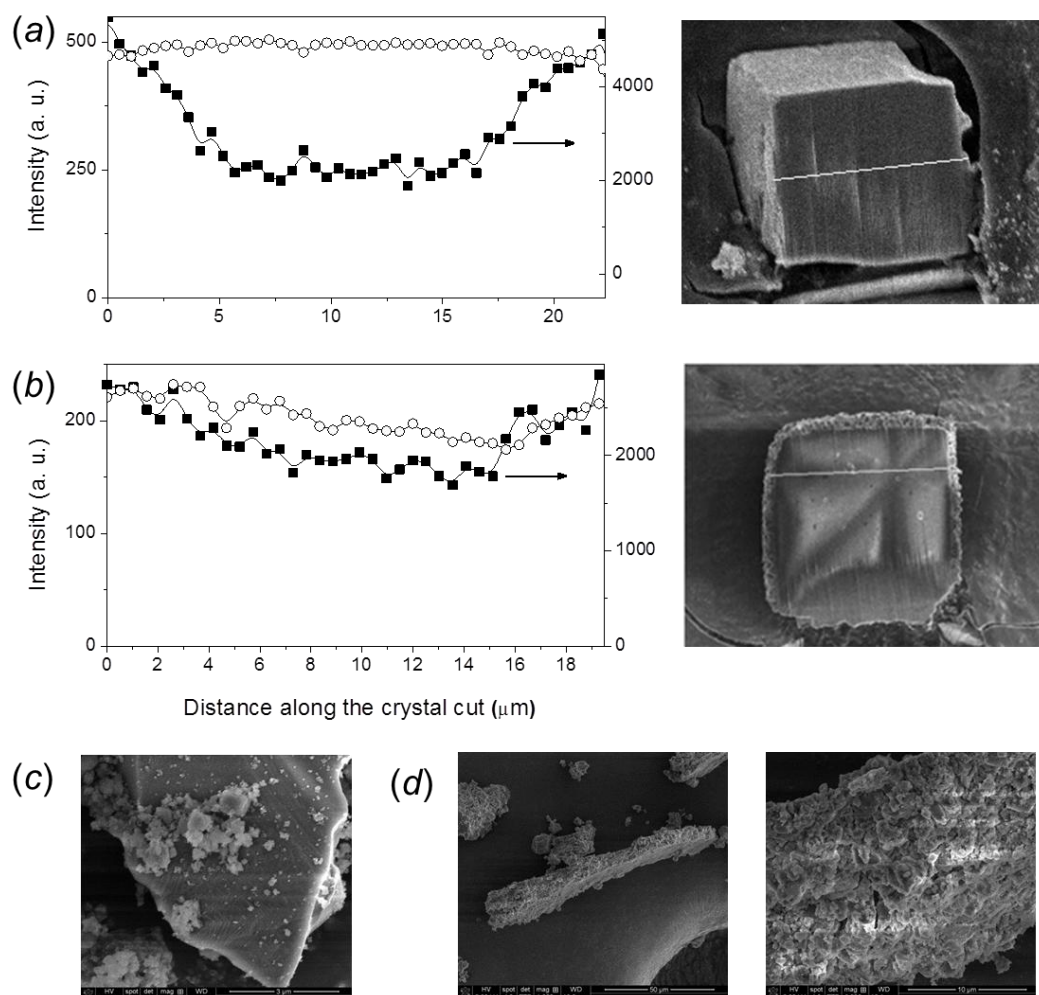


Figure 3.5: EDX line scan (Si (□) and Al (■) signals) of FIB cuts of (a) conventional SSZ-13 and (b) SSZ-13($C_{22-4-4}, 0.50$); SEM images of thoroughly grinded (c) conventional SSZ-13 and (d) SSZ-13($C_{22-4-4}, 0.50$).

To establish possible gradients of the Al concentration in the zeolite crystals, EDX line scans were measured of zeolite crystals cut by FIB (Fig. 3.5). Fig. 3.5a clearly shows that the Si/Al ratio in the centre of a FIB-cut crystal of conventional SSZ-13 is substantially higher than in its periphery. This should be the result of the preferential nucleation and crystallization of SSZ-13 at low Al content as is well known for other zeolites [50]. SSZ-13($C_{22-4-4}, 0.50$) also shows a heterogeneous distribution of Al along the cut surface with a lower Al content towards the centre of the crystal. Nevertheless, the heterogeneity in the

Si/Al ratio is much less pronounced for this mesoporous SSZ-13 crystal. The SEM image in Fig. 3.5b suggests that this crystal does not contain as many internal meso- and macropores as the SEM images of the crystal surfaces (Fig. 2.7, chapter 2) suggested. As this might be a thermal effect of the FIB-cutting procedure rather than a heterogeneous distribution of the mesoporosity inside the crystals, SEM images were recorded of SSZ-13 (Fig. 3.5c) and SSZ-13(C₂₂₋₄₋₄, 0.50) (Fig. 3.5d) after thorough grinding with pestle and mortar. It is clearly seen that the latter zeolite consists of small intergrown crystals throughout the primary particle in stark contrast to the single crystal nature of conventional SSZ-13.

3.3.2 Catalytic activity measurements

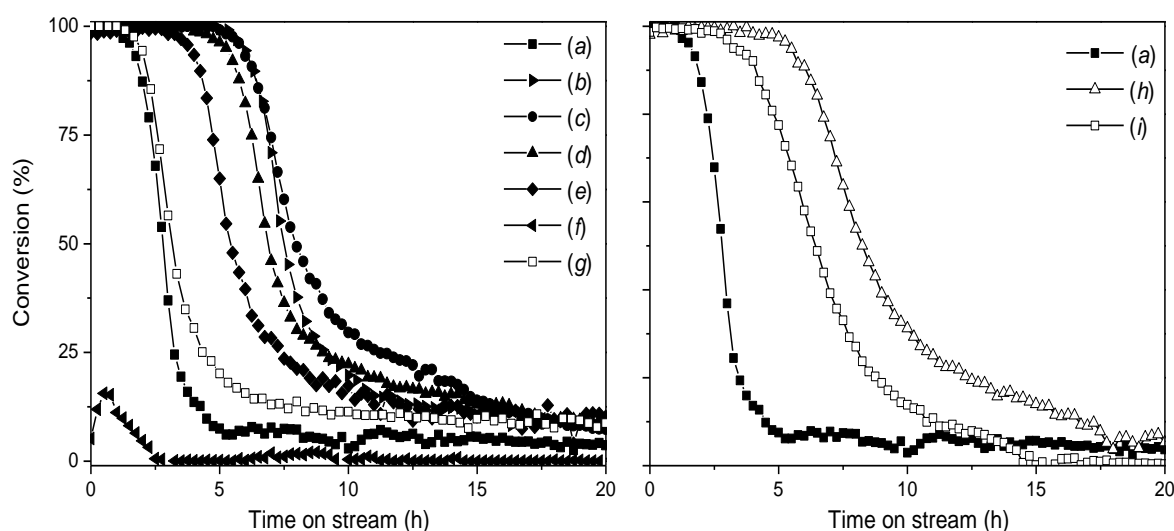


Figure 3.6: Catalytic performance in the MTO reaction (WHSV = 0.8 g.g⁻¹.h⁻¹; T = 350 °C) of (a) conventional SSZ-13, (b) SSZ-13(C₂₂₋₄₋₄, 0.06), (c) SSZ-13(C₂₂₋₄₋₄, 0.17), (d) SSZ-13(C₂₂₋₄₋₄, 0.50), (e) SSZ-13(C₂₂₋₄₋₄, 1.50), (f) SSZ-13(C₂₂₋₄₋₄, ∞), (g) SSZ-13(C₂₂₋₆₋₆, 0.50), (h) SSZ-13(TPOAC, 0.04) and (i) SSZ-13(TPOAC, 0.08).

All of the zeolites were tested for their catalytic activity in the MTO reaction at a WHSV of 0.8 g.g⁻¹.h⁻¹ and a reaction temperature of 350 °C. The time on stream curves are given in Fig. 3.6 and the corresponding selectivities are listed in Table 3.3. All of the zeolite-containing catalysts convert methanol completely during the initial stages of the reaction. Expectedly, amorphous SSZ-13(C₂₂₋₄₋₄, ∞) is almost inactive. Olefins are the dominant products of the MTO reaction when the conversion of methanol is complete. In all

Table 3.3: Lifetime, product distribution^a, and coke content of SSZ-13 and mesoporous SSZ-13 zeolite catalysts for the MTO reaction (WHSV = 0.8 g.g⁻¹.h⁻¹; T = 350 °C) after 1 h time on stream.

Zeolite	Lifetime ^b (h)	CH ₄ (%)	C ₂ ⁼ (%)	C ₂ (%)	C ₃ ⁼ (%)	C ₃ (%)	Aliphatic C ₄ -C ₆ (%)	Coke content ^d (%)
SSZ-13	2.8	1.2	46.4	0.8	44.9	4.6	2.1	16
SSZ-13(C ₂₂₋₄₋₄ , 0.06)	7.5	1.2	47.0	0.4	46.2	3.8	1.4	n.d. ^c
SSZ-13(C ₂₂₋₄₋₄ , 0.17)	8.0	1.0	45.8	0.4	47.7	2.9	2.2	19
SSZ-13(C ₂₂₋₄₋₄ , 0.50)	6.8	1.1	44.5	0.7	47.3	0.4	6.0	32
SSZ-13(C ₂₂₋₄₋₄ , 1.50)	5.3	1.1	45.3	0.4	47.1	4.1	2.0	23
SSZ-13(C ₂₂₋₆₋₆ , 0.50)	3.0	1.1	46.7	0.2	36.0	1.1	14.9	n.d. ^c
SSZ-13(TPOAC, 0.04)	8.2	1.1	46.1	0.4	47.8	2.3	3.4	16
SSZ-13(TPOAC, 0.08)	6.4	1.2	49.4	0.3	44.9	1.9	2.3	14

^a Trace amounts of CO and CO₂ not taken into account; ^b Catalyst lifetime defined as the time passed to reach a conversion of 50 %; ^c Not determined; ^d Based on temperature programmed oxidation after a time on stream of 48 h.

cases, the combined selectivity to ethylene and propylene is greater than 90 % with only small amounts of light paraffins as byproducts. The selectivities depend on the reaction conditions [51]. For longer times on stream, the activity of the zeolites strongly decreases and dimethylether becomes the dominant reaction product. For SSZ-13, the methanol conversion decreases to 50 % after 2.8 h. All of the mesoporous zeolites display a considerably longer lifetime than conventional SSZ-13. A difference between SSZ-13 and the mesoporous SSZ-13 zeolites is also that deactivation of the former is abrupt leading to a nearly inactive sample, whereas for the latter the deactivation is significantly slower. The most stable zeolite is SSZ-13(C₂₂₋₄₋₄, 0.17) with a lifetime of almost 8 h before the methanol conversion decreased to 50 %. The zeolites prepared in the presence of TPOAC also show improved lifetime with SSZ-13(TPOAC, 0.04) exhibiting a similar lifetime as SSZ-13(C₂₂₋₄₋₄, 0.17). The product distribution shows an increased (decreased) higher hydrocarbons (propylene) yield, which is attributed to the presence of ZSM-5 as a competing phase of SSZ-13 in this catalyst. The lifetime of SSZ-13(C₂₂₋₆₋₆, 0.50) is however only 3 h.

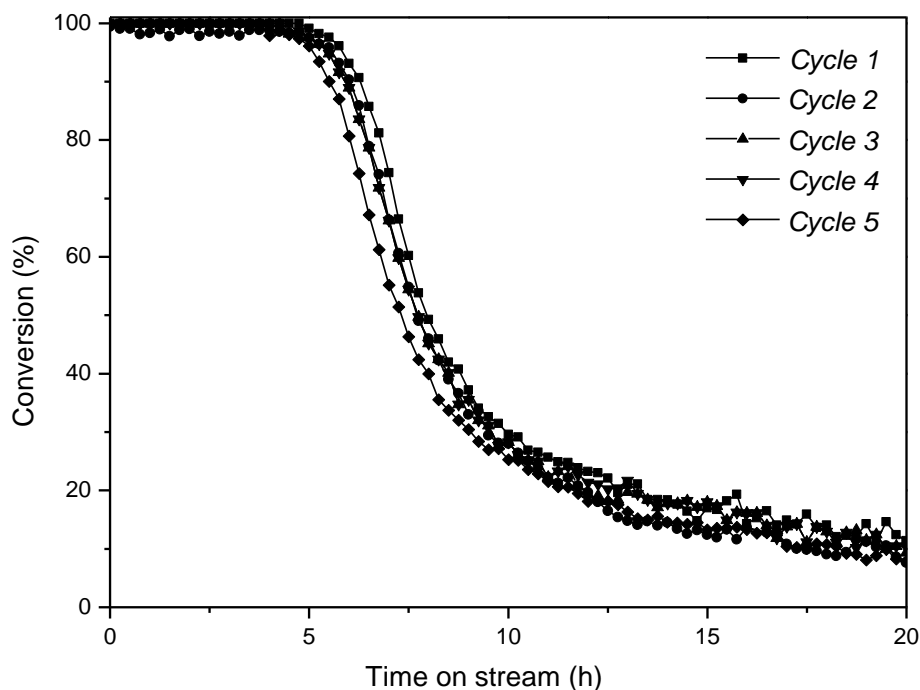


Figure 3.7: Catalytic performance in the MTO reaction ($\text{WHSV} = 0.8 \text{ g.g}^{-1}.\text{h}^{-1}$; $T = 350 \text{ }^\circ\text{C}$) of mesoporous SSZ-13(C_{22-4-4} , 0.17) zeolite after regeneration by in-situ calcination after 5 cycles, respectively.

It has been established that deactivation of MTO catalysts is mainly due to the decreased accessibility of the active sites due to coke deposition [17, 18, 30, 52]. Spectroscopic imaging has evidenced that the formation of larger carbonaceous deposits, which deactivate the catalyst, accumulate in the near-surface region of the crystals [30, 53]. Accordingly, deactivation will depend of the surface to volume ratio of the crystals. Substantial mesoporosity as present in mesoporous SSZ-13 implies high external surface area, *i.e.* the total surface area excluding the micropore surface area, and better accessibility of the micropore space. In line with this, it is found that despite their higher lifetimes the spent mesoporous SSZ-13 zeolite catalysts contain substantially more coke than spent SSZ-13 (Table 3.3). The coke content for the $\text{C}_{22-4-4}\text{Br}_2$ co-templated zeolites increases with the $\text{C}_{22-4-4}\text{Br}_2/\text{TMAOH}$ ratio until it reaches a maximum for SSZ-13(C_{22-4-4} , 0.50). The highest coke content correlates with the highest mesopore volume for this set of zeolites with similar micropore volumes. This finding is another indication for the high interconnectivity of micro- and mesopores. Compared to these zeolites, the SSZ-13(TPOAC) zeolites have higher mesopore and somewhat lower micropore volumes. This is likely due to the somewhat larger mesopores, and certainly for SSZ-13(TPOAC, 0.08), the presence of some amorphous

silica-alumina containing mesopores may play a role as well. The improved catalyst longevity of the SSZ-13(TPOAC) zeolites may also be partially traced back to their lower acidity. Indeed, it has been reported that lower the acidity of H-ZSM-5 results in improved catalyst lifetime during methanol conversion, which should be due to a slower buildup of carbonaceous deposits at the zeolite surface [54]. The relation between catalyst lifetime and concentration of acid sites appears to be less straightforward for SSZ-13 than for ZSM-5 [21, 55], however, such an explanation need not be considered for the present set of SSZ-13(C₂₂₋₄₋₄) zeolites, because they exhibit very similar acidity.

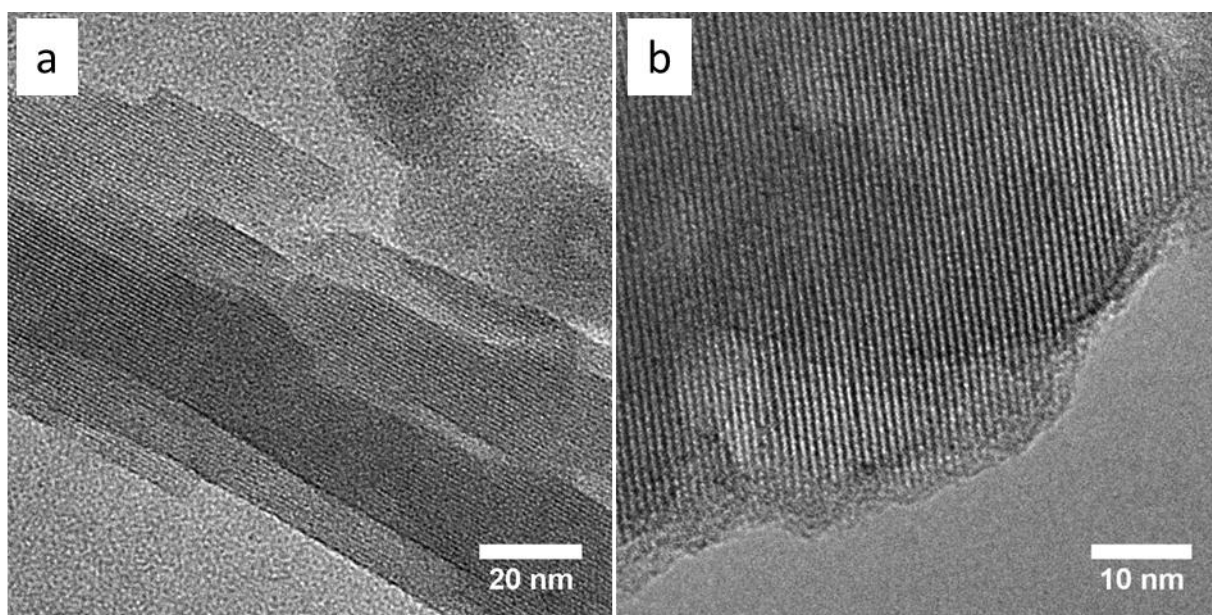


Figure 3.8: TEM images of (a) fresh and spent (b) SSZ-13(C₂₂₋₄₋₄, 0.17) after 48 h time on stream in the MTO reaction.

In order to assess whether the catalytic activity of these zeolites can be restored by oxidation of the coke, SSZ-13(C₂₂₋₄₋₄, 0.17) was subjected to five reaction-oxidation cycles. Fig. 3.7 shows that the excellent regenerability of this catalyst with only a small decrease of the catalytic activity after the fifth recycle. TEM and SEM analysis of the spent sample (Fig. 3.8) did not show any morphological changes or indications of amorphization. This high stability agrees with the earlier discussed high hydrothermal stability of the zeolites and evidences the suitability of such catalysts in a regenerative MTO process cycle. Finally, the deactivation was investigated in more detail by determining the coke content and textural properties process of SSZ-13 and SSZ-13(C₂₂₋₄₋₄, 0.17) as a function of the time on stream (Table 3.4). For both zeolites, a strong decrease of the micropore volume is observed, the initial decrease being more pronounced for SSZ-13(C₂₂₋₄₋₄, 0.17). Although the mesopore volume of SSZ-13(C₂₂₋₄₋₄, 0.17) has decreased after 1 h, it is seen that overall the mesopore

volumes of both zeolites increase during the MTO reaction. Tentatively, these mesopores are associated with the presence of carbonaceous deposits on the external surface of the zeolite crystalline domains. The larger increase of the mesopore volume for SSZ-13 may be related to the predominant formation of such deposits on the external surface of the large cubic crystals. For SSZ-13(C₂₂₋₄₋₄, 0.17) the growth of such deposits occurs in the mesopores and accordingly limits their size. The finding that a much larger part of the micropore volume of SSZ-13(C₂₂₋₄₋₄, 0.17) becomes inaccessible for Ar (physisorption) compared to SSZ-13 is indicative of the much higher utilization of the micropore space of the more stable catalyst. It is worth noting that the micropore volume probed by Ar does not necessarily imply that methanol can access these micropores. Most likely, the deposits on SSZ-13 hinder the accessibility of methanol to the micropores. The presence of micropores in the spent conventional SSZ-13 catalysts indicates that a fraction of these micropores, likely those in the center of the crystal, have not been involved in the catalysis and, accordingly, will not contain the organic catalytic reaction intermediates for the MTO reaction. Comparatively, a much larger fraction of the micropores of SSZ-13(C₂₂₋₄₋₄, 0.17) is utilized in the MTO reaction (due to the presence of highly interconnected mesopores), leading to a lower micropore volume probed by Ar physisorption. Already before complete deactivation, this catalyst does not contain accessible micropores anymore. Following this train of thought, it can be postulated that the mesoporosity of SSZ-13(C₂₂₋₄₋₄, 0.17) is already sufficient to ensure complete utilization of its micropore space, explaining the much higher lifetime compared to SSZ-13. It is therefore reasonable to assume that the micropore space of SSZ-13(C₂₂₋₄₋₄, 0.5) is also completely utilized during the MTO reaction. The shorter lifetime is due to the higher external surface (higher mesopore volume), leading to increased deposition of carbonaceous materials. This is in accordance with the higher coke content of this sample.

Table 3.4: Textural properties of spent SSZ-13 and SSZ-13(C₂₂₋₄₋₄, 0.17) zeolite catalysts as a function of the time on stream determined by Ar physisorption.

Zeolite TOS ^a (h)	SSZ-13				SSZ-13(C ₂₂₋₄₋₄ , 0.17)			
	S_L (m ² .g ⁻¹)	V_{micro} (cm ³ .g ⁻¹)	V_{meso} (cm ³ .g ⁻¹)	Coke ^c (wt %)	S_L (m ² .g ⁻¹)	V_{micro} (cm ³ .g ⁻¹)	V_{meso} (cm ³ .g ⁻¹)	Coke ^c (wt %)
0 ^b	391	0.12	0.07	0	523	0.10	0.11	0
1	346	0.08	0.13	7.1	173	0.03	0.07	5.3
4	193	0.03	0.13	10.5	123	0.01	0.10	15.4
8	303	0.05	0.22	11.1	77	0	0.11	16.9
48	22	0	0.07	13.1	68	0	0.15	19.3

^a Time on stream; ^b Textural properties of the pelleted zeolites; ^c Coke content based on TGA.

3.4 Conclusions

This chapter is to investigate the acidic and the catalytic properties of hierarchical SSZ-13 zeolites prepared by combining N,N,N-trimethyl-1-adamantanammonium hydroxide (TMAdOH) as a structure-directing agent (SDA) with several mesopore-forming agents ($C_{22-4-4}Br_2$, $C_{22-4}Br$, $C_{22-6-6}Br_2$ and TPOAC). The most salient findings of the present study are:

- The hierarchical zeolites exhibit similar Brønsted acidity as a conventional SSZ-13 zeolite. A larger portion of these acid sites are at the external surface for the hierarchical zeolites as compared to SSZ-13.
- Comparatively, the use of other templates does not give zeolites with such favorable properties. The use of the organosilane TPOAC results in inefficient introduction of Al^{3+} in the zeolite framework. Besides, the formation of ZSM-5 as a competing phase is undesirable for the application of these zeolites in the MTO reaction.
- The hierarchical SSZ-13 zeolites display a much longer lifetime as catalysts in the MTO reaction than conventional SSZ-13. The light olefins yield is similar. The increased lifetime is due to better utilization of the micropore space. There are two competing effects of the introduction of mesoporosity: (i) increased accessibility of the micropore space and, accordingly, better utilization of the micropore space and (ii) increased rate of coke formation with increasing external surface (increasing mesopore volume). Maximum catalyst lifetime is obtained at a relatively low $C_{22-4-4}Br_2$ /SDA ratio.
- The hierarchical SSZ-13 zeolites prepared by combining TMAdOH and $C_{22-4-4}Br_2$ as templates can be regenerated at least five times without substantial loss of activity, showing their promise in cyclic MTO processes.

References

- [1] C.D. Chang, A.J. Silvestri, *J. Catal.* 47 (1977) 249.
- [2] Z.M. Liu, C.L. Sun, G.W. Wang, Q.X. Wang, G.Y. Cai, *Fuel Process. Technol.* 62 (2000) 161.
- [3] N.M. Laurendeau, *Prog. Energy Combust. Sci.* 4 (1978) 221.
- [4] D.A. Hickman, L.D. Schmidt, *Science* 259 (1993) 343.
- [5] D. Sutton, B. Kelleher, J.R.H. Ross, *Fuel Process. Technol.* 73 (2001) 155.
- [6] M. Asadullah, S. Ito, K. Kunimori, M. Yamada, K. Tomishige, *J. Catal.* 208 (2002) 255.
- [7] U. Olsbye, S. Svelle, M. Bjorgen, P. Beato, T.V.W. Janssens, F. Joensen, S. Bordiga, K.P. Lillerud, *Angew. Chem. Int. Ed.* 51 (2012) 5810.
- [8] B.V. Vora, T.L. Marker, P.T. Barger, H.R. Nielsen, S. Kvisle, T. Fuglerud, *Stud. Surf. Sci. Catal.* 107 (1997) 87.
- [9] S. Pudar, J. Oxgaard, W.A. Goddard, *J. Phys. Chem. C* 114 (2010) 15678.
- [10] R. Meiers, U. Dingerdissen, W.F. Hölderich, *J. Catal.* 176 (1998) 376
- [11] I.M. Dahl, S. Kolboe, *Catal. Lett.* 20 (1993) 329.
- [12] I.M. Dahl, S. Kolboe, *J. Catal.* 149 (1994) 458.
- [13] I.M. Dahl, S. Kolboe, *J. Catal.* 161 (1996) 304.
- [14] M. Vandichel, D. Lesthaeghe, J. Van der Mynsbrugge, M. Waroquier, V. Van Speybroeck, *J. Catal.* 271 (2010) 67.
- [15] B. Arstad, S. Kolboe, *J. Am. Chem. Soc.* 123 (2001) 8137.
- [16] B. Arstad, S. Kolboe, *Catal. Lett.* 71 (2001) 209.
- [17] M. Stöcker, *Microporous Mesoporous Mater.* 29 (1999) 3.
- [18] G.F. Froment, W.J.H. Dehertog, A.J. Marchi in: J.J. Spivey (Ed), *Catalysis*, The Royal Society of Chemistry, 1992, pp.1.
- [19] D. M. Bibb, R. F. Howe, G. D. McLellan, *Appl. Catal. A: Gen.* 93 (1992) 1.
- [20] S.I. Zones, US Patent (1985) 4544538.
- [21] L.-T. Yuen, S.I. Zones, T.V. Harris, E.J. Gallegos, A. Auroux, *Microporous Mater.* 2 (1994) 105.
- [22] F. Bleken, M. Bjørgen, L. Palumbo, S. Bordiga, S. Svelle, K.P. Lillerud, U. Olsbye, *Top. Catal.* 52 (2009) 218.
- [23] L. Sommer, D. Mores, S. Svelle, M. Stöcker, B.M. Weckhuysen, U. Olsbye, *Microporous Mesoporous Mater.* 132 (2010) 384.
- [24] M. Hartmann, *Angew. Chem. Int. Ed.* 43 (2004) 5880.
- [25] S.A. Lopez-Orozco, A. Inayat, A. Schwab, T. Selvam, W. Schwieger, *Adv. Mater.* 23 (2011) 2602.
- [26] L.H. Chen, X.Y. Li, J.C. Rooke, Y.H. Zhang, X.Y. Yang, Y. Tang, F.S. Xiao, B.L. Su, *J. Mater. Chem.* 22 (2012) 17381.
- [27] H. Xin, A. Koekkoek, Q. Yang, R.A. van Santen, C. Li, E. J. M. Hensen, *Chem. Commun.* (2009) 7590.
- [28] A.J.J. Koekkoek, H. Xin, Q. Yang, C. Li, E.J.M. Hensen, *Microporous Mesoporous Mater.* 145 (2011) 172.

- [29] A.J.J. Koekkoek, V. Degirmenci, E.J.M. Hensen, *J. Mater. Chem.* 21 (2011) 9279.
- [30] D. Mores, E. Stavitski, M.H.F. Kox, J. Kornatowski, U. Olsbye, B.M. Weckhuysen, *Chem. Eur. J.* 14 (2008) 11320.
- [31] R. Chal, C. Gérardin, M. Bulut, S. van Donk, *ChemCatChem.* 3 (2011) 67.
- [32] K. Egeblad, C.H. Christensen, M. Kustova, C.H. Christensen, *Chem. Mater.* 20 (2008) 946.
- [33] J. Pérez-Ramírez, C.H. Christensen, K. Egeblad, C.H. Christensen, J.C. Groen, *Chem. Soc. Rev.* 37 (2008) 2530.
- [34] L. Wu, V. Degirmenci, P.C.M.M. Magusin, B.M. Szyja, E.J.M. Hensen, *Chem. Commun.* 48 (2012) 9492.
- [35] M. Choi, K. Na, J. Kim, Y. Sakamoto, O. Terasaki, R. Ryoo, *Nature* 461 (2009) 246.
- [36] L.-T. Yuen, S.I. Zone in H. Robson (Ed.), *Verified Syntheses of Zeolitic Materials*, 2nd revised ed., Elsevier Science B.V., Amsterdam, 2001, pp. 126.
- [37] D. Freude, M. Hunger, H. Pfeifer, W. Schwieger, *Chem. Phys. Lett.* 128 (1986) 62.
- [38] E. Brunner, *J. Chem. Soc. Faraday Trans.* 86 (1990) 3957.
- [39] V. Degirmenci, O.F. Erdem, A. Yilmaz, D. Michel, D. Uner, *Catal. Lett.* 115 (2007) 79.
- [40] Q. Zhu, J.N. Kondo, T. Tatsumi, S. Inagaki, R. Ohnuma, Y. Kubota, Y. Shimodaira, H. Kobayashi, K. Domen, *J. Phys. Chem. C* 111 (2007) 5409.
- [41] L. Smith, A.K. Cheetham, L. Marchese, J.M. Thomas, P.A. Wright, J. Chen, E. Gianotti, *Catal. Lett.* 41 (1996) 13.
- [42] L.J. Smith, A. Davidson, A.K. Cheetham, *Catal. Lett.* 49 (1997) 143.
- [43] S. Bordiga, L. Regli, D. Cocina, C. Lamberti, M. Bjorgen, K.P. Lillerud, *J. Phys. Chem. B* 109 (2005) 2779.
- [44] M. Hunger, *Catal. Rev. Sci. Eng.* 39 (1997) 345.
- [45] J. Trebosc, J.W. Wiench, S. Huh, V.S.Y. Lin, M. Pruski, *J. Am. Chem. Soc.* 127 (2005) 3057.
- [46] Y.J. Jiang, J. Huang, W.L. Dai, M. Hunger, *Solid State Nucl. Magn. Reson.* 39 (2011) 116.
- [47] G. Piedra, J.J. Fitzgerald, N. Dando, S.F. Dec, G.E. Maciel, *Inorg. Chem.* 35 (1996) 3474.
- [48] W.P. Zhang, X.W. Han, X.M. Liu, X.H. Bao, *J. Mol. Catal. A* 194 (2003) 107.
- [49] J.H. Lunsford, W.P. Rothwell, W. Shen, *J. Am. Chem. Soc.* 107 (1985) 1540.
- [50] R. Singh, P.K. Dutta in: S.M. Auerbach, K.A. Carrado, P.K. Dutta (Eds.), *Handbook of Zeolite Science and Technology*, Marcel Dekker, New York, 2003 pp. 25.
- [51] Y. Kumitaa, J. Gascona, E. Stavitski, J. A. Moulijna, F. Kapteijna, *Appl. Catal. A: General* 391 (2011) 234.
- [52] D.M. Bibby, R.F. Howe, G.D. McLellan, *Appl. Catal. A: Gen.* 93 (1992) 1.
- [53] D. Mores, J. Kornatowski, U. Olsbye, B.M. Weckhuysen, *Chem. Eur. J.* 17 (2011) 2874.
- [54] S.M. Campbell, D.M. Bibby, J.M. Coddington, R.F. Howest, *J. Catal.* 161 (1996) 350
- [55] Q. Zhu, J.N. Kondo, R. Ohmura, Y. Kubota, M. Yamaguchi, T. Tatsumi, *Microporous Mesoporous Mater.* 112 (2008) 153.

Chapter 4

Mesoporous SAPO-34 and high-silica SSZ-13 zeolites as Catalysts for the Methanol-to-Olefins Reaction

Summary

The improvement of the stability of microporous SSZ-13 and SAPO-34 solids for application as catalysts in the methanol-to-olefins reaction was explored. Firstly, a mesoporous SSZ-13 with a Si/Al ratio of 20 zeolite was silylated, resulting in a relatively minor improvement of the lifetime. Secondly, SSZ-13 zeolite with a Si/Al ratio of 50 was synthesized. Lower acidity resulted in a lower rate of deactivation compared to SSZ-13 with a Si/Al ratio of 20. The lifetimes of SSZ-13 with Si/Al ratios of 20 and 50 were 2.8 and 7 h, respectively. Introducing mesoporosity in SSZ-13(50) by use of the organosilane octadecyl-(3-trimethoxysilylpropyl)-ammonium chloride (TPOAC) only resulted in a minor improvement of the lifetime. It was not possible to synthesize mesoporous SSZ-13 at high Si/Al ratios by use of $(C_{22}H_{45}-N^+(CH_3)_2-C_4H_8-N^+(CH_3)_2-C_4H_9)Br_2$ ($C_{22-4-4}Br_2$). Instead, ZSM-5 zeolite was obtained. Attempts to synthesize SAPO-34 by use of $C_{22-4-4}Br_2$ as mesoporegen were also not successful and, instead, competing AlPO-phases were obtained. Mesoporous SAPO-34 was obtained by adding TPOAC, an amphiphilic organosilane, to the synthesis gel. It was then found that intracrystalline mesoporosity did not lower the deactivation rate of SAPO-34 as was found for SSZ-13. The total methanol conversion capacity per acid site for microporous and mesoporous SAPO-34 were comparable. These findings imply that the lower acidity of the acid sites in SAPO-34 lead to the complete utilization of the micropore space of this zeolite. in the methanol-to-olefins reaction to the fore.

4.1 Introduction

Light olefins are key chemical intermediates in the petrochemical industry, which are usually produced through non-catalytic cracking of petroleum feedstock. With the growing importance of alternative feedstocks, most notably cheap natural gas and coal, there is now growing interest in methanol as a chemical intermediate of the synthesis of olefins. The methanol-to-olefins (MTO) reaction has been intensively studied in the last decades [1-5]. HSAPO-34, a silicoaluminophosphate having the chabazite (CHA) pore topology is the commercial catalyst for the MTO reaction. The relatively low acidity of silicoaluminophosphates and the combination of large cavities with a diameter of 9.4 Å, that stabilize the methylated benzene catalytic intermediates, with small 8-ring pore openings (3.8 Å) result in high selectivity to light olefins, typically above 80 %. An inherent drawback of SAPO-34 as MTO catalyst, which is typical for methanol-to-hydrocarbons (MTH) conversion reactions in zeolites, is the deactivation due to formation of carbonaceous deposits. This requires intermittent regeneration of the catalyst. In China, the MTO process is being commercialized on a large scale as part of chemical plants that convert cheap coal via gasification to syngas followed by methanol manufacture, light olefin and polymer production [6]. Catalyst deactivation is coped with by carrying out the MTO reaction in a fluidized bed with a regenerator in which part of the coke is burnt. This capital-intensive process would benefit from catalysts with a longer lifetime, because the size of the regeneration section could be reduced [7].

Recently, we have been shown that the introduction of mesopores in SSZ-13 crystals results in a substantial decrease of the negative effect of coke formation [8, 9]. Further characterization of mesoporous and conventional SSZ-13 showed that the better accessibility of the micropores results in their efficient utilization for the MTO reaction. It was found that coke formation is more extensive, because it occurred on the external zeolite surface that is in the mesopores. For the synthesis of mesoporous SSZ-13, we were inspired by the approaches developed by the Ryoo group [10-12]. However, for our purpose we employed a combination of a conventional structure-directing agent (SDA) for CHA formation (trimethyl-adamantanammonium hydroxide) with a mesopore-generating template. Molecular

modeling approaches identified a template based on two quaternary ammonium centers separated by a butyl chain and terminated by another butyl endgroup and a long hydrocarbon chain, $C_{22}H_{45}-N^+(CH_3)_2-C_4H_8-N^+(CH_3)_2-C_4H_9)Br_2$, as the most suitable. Our approach was recently shown to be more generally applicable for a range of zeolite topologies [13].

When applied in the MTO reaction, the presence of interconnected micro- and mesoporosity in SSZ-13 substantially increases the total methanol conversion capacity [8, 9]. The mesoporous SSZ-13 zeolites exhibited a much longer lifetime than conventional SSZ-13 in the MTO reaction at nearly similar light olefins yield. The increased lifetime is attributed to better utilization of the micropore space. There are two competing effects of the introduction of mesoporosity: (i) increased accessibility of the micropore space and, accordingly, better utilization of the micropore space and (ii) increased rate of coke formation with increasing external surface (increasing mesopore volume). This study points to external coke formation as the main reason for catalyst deactivation for SSZ-13. Maximum catalyst lifetime is obtained at a relatively low mesopore/SDA ratio.

In this work, we investigate further issues related to mesoporous CHA zeolites for the MTO reaction. Firstly, we explore the possibility to further improve the catalytic performance of SSZ-13 zeolite for the MTO reaction. Two approaches were followed, *i.e.* decreasing the Al content of the zeolite framework so as to lower the density of Brønsted acid sites and the rate of coking [14, 15, 16] and by silylating the acid groups at the external zeolite surface. Secondly, we attempted to synthesize mesoporous SAPO-34 using the mesoporegen successfully employed for synthesis of mesoporous SSZ-13, $C_{22}H_{45}-N^+(CH_3)_2-C_4H_8-N^+(CH_3)_2-C_4H_9)Br_2$. For comparison, we also used an amphiphilic organosilane, which has been shown to induce mesopores for AlPO-5 and AlPO-11 molecular sieves [12].

4.2 Experimental

4.2.1 Synthesis of materials

Template synthesis

$C_{22-4-4}Br_2$: The surfactant $(C_{22}H_{45}-N^+(CH_3)_2-C_4H_8-N^+(CH_3)_2-C_4H_9)Br_2$ was synthesized following a published procedure [9]. Firstly, 4.1 g (0.01 mol) 1-bromodocosane (Aldrich,

96 %) was dissolved in 20 ml toluene and added dropwisely into the 20 ml solution of 10.3 g (0.07 mol) N, N, N', N'-tetramethyl-1,4-butanediamine (Aldrich, 98 %) in acetonitrile. The resulting solution was stirred for 3 h at room temperature and then mixed at 70 °C under reflux overnight. After cooling to room temperature, the solution was kept in a refrigerator at 4 °C for 1 h, filtered and washed with diethyl ether. The resulting solid was dried in a vacuum oven at room temperature. The product was $(C_{22}H_{45}-N^+(CH_3)_2-C_4H_8-N(CH_3)_2)Br$. Secondly, 3.7 g (0.007 mol) $(C_{22}H_{45}-N^+(CH_3)_2-C_4H_8-N(CH_3)_2)Br$ and 1.96 g (0.014 mol) 1-bromobutane (Aldrich, 98 %) were dissolved in 110 ml of acetonitrile and then stirred in a reflux condenser at 70 °C overnight. Next, the solid product was quenched in refrigerator at 4 °C for 1 h, filtered, washed with diethyl ether and dried in a vacuum oven at room temperature. The resulting product was $(C_{22}H_{45}-N^+(CH_3)_2-C_4H_8-N^+(CH_3)_2-C_4H_9)Br_2$ (denoted as $C_{22-4-4}Br_2$).

Synthesis of zeolites

SSZ-13(50): SSZ-13 was synthesized as described in literature [17]. An amount of 2 g of a 1 M NaOH solution, 4 g 0.5 M N,N,N-trimethyl-1-adamantanammonium hydroxide (TMAOH, SACHEM, 25 %) and 2 g deionized water were mixed together. 0.05 g aluminum hydroxide (Sigma Aldrich) was added to this solution under vigorous stirring. After 30 min, 0.24 g fumed silica (Sigma) was added. The resulting mixture was stirred at room temperature to obtain a homogeneous gel with the composition 20 TMAOH : 10 Na_2O : Al_2O_3 : 100 SiO_2 : 4400 H_2O , which was then transferred into a Teflon-lined autoclave and kept in an oven at 160 °C for 4 days. The zeolite product was filtered, dried and calcined at 550 °C for 10 h in static air. The proton form of the zeolite was obtained by triple ion exchange of the calcined zeolite with 1 M NH_4NO_3 at 70 °C for 2 h followed by calcination in static air at 550 °C for 4 h.

Meso-SSZ-13(50, C_{22-4-4}): Mesoporous SSZ-13 zeolite with Si/Al = 50 was synthesized in the same manner as SSZ-13 by combining $C_{22-4-4}Br_2$ and TMAOH as templates. The starting molar gel composition was 10 TMAOH : 5 $C_{22-4-4}Br_2$: 10 Na_2O : Al_2O_3 : 100 SiO_2 : 5000 H_2O , which was subjected to crystallization in a Teflon-lined stainless-steel autoclave at 160 °C for 6 days. After crystallization, the solid product was collected by filtration, washed with deionized water, and dried at 110 °C. The catalysts were finally calcined at 550 °C for

10 h in static air. The proton forms of the zeolites were obtained by triple ion exchange of the calcined form with 1 M NH_4NO_3 at 70 °C and calcination at 550 °C for 4 h in static air.

Meso-SSZ-13(50, TPOAC): The mesoporous SSZ-13 zeolites was synthesized by using octadecyl-(3-trimethoxysilylpropyl)-ammonium chloride (TPOAC, ABCR) as a mesopore-directing organosilane surfactant. The gel molar composition was 4 TPOAC: 20 TMdAOH : 10 Na_2O : Al_2O_3 : 100 SiO_2 : 4400 H_2O . The mixture was stirred further at room temperature until a homogeneous gel was obtained. The resulting gel was transferred into a Teflon-lined stainless steel autoclave and kept at 160 °C for 6 days. Thereafter, the solid material was recovered by filtration. The catalysts were finally calcined at 550 °C for 10 h in static air. The proton form of the zeolite was obtained by triple ion exchange of the calcined form with 1 M NH_4NO_3 at 70 °C and calcination at 550 °C for 4 h in static air.

Meso-SSZ-13(C_{22-4-4} , 0.17)-sil: A mesoporous SSZ-13 with Si/Al = 20 synthesized by $\text{C}_{22-4-4}\text{Br}_2$ and TMdAOH as templates was treated with TEOS to deactivate the external surface [18]. To this purpose, 1 g dehydrated SSZ-13(C_{22-4-4} , 0.17) (see chapter 2) in its proton form was suspended in a mixture of 50 ml n-hexane and 0.15 ml TEOS at 50 °C for 1 h. The silylated product was centrifuged, dried at 110 °C, and calcined in air in two steps: the temperature was increased to 120 °C at the rate of 5 °/min for 2 h, and went to 550 °C at 0.2 °C/min for 4 h.

SAPO-34: SAPO-34 was synthesized according to a procedure described in a patent assigned to the Union Carbide Corporation [19]. Example 35 was followed in this work. To this end, aluminum isopropoxide, Ludox HS-30, orthophosphoric acid, and tetraethyl ammonium hydroxide (TEAOH) were used to obtain a homogeneous gel with the composition 2 TEAOH : 0.3 SiO_2 : Al_2O_3 : P_2O_5 : 50 H_2O . This gel was placed in a Teflon-lined autoclave and kept in oven at 200 °C for 5 days. Afterwards, the solid material was recovered by filtration.

Meso-SAPO: Mesoporous SAPO-34 zeolites were synthesized by addition of octadecyl-(3-trimethoxysilylpropyl)-ammonium chloride (TPOAC, ABCR) as a mesopore-directing organosilane surfactant to the synthesis gel of SAPO-34. Two samples were prepared. In the first one, the silica source was stoichiometrically replaced by TPOAC so that a molar gel composition of 0.3 TPOAC : 2 TEAOH : Al_2O_3 : P_2O_5 : 50 H_2O was used. This

sample is denoted by meso-SAPO(TPOAC, ∞), the infinity sign indicating the molar TPOAC/Si ratio. The other sample denoted by meso-SAPO(TPOAC, 0.04) was obtained by addition of a small amount of TPOAC to the synthesis of SAPO-34. The gel composition was 0.012 TPOAC : 2 TEAOH : 0.3 SiO₂ : Al₂O₃ : P₂O₅ : 50 H₂O.

Meso-SAPO(C₂₂₋₄₋₄, n): In this case, 50 % and 100 % of the TEAOH compound in the standard SAPO-34 synthesis was replaced by C₂₂₋₄₋₄Br₂. The gel compositions were C₂₂₋₄₋₄Br₂ : 0.3 SiO₂ : Al₂O₃ : P₂O₅ : 50 H₂O : 2NH₃ H₂O and TEAOH : 0.5 C₂₂₋₄₋₄Br₂ : 0.3 SiO₂ : Al₂O₃ : P₂O₅ : 50 H₂O : NH₃ H₂O, respectively. The synthesis procedure for these two zeolites is similar to conventional SAPO-34. The zeolites are denoted as meso-SAPO(C₂₂₋₄₋₄, n), where n refers to the fraction of TEAOH replaced by C₂₂₋₄₋₄Br₂ in the synthesis gel. All the materials were finally calcined at 550 °C for 5 h in static air before further use.

Meso-SAPO(C₂₂₋₄₋₄, n): In this case, 50 % and 100 % of the TEAOH compound in the standard SAPO-34 synthesis was replaced by C₂₂₋₄₋₄Br₂. The gel compositions were C₂₂₋₄₋₄Br₂ : 0.3 SiO₂ : Al₂O₃ : P₂O₅ : 50 H₂O : 2NH₃ H₂O and TEAOH : 0.5 C₂₂₋₄₋₄Br₂ : 0.3 SiO₂ : Al₂O₃ : P₂O₅ : 50 H₂O : NH₃ H₂O, respectively. The synthesis procedure for these two zeolites is similar to conventional SAPO-34. The zeolites are denoted as meso-SAPO(C₂₂₋₄₋₄, n), where n refers to the fraction of TEAOH replaced by C₂₂₋₄₋₄Br₂ in the synthesis gel. All the materials were finally calcined at 550 °C for 5 h in static air before further use.

4.2.2 Physicochemical characterization

Basic characterization

X-ray diffraction patterns were recorded on a Bruker D4 Endeavor diffractometer using Cu K α radiation in the 2θ range of 5-60 °. Elemental analyses were carried out by ICP-OES (Spectro Ciros CCD ICP optical emission spectrometer with axial plasma viewing). To extract the metals, the catalysts were dissolved in 1.5 ml of an acid mixture of HF/HNO₃/H₂O. Argon adsorption experiments were determined at 87.6 K on a Micromeritics ASAP 2020 instrument in static mode. The samples were outgassed at 400 °C for 8 h prior to the sorption measurements. The Langmuir adsorption isotherm model was used to determine the total surface area (S_L) in the p/p_0 range between 0.05-0.20. The mesopore volume (V_{meso}) and mesopore size distribution was calculated from the adsorption branch of the isotherm by the

Barrett-Joyner-Halenda (BJH) method. The micropore volume (V_{micro}) was determined by the t -plot method (thickness range 0.34-0.40 nm).

Electron microscopy

Scanning electron microscopy (SEM) pictures were taken on a FEI Quanta 200F scanning electron microscope at an accelerating voltage of 3-5 kV. The catalysts were coated with gold prior to measurements. Transmission electron microscopy (TEM) pictures were taken on a FEI Tecnai 20 at 200 kV. The catalysts were suspended in ethanol and dispersed over a carbon coated holey Cu grid with a film prior to measurements.

Vibrational spectroscopy

FTIR spectra of CO adsorbed to the zeolite samples were recorded in the range of 4000-400 cm^{-1} by a Bruker Vertex V70v instrument. The spectra were acquired at a 2 cm^{-1} resolution and averaged over 20 scans. The samples were prepared as thin self-supporting wafers of 5-10 mg/cm^2 and placed inside a controlled environment infrared transmission cell, capable of heating and cooling, gas dosing and evacuation. Prior to CO adsorption, the catalyst wafer was heated to 550 $^{\circ}\text{C}$ at a rate of 2 $^{\circ}\text{C}/\text{min}$ in an oxygen atmosphere. Subsequently, the cell was outgassed at the final temperature until the residual pressure was below 5×10^{-5} mbar. The sample was then cooled to 80 K. CO was introduced into the sample cell via a sample loop (5 μL) connected to a Valco six-port valve.

NMR spectroscopy

Nuclear Magnetic Resonance (NMR) spectra were recorded on a Bruker DMX-500 NMR spectrometer. For the ^{27}Al Magic Angle Spinning (MAS) NMR a standard Bruker MAS probehead was used with rotor diameter of 2.5 mm, at a spinning rate of 20 kHz. The ^{27}Al chemical shift is referenced to a saturated $\text{Al}(\text{NO}_3)_3$ solution.

4.2.3 Catalytic activity measurements

Catalytic activity measurements were carried out in a quartz tubular fixed-bed reactor. Firstly, the zeolites were pressed, crushed and sieved in a particle size fraction between 250 and 500 μm . Secondly, 50 mg of the shaped catalyst was placed in a quartz tube (inner

diameter 4 mm) between two quartz-wool plugs. Prior to the reaction, the catalyst was activated at 550 °C in artificial air (30 ml/min) for 2 h. The methanol-to-olefins reaction was performed at 350 °C for SSZ-13 catalysts and 450 °C for SAPO catalysts. Methanol (Merck, 99%) was introduced to the reactor by flowing He through a saturator kept at -17 °C with the flow rate 30 ml/min. The WHSV was kept at 0.8 g.g⁻¹.h⁻¹ and the effluent was analyzed online by gas chromatography (Compact GC Interscience equipped with TCD and FID detectors with RT-Q-Bond and Al₂O₃/KCl columns). The amount of coke deposited during the reaction was determined by thermogravimetric analysis (TGA) on TGA/DSC 1 STAR system of Mettler Toledo. The temperature was increase to 850 °C at a rate of 5 °C/min under flowing air (50 ml/min).

4.3 Results and Discussion

4.3.1 Synthesis and characterization

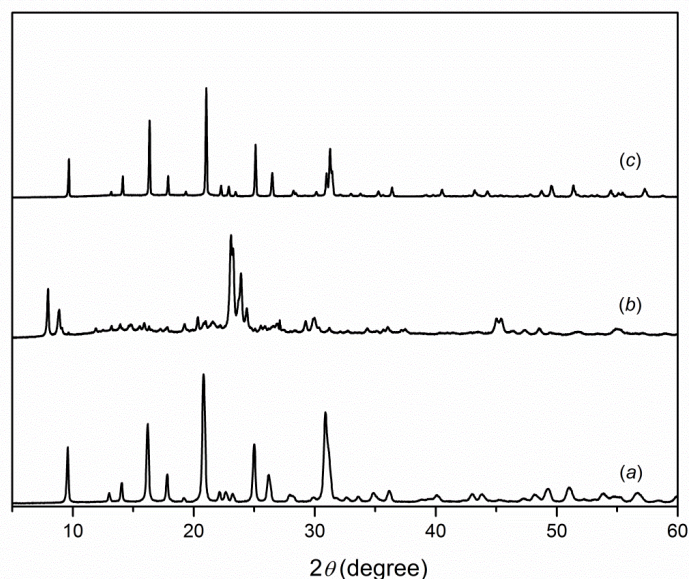


Figure 4.1: XRD patterns of as-synthesized (a) SSZ-13(50), (b) meso-SSZ-13(50, C₂₂₋₄₋₄), and (c) meso-SSZ-13(50, TPOAC).

Fig. 4.1 shows the XRD patterns of SSZ-13 zeolites synthesized at a gel Si/Al ratio of 50. The patterns of SSZ-13(50) and meso-SSZ-13(50, TPOAC) are consistent with predominant formation of crystalline zeolite with the CHA topology. The pattern of meso-SSZ-13(50,

C_{22-4-4}) is that of MFI zeolite. The XRD patterns of the calcined zeolites are very similar (not shown).

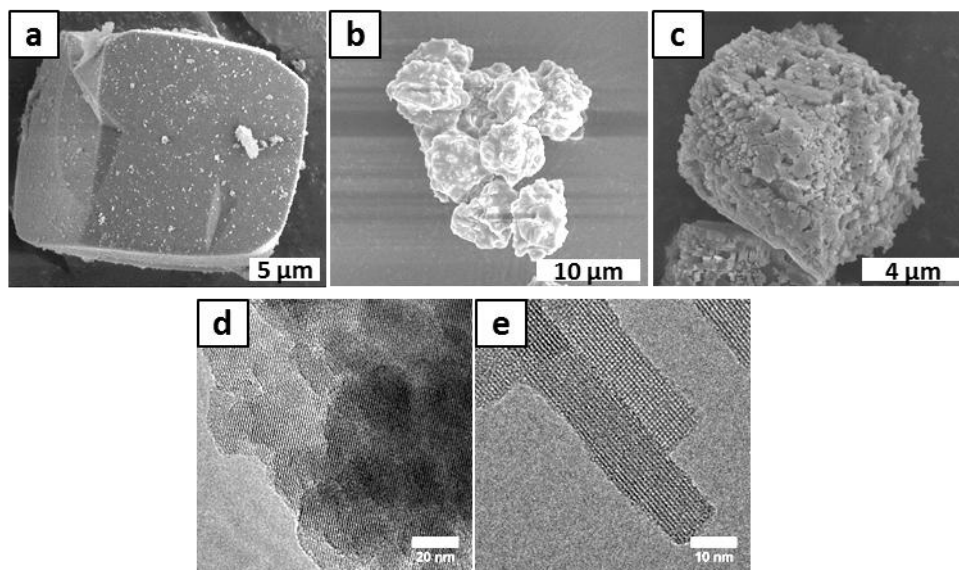


Figure 4.2: SEM (a-c) and TEM (d, e) images of (a) SSZ-13(50), (b, d) meso-SSZ-13(50, C_{22-4-4}), and (c, e) meso-SSZ-13(50, TPOAC).

Characterization by SEM shows relatively large pseudo-cubic crystals for the bulk SSZ-13 zeolite (Figure 4.2). These crystals are more rounded than the crystals synthesized at a Si/Al ratio of 20 [8] (chapter 2). TEM images of meso-SSZ-13(50, C_{22-4-4}) evidence that the crystalline domains of the undesired ZSM-5 are relatively small, suggesting that the mesopore limited the crystal growth also in this case. The zeolite prepared with TPOAC has the same morphology as a similar sample prepared at a Si/Al ratio of 20 [8] (chapter 2) however, with less well-defined cubic crystals (Fig. 4.2c). This material is well-crystallized and made up from many small crystals.

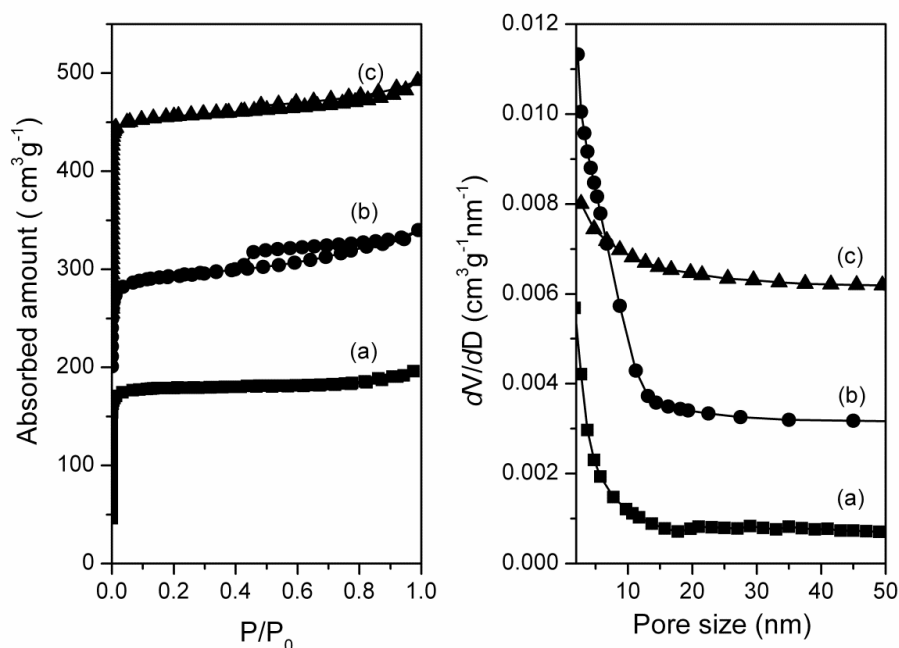


Figure 4.3: Ar physisorption (left) and pore size distribution (right) of (a) SSZ-13(50), (b) meso-SSZ-13(50, C₂₂₋₄₋₄), and (c) meso-SSZ-13(50, TPOAC). The isotherms were vertically offset by equal intervals of 150 cm³.g⁻¹. The pore size distribution was calculated via BJH algorithm using the adsorption branch and vertically offset by equal intervals of 0.003 cm³.g⁻¹.nm⁻¹.

Table 4.1: Textural properties of the calcined SSZ-13 and meso-SSZ-13 materials determined by Ar physisorption.

Sample	Si/Al ratio ^a	S_L^b (m ² .g ⁻¹)	V_{tot}^c (cm ³ .g ⁻¹)	V_{meso}^d (cm ³ .g ⁻¹)	V_{micro}^e (cm ³ .g ⁻¹)
SSZ-13(50)	54	599	0.22	0.01	0.20
meso-SSZ-13(50, TPOAC)	61	792	0.31	0.04	0.22
meso-SSZ-13(50, C ₂₂₋₄₋₄) ^f	51	558	0.24	0.06	0.14
SAPO-34	-	735	0.30	0.06	0.22
meso-SAPO(TPOAC, 0.04)	-	778	0.36	0.11	0.21
meso-SAPO(C ₂₂₋₄₋₄ , 100)	-	247	0.55	0.51	0

^a Si/Al ratio of SSZ-13 zeolites determined by ICP elemental analysis; ^b S_L is the Langmuir surface area obtained in the relative pressure range (p/p_0) of 0.05-0.20; ^c V_{tot} is the total pore volume at $p/p_0 = 0.97$; ^d V_{meso} is the mesopore volume calculated from BJH method; ^e V_{micro} is the micropore volume calculated from t -plot method; ^f Predominantly ZSM-5.

Fig. 4.3 shows Ar physisorption isotherms and BJH pore size distributions of the calcined zeolites. The textural properties derived thereof are summarized in Table 4.1. The isotherm of SSZ-13(50) is a typical type I isotherm, which is characteristic for microporous

materials. The isotherms of the two zeolites synthesized with mesopore-directing agents have the typical type IV isotherms of mesoporous materials. All three materials have high Langmuir surface areas. The total pore volume of meso-SSZ-13(50, C₂₂₋₄₋₄) is substantially lower than for the other two zeolites, consistent with dominant formation of ZSM-5 zeolite, which usually exhibits pore volumes around 0.15 cm³.g⁻¹. The use of TPOAC in SSZ-13 synthesis only led to a relatively small increase of the mesopore volume as compared to the use of C₂₂₋₄₋₄Br₂ for SSZ-13 with a Si/Al ratio of 20 [8, 9] (chapter 2). The pore size distribution curves in Fig. 4.3 do not point to the formation of ordered mesoporosity.

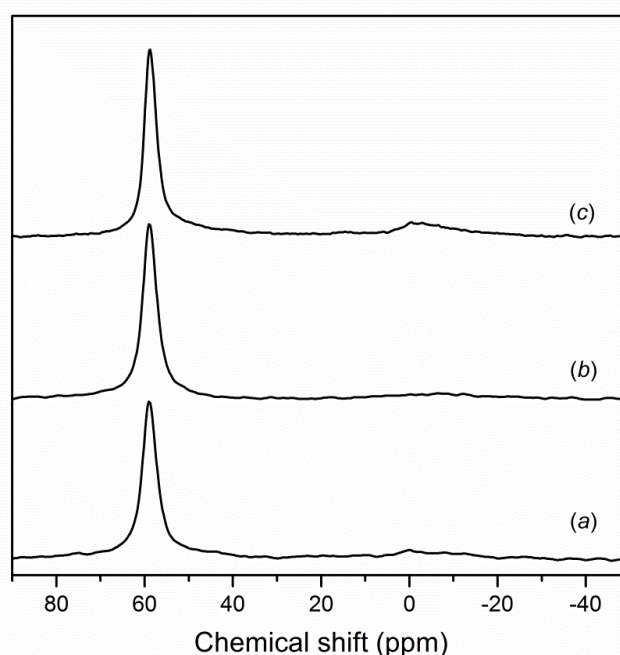


Figure 4.4: ²⁷Al MAS NMR spectra of (a) SSZ-13(50), (b) meso-SSZ-13(50, TPOAC) and (c) meso-SSZ-13(50, C₂₂₋₄₋₄). The spectra are normalized by weight and referenced to a saturated Al(NO₃)₃ solution.

Fig. 4.4 depicts the ²⁷Al MAS NMR spectra of these three zeolites are dominated by a feature around 59 ppm, which is characteristic for tetrahedrally coordinated Al atoms in the zeolite framework. A small feature around 0 ppm is assigned to octahedral Al species, which are not properly built into the zeolite framework. Deconvolution of ²⁷Al MAS NMR spectra shows that more than 90 % of the Al species is built into the zeolite framework in all three samples.

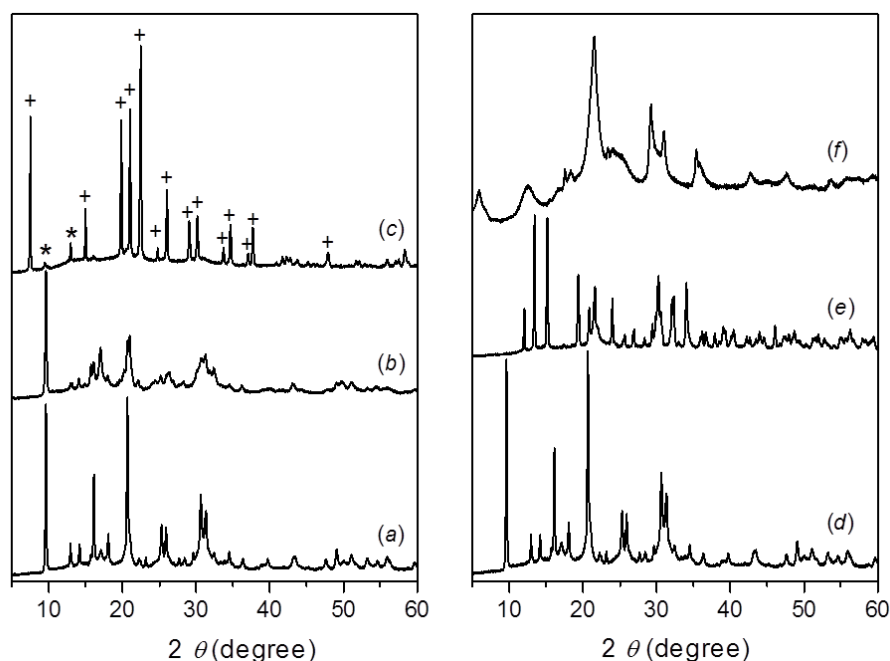


Figure 4.5: XRD patterns of as-synthesized (a) SAPO-34, (b) meso-SAPO(TPOAC, 0.04), (c) meso-SAPO(TPOAC, ∞), (d) SAPO-34, (e) meso-SAPO(C_{22-4-4} , 50), and (f) meso-SAPO(C_{22-4-4} , 100) (* and + indicate reflections of CHA and AFI phases).

Fig. 4.5 shows XRD patterns for SAPO-34, meso-SAPO(TPOAC) and meso-SAPO(C_{22-4-4}). Compared to the SAPO-34 reference, the reflections for meso-SAPO(TPOAC, 0.04) are substantially lower and broader, which is probably indicative of the smaller size of the crystalline domains for the mesoporous material. When all Si from the Ludox HS-30 silica source in the synthesis gel has been replaced by TPOAC, AIPO-5 (AFI topology) was obtained with only a minor amount of SAPO-34 (Fig. 4.5c). This zeolite contains 1-dimensional 12-ring channels. Similar to the successful synthesis of mesoporous SSZ-13 [8] (chapter 2), we also attempted to use the diquatery ammonium-type surfactant $C_{22-4-4}Br_2$ to obtain mesoporous SAPO-34. Two different synthesis gel compositions were used in which all or half of the TEAOH in a typical gel for SAPO-34 synthesis was replaced by $C_{22-4-4}Br_2$ (equivalent amount of N atoms). The XRD patterns of meso-SAPO(C_{22-4-4} , 50) and meso-SAPO(C_{22-4-4} , 100) are shown in Figs. 4.5e and 4.5f, respectively. In neither case, SAPO-34 was formed. Meso-SAPO(C_{22-4-4} , 50) turned out to be AIPO-15 zeolite [20, 21], whilst the structure of the other material could not be resolved from known databases.

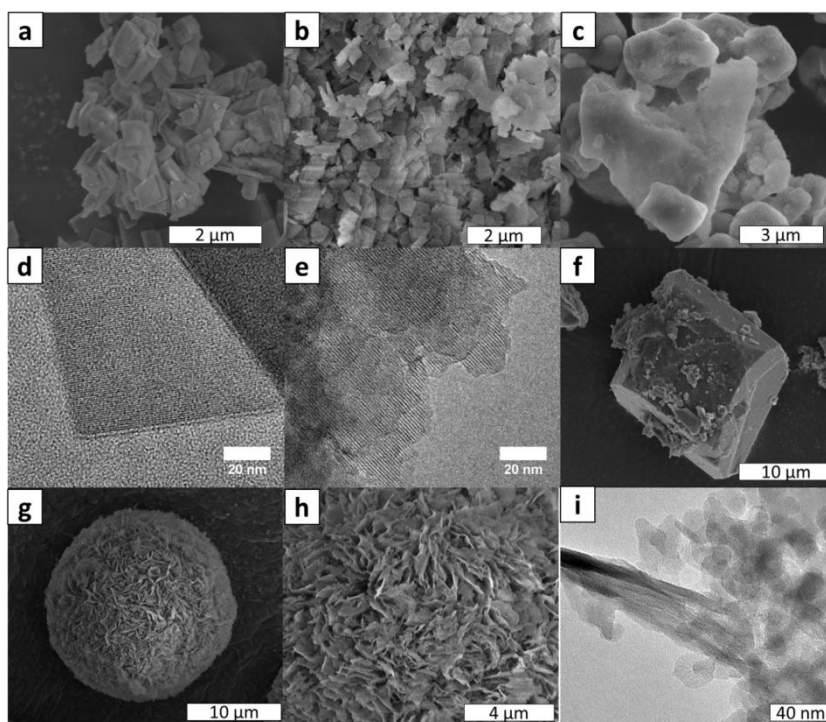


Figure 4.6: Electron microscopy images of (a) conventional SAPO-34, (b, d) meso-SAPO(TPOAC, 0.04), (c, e) meso-SAPO(TPOAC, ∞), (f) meso-SAPO(C_{22-4-4} , 50), (g-i) meso-SAPO(C_{22-4-4} , 100).

SAPO-34 consists of small particles intergrown into larger agglomerates (Fig. 4.6). The crystals of meso-SAPO(TPOAC, 0.04) are slightly smaller than those of SAPO-34. The AlPO-5 sample consists of large intergrown particles. The SEM image of AlPO-15 derived from the meso-SAPO(C_{22-4-4} , 50) shows large crystals with a square prism morphology without any sign of mesoporosity. The scanning and transmission electron micrographs for meso-SAPO(C_{22-4-4} , 100) are very different and show the formation of agglomerates of a layered material. Its layered nature is consistent with the low-angle diffraction peak in Fig. 4.5f. The significant background in this XRD pattern around 23° and the observation of globular particles by TEM (Fig. 4.5i) indicates that also a significant amount of amorphous silica was formed. All this suggests that crystallization of this material is far from complete.

The Ar physisorption isotherms of SAPO-34, meso-SAPO(TPOAC, 0.04) and meso-SAPO(C_{22-4-4} , 100) are shown in Fig. 4.7 and the textural properties are listed in Table 4.1. The isotherm of SAPO-34 is typical type I. The isotherm of meso-SAPO(TPOAC, 0.04) is a combination of type I and IV, which is characteristic of porous materials containing micro- and mesopores. Meso-SAPO(TPOAC, 0.04) has a similar surface area and micropore

volume as SAPO-34, but its mesopore volume is substantially higher ($0.11 \text{ cm}^3 \cdot \text{g}^{-1}$ vs. $0.03 \text{ cm}^3 \cdot \text{g}^{-1}$ for SAPO-34). It can be seen that the micropore volumes of SAPO-34 and meso-SAPO(TPOAC, 0.04) are very similar to the micropore volume of SSZ-13(50). The textural properties of meso-SAPO(C_{22-4-4} , 100) show that this layered material does not contain micropores.

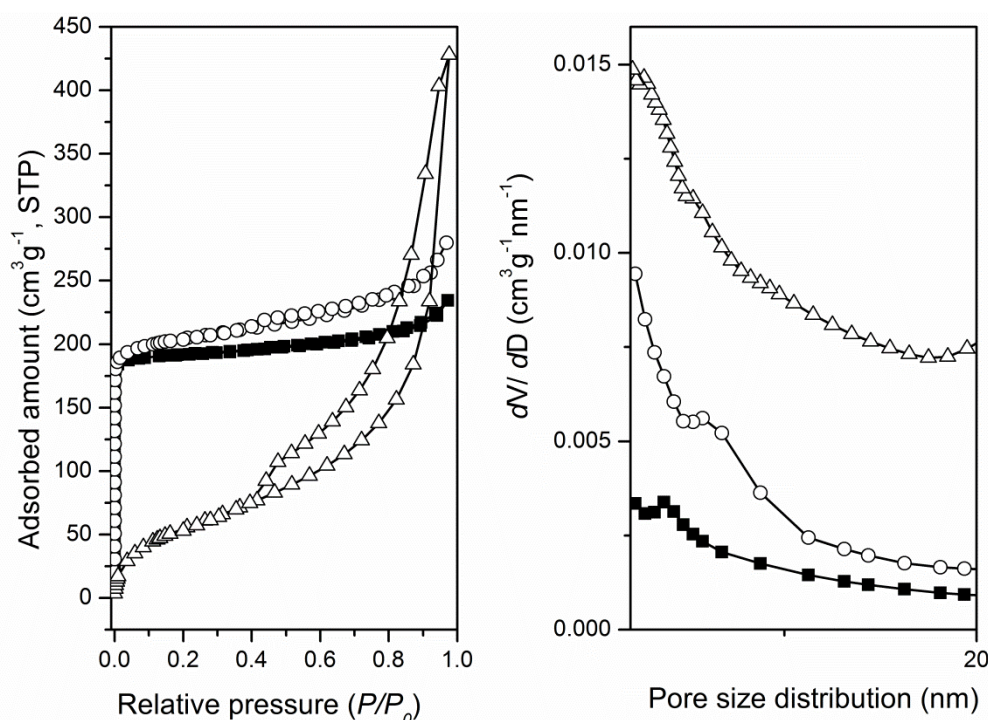


Figure 4.7: Ar physisorption (left) and PSD (right) of (■) SAPO-34, (○) meso-SAPO(TPOAC, 0.04) and (Δ) meso-SAPO(C_{22-4-4} , 100). The pore size distribution was calculated via BJH algorithm using the adsorption branch.

Summarizing, a small amount of mesopores can be introduced in high-silica ($\text{Si}/\text{Al} = 50$) SSZ-13 by use of TPOAC. Attempts to employ $\text{C}_{22-4-4}\text{Br}_2$ as mesoporegen to synthesize hierarchical SSZ-13 at this Si/Al ratio were unsuccessful. Similar observations were made when these strategies were employed to SAPO-34 synthesis. Addition of small amounts of TPOAC to the synthesis gel of SAPO-34 led to generation of significant mesoporosity. An increase of the TPOAC content led to nearly exclusive formation of AIPO-5 instead of SAPO-34. The use of $\text{C}_{22-4-4}\text{Br}_2$ during SAPO-34 synthesis resulted in formation of other zeolite phases.

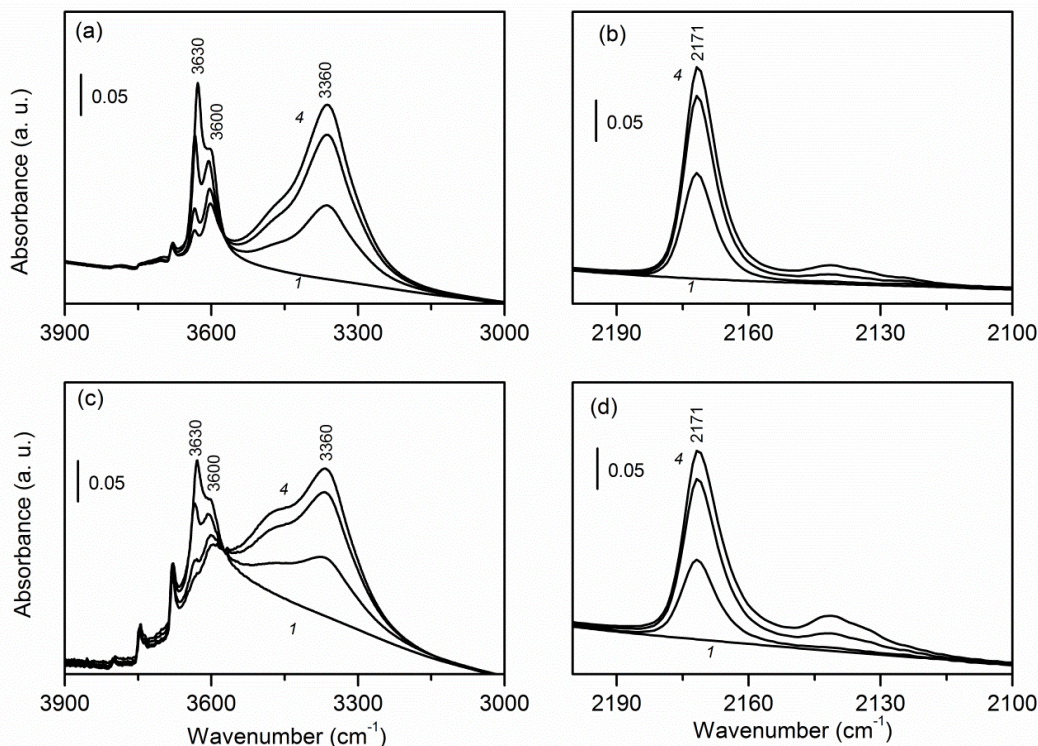


Figure 4.8: FTIR spectra of CO adsorbed on SAPO-34 (a, b) and meso-SAPO(TPOAC, 0.04) (c, d) at liquid N₂ temperature : (left) OH stretching region, and (right) CO stretching region (trace 1 is the spectrum of dehydrated zeolite before CO adsorption; traces 2-4 after introduction of 0.55, 0.85, 1.20, 1.85 μmol CO in the IR cell; the spectra normalized by sample weight).

Before discussing the catalytic activity of some of these materials in the MTO reaction, we will first compare the acidity of SAPO-34 and meso-SAPO(TPOAC, 0.04). Fig. 4.8 displays the FTIR spectra of increasing doses of CO adsorbed on calcined SAPO-34 and meso-SAPO(TPOAC, 0.04). The high-frequency (HF) band at 3630 cm^{-1} and the low-frequency (LF) band at 3600 cm^{-1} are assigned to Brønsted acid sites. The intensities of these bands for meso-SAPO(TPOAC, 0.04) are lower than those for SAPO-34, which indicates that the mesoporous zeolite has a smaller number of Brønsted acid sites. Upon CO adsorption, the bands due to Brønsted acid sites shift to 3360 cm^{-1} . The equal red-shift of the hydroxyl frequency, $\Delta\nu(\text{OH}) = -270\text{ cm}^{-1}$, demonstrates that the strength of the acid sites in these zeolites is very similar. The shift is smaller than observed for aluminosilicate zeolites, which are indeed considered to be stronger Brønsted acids [22, 23]. Upon increasing the CO pressure, the HF band erode faster than the LF band, which points to stronger acidity or better accessibility of the former hydroxyl groups. The spectra representing the CO stretching are

also shown. The band at 2171 cm^{-1} appearing upon CO exposure is ascribed to CO adsorbed on Brønsted acid sites. Consistent with the view put forward by Almutairi et al., the polarization of the CO bond is not an adequate indicator of Brønsted acidity, as the blue shift of perturbed CO to 2171 cm^{-1} is similar to that for the stronger acidic HZSM-5 zeolite [14, 24].

4.3.2 Catalytic activity measurements

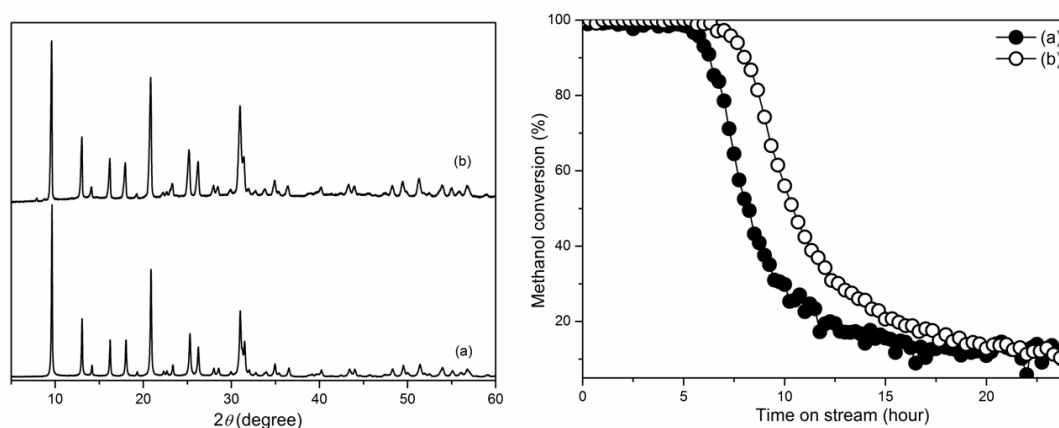


Figure 4.9: (left) XRD patterns and (right) catalytic performance in the MTO reaction (WHSV = $0.8\text{ g}\cdot\text{g}^{-1}\cdot\text{h}^{-1}$; $T = 350\text{ }^{\circ}\text{C}$) of calcined (a) meso-SSZ-13(C_{22-4-4} , 0.17) and (b) meso-SSZ-13(C_{22-4-4} , 0.17)-sil.

We first discuss the performance of silylated mesoporous SSZ-13 in the MTO reaction. The rationale of silylating the most promising mesoporous SSZ-13 zeolite, meso-SSZ-13(C_{22-4-4} , 0.17) with a Si/Al ratio of 20 [8, 9] (chapter 2) was to evaluate whether deactivation of the external surface had a beneficial effect on catalyst stability. Treatment of meso-SSZ-13(C_{22-4-4} , 0.17) with TEOS did not significantly affect the crystallinity of the mesoporous SSZ-13 zeolite (Fig. 4.9a), lowered the silanol density to some extent. Fig. 4.9b shows the performance in the MTO reaction with reaction time. Clearly, the rate of coke formation was lowered due to the deactivation of acid sites on the external surface. The product distributions (mainly C_2 and C_3 olefins) were similar for both zeolites (Table 4.2). These results indicate that there is room for improvement of the total methanol conversion capacity of mesoporous SSZ-13 by lowering the rate of coke formation on the external surface.

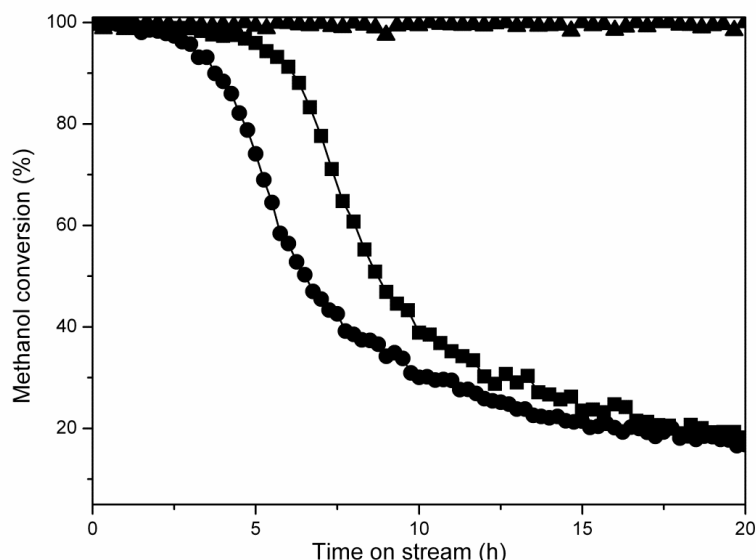


Figure 4.10: Catalytic performance in the MTO reaction (WHSV = 0.8 $\text{g}\cdot\text{g}^{-1}\cdot\text{h}^{-1}$; $T = 350\text{ }^{\circ}\text{C}$) of (●) SSZ-13(50), (▲) meso-SSZ-13(50, $\text{C}_{22-4.4}$) and (■) meso-SSZ-13(50, TPOAC).

Table 4.2: Lifetime and product distribution^a of zeolite catalysts for the MTO reaction (WHSV = 0.8 $\text{g}\cdot\text{g}^{-1}\cdot\text{h}^{-1}$; $T = 350\text{ }^{\circ}\text{C}$) after 1 h time on stream.

Zeolite	t_{50} ^b (h)	CH_4 (%)	C_2 ⁼ (%)	C_2 (%)	C_3 ⁼ (%)	C_3 (%)	Aliphatic $\text{C}_4\text{-C}_6$ (%)
SSZ-13(50)	7	1.4	52.6	0.2	41.5	2.7	1.5
meso-SSZ-13(50, TPOAC)	9	1.2	51.4	0.2	44.1	1.6	1.4
meso-SSZ-13($\text{C}_{22-4.4}$, 0.17) ^[d]	8	1.0	45.8	0.4	47.7	2.9	2.2
meso-SSZ-13($\text{C}_{22-4.4}$, 0.17)-sil	10	1.3	48.5	0.3	45.7	2.9	1.3

^aTrace amounts of CO and CO_2 not taken into account; ^bCatalyst lifetime defined as the time passed to reach a conversion of 50 %; ^c Not determined; ^d from [8](chapter 3).

The catalytic activities of the SSZ-13 zeolites with a Si/Al ratio of 50 at a WHSV of 0.8 $\text{g}\cdot\text{g}^{-1}\cdot\text{h}^{-1}$ are shown in Fig. 4.10 and the corresponding performance data are listed in Table 4.2. Initially, all catalysts show complete conversion of methanol to products with carbon-carbon bonds. For SSZ-13(50), the lifetime in MTO reaction is about 7 h, which is significantly higher than that of SSZ-13(20) (2.8 h) [8, 9] (chapter 3). This shows that a lower Brønsted acid site density results in a lower rate of deactivation. When additional mesoporosity is introduced in SSZ-13(50) by use of TPOAC (meso-SSZ-13(50, TPOAC)), the lifetime of the catalyst is further improved. The increase in lifetime upon mesopore introduction in SSZ-13(50) is however much lower than earlier found for SSZ-13(20) [8, 9] (chapter 3). This

should be due to the lower rate of coke formation of SSZ-13(50), which results in better utilization of the micropore space. The most stable zeolite is meso-SSZ-13(50, C₂₂₋₄₋₄), a HZSM-5 zeolite, which typically show more stable performance in the methanol conversion reaction. As were primarily interested in CHA zeolite in this study, we did not determine the stability of the ZSM-5 zeolite.

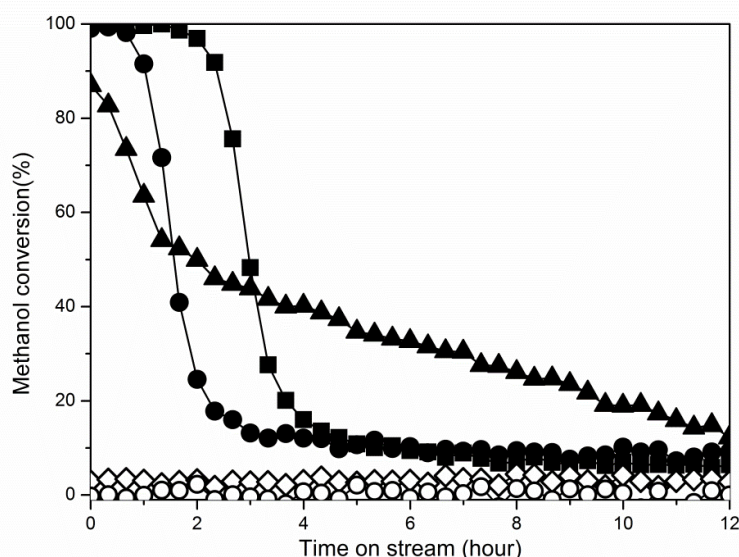


Figure 4.11: Catalytic performance in the MTO reaction (WHSV = 0.8 g.g⁻¹.h⁻¹; T = 450 °C) of (■) SAPO-34, (●) meso-SAPO(TPOAC, 0.04), (▲) meso-SAPO(TPOAC, ∞), (◇) meso-SAPO(C₂₂₋₄₋₄, 50) and (○) meso-SAPO(C₂₂₋₄₋₄, 100).

Table 4.3: Lifetime and product distribution^a of SAPO-34 and meso-SAPO(TPOAC, 0.04) zeolite catalysts for the MTO reaction (WHSV = 0.8 g.g⁻¹.h⁻¹; T = 450 °C) after 1 h time on stream.

Zeolite	Lifetime ^b (h)	CH ₄ (%)	C ₂ ⁼ (%)	C ₂ (%)	C ₃ ⁼ (%)	C ₃ (%)	Aliphatic C ₄ -C ₆ (%)
SAPO-34	3.0	2.1	41.9	0.2	39.5	0	16.3
meso-SAPO(TPOAC, 0.04)	1.5	3.8	40.7	0.2	37.9	0	17.4
meso-SAPO(TPOAC, ∞)	2.0	4.5	16.1	0.2	34.9	0.5	43.8

^a Trace amounts of CO and CO₂ not taken into account; ^b Catalyst lifetime defined as the time passed to reach a conversion of 50 %.

Fig. 11 shows the catalytic properties of the SAPO materials in the MTO reaction. The lifetime and the product distributions are given in Table 4.3. Meso-SAPO(TPOAC, ∞) shows some activity with a product distribution typical for ZSM-5 zeolite. The methanol conversion for meso-SAPO(C₂₂₋₄₋₄, 50) and meso-SAPO(C₂₂₋₄₋₄, 100) is very low. Both microporous

SAPO-34 and meso-SAPO(TPOAC, 0.04) initially show complete conversion of methanol with good selectivity to C₂ and C₃ olefins. Deactivation of the mesoporous SAPO-34 zeolite sets in earlier than for the conventional SAPO-34 one. The lifetimes of SAPO-34 and meso-SAPO(TPOAC, 0.04) are 3 and 1.5 h, respectively. Thus, whilst the performance of SSZ-13 can be improved by introducing mesoporosity, such improvement could not be brought about for SAPO-34.

Table 4.4: Textural properties of spent SAPO-34 and meso-SAPO(TPOAC, 0.04) catalysts as a function of the time on stream determined by Ar physisorption.

TOS ^a (h)	SAPO-34				meso-SAPO-34			
	S_L (m ² .g ⁻¹)	V_{micro} (cm ³ .g ⁻¹)	V_{meso} (cm ³ .g ⁻¹)	Coke ^b (wt. %)	S_L (m ² .g ⁻¹)	V_{micro} (cm ³ .g ⁻¹)	V_{meso} (cm ³ .g ⁻¹)	Coke ^c (wt. %)
1	347	0.09	0.08	3.5	300	0.08	0.09	3.6
4	295	0.07	0.10	11.7	284	0.07	0.11	6.9
12	164	0.04	0.07	12.8	191	0.05	0.08	8.0
48	149	0.04	0.06	13.7	141	0.07	0.10	10.0

^a Time on stream; ^b Coke content based on TGA.

It is well known that the Brønsted acid of SAPO-34 is much weaker than SSZ-13 [22, 23]. Accordingly, it is expected that coking in SSZ-13 proceeds at a higher rate than in SAPO-34. The lower rate of coke formation for SAPO-34 may thus lead to more efficient utilization of the micropore space. As a consequence, there is no benefit by generating mesoporosity in SAPO-34. If this would be the case, the lower stability of mesoporous SAPO-34 should be due to the lower concentration of Brønsted acid sites. A rough estimation based on the difference in the intensity of the CO stretching band around 2171 cm⁻¹ shows that meso-SAPO(TPOAC, 0.04) contains about 40% less acid sites than SAPO-34. This difference coheres very well with the shorter lifetime, so that the total methanol conversion capacity of the two zeolites per Brønsted acid site is comparable. To fortify this line of reasoning, Table 4.4 shows the textural properties and coke content of SAPO-34 and meso-SAPO(TPOAC, 0.04) as the function of the time on the stream. After a reaction time of 1 h, already a large part of the high Langmuir surface area of the parent samples (> 700 m².g⁻¹) has become inaccessible by coke. It is also seen that the micropore volume has decreased below 0.10 cm³.g⁻¹ (initial value ~0.21 cm³.g⁻¹). With increasing time on stream the surface

area of the two materials decreases in a very similar manner. The coke build-up is slightly slower for meso-SAPO(TPOAC, 0.04), which may be attributed to the lower acidity of this sample. Yang et al. recently reported that nanosizing SAPO-34 crystals led to a decrease in coke formation and, concomitant remarkable increase of the lifetime in the MTO reaction [25]. This discrepancy may be caused by the higher Brønsted acid intensity and the larger particle size of their reference sample, and the higher WHSV of MTO employed by these authors.

4.4 Conclusions

In order to improve the stability of SSZ-13 zeolite for the MTO reaction, two methods have been explored. Firstly, a mesoporous SSZ-13(20) zeolite was silylated, resulting in minor improvement of the lifetime in the MTO reaction. Secondly, SSZ-13 zeolite with a Si/Al ratio of 50 was synthesized. Lower acidity results in a lower rate of deactivation compared to SSZ-13 with a Si/Al ratio of 20. Introducing mesoporosity in SSZ-13(50) by use of TPOAC only results in a minor improvement of the lifetime. This is likely because the lower rate of coke formation for SSZ-13(50) as compared to SSZ-13(20) results in better utilization of the micropore space. It was not possible to synthesize mesoporous SSZ-13 at high Si/Al ratios with the $C_{22-4-4}Br_2$ template. Instead, ZSM-5 zeolite was obtained.

Attempts to synthesize SAPO-34 by use of $C_{22-4-4}Br_2$ as mesoporegen were also not successful and other AlPO-phases were obtained. By addition of TPOAC a mesoporous SAPO-34 could be obtained. However, in this case the intracrystalline mesoporosity did not lower the deactivation rate. The total methanol conversion capacity per acid site for microporous and mesoporous SAPO-34 was comparable. These findings are interpreted in terms of complete utilization of the micropore of SAPO-34 in the MTO reaction. The very different findings for SSZ-13, whose micropore space remains underutilized unless mesopores are introduced, relate to the much lower acidity of silicoaluminophosphates. Accordingly, there is no benefit of additional mesoporosity. Consistent with this, it is found that the deactivation for micro- and mesoporous SAPO-34 zeolites proceeds in a very similar manner with time on stream.

Reference

- [1] C.D. Chang, *Catal. Rev.-Sci. Eng.* 26 (1984) 323-345.
- [2] M. Stocker, *Microporous Mesoporous Mater.* 29 (1999) 3-48.
- [3] J.F. Haw, W.G. Song, D.M. Marcus, and J.B. Nicholas, *Acc. Chem. Res.* 36 (2003) 317-326.
- [4] F.J. Keil, *Microporous Mesoporous Mater.* 29 (1999) 49-66.
- [5] U. Olsbye, S. Svelle, M. Bjorgen, P. Beato, T.V.W. Janssens, F. Joensen, S. Bordiga, and K.P. Lillerud, *Angew. Chem. Int. Ed.* 51 (2012) 5810-5831.
- [6] J. Liang, H.Y. Li, S. Zhao, W.G. Guo, R.H. Wang, and M.L. Ying, *Appl. Catal.* 64 (1990) 31-40.
- [7] Z.M. Liu, C.L. Sun, G.W. Wang, Q.X. Wang, and G.Y. Cai, *Fuel Process. Technol.* 62 (2000) 161-172.
- [8] L. Wu, V. Degirmenci, P.C.M.M. Magusin, N.J.H.G.M. Lousberg, and E.J.M. Hensen, *J. Catal.* 298 (2013) 27-40.
- [9] L. Wu, V. Degirmenci, P. Magusin, B.M. Szyja, and E.J.M. Hensen, *Chem. Commun.* 48 (2012) 9492-9494.
- [10] M. Choi, H.S. Cho, R. Srivastava, C. Venkatesan, D.H. Choi, and R. Ryoo, *Nat. Mater.* 5 (2006) 718-723.
- [11] M. Choi, K. Na, J. Kim, Y. Sakamoto, O. Terasaki, and R. Ryoo, *Nature* 461 (2009) 246-250.
- [12] M. Choi, R. Srivastava, and R. Ryoo, *Chem. Commun.* (2006) 4380-4382.
- [13] C. Jo, J. Jung, H.S. Shin, J. Kim, and R. Ryoo, *Angew. Chem. Int. Ed.* 52 (2013) 10014-10017.
- [14] S.M.T. Almutairi, B. Mezari, E.A. Pidko, P.C.M.M. Magusin, and E.J.M. Hensen, *J. Catal.* 307 (2013) 194-203.
- [15] M. Guisnet, L. Costa, and F.R. Ribeiro, *J. Mol. Catal. A: Chem.* 305 (2009) 69-83.
- [16] Y. Kumitaa, J. Gascona, E. Stavitski, J. A. Moulijna, F. Kapteijna, *Appl. Catal. A: General* 391 (2011) 234-243.
- [17] L.T. Yuen, and S.I. Zone. 2001. *Verified Syntheses of Zeolitic Materials.*
- [18] S.R. Zheng, H.R. Heydenrych, A. Jentys, and J.A. Lercher, *J. Phys. Chem. B* 106 (2002) 9552-9558.
- [19] B.M. Lok, C.A. Messina, R.L. Patton, R.T. Gajek, T.R. Cannon, and E.M. Flanigen. (1984) U.S. Patent. 4440871.
- [20] J.J. Pluth, J.V. Smith, J.M. Bennett, and J.P. Cohen, *Acta Crystallogr. Sect. C* 40 (1984) 2008-2011.
- [21] J.B. Parise, *Acta Crystallogr., Sect. C* 40 (1984) 1641-1643.

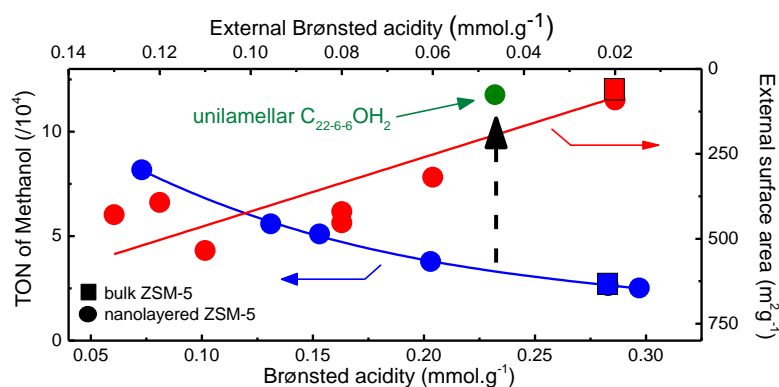
- [22] S. Bordiga, L. Regli, D. Cocina, C. Lamberti, M. Bjorgen, and K.P. Lillerud, *J. Phys. Chem. B* 109 (2005) 2779-2784.
- [23] F. Bleken, M. Bjorgen, L. Palumbo, S. Bordiga, S. Svelle, K.P. Lillerud, and U. Olsbye, *Top. Catal.* 52 (2009) 218-228.
- [24] S.M.T. Almutairi, B. Mezari, G.A. Filonenko, P. Magusin, M.S. Rigutto, E.A. Pidko, and E.J.M. Hensen, *ChemCatChem* 5 (2013) 452-466.
- [25] G. Yang, Y. Wei, S. Xu, J. Chen, J. Li, Z. Liu, J. Yu, R. Xu, *J. Phys. Chem. C* 117 (2013) 8214-8222.

Chapter 5

Acidic Properties of Nanolayered ZSM-5 Zeolites

Summary

The acidic properties of nanolayered ZSM-5 synthesized with the aid of multiquaternary ammonium surfactants were investigated in detail. Acidity characterization reveals that the Brønsted acid sites (BAS) are similar in strength to those in bulk HZSM-5. Nanolayered zeolites contain a higher amount of BAS at their external (mesopore) surface. Unilamellar zeolites have a higher concentration of external BA and silanol sites than multilamellar ones. The number of BAS in the nanolayered zeolites is considerably lower than the tetrahedral Al content, the difference increasing with nanolayer thickness. Except for one particular sample (nanolayered ZSM-5 synthesized from $C_{22-6-6}OH_2$), the total turnover of methanol normalized per BAS trends inversely with the concentration of BAS. There is no correlation with the concentration of external BAS. Catalyst deactivation due to coke mainly depends on the BAS concentration. A unilamellar ZSM-5 zeolite prepared using $C_{22-6-6}OH_2$ displayed substantially improved performance in terms of a much lower rate of coke deactivation in line with earlier data Choi et al. [10]. Since the acidic and textural properties of this zeolite did not differ significantly from the others, it remains to be determined why this zeolite performs so much better.



5.1 Introduction

Zeolites are crystalline microporous aluminosilicates widely used in the chemical industry as catalysts [1, 2]. Essential to the broad range of catalytic applications is their strong acidity and stability at elevated reaction temperatures. The strong Brønsted acidity of zeolites resides in tetrahedral Al^{3+} substitutions in the microporous crystalline silica framework, their combination giving rise to size- and shape-selective acid catalysis. Zeolites are usually synthesized in the form of micrometer-sized crystals, which may lead to mass transport limitations during catalytic reactions. Strategies to counter reduced effectiveness factors can be divided in the synthesis of wide-pore zeolites, which remains a challenging research topic, and approaches to decrease the diffusion path inside zeolites. Of the latter, the synthesis of nanosized zeolite crystals [3], delamination of zeolites [4] and generation of mesoporosity in zeolites by bottom-up or top-down methods have received most attention. Several reviews in this active area of research are available [5-9]. Zeolites with reduced diffusion path have shown improved performance in reactions that suffer from deactivation by coke deposition [10-13]. The increased capacity to cope with coke formation is the result of an increased effectiveness factor, which means that a larger part of the zeolite crystal can be utilized before deactivation makes its inner parts inaccessible.

Although the synthesis of zeolites has been studied for several decades, the fine details about the mechanism of their formation remain limited [14, 15]. Advances in zeolite synthesis have made it possible to prepare nanolayered ZSM-5 zeolites with thickness of the individual sheets of as small as 2 nm with good thermal and hydrothermal stability [10]. The formation of such nanosheets is possible by the use of multi-quaternary ammonium structure directing agents (SDA) with a sufficiently long hydrophobic tail [16]. The SDA prefers to be aligned along the *b*-direction in the MFI pore network, *viz.* in the straight channels so that zeolite growth occurs in the *a*- and *c*-directions, resulting in thin 2D zeolite layers. By varying the number of quaternary ammonium groups in the SDA the thickness can be varied between 2 and 6 nm [16]. The nanosheets can be ordered in a regular fashion into multilamellar stacks or in a disordered fashion (unilamellar zeolite). Initial experiments indicated that the type of counterion is decisive in the morphology control [10], whereas a

later study shows that control of the synthesis gel pH is important [17].

In view of the importance of acidity, detailed investigations of the nature (Brønsted vs. Lewis), the location (internal vs. external) and strength of the acid sites in hierarchical or nanosized zeolites is desirable. For instance, generation of mesoporosity in zeolite crystals results in much higher accessibility of Brønsted acid sites [18], which will affect the zeolite's shape selective properties. The presence of Brønsted acid sites at the mesopore surface of the nanosheets and their applicability to catalyze reactions with large molecules is evident from the early work of Ryoo and co-workers [10]. The same work also showed that coke formation during conversion of methanol to hydrocarbons occurred preferentially in the mesopores, resulting in a significant increase of catalyst longevity. A reinterpretation of these data is that the larger external surface/micropore volume results in more efficient use of the micropore volume. Then, a larger amount of methanol can be converted before the catalyst deactivates due to excessive coke formation. Such interpretation has recently been put forward for a highly mesoporous SSZ-13 zeolite in the methanol-to-olefins (MTO) reaction [19] and is also consistent with the observation of significantly increased catalyst longevity for nanolayered Fe/ZSM-5 in the oxidation of benzene to phenol with nitrous oxide [12]. Besides the locus of the acid sites, another important issue relates to their strength. Down-sizing the microporous domain of zeolite might result in decreased acidity, perhaps due to less rigid ordering of the zeolite crystal in nanostructured forms. Two other recent studies investigate the effect of sheet thickness on the catalytic activity in *n*-alkane hydroconversion, a common reaction that mainly probes strong Brønsted acidity, of these nanolayered zeolites. Verheyen et al. studied *n*-decane hydroconversion and mainly identified differences in the yields of mono- vs. dibranched products, which were attributed to the shorter diffusion path in the nanolayers [20]. Kim et al. also observed relatively little influence of such down-sizing in the hydroconversion of *n*-heptane, differences mostly limited to changes in the branched isomer yield [21]. These differences were not discussed in terms of a possible increased density of acid sites at the external surface of the sheets. Both studies reported some differences in the acid catalytic properties, which did not trend well with acidity characterization.

Our present study focuses on the acidity of multilamellar and unilamellar ZSM-5 zeolites and their catalytic performance in the methanol-to-hydrocarbons (MTH) reaction. We have

followed the synthesis approach of Ryoo and co-workers [16]. The morphology and structure of the nanolayered zeolites was investigated by XRD, SEM, TEM, Ar physisorption and UV-Raman and NMR spectroscopy. Using ^{29}Si NMR, we specifically investigated the template-silicate interactions in the as-synthesized zeolites. Acidity was characterized by a combination of IR spectroscopy using probe molecules such as carbon monoxide, pyridine and 2,4,6-collidine as well as ^{27}Al and ^1H MAS NMR spectroscopy. The catalytic properties of the zeolites in the MTH reaction at 400 °C were also determined.

5.2 Experimental section

5.2.1 Synthesis of templates

$[\text{C}_{22}\text{H}_{45}\text{-N}^+(\text{CH}_3)_2\text{-C}_6\text{H}_{12}\text{-N}^+(\text{CH}_3)_2\text{-C}_6\text{H}_{13}]\text{Br}_2$ (denoted as $\text{C}_{22-6-6}\text{Br}_2$): For synthesis of $\text{C}_{22-6-6}\text{Br}_2$ we followed the procedure outlined before [13, 19]. Briefly, N,N,N',N'-tetramethyl-1,6-diaminohexane was reacted with 1-bromo-undecane in order to obtain C_{22-6}Br . This intermediate was subsequently reacted with 1-bromohexane to obtain $\text{C}_{22-6-6}\text{Br}_2$.

$[\text{C}_{22}\text{H}_{45}\text{-N}^+(\text{CH}_3)_2\text{-C}_6\text{H}_{12}\text{-N}^+(\text{CH}_3)_2\text{-C}_6\text{H}_{12}\text{-N}^+(\text{CH}_3)_2\text{-C}_6\text{H}_{13}]\text{Br}_3$ (denoted as $\text{C}_{22-6-6-6}\text{Br}_3$): The surfactant was synthesized starting from $\text{C}_{22-6-6}\text{Br}_2$. To this end, 0.1 mol $\text{C}_{22-6-6}\text{Br}_2$ and 0.3 mol N,N-dimethylhexylamine (Aldrich, 98%) were dissolved in 30 ml dried propanol and refluxed at 90 °C for 36 h. After cooling to room temperature, the solid product was kept in a refrigerator at 4 °C for 1 h, filtered, washed with cold diethyl ether and dried in a vacuum oven at 50 °C. The resulting product was $\text{C}_{22-6-6-6}\text{Br}_3$.

$[\text{C}_{22}\text{H}_{45}\text{-N}^+(\text{CH}_3)_2\text{-C}_6\text{H}_{12}\text{-N}^+(\text{CH}_3)_2\text{-C}_6\text{H}_{12}\text{-N}^+(\text{CH}_3)_2\text{-C}_6\text{H}_{12}\text{-N}^+(\text{CH}_3)_2\text{-C}_6\text{H}_{13}]\text{Br}_4$ (denoted as $\text{C}_{22-6-6-6-6}\text{Br}_4$): 0.1 mol $\text{C}_{22-6-6-6}\text{Br}_2$ and 1.0 mol N, N, N', N'-tetramethyl-1,6-hexanediamine (Aldrich, 99 %) were dissolved in 30 ml dried propanol and refluxed at 90 °C for 24 h. Afterwards, the liquid mixture was aged at room temperature for 24 h until the product $[\text{C}_{22}\text{H}_{45}\text{-N}^+(\text{CH}_3)_2\text{-C}_6\text{H}_{12}\text{-N}^+(\text{CH}_3)_2\text{-C}_6\text{H}_{12}\text{-N}^+(\text{CH}_3)_2\text{-C}_6\text{H}_{12}\text{-N}(\text{CH}_3)_2]\text{Br}_3$ ($\text{C}_{22-6-6-6-0}\text{Br}_3$) precipitated. The solid product was filtered, washed and dried in vacuum oven at room temperature. Then, 0.1 mol $\text{C}_{22-6-6-6-0}\text{Br}_3$ and 0.2 mol 1-bromohexane (Aldrich, 98 %) were dissolved in 35 ml dried propanol and refluxed overnight at 90 °C. After cooling to

room temperature, the mixture was kept in refrigerator at 4 °C for 1 h, filtered, washed with cold diethyl ether and dried in a vacuum oven at room temperature. The resulting product was $C_{22-6-6-6}Br_4$.

Hydroxyl forms of these surfactants were obtained by treating the bromide form with an anion-exchange resin (Amberlite, IRN-78) in a flask overnight.

5.2.2 Synthesis of materials

Synthesis of uni- and multilamellar MFI zeolite nanosheets

Multilamellar and unilamellar MFI materials were synthesized using, respectively, the bromide and hydroxide form of the surfactants. The gel compositions with a target Si/Al ratio of 50 are shown in Table 5.1.

For a typical synthesis procedure, 0.48 g NaOH and 0.13 g $Al_2(SO_4)_3 \cdot 18H_2O$ was dissolved in 13.6 g distilled water followed by addition of the surfactant under stirring at 60 °C. The solution was stirred for 1 h. After cooling to room temperature, 1.17 g H_2SO_4 (30%) was added under stirring. Then 4.16 g tetraethylorthosilicate (TEOS) [Sigma-Aldrich, 98% (wt/wt)] was added rapidly. The solution was again heated to 60 °C and stirred for 30 min. The homogeneous gel was finally transferred to a Teflon-lined autoclave and heated to 150 °C under rotating condition. The zeolite samples are denoted as follows: MesoMFI(x , y) with x representing the number of quaternary ammonium ions in the surfactant template and y the anion. The proton forms of the zeolites were obtained by triple ion exchange of the calcined zeolite with 1 M NH_4NO_3 at 80 °C for 2 h and calcination in static air at 550 °C for 4 h. Two additional samples were synthesized using the same procedure using the $C_{22-6-6}Br_2$ template, but with Si/Al ratios of 20 and infinite. These zeolites were used only for NMR studies.

Table 5.1: Molar composition of synthesis gels and hydrothermal synthesis conditions for the preparation of nanostructured MFI zeolites (hydrothermal synthesis in teflon-lined autoclaves was done under rotation at 60 rpm at 150 °C).

Zeolite	SDA	Gel composition in molar ratio						Time (days)
		SDA	TEOS	Al ₂ (SO ₄) ₃	NaOH	H ₂ SO ₄	H ₂ O	
MesoMFI(2, Br)	C ₂₂₋₆₋₆ Br ₂	10	100	1	60	18	4000	5
MesoMFI(3, Br)	C ₂₂₋₆₋₆₋₆ Br ₃	7	100	1	60	18	4000	5
MesoMFI(4, Br)	C ₂₂₋₆₋₆₋₆₋₆ Br ₄	5	100	1	60	18	4000	5
MesoMFI(2, OH)	C ₂₂₋₆₋₆ OH ₂	15	100	1	0	0	6000	12
MesoMFI(3, OH)	C ₂₂₋₆₋₆₋₆ OH ₃	10	100	1	0	0	6000	12
MesoMFI(4, OH)	C ₂₂₋₆₋₆₋₆₋₆ OH ₄	7.5	100	1	0	0	6000	12
Siliceous MesoMFI(2, Br)	C ₂₂₋₆₋₆ Br ₂	10	102	0	60	18	4000	5
Si/Al=20 MesoMFI(2, Br)	C ₂₂₋₆₋₆ Br ₂	10	96	2.4	60	18	4000	5

5.2.3 Physicochemical properties

Basic characterization

X-ray diffraction patterns were recorded on a Bruker D4 Endeavor diffractometer using Cu K α radiation in the 2θ range of 5-60 °. Elemental analyses were carried out by ICP-OES (Spectro Ciros CCD ICP optical emission spectrometer with axial plasma viewing). To extract the metals, the catalysts were dissolved in 1.5 ml of an acid mixture of HF/HNO₃/H₂O. Argon adsorption experiments were determined at 87.6 K on a Micromeritics ASAP 2020 instrument in static mode. The samples were outgassed at 350 °C for 8 h prior to the sorption measurements. The Brunauer-Emmett-Teller (BET) adsorption isotherm model was used to determine the total surface area (S_B) in the p/p_0 range between 0.05-0.25. The mesopore volume (V_{meso}) and mesopore size distribution was calculated from the adsorption branch of the isotherm by the Barrett-Joyner-Halenda (BJH) method. The micropore volume was determined by NLDFT method (Ar at 87 K on oxides as the model, assuming cylindrical pores, without regularization).

Electron microscopy

Scanning electron microscopy (SEM) pictures were taken on a FEI Quanta 200F scanning electron microscope at an accelerating voltage of 3-5 kV. The catalysts were coated with gold prior to measurements. Transmission electron microscopy (TEM) pictures were taken on a FEI Tecnai 20 at 200 kV. The catalysts were suspended in ethanol and dispersed over a carbon coated holey Cu grid with a film prior to measurements.

Vibrational spectroscopy

UV Raman spectra were recorded with a Jobin-Yvon T64000 triple stage spectrograph with spectral resolution of 2 cm⁻¹ operating in double subtractive mode. The laser line at 325 nm of a Kimmon He-Cd laser was used as exciting source. The power of the laser on the sample was 4 mW.

FTIR spectra were recorded in the range of 4000-400 cm⁻¹ by a Bruker Vertex V70v instrument. The spectra were acquired at a 2 cm⁻¹ resolution and averaged over 20 scans. The samples (5-10 mg) were prepared as thin self-supporting wafers with a diameter of 13 mm

and placed inside a controlled-environment infrared transmission cell, capable of heating and cooling, gas dosing and evacuation. For pretreatment, the zeolite wafer was first heated to 550 °C at a rate of 2 °C/min in an oxygen atmosphere before the measurement. Then the cell was outgassed at the final temperature until the residual pressure was below 5×10^{-5} mbar. For CO adsorption, the sample was cooled to 77 K and CO was introduced into the cell via a sample loop (5 μ L) connected to a Valco six-port valve. For pyridine and 2,4,6-collidine (2,4,6-trimethylpyridine) adsorption, pyridine (Py) and 2,4,6-collidine (Coll) were introduced from an ampoule into the cell at their vapor pressures at room temperature. The exposure time was 20 min was followed by desorption for 1 h at temperatures of 150, 300 and 500 °C. Spectra after evacuation treatments were recorded after cooling the sample to 150 °C. To quantify the total amount of Brønsted Lewis acid sites, the molar extinction coefficient value of 0.73 and 1.11 $\text{cm} \cdot \mu\text{mol}^{-1}$ was used, respectively [22]. To quantify the external Brønsted acid sites, the molar extinction coefficient of 10.1 $\text{cm} \cdot \mu\text{mol}^{-1}$ of collidine was employed [23].

NMR spectroscopy

Nuclear Magnetic Resonance (NMR) spectra were recorded on a Bruker DMX500 NMR spectrometer operating at a magnetic field of 11.7 T. For the ^{27}Al Magic Angle Spinning (MAS) NMR a standard Bruker MAS probe head was used with 2.5 mm rotors spinning at a rate of 20 kHz. The ^{27}Al chemical shift is referred to a saturated $\text{Al}(\text{NO}_3)_3$ solution. In a typical experiment, about 10 mg of well-hydrated sample was packed in the rotor and accurately weighed. The NMR spectra were also recorded after treating the sample in a flow of ammonia (10 % NH_3 in He) at 120 °C.

For ^1H MAS NMR measurements the zeolites were first subjected to a dehydration procedure. A known amount of sample was placed in special glass tube suitable for NMR (Wilmad Glass Company). This tube was connected to a vacuum line. The zeolite was activated at a temperature of 450 °C at a pressure lower than 10^{-5} mbar for 6 h. Afterwards, the sample was cooled to room temperature and sealed. The sealed glass tubes containing the activated samples were placed into a 4 mm MAS NMR rotor made of zirconia. Detailed of this special preparation of NMR samples suitable for MAS are described in literature [24, 25]. A Bruker 4-mm MAS probe head was used with a sample-rotation rate of 6 kHz.

For ^{29}Si NMR measurement, the sample rotation rate was 10 kHz. Two-dimensional $^{29}\text{Si}\{^1\text{H}\}$ heteronuclear correlation (HETCOR) NMR spectra were recorded with a rectangular contact pulse of 3 ms with carefully matched amplitudes on both channels at room temperature and 60°C , respectively. Tetramethylsilane (TMS) was employed as an external reference for the chemical shift for ^1H and ^{29}Si NMR.

5.2.4 Catalytic activity measurements

Catalytic activity measurements for the methanol-to-hydrocarbons reaction were carried out in a quartz tubular fixed-bed reactor with 4 mm inner diameter. Firstly, the zeolites were pressed, crushed and sieved in a particle size fraction between 250 and 500 μm . Secondly, the shaped catalyst (50 mg) was placed in a fixed-bed reactor between two quartz-wool plugs. Prior to the reaction, the catalyst was activated at 550°C in artificial air (30 ml/min) for 2 h. The methanol-to-hydrocarbons reaction was performed at 400°C . Methanol (Merck, 99%) was introduced to the reactor by flowing He through a saturator kept at 19°C with the flow rate 30 ml/min. The WHSV was kept at $6\text{ g}\cdot\text{g}^{-1}\cdot\text{h}^{-1}$ and the effluent was analyzed online by gas chromatography (Compact GC Interscience equipped with TCD and FID detectors with RT-Q-Bond and $\text{Al}_2\text{O}_3/\text{KCl}$ columns). The coke deposited during reaction was measured by thermogravimetric analysis (TGA) on TGA/DSC 1 STAR system of Mettler Toledo. The temperature was increased to 850°C at a rate of $5^\circ\text{C}/\text{min}$ under flowing air (50 ml/min).

5.3 Results and discussion

5.3.1 Structure and morphology

The XRD patterns of the as-synthesized zeolites are shown in Fig. 5.1. All patterns contain characteristic MFI diffraction peaks at 8.0, 8.9, 23.2 and 24.1° . The broad diffraction peak between 20 and 30° due to amorphous silica increases for samples prepared with longer templates (more N bases). The crystallinities of the multilamellar nanolayered ZSM-5 zeolites appear higher than those of the unilamellar ones. Especially, the unilamellar sample

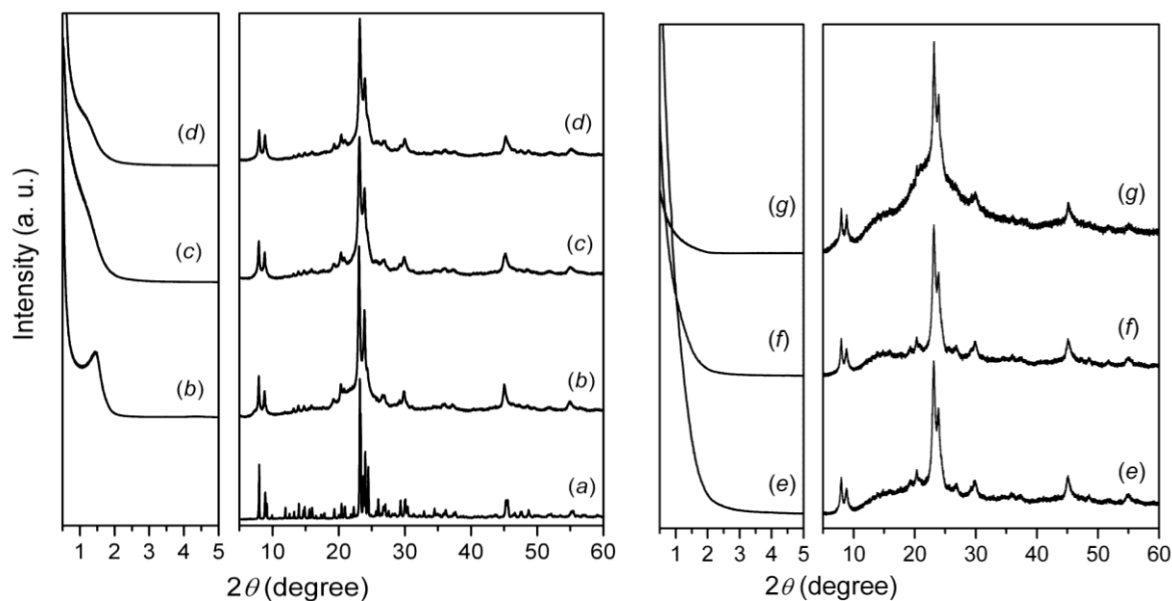


Figure 5.1: Small- and wide-angle XRD patterns of as-synthesized multilamellar (left) and unilamellar (right) MFI nanosheets: (a) bulk ZSM-5, (b) MesoMFI(2, Br), (c) MesoMFI(3, Br), (d) MesoMFI(4, Br), (e) MesoMFI(2, OH), (f) MesoMFI(3, OH) and (g) MesoMFI(4, OH).

prepared with the 4N template contains a significant fraction of amorphous silica. The low-angle region of the XRD pattern of MesoMFI(2, Br) shows a peak around 1.45° , which is indicative of stacking of the nanosheets in multilamellar MFI [26]. This feature can only be observed as a shoulder in MesoMFI(3, Br) and can hardly be distinguished in MesoMFI(4, Br). This implies that the stacking is less prominent for the multilamellar zeolites synthesized with 3N and 4N templates surfactants. Expectedly, the unilamellar MesoMFI(OH) do not contain any clear feature at low angle. These trends in crystallinity are corroborated by UV-Raman spectra of calcined zeolites (Fig. 5.2). The spectrum of the bulk ZSM-5 reference zeolite contains five bands at 291, 380, 461, and 802 cm^{-1} , which are characteristic for MFI zeolite [27, 28]. The most intense band at 380 cm^{-1} is due to vibrations of the double-five ring in MFI [27-29] and is sensitive to the degree of MFI crystallinity [30]. By use of this criterion, the crystallinities of the multilamellar nanolayered zeolites are slightly higher than those of the unilamellar ones in agreement with the XRD results. The spectrum of MesoMFI(4, OH) shows a significant background due to fluorescence radiation, which is usually attributed to small amounts of remaining coke species. It was verified that re-calcination of this sample did not lead to changes in the spectra.

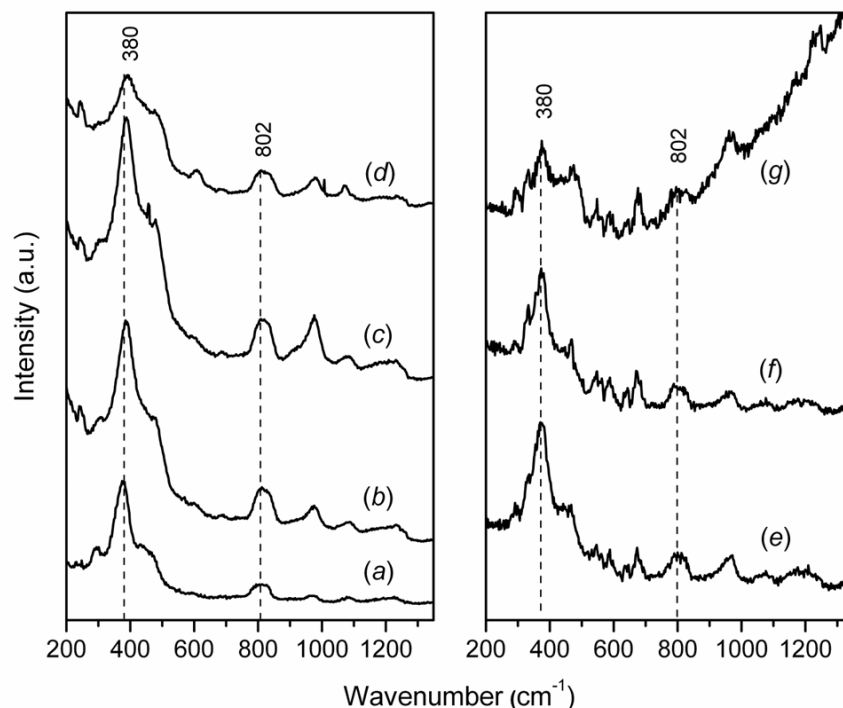


Figure 5.2: UV-Raman spectra of (a) bulk ZSM-5, (b) MesoMFI(2, Br), (c) MesoMFI(3, Br), (d) MesoMFI(4, Br), (e) MesoMFI(2, OH), (f) MesoMFI(3, OH) and (g) MesoMFI(4, OH).

Scanning and transmission electron micrographs of as synthesized multilamellar and unilamellar ZSM-5 zeolites are collected in Figs. 5.3-5.5. Scanning electron micrographs of the multilamellar zeolites are given in Fig. 5.3 and correspond well to earlier reported morphologies observed by Ryoo's group [16]. MesoMFI(2, Br) exhibits a plate-like morphology with large micrometer-sized primary particles being composed of three-dimensionally intergrown nanosheets aggregates. MesoMFI(3, Br) has a similar morphology. Such small MFI crystals are not so well visible in the SEM image of MesoMFI(4, Br). The images suggest that the material is also highly porous. The transmission electron micrographs in Figs. 5.4a-f show that MesoMFI(2, Br) and MesoMFI(3, Br) are nanolayered zeolites. The thickness of the sheets is not uniform. In Fig. 5.4d, the middle sheet has a thickness of 2.6 nm and the two outer ones of 3.7 nm. For MesoMFI(3, Br) the sheets seem to be thicker, although the nanosheet thickness is not uniform upon inspection of several electron micrographs. Clearly, the morphology of MesoMFI(4, Br) is different. There are very small spherical crystalline domains with a size of 10-20 nm, which are aggregated together. Fig. 5.5 shows SEM and TEM images of the unilamellar zeolites.

Clearly, these zeolites are not as ordered on the mesoscale as the multilamellar zeolites. The TEM images clearly show the formation of sheet-like zeolites. The thickness appears to increase with increasing N centers in the template. Although stacking of the sheets is largely absent for MesoMFI(2, OH), the other two samples have their sheets organized next to each other throughout the sample.

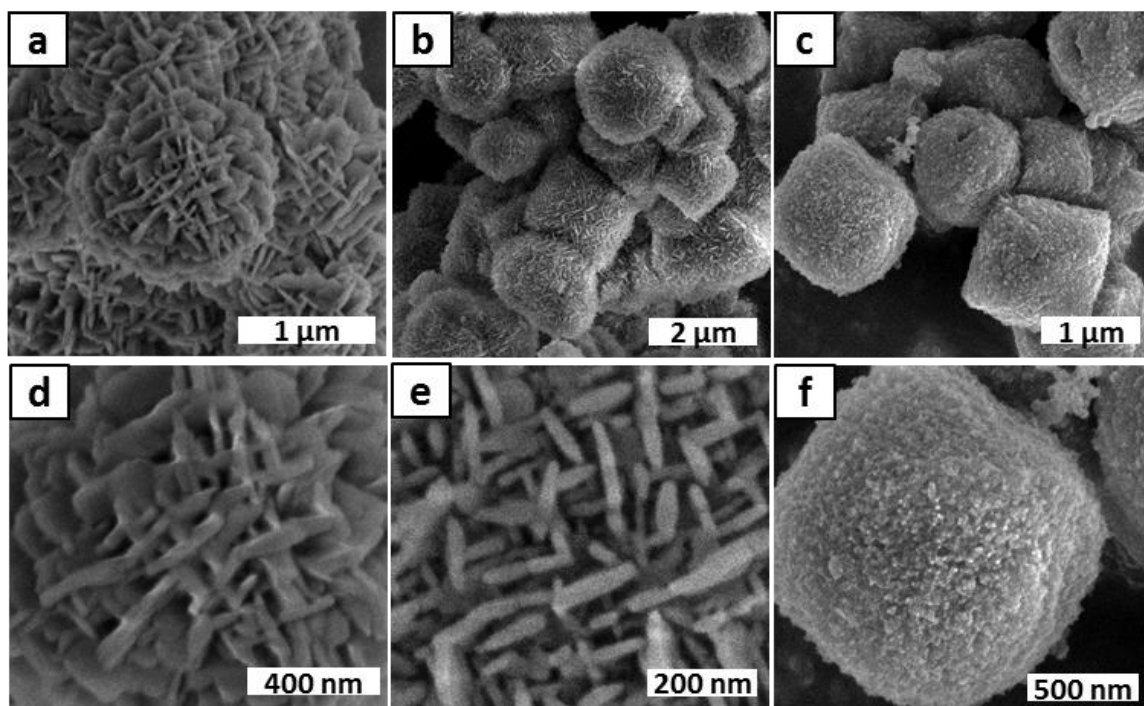


Figure 5.3: SEM images of (a, d) MesoMFI(2, Br), (b, e) MesoMFI(3, Br) and (c, f) MesoMFI(4, Br).

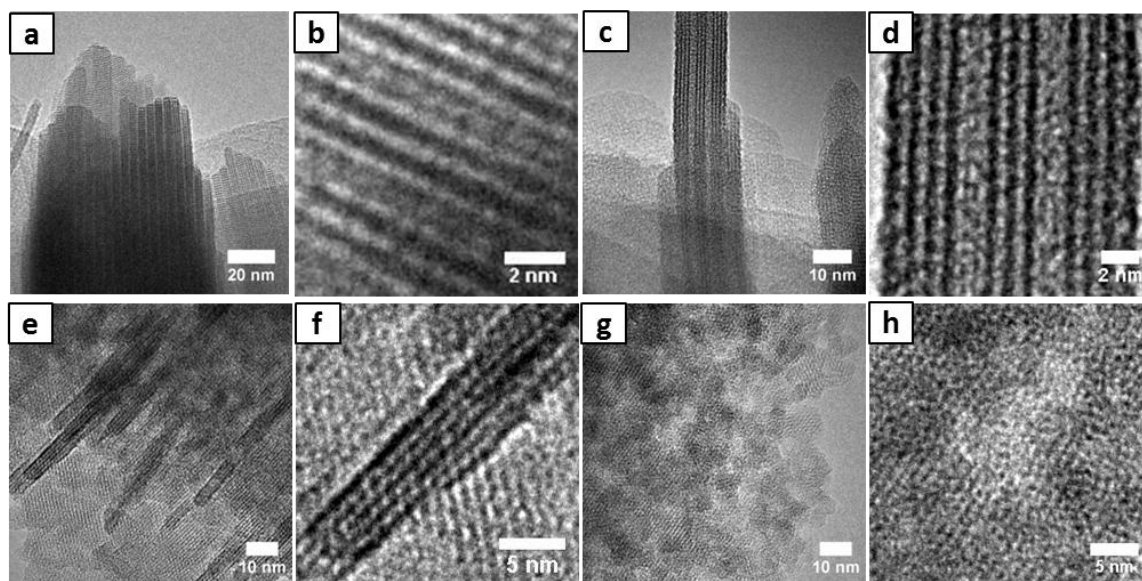


Figure 5.4: TEM images of (a, b, c, d) MesoMFI(2, Br), (e, f) MesoMFI(3, Br) and (g, h) MesoMFI(4, Br).

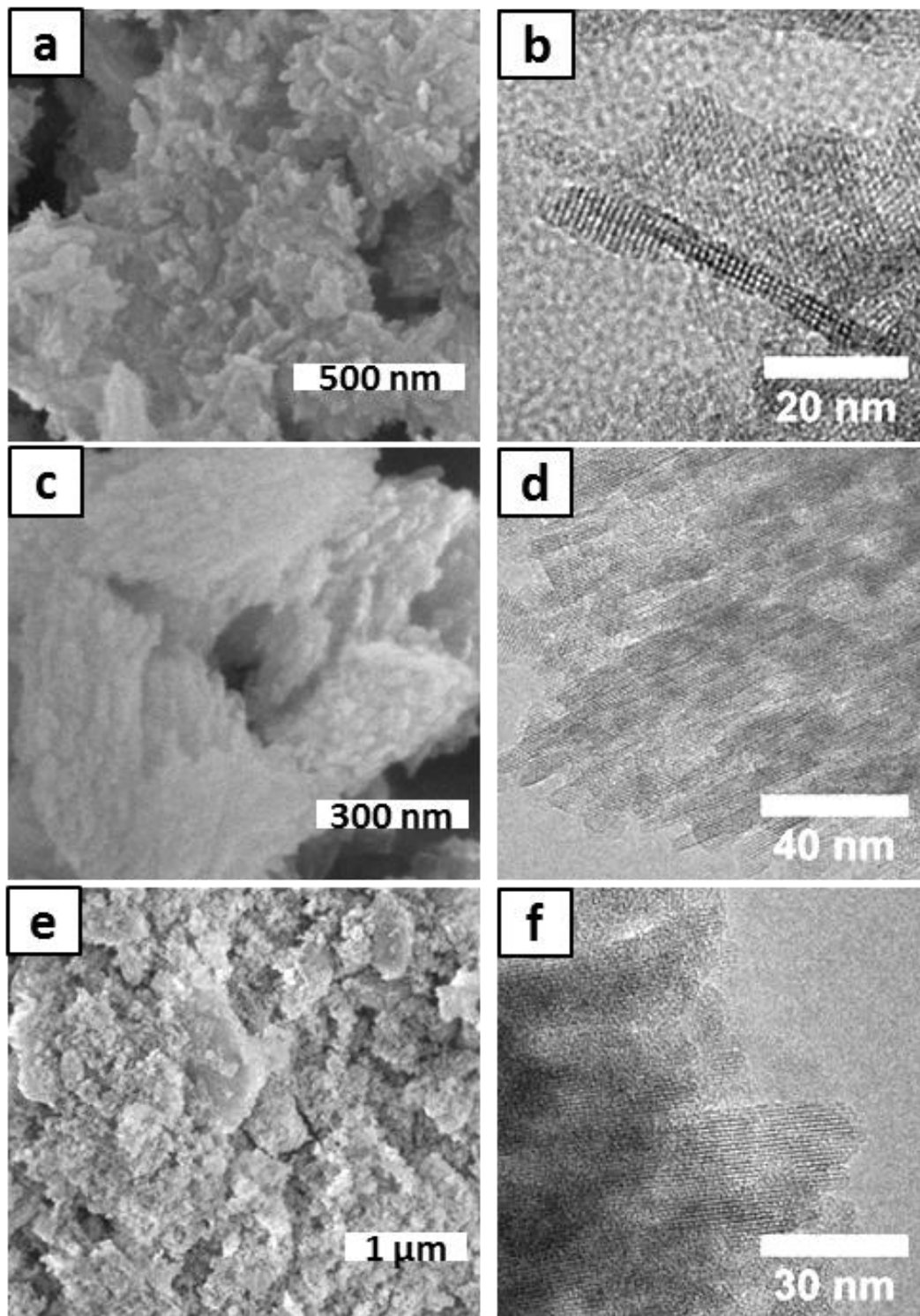


Figure 5.5: SEM (left) and TEM (right) images of (a, b) MesoMFI(2, OH), (c, d) MesoMFI(3, OH) and (e, f) MesoMFI(4, OH).

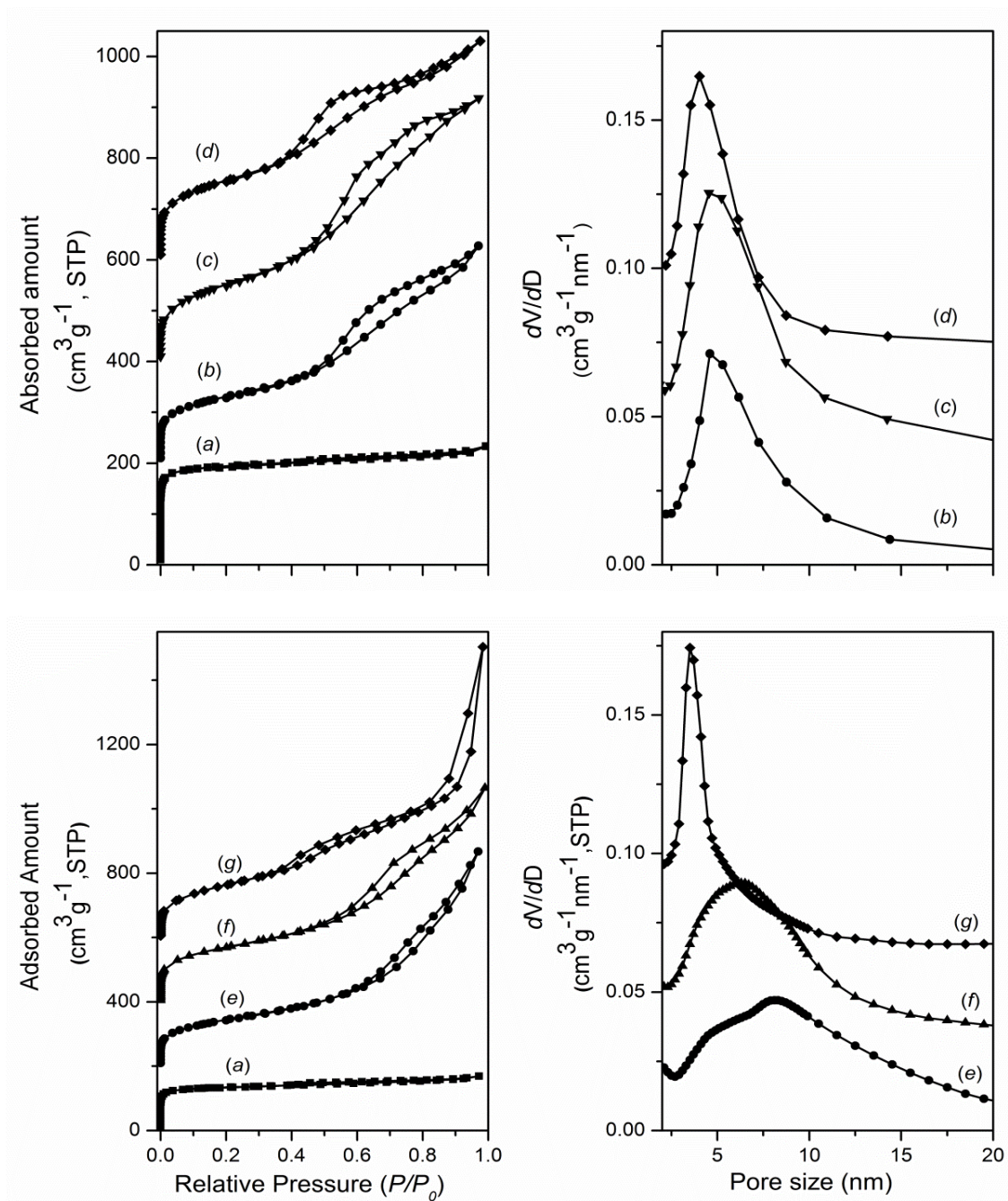


Figure 5.6: Argon physisorption (left) and pore size distribution (right) of (a) bulk ZSM-5, (b) MesoMFI(2, Br), (c) MesoMFI(3, Br), (d) MesoMFI(4, Br), (e) MesoMFI(2, OH), (f) MesoMFI(3, OH) and (g) MesoMFI(4, OH). The isotherms were vertically offset by equal intervals. The pore size distributions were calculated by use of the BJH algorithm using the adsorption branch of the isotherm. The pore size distribution curves were vertically offset by equal intervals.

Table 5.2: Textural properties of the calcined MFI zeolites determined by Ar physisorption.

Zeolite	$S_{\text{BET}}^{\text{a}}$ ($\text{m}^2 \cdot \text{g}^{-1}$)	$V_{\text{tot}}^{\text{b}}$ ($\text{cm}^3 \cdot \text{g}^{-1}$)	$V_{\text{meso}}^{\text{c}}$ ($\text{cm}^3 \cdot \text{g}^{-1}$)	$S_{\text{meso}}^{\text{c}}$ ($\text{m}^2 \cdot \text{g}^{-1}$)	$V_{\text{micro, NLDFT}}^{\text{d}}$ ($\text{cm}^3 \cdot \text{g}^{-1}$)	$V_{\text{micro}}^{\text{e}}$ ($\text{cm}^3 \cdot \text{g}^{-1}$)	$S_{\text{micro}}^{\text{e}}$ ($\text{m}^2 \cdot \text{g}^{-1}$)	$S_{\text{ext}}^{\text{e}}$ ($\text{m}^2 \cdot \text{g}^{-1}$)
ZSM-5(40) ^f	373	0.21	0.06	45	0.16	0.13	281	91
ZSM-5(27) ^g	326	0.18	0.04	31	n.d.	0.14	236	79
MesoMFI(2, Br)	402	0.55	0.47	279	0.11	0.02	92	319
MesoMFI(3, Br)	481	0.65	0.59	391	0.09	0	28	453
MesoMFI(4, Br)	487	0.55	0.46	339	0.12	0.01	67	420
MesoMFI(2, OH)	457	0.85	0.77	316	0.14	0.04	49	393
MesoMFI(3, OH)	532	0.85	0.73	344	0.13	0.02	91	429
MesoMFI(4, OH)	527	1.15	1.05	395	0.04	0	-	535

^a S_{BET} is the Brunauer-Emmett-Teller (BET) surface area obtained in the relative pressure range (p/p_0) of 0.1-0.3; ^b V_{tot} is the total pore volume at $p/p_0 = 0.97$; ^c V_{meso} and S_{meso} are the mesopore volume and surface area determined by the BJH method making use of the adsorption branch of the isotherm; ^d $V_{\text{micro, NLDFT}}$ is the micropore volume calculated from NLDFT (Ar at 87 K on oxides as the model, assuming cylindrical pores, without regularization, pores below 2 nm). ^e V_{micro} , S_{micro} , S_{ext} are micropore volume and surface area and external surface area determined by the t -plot method via the Broekhoff-de Boer model in the thickness range 0.34-0.50 nm. ^f Akzo Nobel Catalysts (now Albemarle Catalysts). ^g AlSiPenta (SüdChemie, now Clariant).

The Ar physisorption isotherms and the BJH pore size distributions (PSD) in the mesopore range of the calcined zeolites are given in Fig. 5.6. The corresponding textural properties are listed in Table 5.2. The bulk ZSM-5 zeolite has a type I isotherm, which is characteristic of microporous materials. For the nanolayered ZSM-5 zeolites, the typical type IV isotherm with distinct hysteresis loops can be recognized, indicative of the presence of mesopores in zeolites. All these samples contain mesopores. The micropore volume of bulk ZSM-5 zeolite is $0.12 \text{ cm}^3 \cdot \text{g}^{-1}$ according to the t -plot method, and $0.16 \text{ cm}^3 \cdot \text{g}^{-1}$ according to the NLDFT method (pores smaller than 2 nm). When for the NLDFT method only the pores smaller than 1 nm are included the micropore volume amounts to $0.13 \text{ cm}^3 \cdot \text{g}^{-1}$. The low micropore volume of MesoMFI(4, OH) is consistent with the high content of amorphous silica. In line with known limitations of the t -plot method for nanostructured ZSM-5 [31], it is found that the micropore volumes for the multi- and unilamellar zeolites are very low. The reason is the much higher ratio of external surface compared to the surface of the micropore channels [32]. The t -plot method probes a much larger external surface area for these nanolayered zeolites than for the bulk ZSM-5 zeolite. Their BET surface areas are also higher than the BET surface area of bulk ZSM-5.

The PSDs of the multilamellar zeolites are somewhat narrower than those of the unilamellar zeolites. The PSD of MesoMFI(4, OH) is an exception and points to the presence of uniformly sized mesopores around 3.5 nm in this largely amorphous material. Likely, a disordered mesoporous material has been formed around micelles of the surfactant. This would be consistent with the high mesopore volume ($1.05 \text{ cm}^3 \cdot \text{g}^{-1}$). The mesopore volumes for the other multi- and unilamellar zeolites are between 0.6 and $0.85 \text{ cm}^3 \cdot \text{g}^{-1}$, respectively. Typically, unilamellar ZSM-5 zeolites have a higher mesopore volume and surface area than multilamellar ones. This may be due to the larger average distances between the non-stacked sheets in the former, although another factor may be the collapse of the interlayer mesopores of multilamellar zeolites during calcination [26]. The former is substantiated by the observation that the mesopore volumes of the unilamellar zeolites are higher, whilst the mesopore surface areas are comparable with the multilamellar zeolites. The PSDs in the mesopore range of multilamellar MFI are quite similar and center around 4.7, 4.6 and 4.0 nm for zeolites prepared with 2N, 3N and 4N templates, respectively. This points to retention of

the stacking of zeolite sheets as seen in the TEM of the as-synthesized zeolites. The PSDs of the unilamellar MFI zeolites show more variation in the same series (7.9, 6.3 and 3.5 nm, respectively), which might due to less ordered stacking of the layers and, for MesoMFI(4, OH), due to the presence of a mesostructured amorphous silica phase.

^{29}Si NMR

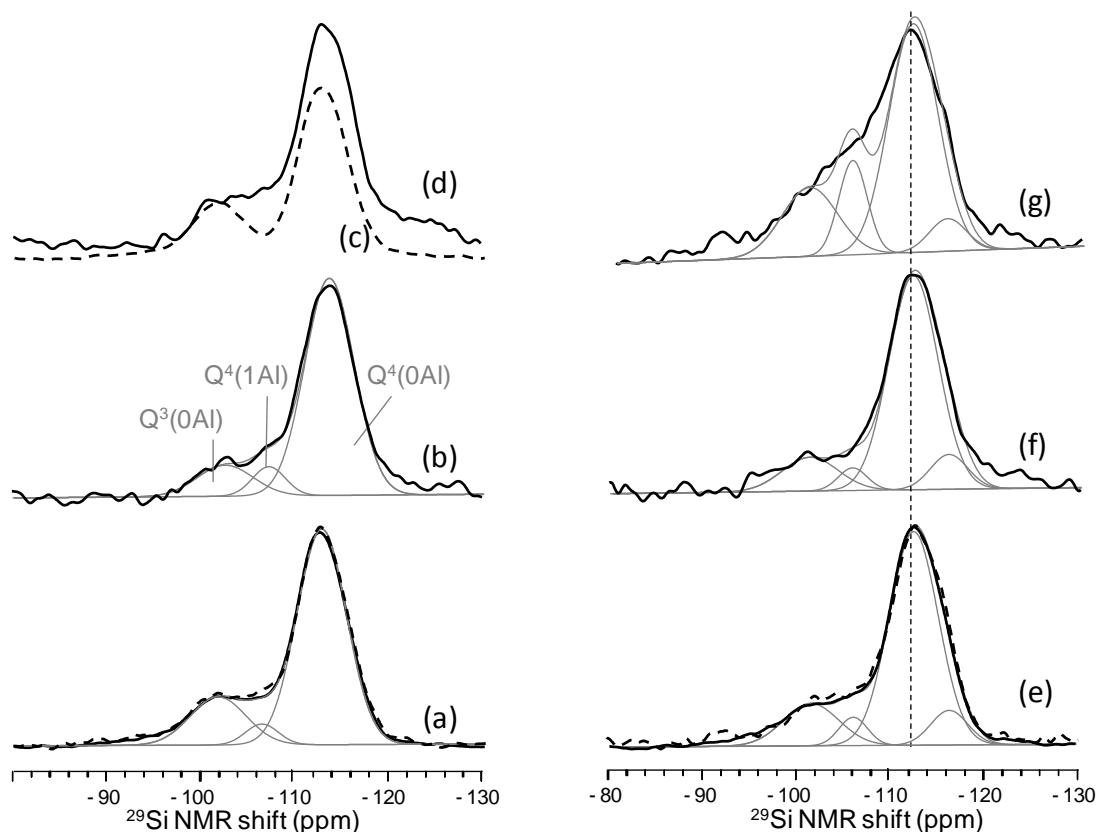


Figure 5.7: Cross-polarization (CP) ^{29}Si MAS NMR spectra of (a) MesoMFI(2, Br) (dash line: direct-excitation ^{29}Si NMR spectrum), (b) MesoMFI(3, Br), (c) siliceous MesoMFI(2, Br), (d) MesoMFI(4, Br), (e) MesoMFI(2, OH) (dash line: direct-excitation ^{29}Si NMR spectrum), (f) MesoMFI(3, OH) and (g) MesoMFI(4, OH). (c) and (d) are plotted together to confirm the $\text{Q}^4(1\text{Al})$ signal component, as labeled in (b). The grey lines indicate the deconvolution of the spectra in terms of 3 or 4 signal components at -102, -108, -112 and -116 ppm. All spectra were measured at 333 K.

Fig. 5.7 shows 1D ^{29}Si cross-polarization (CP) MAS spectra of multilamellar and unilamellar MFI zeolites synthesized with templates containing 2, 3 or 4 ammonium centers. All spectra contain a predominant signal at -113 ppm and weaker overlapping signals on the downfield side. $^{29}\text{Si}\{^1\text{H}\}$ CP is a way to enhance the ^{29}Si NMR signal of solids by use of the higher proton polarization, and is therefore useful to record ^{29}Si NMR spectra in a relatively

short time compared to direct-excitation (DE) spectra. The latter spectra require much more measuring time because of the low ^{29}Si spin polarization and slow ^{29}Si spin-lattice relaxation. Although this is not generally the case for template-free (calcined) zeolites and silicates, CP and DE ^{29}Si NMR spectra of the *as prepared* multi- and unilamellar MFI zeolites are almost the same, as illustrated for MesoMFI(2, Br) and MesoMFI(2, OH) (Figs. 5.7a,d). This suggests that detailed analysis of the CP ^{29}Si NMR spectra yields a quantitative picture of the various types of ^{29}Si atoms in the nanolayered zeolites. To identify such signal components in the ^{29}Si NMR spectra, the spectrum of *siliceous* MesoMFI(2, Br) sample has also been recorded (Fig. 5.7d). This spectrum shows two signals at -102 and -112 ppm, which are respectively assigned to $\text{Q}^3 = \underline{\text{Si}}(\text{OSi})_3(\text{OH})$ and $\text{Q}^4 = \underline{\text{Si}}(\text{OSi})_4$ silicon atoms [33, 34]. Lineshape deconvolution with the same two components of the other spectra indicates the presence of a third lineshape component at -108 ppm, which is attributed to $\text{Q}^4(1\text{Al}) = \underline{\text{Si}}(\text{OSi})_3(\text{OAl})$ silicon atoms [34, 35]. An additional minor lineshape component at -116 ppm is needed to describe the slightly asymmetric $\text{Q}^4(0\text{Al})$ resonance of the MesoMFI(2-4,OH) samples. This suggests more structural heterogeneity in the MesoMFI(2-4,OH) samples compared to the MesoMFI(2-4,Br) samples. However, we are reluctant to attribute any distinct physical meaning to this minor component. Spectral deconvolution by use of a constrained fit model with fixed line positions and widths yields the $\text{Q}^3(0\text{Al}) : \text{Q}^4(0\text{Al})$ and $\text{Q}^4(1\text{Al}) : \text{Q}^4(0\text{Al})$ ratios of the multi- and unilamellar MFI zeolites synthesized with the different template molecules (Table 5.3). For MesoMFI(2-4,OH) we combine hereby the -112 and -116 ppm signal intensities to estimate the $\text{Q}^4(0\text{Al})$ fraction. The $\text{Q}^3(0\text{Al}) : \text{Q}^4(0\text{Al})$ ratio indicates the condensation degree of the nanolayered MFI lattices, and, in particular, the silanol density. Naively, one would expect silanol moieties to be especially present at the nanolayer surfaces and their density therefore to correlate inversely proportional to the layer thickness. However, the $\text{Q}^3 : \text{Q}^4$ ratios of MesoMFI(2, Br), MesoMFI(3, Br) and MesoMFI(4, Br) are practically the same. This suggests that either the layer thickness of these systems does not vary with the number of ammonium centers in the template, or that the silanol density is not mainly determined by the layer thickness. For unknown reasons, the $\text{Q}^3 : \text{Q}^4$ ratio is slightly higher for the multilamellar than for the unilamellar zeolites with the exception of MesoMFI(4, OH), which turned out to be partly amorphous. Likewise the

$Q^4(1Al) : Q^4(0Al)$ ratio does not vary with the number of ammonium centers. This indicates that the incorporation of Al atoms is roughly the same for all multi- and unilamellar MFI zeolites with targeted Si/Al ratio 50.

Table 5.3: Deconvolution results of the ^{29}Si MAS NMR spectra.

Sample	$Q^3(0Al)$ (%)	$Q^4(1Al)$ (%)	$Q^4(0Al)$ (%)	$Q^3 : Q^4^a$	$Q^4(1Al) : Q^4(0Al)$
MesoMFI(2, Br)	19	5	76	0.23	0.07
MesoMFI(3, Br)	13	7	80	0.15	0.09
MesoMFI(4, Br)	15	7	78	0.18	0.09
MesoMFI(2, OH)	16	5	79	0.19	0.06
MesoMFI(3, OH)	13	4	82	0.15	0.05
MesoMFI(4, OH)	20	14	66	0.25	0.21

^a: $Q^3/Q^4 = Q^3(0Al)/\{Q^4(0Al) + Q^4(1Al)\}$

1H NMR and $^{29}Si\{^1H\}$ HETCOR

Fig. 5.8 shows the 1D 1H MAS NMR and 2D $^{29}Si\{^1H\}$ HETCOR NMR spectra of as-synthesized multilamellar and unilamellar MFI zeolites with different Si/Al ratios. The 1D 1H NMR spectra are dominated by the narrow CH_2 signal of the C_{22} tail of the template molecules. Smaller signals at 0.9 and 2.3 ppm belong to the terminal methyl moiety and the CH_2 at the next-neighbor position to nitrogen atoms in the C_{22} tails (atom position 9 in the template molecule structure in Fig. 5.9). The narrow lineshape of the 1.3 and 0.9 ppm signals indicates that at the elevated measurement temperature (333 K) the C_{22} tails are very mobile. Only ^{29}Si and 1H atoms that are close together (< 1 nm) give rise to correlation signals in the 2D HETCOR spectra [35-37]. The projection of the 2D HETCOR spectrum on the 1H NMR shift axis shows the features of the hydrogen atoms close to the silicon atoms, and therefore belonging to the parts of the template molecules well embedded within the zeolite layers. The 1H projection spectra generally contain two relatively broad 1H NMR resonances, one at 3.4 ppm attributed to CH_2 and CH_3 moieties next to the N centers, and another around 1.0 ppm belonging to CH_2 and CH_3 moieties in the two C_6 segments. The relatively large linewidth of these two signals in the 1H projection is typical of relatively immobile template moieties. The

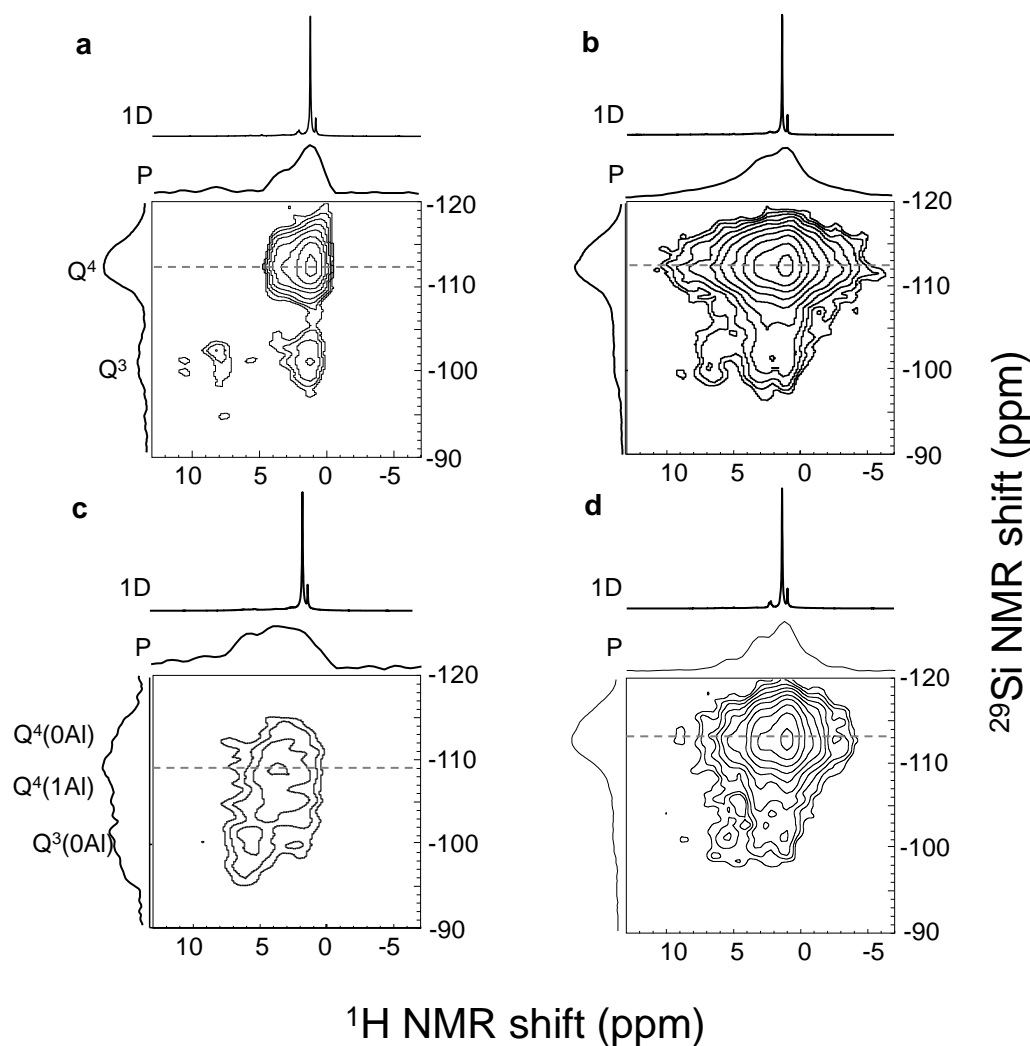


Figure 5.8: 2D $^{29}\text{Si}\{^1\text{H}\}$ HETCOR NMR spectra of as-synthesized (a) siliceous MesoMFI(2, Br), (b) MesoMFI(2, Br) with Si/Al = 45, (c) MesoMFI(2, Br) with Si/Al = 20, (d) MesoMFI(2, OH) with Si/Al = 31. The 2D NMR spectra are plotted with the (^{29}Si NMR) direct frequency axis in vertical direction, and ^1H and ^{29}Si NMR projections along the horizontal and vertical axis, respectively; corresponding 1D ^1H MAS NMR spectra are shown above the 2D spectra for comparison. The horizontal dashed lines illustrate the position of the ^1H cross-sections at the maximal ^{29}Si NMR intensity, as plotted in Fig. 11 (grey curves). All spectra were measured at 333 K.

immobilized ammonium centers and C_6 segments showing up in 2D HETCOR are consistent with the template being partly embedded with the ammonium centers in the aluminosilicate structure and the mobile C_{22} tail dangling outside. For the siliceous MesoMFI(2, Br) an additional correlation between Q^3 silicon atoms with $\delta_{\text{Si}} = -100$ ppm and hydrogen with $\delta_{\text{H}} = 8$ ppm can be recognized (Fig. 5.8a), whereas the usual ^1H NMR shift range of SiOH moieties in template-free zeolites is typically 1.5 – 2 ppm. Because ^1H shift of 8 ppm is also

reported for NH---O bridges in polyamides [38] and supramolecular uracil-pyridine based molecules [39], we tentatively assign this additional correlation to SiOH---NR₃ hydrogen bridges between silanol moieties and tri-alkyl aminocenters in incompletely alkylated template impurities. The presence of such impurity is also confirmed by ¹³C NMR (Fig. 5.9). For multi- and unilamellar MFI with a low, but finite Al content (Si/Al=31-45), the ¹H shift correlation changes to lower shift values (6.5 and 5 ppm for the multi- and unilamellar MFI, respectively). A possible explanation is fast exchange of the Si-OH ---NR₃ hydrogen bonds with water retained by these zeolites, which are relatively more hydrophilic than the siliceous MFI zeolite.

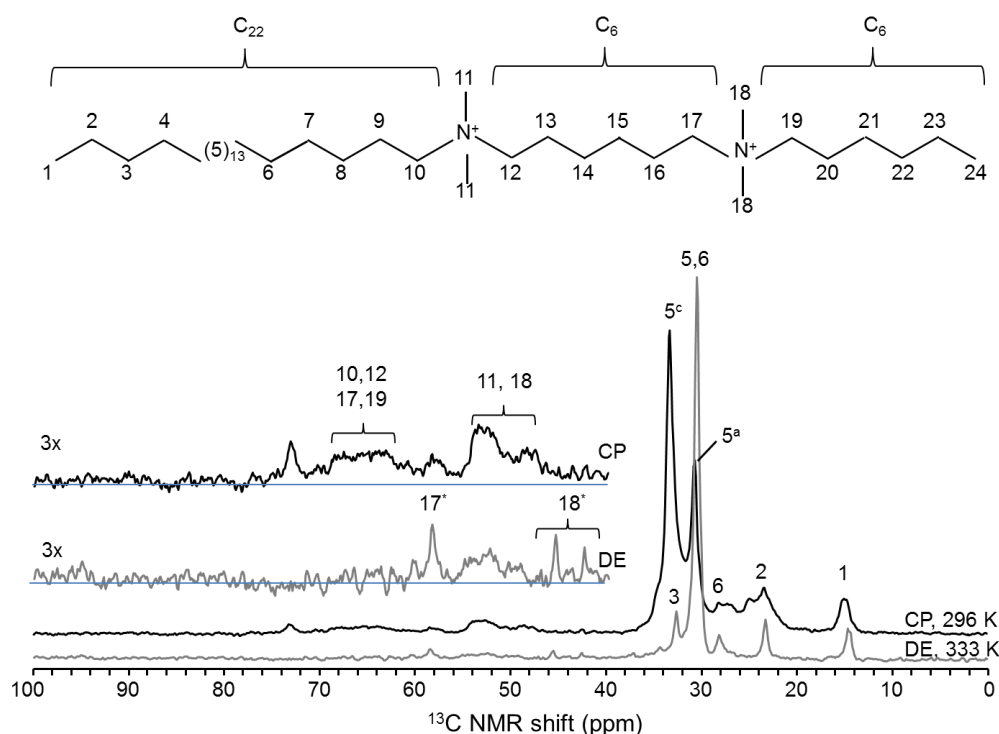


Figure 5.9: ¹³C MAS NMR spectra of siliceous multilamellar MFI synthesized with 2N template molecules (22-6-6). (black) cross-polarization (CP) at 298 K; (grey) direct excitation at 333 K. The insert depicts the three times magnified CP and DE spectra. Numbers without stars above the signals refer to template atom positions in the template molecule structure indicated at the top. The two numbers 17* and 18* above signals in the magnified DE spectra refer to the N-CH₂ and N-CH₃ groups in the template impurity 22-6-0 probably resulting from incomplete alkylation during the template synthesis.

At high Al content (Si/Al = 20), cross-polarization is relatively weak and it takes relatively much time to record a 2D HETCOR spectrum (Fig. 5.8c). Compared to the lower

Al containing zeolites, the highest peak top in the ^{29}Si NMR projection (Fig. 5.8b) shifts downfield to -108 ppm, probably as a result of the high $\text{Q}^4(1\text{Al})$ signal contribution. The broad lineshape suggests that the $\text{Q}^3(0\text{Al})$ contribution to Si NMR signal at -100 ppm is also relatively high and the condensation degree of this particular zeolite therefore relatively low. Unlike for the low Al containing MFI zeolites, the 1.0 ppm signal in the ^1H projection is relatively weak compared to the 3.4 ppm signal, or perhaps even absent. As may be noted, especially at high Al content the ^1H NMR signal at 3.4 ppm may also contain a significant contribution from Brønsted acid protons. All this indicates that the template molecules are less embedded into the aluminosilicate formed at $\text{Si}/\text{Al} = 20$ than in the zeolites formed at higher Si/Al ratio. Indeed, XRD indicates that this material is fairly amorphous (Fig. 5.10).

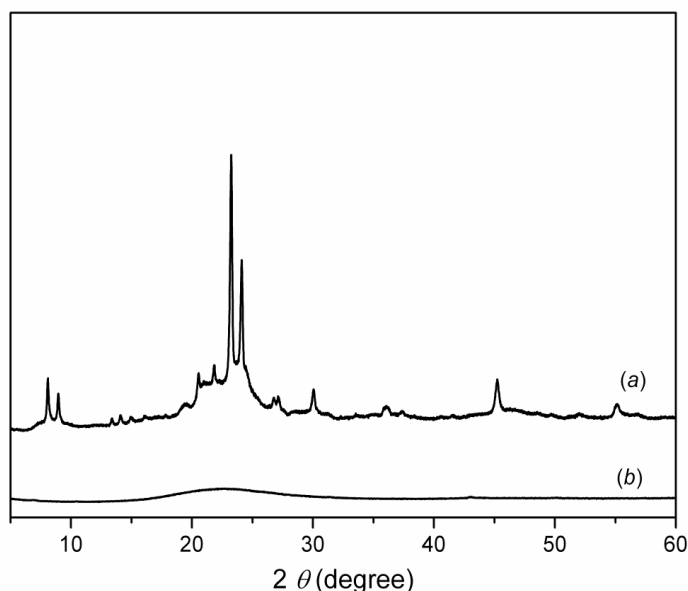


Figure 5.10: XRD patterns of (a) siliceous MesoMFI(2, Br) and (b) MesoMFI(2, Br) with $\text{Si}/\text{Al}=20$.

^{13}C NMR

As an example, ^{13}C NMR spectra (Fig. 5.9) of the *siliceous* MesoMFI(2, Br) were recorded to check the molecular integrity of the template, and confirm the mobility of the C_{22} tails indicated by ^1H NMR. Beforehand we expect that the ^{13}C resonances of *mobile* CH_2 and CH_3 moieties in the template molecules show up as narrow signals in direct-excitation (DE) NMR spectra, whereas *immobile* template moieties should especially give rise to signals in ^1H - ^{13}C cross-polarization (CP) NMR. Indeed, the DE ^{13}C NMR spectrum of *siliceous* MesoMFI(2, Br) at 333 K contains a number of narrow CH_2 signals between 20 and 35 ppm

with a combined peak area of 16.5 +/- 0.5 with respect to the (single) methyl signal at 14 ppm. The shift range, line widths and peak area are consistent with the high mobility of the C₂₂ tails (or, at least, the 17-18 terminal carbon positions) as reflected in ¹H NMR. At higher magnification, three minor narrow signals are visible at 58, 46 and 42 ppm. These are assigned to N-CH_{2,3} moieties in the 22-6-0 impurities resulting from incomplete alkylation in the second step of the template synthesis. In comparison, CP NMR at 298 K shows additional overlapping signals at 48 and 53, as well as between 61 and 70 ppm. The first two resonances are assigned to the N-CH₃ moieties in the template molecules, while the latter belong to the corresponding N-CH₂ moieties. The fact that they show up particularly well in CP NMR confirms the immobilization of this part of the template molecules in the silicate structure. At first sight, the partial splitting of the N-CH₃ signals may seem associated with the two inequivalent ammonium centers in the C₂₂₋₆₋₆ template molecules (template atom positions 11 and 18 in Fig. 5.9). However, the equal occurrence of the two N centers in the template structure does not explain the intensity difference between the two. Moreover, broad overlapping signals with a similar bimodal lineshape have also been observed by Ryoo c.s. for the MFI nanolayers synthesized with different template molecules, 18-6-6-18, thus with three ammonium centers at the ratio 2 : 1 (Fig. S11 in [35]). The N-CH₃ lineshape similarity for the different template molecules in our and Ryoo's study suggests that the observed splitting may have little to do with the detailed molecular structure of the templates. Perhaps it does more strongly reflect the different locations of the template ammonium centers embedded in the MFI structure. As computational modeling suggests, the different N centers within every template molecule are embedded at different distances from the nanolayer zeolite surface in the as-prepared MFI structures, which could well give rise to the observed resonance splitting. In passing, we further note that the predominant CH₃ signal at 30.5 ppm in the DE ¹³C NMR spectrum at 333 K partly shifts to 33.5 ppm in the CP NMR spectrum at 298 K. Since this spectral change is correlated with the temperature-induced motional narrowing in ¹H NMR (Fig. 5.11a), we propose that the observed splitting in ¹³C NMR at 298 K is caused by a ordering of the C₂₂ tails. After all, the C₂₂ tails are already tethered with their oligo-ammonium termini stuck within the silicate structures. The changed average conformation and packing effects in the ordered C₂₂ nano-domains, may well result in an

altered chemical shift, comparable to the shift difference between the ^{13}C NMR signal of crystalline (33 ppm) and amorphous (31 ppm) domains in semi-crystalline polyethylene [40].

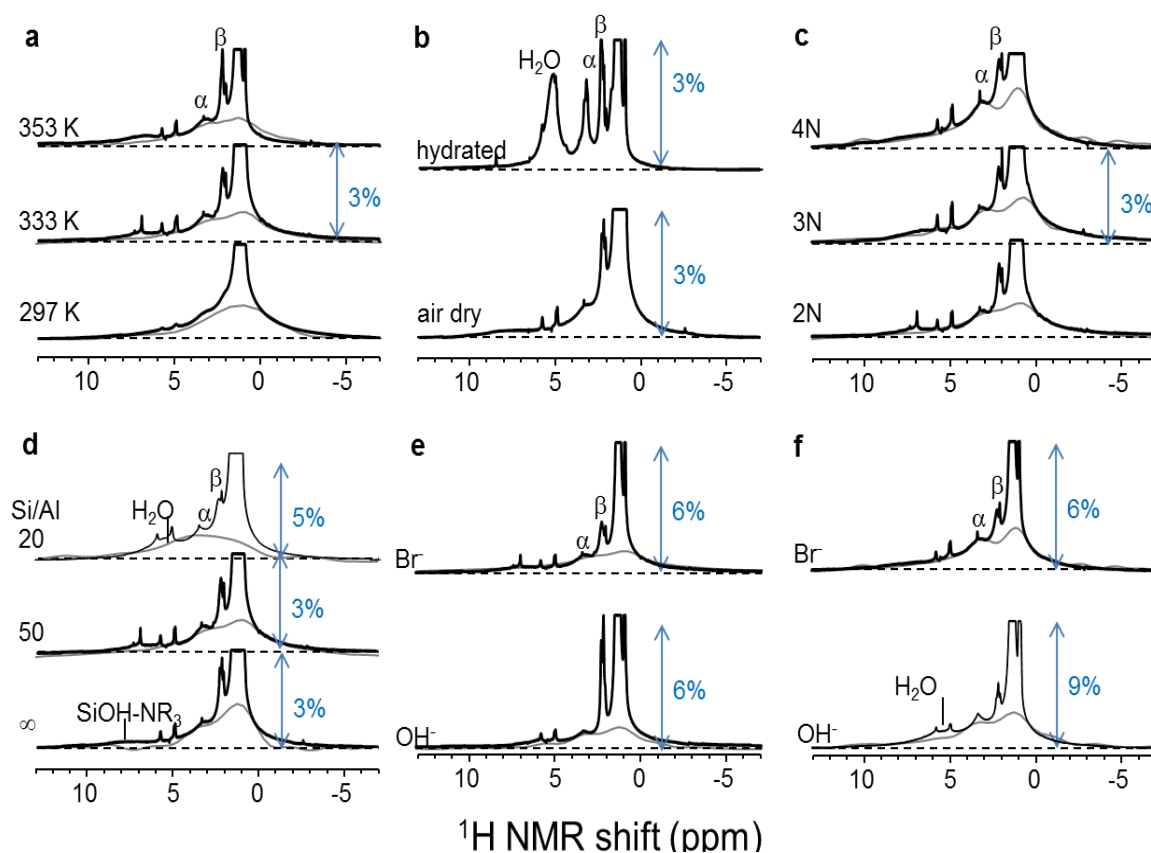


Figure 5.11: ^1H MAS NMR spectra (black lines) of as-synthesized (a) MesoMFI(2, Br) recorded at 297, 333 and 353 K, respectively; (b) siliceous MesoMFI(2, Br) after hydrated in moisturous atmosphere for 48 h and dried at 110 °C in the air for overnight, respectively; (c) multilamellar MFI synthesized by use of templates with 2, 3, and 4 ammonium centers, respectively; (d) MesoMFI(2, Br) with Si/Al ratio of 20, 50, and ∞ , respectively; (e) MesoMFI(2, Br) and MesoMFI(2, OH), (f) MesoMFI(4, Br) and MesoMFI(4, OH). The grey lines indicate the (horizontal) ^1H NMR cross-sections in the 2D HETCOR spectra at the ^{29}Si NMR position of the maximal signal intensity. The corresponding ^{29}Si NMR shift δ_{Si} is generally -113 ppm (assigned to $\text{Q}^4(0\text{Al})$ silicon atoms), except for the Si/Al=20 system where δ_{Si} equals -108 ppm (combination of $\text{Q}^4(0\text{Al})$ and $\text{Q}^4(1\text{Al})$ silicon atoms). Unless specified otherwise, all samples had a Si/Al ratio 50 and all spectra were recorded at 333 K. The peak label α refers to N-CH₂ and N-CH₃ moieties (e.g., positions 10, 11, 12, 17, 18 and 19 in the 2N template molecule structure depicted in Fig. 5.10) and the label β refers to next neighboring CH₂ moieties (positions 9, 13, 16, 20 in Fig. 5.9).

Fig. 5.11 shows 1D ^1H MAS NMR spectra of as-synthesized nanolayered ZSM-5 zeolites at varied conditions, such as the NMR detection temperature, the number of ammonium centers in the template, the template counterion (Br^- and OH^- for the multi- and unilamellar

zeolites, respectively) and Al content. For comparison, Fig. 5.11 also presents the ^1H cross-sections (grey curves) at $\text{Q}^4(0\text{Al})$ shift position (-112 ppm) in the 2D HETCOR spectra of the corresponding samples. These cross-sections reflect the ^1H NMR lineshape of the part of the template embedded within the nanolayered zeolites. The magnified spectra of MesoMFI(2, Br) with $\text{Si}/\text{Al} = 50$ recorded at 298, 333 and 353 K are shown in Fig. 5.11a. At room temperature the ^1H NMR lineshape is still relatively broad and the chemical resolution in the 1D ^1H NMR spectra and ^1H cross-sections of the 2D HETCOR spectra rather poor. At 333 K, motional line narrowing is observed for the methylene and methyl signals of the C_{22} tail at 1.3 and 0.9 ppm. Raising the temperature to 353 K has little further influence on the ^1H NMR spectrum. Apparently, between 298 and 333 K the C_{22} tails being tethered to the external zeolite surface undergo melting from a relative ordered immobile state to a disordered mobile state. Since the ^1H traces of the 2D HETCOR spectra recorded at 333 K and 353 K are very similar, the lower of the two temperatures was chosen to conduct all further experiments. As mentioned before, the partly resolved signals at 1.0 and 3.4 ppm in the ^1H cross-sections of the HETCOR spectra at 333 K are much broader than the narrow signals at 1.3 and 0.9 ppm in the 1D ^1H NMR spectrum. At high magnification the broad signal of the CH_2 and CH_3 moieties next to N at 3.4 ppm also shows up in the 1D ^1H NMR spectrum. The fact that this signal is equally broad in 1D ^1H NMR spectra and the HETCOR cross-sections indicates that the ammonium centers are exclusively located inside the zeolite framework.

To investigate the effect of water in the system, the ^1H MAS spectra of *siliceous* MesoMFI(2, Br) with and without excessive hydration were compared in Fig. 5.11b. In the spectrum of the hydrated sample, a strong additional signal with the typical shift of bulk water ~ 5 ppm was observed. Upon hydration, the broad signal at 8 ppm observed for the air dried siliceous zeolite disappears, as consistent with fast chemical exchange of protons between the $\text{SiOH}-\text{NR}_3$ hydrogen bonds and water. Interestingly, the N- $\text{CH}_{2,3}$ signal at 3.4 ppm becomes significantly narrower upon hydration, revealing that water affects the binding between the ammonium centers and the surrounding silicate phase.

In Fig. 5.11c the ^1H MAS spectra of multilamellar MFI nanosheets synthesized with template molecules with 2, 3 and 4 ammonium centers are compared. The signals of protons

1, 2 and 3 scales linearly with the number of ammonium centers, which confirms the chemical structure of the templates.

The ^1H MAS spectra of the multilamellar MFI nanosheets with various Si/Al ratios are given in Fig. 5.11d. MesoMFI(2, Br) with high Al density (Si/Al =20) have obvious higher / narrower signals associated with protons 1, 2 and 3 around the ammonium centers. This indicates increased mobility, which is unexpected, because the cationic ammonium centers are expected to bind relatively strongly to the conjugate-base sites generated by framework Al. The difference is due to the amorphous nature of MesoMFI(2, Br) confirmed by XRD analysis (Fig. 5.10). Parallel to the Al increase there is also a shift/increase of a broad component at 7-8 ppm (SiOH--N) for the siliceous system to a somewhat narrower component at 5 ppm (H_2O). Higher Al density increases the uptake of H_2O , which may interact with the zeolite-template binding, thereby acting as a “lubricant” and increasing the template mobility.

The ^1H MAS spectra of the MFI nanosheets synthesized in the presence of different template counterions Br^- and OH^- are compared in Figs. 5.11e and f for 2N and 4N templates, respectively. The OH^- instead of the Br^- anionic form of the template results in narrower signals around 2.3 ppm. Apparently, the rotational mobility of the template moieties at position 3 is increased. Again this may be an indirect effect of water, because the unilamellar zeolites appear to contain slightly more water. Increased template mobility may play a role in the formation of a unilamellar, rather than multilamellar structures. The increasing effect of OH^- on the template mobility appears to be confirmed for the zeolites formed with 4N templates, as well (Fig. 5.11f). In this case, even the $\text{N-CH}_{2,3}$ moieties become more mobile, and there is strong evidence for a higher H_2O content. However, it should be kept in mind that the unilamellar MFI zeolite synthesized with 4N template in the OH^- form has lower crystallinity (Fig. 5.1g). This sample has also a lower condensation degree (Table 5.3; Fig. 5.7g). Thus, the template molecules are probably less embedded into the aluminosilicate structure than for the other multi- and unilamellar MFI zeolites.

5.3.2 Acidity characterization

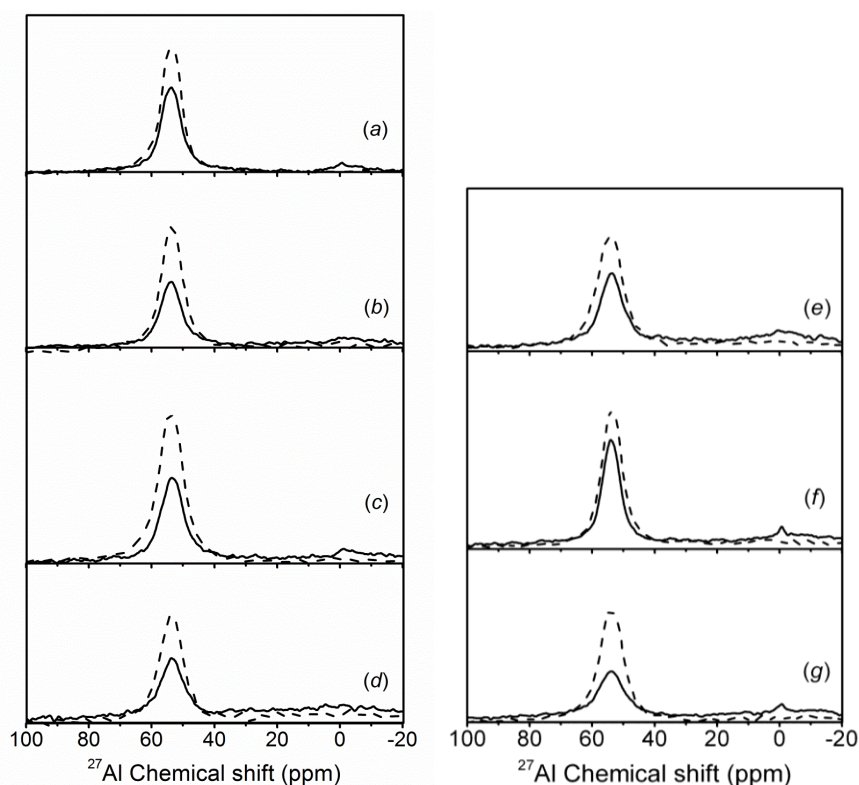


Figure 5.12: ^{27}Al MAS NMR spectra before (solid line) and after (dashed line) ammonia exposure of (a) bulk ZSM-5, (b) MesoMFI(2, Br), (c) MesoMFI(3, Br), (d) MesoMFI(4, Br), (e) MesoMFI(2, OH), (f) MesoMFI(3, OH) and (g) MesoMFI(4, OH).

^{27}Al MAS NMR spectra are shown in Fig. 5.12. All spectra are dominated by a strong signal around 56 ppm corresponding to tetrahedral framework Al (FAI) and contain a weaker broad band centered around 0 ppm corresponding to extraframework Al (EFAI) species in octahedral coordination. None of the spectra contains a clear feature around 30 ppm, typical for distorted tetrahedral Al and/or five-coordinated Al species, although close inspection shows that there is a weak broad band present in this region. NH_3 adsorption resulted in a significant increase of the tetrahedral signal at the expense of the octahedral signal and also invisible Al atoms. This evidences that the octahedral Al atoms in the zeolites remain closely associated with the zeolite framework [41]. Their coordination is flexible, because they are not part of an extensively agglomerated extraframework Al-oxide phase [42]. After careful baseline correction the NMR spectra were integrated in two regions 100 – 30 ppm and 30 – -50 ppm, representing FAI and EFAI, respectively. The weight-normalized peak areas were scaled relatively to the tetrahedral Al peak area of bulk HZSM-5(40) as a measure for the FAI

Table 5.4: Si/Al ratio, the concentration of Al ([Al]), framework Al ([FAI]) and extraframework Al ([EFAI]) in HZSM-5 and the mesoMFI zeolites as determined from ICP and ^{27}Al NMR, compared to the concentration of Brønsted Acid Sites ([BAS]), Lewis Acid Sites ([LAS]) and external Brønsted acid sites ([eBAS]) from IR measurement with pyridine and 2,4,6-collidine adsorption.

Sample	Si/Al ratio ¹	[Al] ¹ (mmol g ⁻¹)	²⁷ Al NMR			Pyridine IR		collidine IR
			[FAI] ² (mmol g ⁻¹)	[EFAI] ³ (mmol g ⁻¹)	[FAI] _{NH3} ⁴ (mmol g ⁻¹)	[BAS] (mmol g ⁻¹)	[LAS] (mmol g ⁻¹)	[external BAS] (mmol g ⁻¹)
HZSM-5(40)	40	0.41	0.32	0.09	0.39	0.28	0.07	0.022
HZSM-5(27)	27	0.60	0.56	0.04	0.60	0.53	0.11	0.018
MesoMFI(2, Br)	45	0.36	0.24	0.13	0.38	0.20	0.09	0.055
MesoMFI(3, Br)	47	0.35	0.30	0.16	0.46	0.15	0.10	0.079
MesoMFI(4, Br)	46	0.35	0.23	0.20	0.30	0.07	0.10	0.078
MesoMFI(2, OH)	31	0.52	0.28	0.19	0.42	0.23	0.18	0.117
MesoMFI(3, OH)	32	0.51	0.34	0.16	0.46	0.30	0.20	0.127
MesoMFI(4, OH)	41	0.40	0.21	0.09	0.40	0.13	0.23	0.105

¹ determined by ICP analysis; ² the peak area integrated from 100 to 30 ppm; ³ the peak area integrated from 30 to -50 ppm; ⁴ based on the ^{27}Al NMR spectra with NH_3 adsorption.

and EFAl densities in the various MesoMFI zeolites (Table 5.4). The FAl and EFAl densities obtained in this way from ^{27}Al NMR agree within 25% with the overall Al concentrations obtained from ICP. The quadrupolar interaction of Al nuclei with local electric field gradients may cause broadening of the ^{27}Al NMR signal of Al atoms with lower or distorted coordination symmetries beyond detection [43]. The rough consistency between the Al concentrations determined from ICP and ^{27}Al NMR indicates that the ^{27}Al NMR visibility of Al in the MesoMFI zeolites is not drastically different from that of Al in the parent ZSM-5(40). Except for MesoMFI(4, Br) and MesoMFI(4, OH), the sum of the FAl and EFAl concentrations before NH_3 treatment is roughly the same as the FAl concentrations alone after NH_3 for all the samples. Summarizing, the ^{27}Al NMR spectra show that all zeolites contain predominantly tetrahedral Al. A small fraction of the Al species is reversibly dislodged from the framework, but remains highly dispersed.

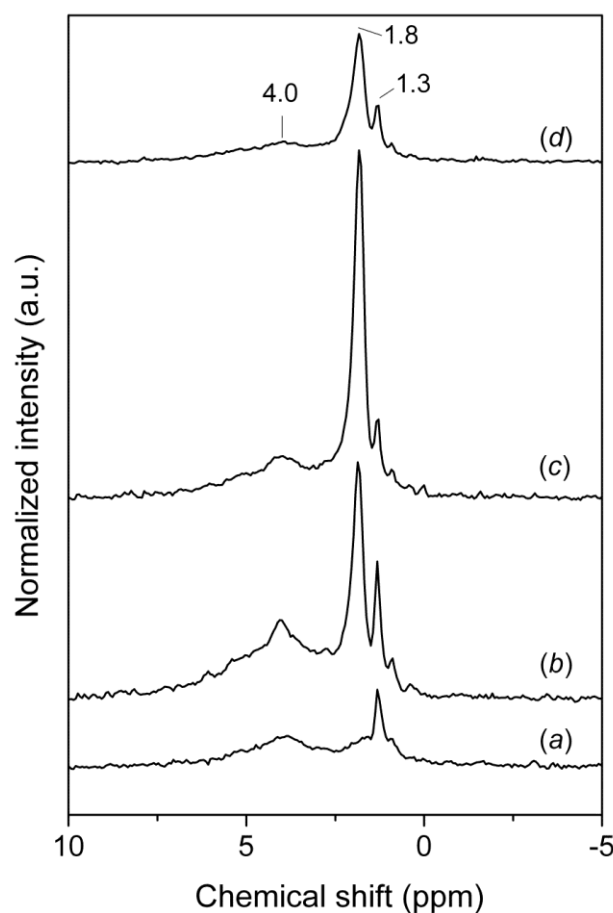


Figure 5.13: ^1H MAS MAS NMR spectra of dehydrated (a) bulk ZSM-5 (Si/Al=40), (b) MesoMFI(2, Br), (c) MesoMFI(3, Br) and (d) MesoMFI(4, Br). The spectra were normalized by the weight of the catalyst. The ppm scale is with respect to liquid tetramethylsilane.

Fig. 5.13 displays ^1H MAS NMR spectra for dehydrated calcined multilamellar and bulk ZSM-5 zeolites. The spectra contain clear peaks around 1.3, 1.8 and 4.0 ppm relative to liquid tetramethylsilane. The peak at 1.8 ppm is hardly visible for bulk HZSM-5. Silanol groups at the external surface of zeolite crystals or at framework defects have chemical shifts of 1.2-2.2 ppm [44]. The ^1H NMR shifts of bridging hydroxyl groups cover the range of 3.6-7.0 ppm. The broad feature between 3 and 7 ppm may be due to H-bonded silanols [45] and/or disturbed bridging hydroxyl groups that interact with basic framework oxygen anions [46]. Additional weak features are observed at 0, 0.3 and 0.9 ppm, the former two probably belonging to hydroxyl groups connected to metal cations, which are most likely residual Na^+ . The spectra of the multilamellar zeolites contain a much stronger signal around 1.8 ppm. The increased silanol density is due to the much higher external surface area of the multilamellar zeolites. As the signals of these silanol groups did not shift to lower field [44], it can be inferred that they remain isolated at the surface of the zeolite nanosheets. The signal at 1.3 ppm has also been related to silanol groups, although no specific assignment has been given in literature. The spectra also contain a band at around 4.0 ppm due to hydroxyl groups bridging between aluminum- and silicon-occupied tetrahedrons. The signal is visible for bulk HZSM-5 and MesoMFI(2, Br), but to a much lesser extent for the other two zeolites. The feature is very small for MesoMFI(4, Br). Deconvolution to obtain the concentration of Brønsted acid sites is not straightforward, because part of the bridging hydroxyl groups also give rise to a broad disturbed Si(OH)Al signal [44]. Moreover, it should be realized that hydroxyl groups in typical aluminum hydroxides and oxides are located in the range 2.9-5.8 ppm [47]. The exact position depends on the Al coordination number of the hydroxyl group. As the ^{27}Al NMR spectra show the presence of extraframework Al in these zeolites, there might well be a contribution of Al-OH groups in these spectra. This makes it difficult to accurately determine the concentration of Brønsted acid sites in aluminosilicates by ^1H NMR spectroscopy [48] and we did not pursue this in the present study. Comparison of the ^1H NMR spectra suggests that the Brønsted acidity decreases with increasing template length for the multilamellar ZSM-5 zeolites.

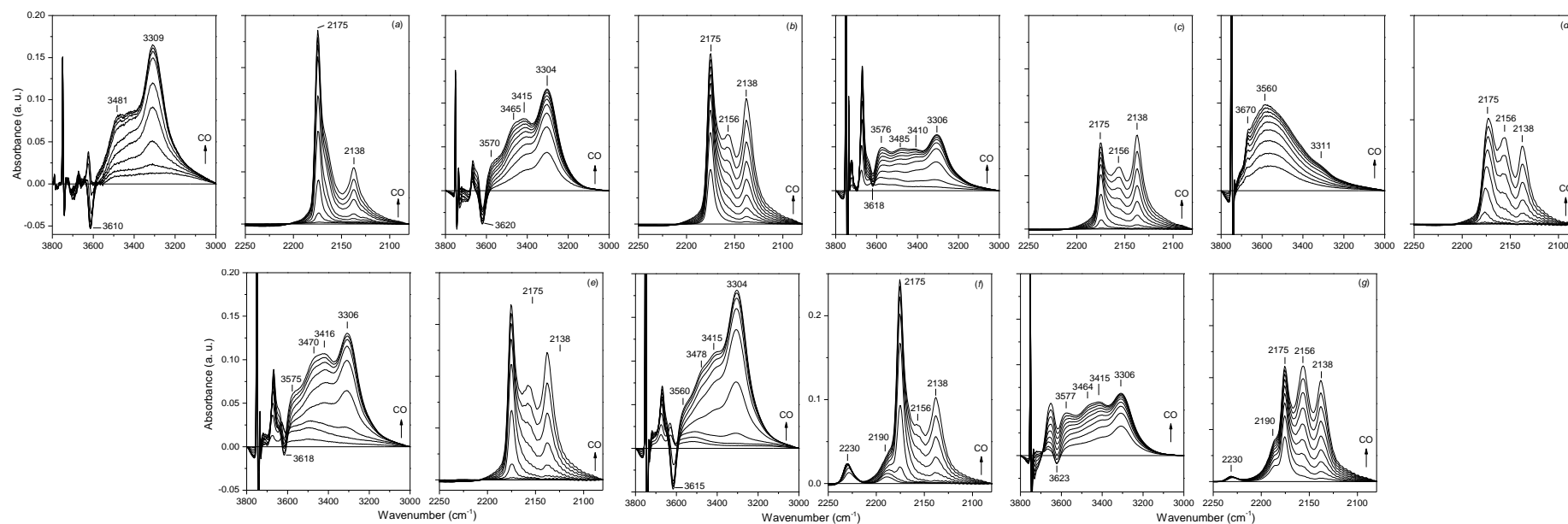


Figure 5.14: Hydroxyl (left) and carbonyl (right) stretch regions of FTIR spectra of dehydrated (a) bulk zeolite, (b) MesoMFI(2, Br), (c) MesoMFI(3, Br), (d) MesoMFI(4, Br), (e) MesoMFI(2, OH), (f) MesoMFI(3, OH) and (g) MesoMFI(4, OH) at 80 K as a function of the CO coverage (difference spectra vs. spectra of dehydrated zeolite and normalized by weight).

Fig. 5.14 shows the carbonyl and hydroxyl stretch regions of IR spectra of adsorbed CO of all zeolites. The strong band at 3309 cm^{-1} for HZSM-5 (Fig. 5.14a) due to strongly acidic bridging OH groups perturbed by CO is associated with the negative feature at 3610 cm^{-1} , the usual location for the unperturbed bridging OH groups in HZSM-5. The feature at 3481 cm^{-1} appears at higher CO coverage and has a lower red shift pointing to the presence of OH groups of lower acidity. A band around this position was also observed in amorphous silica-alumina [48]. Accordingly, we argue that it relates to some amorphous silica-alumina phase in the HZSM-5 sample. The band at 3623 cm^{-1} belongs to perturbed silanol groups. In the CO stretching region, bands at 2175 cm^{-1} and 2138 cm^{-1} derive from CO adsorption to acidic sites and physisorbed CO, respectively. The spectra for MesoMFI(2, Br) are qualitatively similar with some small differences (Fig. 5.14b). The concentration of BAS is slightly lower, as follows from the lower intensities of the bands at 3304 cm^{-1} and 2175 cm^{-1} . The band around 2156 cm^{-1} belonging to CO on silanol groups is much more intense for the nanolayered zeolites than for bulk ZSM-5, consistent with the ^1H NMR results. More ammonium centers (Figs. 5.14c and d) results in decrease of the Brønsted acidity. The band around 3300 cm^{-1} is less intense in MesoMFI(3, Br) and is only visible as a shoulder in MesoMFI(4, Br). The spectra for the unilamellar zeolites are qualitatively similar. Those of MesoMFI(2, OH) and MesoMFI(2, Br) are very comparable. For nanolayered zeolites, the concentration of BAS is highest in MesoMFI(3, OH). MesoMFI(4, OH) exhibits very low Brønsted acidity. The latter two zeolites also contain EFAl species, in the form of strong and weak Lewis acidic sites characterized by features at 2230 and 2190 cm^{-1} , respectively. In summary, CO_{ads} IR spectroscopy points to a more heterogeneous speciation of Al in the nanolayered zeolites compared to bulk HZSM-5. For multilamellar zeolites, the acidity strongly decreases with an increase of the number of quaternary ammonium centers in the template. For unilamellar zeolites, this trend is less obvious. The samples prepared with the 4N templates exhibit weak Brønsted acidity.

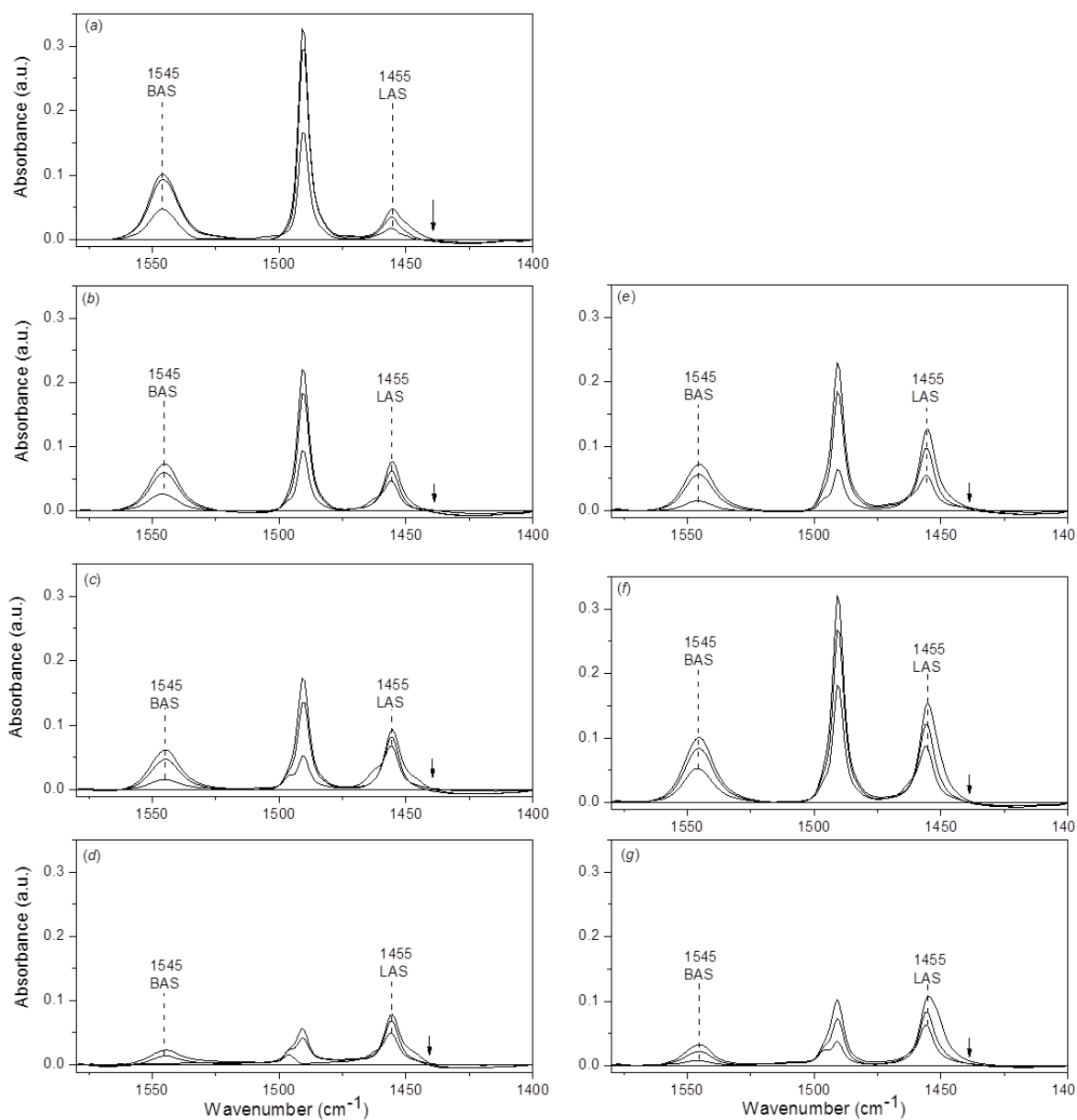


Figure 5.15: IR spectra of pyridine adsorbed on (a) bulk ZSM-5 (Si/Al=40), (b) MesoMFI(2, Br), (c) MesoMFI(3, Br), (d) MesoMFI(4, Br), (e) MesoMFI(2, OH), (f) MesoMFI(3, OH) and (g) MesoMFI(4, OH) after desorbing at 150 °C, at 300 °C, at 500 °C, respectively (along the direction of arrow).

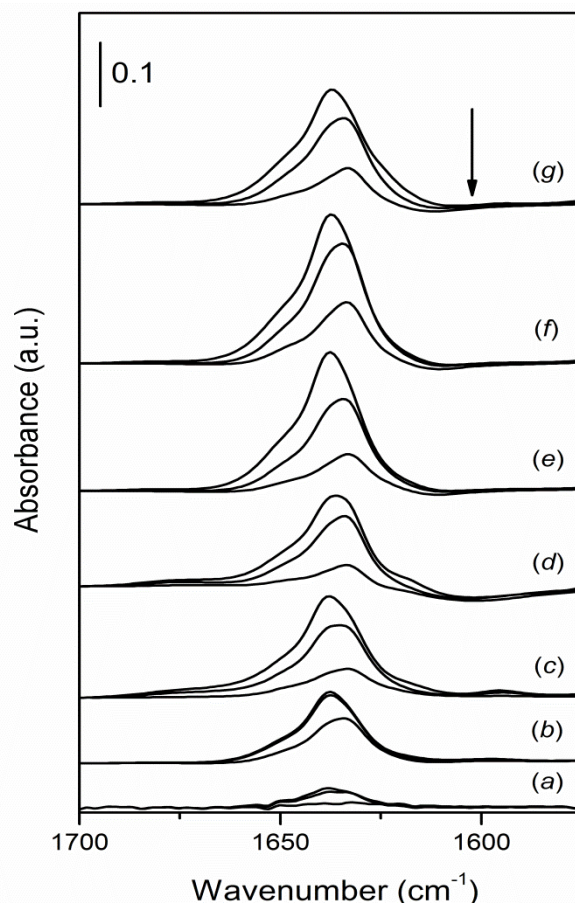


Figure 5.16: IR spectra of 2,4,6-collidine adsorbed on (a) bulk ZSM-5 (Si/Al=40), (b) MesoMFI(2, Br), (c) MesoMFI(3, Br), (d) MesoMFI(4, Br), (e) MesoMFI(2, OH), (f) MesoMFI(3, OH) and (g) MesoMFI(4, OH) after desorbing at 150 °C, at 300 °C, at 500 °C, respectively (along the direction of arrow).

Table 5.5: Concentration of Brønsted and Lewis acid sites determined by IR spectra of adsorbed pyridine.

Sample	BAS-150 (mmol/g) ¹	BAS-300 (mmol/g) ²	BAS-500 (mmol/g) ³	LAS-150 (mmol/g) ¹	LAS-300 (mmol/g) ²	LAS-500 (mmol/g) ³
ZSM-5(40)	0.28	0.26	0.12	0.07	0.04	0.02
MesoMFI(2, Br)	0.20	0.17	0.08	0.09	0.06	0.05
MesoMFI(3, Br)	0.15	0.11	0.05	0.10	0.08	0.06
MesoMFI(4, Br)	0.07	0.03	0	0.10	0.08	0.08
MesoMFI(2, OH)	0.23	0.18	0.05	0.18	0.15	0.08
MesoMFI(3, OH)	0.30	0.24	0.16	0.20	0.14	0.11
MesoMFI(4, OH)	0.13	0.10	0.04	0.23	0.15	0.11

¹ determined after evacuation at 150 °C; ² determined after evacuation at 300 °C; ³ determined after evacuation at 500 °C.

Table 5.6: Concentration of external Brønsted acid sites determined by IR spectra of adsorbed 2, 4, 6-collidine.

Sample	External BAS-150 (mmol/g) ¹	External BAS-300 (mmol/g) ²	External BAS-500 (mmol/g) ³
ZSM-5(40)	0.022	0.021	0.016
MesoMFI(2, Br)	0.055	0.032	0.006
MesoMFI(3, Br)	0.079	0.057	0.023
MesoMFI(4, Br)	0.078	0.053	0.019
MesoMFI(2, OH)	0.117	0.075	0.026
MesoMFI(3, OH)	0.127	0.096	0.043
MesoMFI(4, OH)	0.105	0.071	0.024

¹ determined after evacuation at 150 °C; ² determined after evacuation at 300 °C; ³ determined after evacuation at 500 °C.

The nature and location of acidity were further examined by use of IR spectroscopy of adsorbed pyridine and 2,4,6-collidine (spectra shown in Figs. 5.15 and 5.16). Values for total Brønsted and Lewis acidities determined after evacuation at 150 °C are listed in Table 5.4 (acidities determined after higher evacuation temperatures in Tables 5.5 and 5.6). For pyridine, the spectra contain bands at 1455 cm⁻¹ due to LAS, 1490 cm⁻¹ due to LA and BA sites and 1545 cm⁻¹ representative of BAS due to protonation of pyridine [49]. It was verified that the stretching bands of the bridging OH groups (3610-3620 cm⁻¹) vanished in the presence of pyridine (Fig. 5.17). Bulk HZSM-5 contains significantly fewer BAS than expected on the basis of its Al content (~0.40 mmol/g). This is due to the defective nature of this zeolite (small crystallite size, fraction tetrahedral Al ~78%, after NH₃ exposure 95 %). The number of BAS for a highly crystalline HZSM-5 zeolite (AlSiPenta, SM-55, Si/Al = 27, fraction tetrahedral Al ~93%, after NH₃ exposure 100%) determined in the same way was very close to the expected value (~0.53 mmol/g). Clear differences are noted within the set of nanolayer ZSM-5 zeolites. Except for MesoMFI(3, OH), all the nanolayered zeolites contain fewer BAS than bulk HZSM-5. For multilamellar zeolites, the number of BAS decreases with increasing number of ammonium centers in the SDA. The ratio of the number of BAS probed by pyridine IR and FAI concentration determined by ²⁷Al NMR strongly decreases with the sheet thickness. The variation in LAS density among the samples is relatively small. In general, the BAS densities in the unilamellar zeolites are higher than in the multilamellar

zeolites. There is no clear trend in the acidity as function of the number of ammonium centers. MesoMFI(4, OH) and MesoMFI(4, Br) have the lowest acidity. Inspection of Table 5.5 also shows that the amount of strong BAS (evacuation at 500 °C) is very low for these two samples. Finally, the concentration of LAS in the unilamellar zeolites is significantly higher than in the other ones, consistent with the CO IR data.

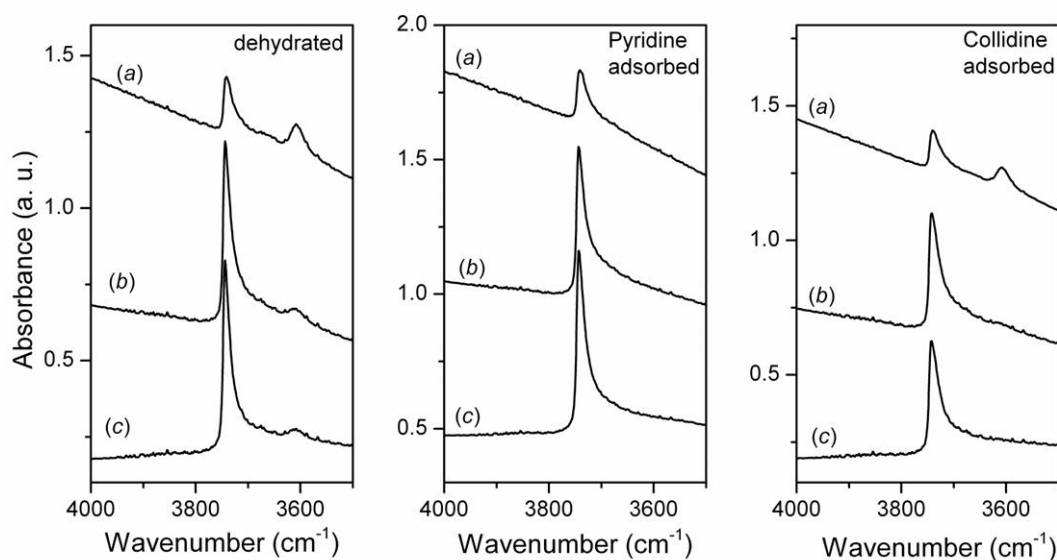


Figure 5.17: IR spectra of dehydrated, pyridine-adsorbed and collidine-adsorbed (a) bulk ZSM-5, (b) MesoMFI(2, Br) and (c) MesoMFI(2, OH).

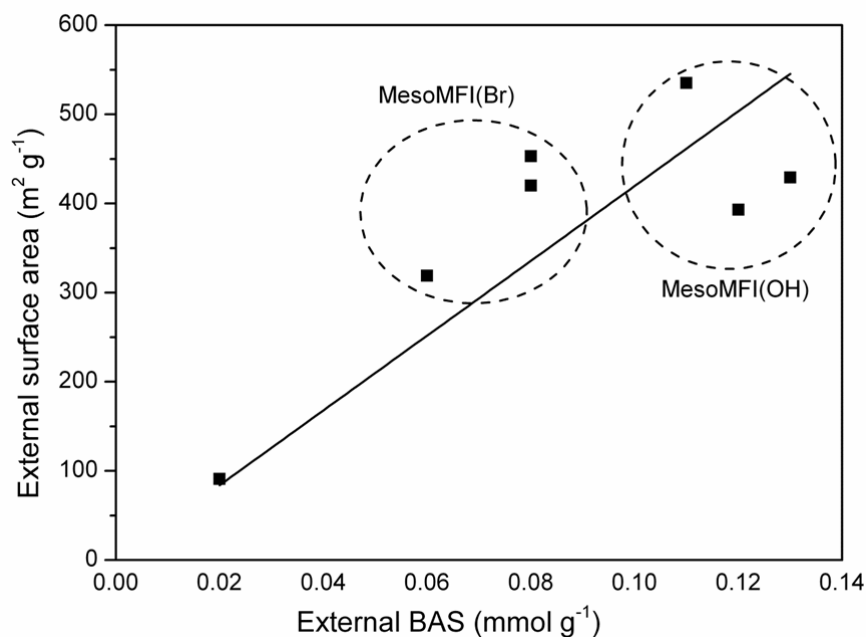


Figure 5.18: External surface area versus the concentration of external Brønsted acid sites (BAS).

Because of its kinetic diameter, 2,4,6-collidine can be used as a probe for the BAS at the

external surface of ZSM-5 crystals [8]. The spectra (Fig. 5.16) show a single broad feature around 1635 cm^{-1} due to protonated probe molecules [50]. Adsorption of 2,4,6-collidine does not result in complete disappearance of the bridging hydroxyl group, which is more evident for the bulk HZSM-5 zeolite than for the other zeolites (Fig. 5.17). The concentrations of external BAS are given in Table 5.4 (complete data in Table 5.6). Less than 10 % of the BAS in bulk HZSM-5 are located at the external surface, in reasonable agreement with literature values for HZSM-5 [18]. The amount of external BAS is higher in the nanolayered zeolites, which trends with their much higher external surface area (Fig. 5.18). For multilamellar zeolites, it is found that with increasing number of ammonium centers in the template a larger fraction of the total acidity is located at the external surface. For instance, all the BAS accessible for pyridine in MesoMFI(4, Br) are also accessible for the larger probe. This would appear to imply that all BAS are located at the external surface of the zeolite sheets for this sample. This contrasts the much higher FAI concentration of this sample. The FAI concentration does not significantly vary for the multilamellar samples (cf. Table 5.4). A tentative explanation is that a fraction of internal BAS is inaccessible. The reason may be that part of the interlayer mesopore space collapses during calcination and compacting procedures [17]. However, the disappearance of the IR signal due to bridging hydroxyl groups upon adsorption of pyridine or CO indicates that all BAS are accessible. Therefore, it is more likely that part of the FAI atoms are part of an amorphous silica phase. This would suggest that the crystallinity of the nanolayered zeolites decreases with increasing template length. Damage to the crystalline structure upon compacting may also be a cause of decreased acidity. For unilamellar zeolites, a significant fraction of the Brønsted acidity is accessible for 2,4,6-collidine and the fraction is again highest for MesoMFI(3, OH). There is, however, no clear trend for the set of multilamellar zeolites. For unilamellar MFI zeolite, although the external BAS concentrations are, of course, systematically lower than the total FAI concentrations from ^{27}Al NMR, the trend is consistent. For instance, MesoMFI(3, OH) with the highest FAI concentration (0.34 mmol g^{-1}) also tends to have the highest external BAS concentration (0.13 mmol g^{-1}). The similar trends of FAI concentration and the external BAS concentrations suggest that Al is homogeneously distributed over the unilamellar MFI without a preference for the surface or the interior of the sheets. Note that strictly speaking

the similar trend in total FAI concentrations and external BAS concentrations within the unilamellar series only indicates a rough, sample-independent proportionality between the surfaces and bulk Al concentrations.

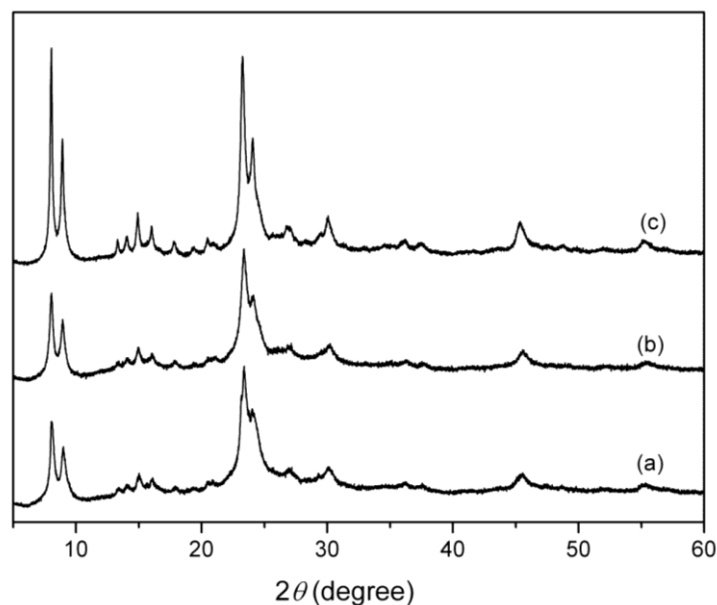


Figure 5.19: XRD patterns of calcined (a) MesoMFI(2, Br) and (b) MesoMFI(4, Br) and (c) MesoMFI(2, OH) after the compacting at 222 MPa.

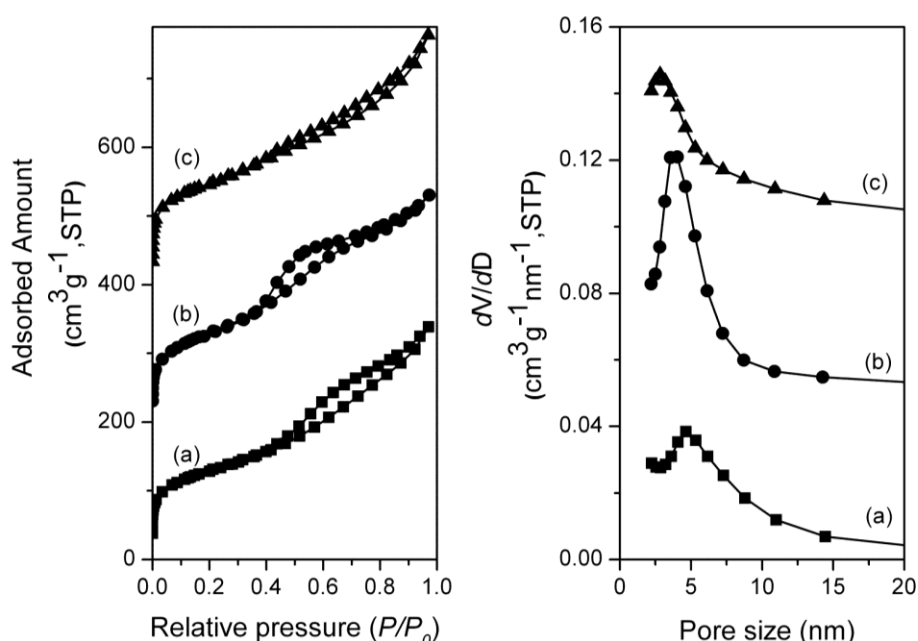


Figure 5.20: Argon physisorption (left) and pore size distribution (right) of (a) MesoMFI(2, Br) and (b) MesoMFI(4, Br) and (c) MesoMFI(2, OH) after the compacting at 222 MPa. The pore size distributions were calculated by use of the BJH algorithm using the adsorption branch of the isotherm. The isotherms and the pore size distribution curves were vertically offset by equal intervals.

Table 5.7: Textural properties of the compacted calcined MFI zeolites determined by Ar physisorption.

Zeolite	$S_{\text{BET}}^{\text{a}}$ ($\text{m}^2 \cdot \text{g}^{-1}$)	$V_{\text{tot}}^{\text{b}}$ ($\text{cm}^3 \cdot \text{g}^{-1}$)	$V_{\text{meso}}^{\text{c}}$ ($\text{cm}^3 \cdot \text{g}^{-1}$)	$S_{\text{meso}}^{\text{c}}$ ($\text{m}^2 \cdot \text{g}^{-1}$)	$V_{\text{micro, NLDFT}}^{\text{d}}$ ($\text{cm}^3 \cdot \text{g}^{-1}$)	$V_{\text{micro}}^{\text{e}}$ ($\text{cm}^3 \cdot \text{g}^{-1}$)	$S_{\text{micro}}^{\text{e}}$ ($\text{m}^2 \cdot \text{g}^{-1}$)	$S_{\text{ext}}^{\text{e}}$ ($\text{m}^2 \cdot \text{g}^{-1}$)
MesoMFI(2, Br)	380	0.43	0.34	204	0.12	0.04	95	285
MesoMFI(4, Br)	399	0.43	0.34	265	0.10	0.01	43	356
MesoMFI(2, OH)	492	0.48	0.35	215	0.15	0.05	162	330

^a S_{BET} is the Brunauer-Emmett-Teller (BET) surface area obtained in the relative pressure range (p/p_0) of 0.1-0.3; ^b V_{tot} is the total pore volume at $p/p_0 = 0.97$; ^c V_{meso} and S_{meso} are the mesopore volume and surface area determined by the BJH method making use of the adsorption branch of the isotherm; ^d $V_{\text{micro, NLDFT}}$ is the micropore volume calculated from NLDFT (Ar at 87 K on oxides as the model, assuming cylindrical pores, without regularization, pores below 2 nm). ^e V_{micro} , S_{micro} , S_{ext} are micropore volume and surface area and external surface area determined by the t -plot method via the Broekhoff-de Boer model in the thickness range 0.34-0.50 nm.

Three calcined nanolayered MFI zeolites (MesoMFI(2, Br), MesoMFI(4, Br) and MesoMFI(2, OH)) have been compacted at 222 MPa for 30 sec. The XRD patterns of these samples are shown in Fig. 5.19. After compacting, the XRD reflections at 23.2 and 24.1 ° in all samples have decreased substantially, whereas those at 8.0 and 8.9 ° remained nearly constant. This suggests a decrease in the long-range ordering in the crystals. The changes in the XRD patterns due to compacting are less substantial for the unilamellar MesoMFI(2, OH) compared to multilamellar ZSM-5. The textural properties of compacted zeolites were determined by Ar physisorption. The isotherms and BJH mesopore size distribution are shown in Fig. 5.20 and the textural properties were summarized in Table 5.7. For multilamellar MFI, the mesopore volume decreased about 25 % after compacting, while the micropore volume remained constant. For unilamellar MFI, the mesopore volume decreased about 45 %, the larger decrease being consistent with the more open sheet arrangement of unilamellar zeolites. Despite the larger decrease, MesoMFI(2, OH) still has a larger mesopore volume than MesoMFI(2, Br) and MesoMFI(4, Br).

5.3.3 Catalytic activity measurements

The acid catalytic activity of the nanolayered zeolites was evaluated in the MTH reaction at a WHSV of 6 g g⁻¹ h⁻¹ and a reaction temperature of 400 °C. Fig. 5.21 shows the methanol conversion as a function of the time on stream. Dimethyl ether (DME) is considered as an unconverted species, so that the conversion represents the fraction of methanol to products involving carbon-carbon bonds (CO and CO₂ selectivities were negligible). Further details about the product mixture after 1 h time on stream are collected in Table 5.8. At the initial stages of the reaction, all the zeolites convert methanol nearly completely, except for MesoMFI(4, Br) and MesoMFI(4, OH). The latter zeolite catalysts exhibit very low methanol conversion and predominantly produce DME. The product composition of the active zeolites is similar to what has been reported for MTH over medium-pore zeolites such as HZSM-5 [51, 52] with a relatively high propylene/ethylene ratio and formation of higher olefins, aromatics and some paraffins. This product composition is to be compared to methanol conversion over small-pore zeolites such as SAPO-34 and SSZ-13 [13, 53], which mainly yield light olefins. Comparatively, HZSM-5 zeolite also catalyzes consecutive reactions of

intermediate olefins into higher olefins and aromatics by oligomerization and ring-closure reactions and, to some extent, into paraffins due to hydrogen transfer reactions. The product selectivities for the most active zeolites are quite similar after 1 h time on stream. The carbon-carbon bond forming reactions also give rise to heavier products that eventually lead to coke deposits and deactivation of the zeolites.

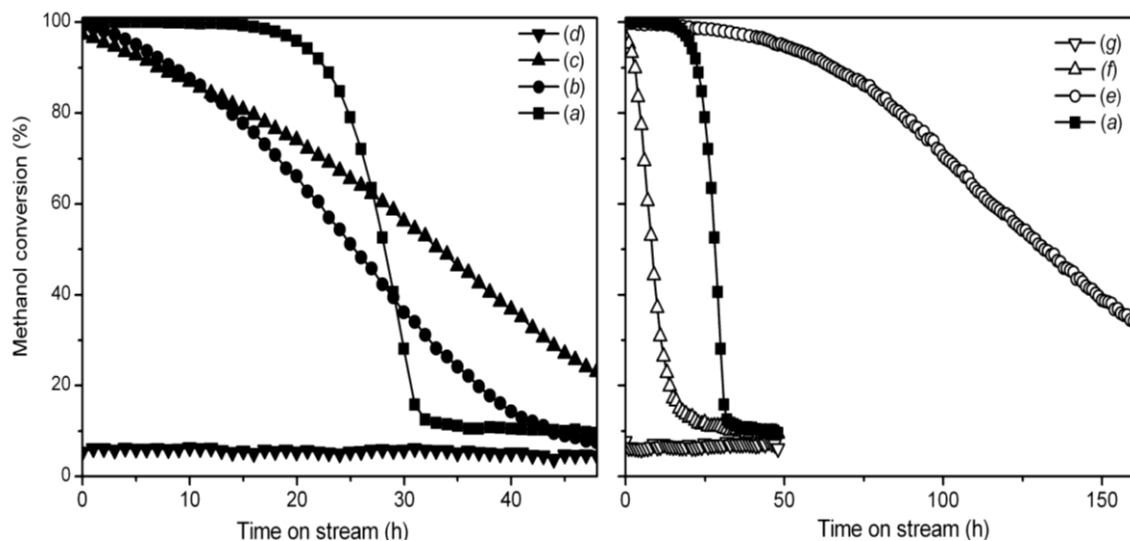


Figure 5.21: Methanol conversion of (a) bulk ZSM-5, (b) MesoMFI(2, Br), (c) MesoMFI(3, Br), (d) MesoMFI(4, Br), (e) MesoMFI(2, OH), (f) MesoMFI(3, OH) and (g) MesoMFI(4, OH).

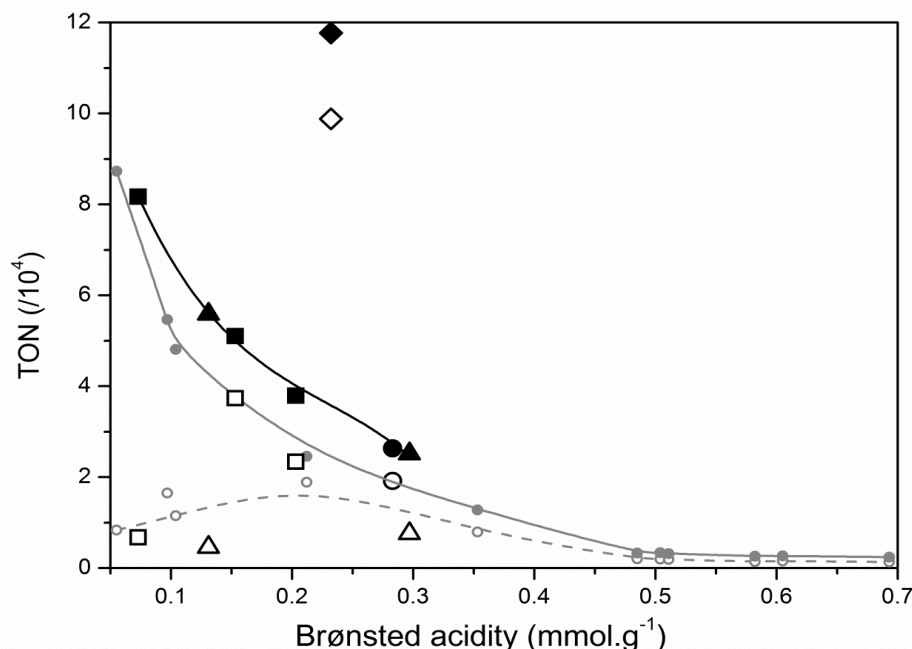


Figure 5.22: (Solid symbols) $\text{TON}_{\text{total}}$ and (open symbols) $\text{TON}_{\text{product}}$ as a function of the concentration of Brønsted acid sites: (●) bulk HZSM-5, (■) MesoMFI(Br), (◆) MesoMFI(2, OH), (▲) MesoMFI(3, OH) and MesoMFI(4, OH) ($T = 400\text{ °C}$; $\text{WHSV} = 6\text{ g}\cdot\text{g}^{-1}\cdot\text{h}^{-1}$). The data with grey color refers to MTH results for steamed HZSM-5 measured at a reaction temperature at 350 °C at similar WHSV [54].

Table 5.8: Lifetime, product distribution, and coke content of nanosheets MFI zeolite catalysts for the MTO reaction (WHSV = 6 g.g⁻¹.h⁻¹; T = 400 °C) after 1 h time on stream.

Zeolite	TON _{product} ^a	TON _{total} ^b	t _{50%} ^c (h)	C ₁ (%)	C ₂ ⁼ (%)	C ₂ (%)	C ₃ ⁼ (%)	C ₃ (%)	C ₄ (%)	C ₅₊ (%)	Coke content (%) ^d
ZSM-5(40)	1.9 × 10 ⁴	2.6 × 10 ⁴	28	0.4	10	<0.1	30	3	38	18	14
MesoMFI(2, Br)	2.3 × 10 ⁴	3.8 × 10 ⁴	25	0.5	6	<0.1	36	2	36	19	10
MesoMFI(3, Br)	>3.7 × 10 ⁴	>5.1 × 10 ⁴	33	0.5	7	<0.1	33	3	36	22	15
MesoMFI(4, Br)	6.8 × 10 ³	8.2 × 10 ⁴	n.d. ^e	n.d.	n.d.	n.d.	n.d.	n.d.	n.d.	n.d.	< 1
MesoMFI(2, OH)	>9.9 × 10 ⁴	>11.8 × 10 ⁴	132	0.3	5	<0.1	37	1	39	17	15
MesoMFI(3, OH)	7.6 × 10 ³	2.5 × 10 ⁴	8	1.1	3	<0.1	35	1	29	29	9
MesoMFI(4, OH)	4.6 × 10 ³	5.6 × 10 ⁴	n.d.	n.d.	n.d.	n.d.	n.d.	n.d.	n.d.	n.d.	6

^a turnover number: number of moles of methanol converted into products other than DME in 48 h per BAS; the concentration of BAS is the value from pyridine IR after evacuation at 150 °C; ^b turnover number: number of moles of total methanol converted into products in 48 h per BAS; the concentration of BAS is the value from pyridine IR after evacuation at 150 °C; ^c Time on stream passed to reach 50 % of the initial conversion; ^d Determined by TGA; ^e not determined.

Bulk HZSM-5(40) rapidly deactivated after 20 h time on stream. The time on stream at which the methanol conversion decreased to 50% ($t_{50\%}$) is 28 h. Although deactivation for MesoMFI(2, Br) and MesoMFI(3, Br) occurred at similar times, it is immediately clear from Fig. 5.21 that their deactivation rate is much less pronounced compared to bulk HZSM-5. This is due to the lower concentration of BAS in multilamellar zeolites. To better compare catalyst longevity in the MTH reaction, we define turnover numbers as the number of moles of methanol converted ($\text{TON}_{\text{total}}$, including DME formation) and the number of moles of methanol converted into products with carbon-carbon bonds ($\text{TON}_{\text{product}}$) per mole of Brønsted acid site (pyridine IR values in Table 5.4). The TON values are included in Table 5.8. Thus, $\text{TON}_{\text{product}}$ increases in the order MesoMFI(3, Br) > MesoMFI(2, Br) > HZSM-5 > MesoMFI(4, Br) for the multilamellar zeolites. In contrast, when $\text{TON}_{\text{total}}$ is compared one finds the order to be MesoMFI(4, Br) > MesoMFI(3, Br) > MesoMFI(2, Br) > HZSM-5. The latter trend is consistent with the increased rate of deactivation with increasing Brønsted acidity [54]. The acidity of MesoMFI(4, Br) is so low so that DME is the only main product and only very small amounts of reaction products from C-C bond formation. The maximum in $\text{TON}_{\text{product}}$ for MesoMFI(3, Br) shows that balanced Brønsted acidity is required for maximum formation rate of products with carbon-carbon bonds in line with conclusions from a recent study on steamed HZSM-5 zeolite samples [54]. Too low acidity predominantly results in DME formation with low rates of carbon-carbon forming (including coking) reactions, whereas too high acidity causes rapid deactivation due to extensive coking.

Fig. 5.22 shows the trend of the TON with total BAS. It is very similar to the one reported for steamed HZSM-5(27), whose data are included in the figure [54]. Note that the TON values for (steamed) HZSM-5(27) were measured at a lower reaction temperature of 350 °C. $\text{TON}_{\text{total}}$ for the present set of zeolites increases substantially with decreasing BAS. It is important to mention that $\text{TON}_{\text{total}}$ does not trend with the external BAS concentration (cf. Table 5.8). These two observations indicate that all the BAS (probed by pyridine) are involved in formation of deactivating coke species. It also means that deactivating coke is mainly formed in the micropores. This is consistent with the corollary from many previous works that coking takes place due to formation of olefinic products covering the acid sites in HZSM-5 at early stages of methanol conversion reactions and polyaromatics formation

thereafter [55]. The higher $\text{TON}_{\text{total}}$ values of the nanolayered zeolites compared to steamed HZSM-5, even when measured at lower reaction temperature, underpin the decreased rate of coke formation per acid site in the former zeolites. This is most likely an effect of the nanolayered nature of the mesoMFI zeolites. In (steamed) bulk HZSM-5, part of the BAS in the crystals' interior remains unused during the MTH reaction. During coke oxidation by TGA analysis in (artificial) air of spent catalysts the maximum in the weight loss rate was found around 540 °C, implying predominant formation of polyaromatic species [55]. The unilamellar zeolites MesoMFI(3, OH) and MesoMFI(4, OH) behave in a similar way as the corresponding multilamellar zeolites. Because of its high Brønsted acidity, MesoMFI(3, OH) cokes and deactivates rapidly and its $\text{TON}_{\text{total}}$ is close to that of bulk HZSM-5. Related to this is the lower $\text{TON}_{\text{product}}$. MesoMFI(4, OH) has a very low activity because of the low BAS concentration. It is worthwhile mentioning that the coking behavior of SSZ-13 in the related methanol-to-olefins reaction is different in the sense that the coke content (and lifetime) significantly increase when mesopores are generated [13]. This is consistent with deactivation for chabazite zeolite being the result of coke formation at their external surface [56].

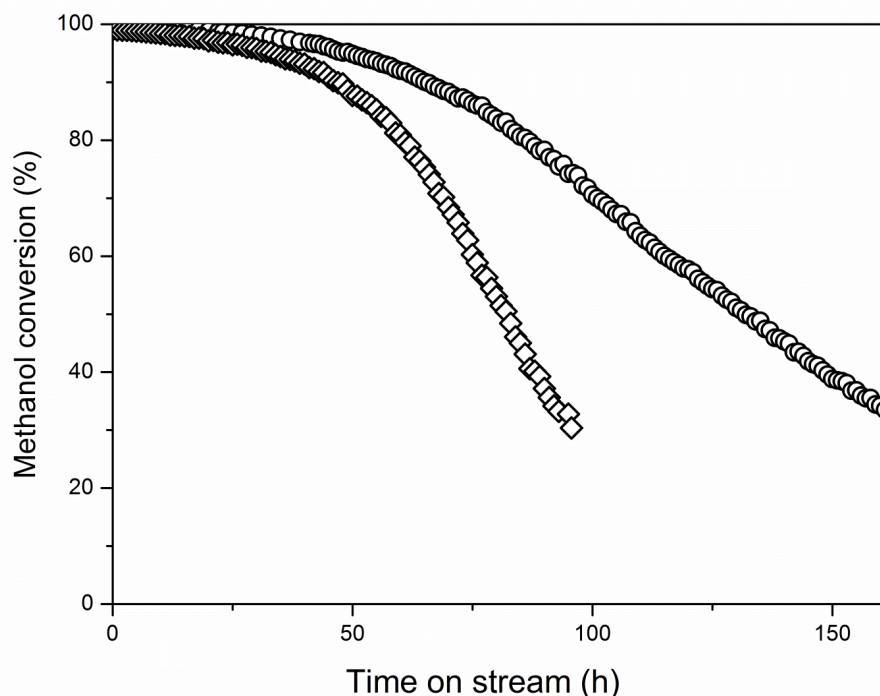


Figure 5.23: Methanol conversion of two different batches of MesoMFI(2, OH).

Surprisingly, $\text{TON}_{\text{product}}$ and $\text{TON}_{\text{total}}$ of MesoMFI(2, OH) are much higher than of all

other zeolites. The MTH activity of MesoMFI(2, OH) was remeasured and the results were very similar. Another sample was synthesized in the same manner, calcined and tested in the MTH reaction (Fig. 5.23). Although the rate of deactivation is somewhat higher than the original sample, this zeolite also substantially outperforms the other zeolites. Note that the four-to-five-fold increase of the $\text{TON}_{\text{product}}$ of MesoMFI(2, OH) compared to bulk HZSM-5 is very similar to the increased lifetime reported by the Ryoo group in their original paper using unilamellar ZSM-5 zeolite synthesized by use of $\text{C}_{22-6-6}\text{OH}_2$ in the same reaction [10]. The coke content is around 15 wt%, similar to the other zeolites in the present study, but significantly lower than the values reported in the Ryoo paper. The latter difference may be explained as follows. Deactivation is due to coke deposition in the micropores. As a result of their large external (mesopore) surface area, the nanolayered zeolites will also produce more external coke. Thus, in the long reaction experiment carried out in Ref. [10], the contribution of external coke may be much higher than in the present experiments. Currently, we have not been able to provide a reasonable explanation for the much lower rate of coke deactivation of MesoMFI(2, OH). From the characterization data, it is clear that its textural properties, Al speciation and acidity do not stand out from the other nanolayered ZSM-5 zeolites. To be clear, the rate of deactivation of all nanolayered zeolites except MesoMFI(2, OH) trends similarly with the concentration of BAS as reported for steamed bulk HZSM-5 [54]. This is consistent with the notion that deactivation is due to deposition of coke on the internal BAS. In essence, this implies that the generation of mesoporosity for HZSM-5 zeolite will not significantly decrease the rate of deactivation due to coking. However that may be, MesoMFI(2, OH) displays a much lower rate of coke formation on its internal surface during the MTH reaction and, if its origin could be understood, it might lead to the synthesis of substantially improved methanol conversion zeolite catalysts.

5.4 Conclusions

The purpose of this study was to investigate the acidic properties of nanolayered ZSM-5 zeolites synthesized by use of multiquaternary ammonium surfactants. Although the resulting zeolites are close to the materials reported by Ryoo et al. [10] with regards to structure and

morphology, accurate control of thickness of the constituent nanosheets as recently shown by the Ryoo group [16] was not achieved. As a detailed study of the acidity of such nanolayered zeolites is currently lacking, we consider the following salient points on the present set of nanolayered ZSM-5 zeolites important:

- At typical Si/Al ratios of 30-50, a significant fraction of the Al atoms (~25-40 %) does not end up in the framework of the nanolayered ZSM-5 zeolites. The extraframework Al atoms are highly dispersed as they are observed to revert to tetrahedral coordination upon coordination of ammonia. Such behavior is not uncommon for defect-rich bulk ZSM-5 zeolites. A multilamellar zeolite prepared at a Si/Al ratio of 20 was largely amorphous.
- Acidity characterization reveals that the BAS are of similar strength as those in bulk HZSM-5. Nanolayered zeolites contain a higher amount of BAS at their external (mesopore) surface. The nanolayered zeolites also contain a somewhat larger amount of Lewis acid sites than bulk HZSM-5. The unilamellar zeolites have a higher concentration of Lewis, external Brønsted acid and silanol sites than multilamellar zeolites, indicative of the more defective nature of the former.
- The number of BAS in the nanolayered zeolites is considerably lower than the framework Al content, the difference increasing with nanosheet thickness. The origin of this trend is most likely related to differences in crystallinity.
- Except for one particular sample (nanolayered ZSM-5 synthesized from $C_{22-6-6}OH_2$ template), the total methanol turnover normalized per BAS of these zeolites trends inversely with the BAS concentration. There is no strong correlation with the external BAS. Thus, catalyst deactivation due to coking depends mainly on the total concentration of BAS. Fewer BAS results in less coke formation and a higher turnover number of methanol.
- A unilamellar ZSM-5 zeolite prepared using $C_{22-6-6}OH_2$ displayed substantially improved performance in terms of a much lower rate of coke deactivation in line with the report of Ryoo and co-workers [10]. Since the acidic and textural properties of this zeolite were not significantly different from the others, it remains to be determined why this material performs so much better.

References

- [1] A. Corma, *Chem. Rev.* 95 (1995) 559-614.
- [2] G. Busca, *Chem. Rev.* 107 (2007) 5366-5410.
- [3] L. Tosheva, and V.P. Valtchev, *Chem. Mater.* 17 (2005) 2494-2513.
- [4] A. Chica, U. Diaz, V. Fornes, and A. Corma, *Catal. Today* 147 (2009) 179-185.
- [5] K. Egeblad, C.H. Christensen, M. Kustova, and C.H. Christensen, *Chem. Mater.* 20 (2008) 946-960.
- [6] J. Perez-Ramirez, C.H. Christensen, K. Egeblad, C.H. Christensen, and J.C. Groen, *Chem. Soc. Rev.* 37 (2008) 2530-2542.
- [7] R. Chal, C. G é rardin, M. Bulut, and S. van Donk, *ChemCatChem* 3 (2011) 67-81.
- [8] L.-H. Chen, X.-Y. Li, J.C. Rooke, Y.-H. Zhang, X.-Y. Yang, Y. Tang, F.-S. Xiao, and B.-L. Su, *J. Mater. Chem.* 22 (2012) 17381-17403.
- [9] K. Moller, and T. Bein, *Chem. Soc. Rev.* 42 (2013) 3689-3707.
- [10] M. Choi, K. Na, J. Kim, Y. Sakamoto, O. Terasaki, and R. Ryoo, *Nature* 461 (2009) 246-250.
- [11] J. Kim, M. Choi, and R. Ryoo, *J. Catal.* 269 (2010) 219-228.
- [12] A.J.J. Koekkoek, W. Kim, V. Degirmenci, H. Xin, R. Ryoo, and E.J.M. Hensen, *J. Catal.* 299 (2013) 81-89.
- [13] L. Wu, V. Degirmenci, P.C.M.M. Magusin, N.J.H.G.M. Lousberg, and E.J.M. Hensen, *J. Catal.* 298 (2013) 27-40.
- [14] C.S. Cundy, and P.A. Cox, *Chem. Rev.* 103 (2003) 663-701.
- [15] A. Aerts, C.E.A. Kirschhock, and J.A. Martens, *Chem. Soc. Rev.* 39 (2010) 4626-4642.
- [16] W. Park, D. Yu, K. Na, K.E. Jelfs, B. Slater, Y. Sakamoto, and R. Ryoo, *Chem. Mater.* 23 (2011) 5131-5137.
- [17] K. Na, W. Park, Y. Seo, and R. Ryoo, *Chem. Mater.* 23 (2011) 1273-1279.
- [18] F. Thibault-Starzyk, I. Stan, S. Abello, A. Bonilla, K. Thomas, C. Fernandez, J.P. Gilson, and J. Perez-Ramirez, *J. Catal.* 264 (2009) 11-14.
- [19] L.L. Wu, V. Degirmenci, P.C.M.M. Magusin, B.M. Szyja, and E.J.M. Hensen, *Chem. Commun.* 48 (2012) 9492-9494.
- [20] E. Verheyen, C. Jo, M. Kurttepel, G. Vanbutsele, E. Gobechiya, T.s.I. Kor Ñ pyi, S. Bals, G. Van Tendeloo, R. Ryoo, C.E.A. Kirschhock, and J.A. Martens, *J. Catal.* 300 (2013) 70-80.
- [21] J. Kim, W. Kim, Y. Seo, J.C. Kim, and R. Ryoo, *J. Catal.* 301 (2013) 187-197.
- [22] J. Datka, A.M. Turek, J.M. Jehng, and I.E. Wachs, *J. Catal.* 135 (1992) 186-199.
- [23] N.S. Nesterenko, F. Thibault-Starzyk, V. Montouilliout, V.V. Yushchenko, C. Fernandez, J.P. Gilson, F. Fajula, and I.I. Ivanova, *Kinet. Catal.* 47 (2006) 40-48.

- [24] E. Brunner, *J. Chem. Soc., Faraday Trans.*, 86 (1990) 3957-3960.
- [25] V. Degirmenci, O.F. Erdem, A. Yilmaz, D. Michel, and D. Uner, *Catal. Lett.* 115 (2007) 79-85.
- [26] K. Na, M. Choi, W. Park, Y. Sakamoto, O. Terasaki, and R. Ryoo, *J. Am. Chem. Soc.* 132 (2010) 4169-4177.
- [27] P.K. Dutta, and M. Puri, *J. Phys. Chem.* 91 (1987) 4329-4333.
- [28] A.J.J. Koekkoek, C.H.L. Tempelman, V. Degirmenci, M.L. Guo, Z.C. Feng, C. Li, and E.J.M. Hensen, *Catal. Today* 168 (2011) 96-111.
- [29] P.K. Dutta, K.M. Rao, and J.Y. Park, *J. Phys. Chem.* 95 (1991) 6654-6656.
- [30] S. Mintova, B. Mihailova, V. Valtchev, and L. Konstantinov, *J. Chem. Soc., Chem. Commun.* (1994) 1791-1792.
- [31] M.A. Camblor, A. Corma, and S. Valencia, *Microporous Mesoporous Mater.* 25 (1998) 59-74.
- [32] A. Aerts, A. van Isacker, W. Huybrechts, S.P.B. Kremer, C.E.A. Kirschhock, F. Collignon, K. Houthoofd, J.F.M. Denayer, G.V. Baron, G.B. Marin, P.A. Jacobs, and J.A. Martens, *Appl. Catal. A: Gen* 257 (2004) 7-17.
- [33] C.A. Fyfe, G.C. Gobbi, J. Klinowski, J.M. Thomas, and S. Ramdas, *Nature* 296 (1982) 530-533.
- [34] C.A. Fyfe, Y. Feng, H. Grondey, G.T. Kokotailo, and H. Gies, *Chem. Rev.* 91 (1991) 1525-1543.
- [35] K. Na, C. Jo, J. Kim, K. Cho, J. Jung, Y. Seo, R.J. Messinger, B.F. Chmelka, and R. Ryoo, *Science* 333 (2011) 328-332.
- [36] M.T. Janicke, C.C. Landry, S.C. Christiansen, D. Kumar, G.D. Stucky, and B.F. Chmelka, *J. Am. Chem. Soc.* 120 (1998) 6940-6951.
- [37] P.C.M.M. Magusin, V.E. Zorin, A. Aerts, C.J.Y. Houssin, A.L. Yakovlev, C.E.A. Kirschhock, J.A. Martens, and R.A. van Santen, *J. Phys. Chem. B* 109 (2005) 22767-22774.
- [38] H.W. Beckham, and H.W. Spiess, *Macromol. Chem. Phys.* 195 (1994) 1471-1482.
- [39] D. Banerjee, M.A.C. Broeren, M.H.P. van Genderen, E.W. Meijer, and P.L. Rinaldi, *Macromolecules* 37 (2004) 8313-8318.
- [40] J. Leisen, K. Schmidt-Rohr, and H.W. Spiess, *J. Non-Cryst. Solids* 172 (1994) 737-750.
- [41] J.A. van Bokhoven, A.M.J. van der Eerden, D.C. Koningsberger, G.G. R. Aiello, and F. Testa, *Stud. Surf. Sci. Catal.*, Elsevier. 143B (2002) 1885-1890.
- [42] E.J.M. Hensen, D.G. Poduval, P.C.M.M. Magusin, A.E. Coumans, and J.A.R. van Veen, *J. Catal.* 269 (2010) 201-218.
- [43] H. Kraus, M. Müller, R. Prins, and A.P.M. Kentgens, *J. Phys. Chem. B* 102 (1998) 3862-3865.
- [44] M. Hunger, *Catal. Rev.* 39 (1997) 345-393.

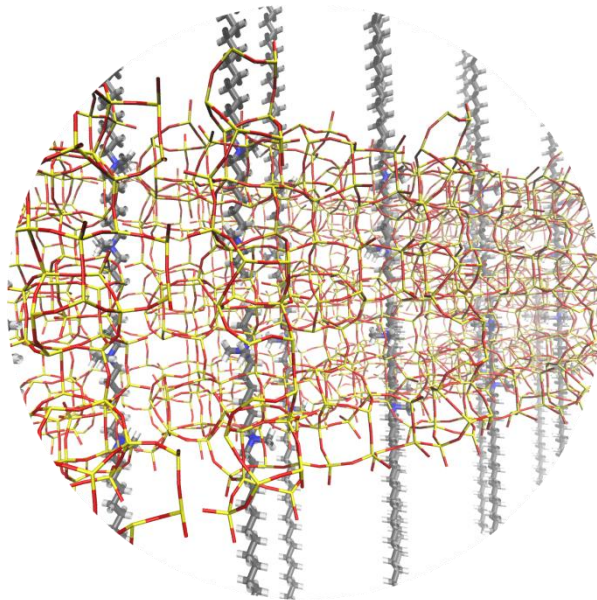
-
- [45] V.L. Zholobenko, L.M. Kustov, V.Y. Borovkov, and V.B. Kazansky, *Zeolites* 8 (1988) 175-178.
- [46] C. Paze, A. Zecchina, S. Spera, A. Cosma, E. Merlo, G. Spano, and G. Girotti, *Phys. Chem. Chem. Phys.* 1 (1999) 2627-2629.
- [47] G. Piedra, J.J. Fitzgerald, N. Dando, S.F. Dec, and G.E. Maciel, *Inorg. Chem.* 35 (1996) 3474-3478.
- [48] E.J.M. Hensen, D.G. Poduval, V. Degirmenci, D. Ligthart, W.B. Chen, F. Mauge, M.S. Rigutto, and J.A.R. van Veen, *J. Phys. Chem. C* 116 (2012) 21416-21429.
- [49] C.A. Emeis, *J. Catal.* 141 (1993) 347-354.
- [50] F. Thibault-Starzyk, A. Vimont, and J.P. Gilson, *Catal. Today* 70 (2001) 227-241.
- [51] C.D. Chang, C.T.W. Chu, and R.F. Socha, *J. Catal.* 86 (1984) 289-296.
- [52] M. Bjorgen, S. Svelle, F. Joensen, J. Nerlov, S. Kolboe, F. Bonino, L. Palumbo, S. Bordiga, and U. Olsbye, *J. Catal.* 249 (2007) 195-207.
- [53] F. Bleken, M. Bjorgen, L. Palumbo, S. Bordiga, S. Svelle, K.P. Lillerud, and U. Olsbye, *Top. Catal.* 52 (2009) 218-228.
- [54] S.M.T. Almutairi, P.C.M.M. Magusin, B. Mezari, E.A. Pidko, and E.J.M. Hensen, *J. Catal.* (2013) in press.
- [55] D.M. Bibby, R.F. Howe, and G.D. McLellan, *Appl. Catal. A: Gen* 93 (1992) 1-34.
- [56] D. Mores, E. Stavitski, M.H.F. Kox, J. Kornatowski, U. Olsbye, and B.M. Weckhuysen, *Chem. Eur. J.* 14 (2008) 11320-11327.

Chapter 6

Synthesis and Catalytic Properties of Nanolayered ZSM-5 Zeolite with a Si/Al ratio of 20

Summary

The synthesis of nanolayered ZSM-5 zeolites with a Si/Al content of 20 is explored. Whilst at a crystallization temperature of 150 °C nanolayered ZSM-5 zeolite can be synthesized at a Si/Al ratio of 50, increasing the Al content to a Si/Al ratio of 20 results in X-ray amorphous materials with very low Brønsted acidity. The crystallization rate can be improved when the hydrothermal synthesis is carried out at 170 °C. The crystallinity of the nanolayered zeolites can be improved by tailoring the originally proposed $R-N^+(CH_3)_2-C_6H_{12}-N^+(CH_3)_2-C_6H_{13}$ (R = long alkyl chain). By replacing the hexyl end group by a propyl end group, in principle all intersections of the nanolayered ZSM-5 zeolite can be occupied by quaternary ammonium ions. The zeolite synthesized with a propyl-terminated template exhibited higher crystallinity than the hexyl-terminated ones. This also led to higher Brønsted acidity. Nevertheless, the total acidity is significantly lower than that of bulk HZSM-5 at comparable Si/Al ratio. The reason is the difficulty of building a significant amount of tetrahedral Al in the thin zeolite nanolayers. Another aspect is that the Al atoms that do not end up in the zeolite framework may act to replace protons and, accordingly, decrease Brønsted acidity. The catalytic performance in *n*-heptane hydroconversion trends well with the Brønsted acidity as probed by CO_{ads} and Py_{ads} IR. In the methanol-to-hydrocarbons reaction optimum methanol conversion capacity is observed for samples with intermediate Brønsted acidity.



6.1 Introduction

Zeolites are crystalline microporous aluminosilicates, which have been widely used as catalysts for hydrocarbon conversion since the early 1960s [1-3]. Their usefulness as catalysts derives from the combination of a microporous framework that gives rise to size- and/or shape-selectivity and the presence of strong Brønsted acid sites, which can be controlled within a certain range [4]. The Brønsted acidity of zeolites is due to tetrahedral Al³⁺ substitutions for Si⁴⁺ in the microporous SiO₂ network. For high silica zeolites, the total Brønsted acidity is mainly determined by the framework Si/Al ratio. Despite these favorable properties, the microporous nature of the often micrometer-sized zeolite crystals may result in mass transport limitations during catalytic reactions. To overcome such limitations, various strategies have been applied, such as synthesizing very small zeolite crystals [5], delaminating zeolites [6], synthesizing zeolites with extra large pores [7-9] and introducing mesoporosity in microporous zeolite crystals [10-14]. The topic of hierarchical zeolites has attracted considerable attention in the last decade. Ryoo's group has made substantial progress in synthesizing nanolayered ZSM-5 zeolite with the crystal size in the *b*-direction limited to one unit cell [15, 16]. These nanostructured zeolites have great potential in acid-catalyzed reactions and, in particular, it has been shown that the lifetime of such a nanolayered zeolite in the methanol-to-hydrocarbons (MTH) reaction was greatly improved over that of bulk ZSM-5 zeolite.

In the MTH reaction, methanol is converted to dimethyl ether (DME), light olefins, high-octane gasoline or distillates. The product distribution can be finetuned by proper choice of the zeolite topology [17]. Recently, the methanol-to-olefins (MTO) process has been commercialized in China, mainly driven by high crude oil prices and strong market demand for chemicals and availability of cheap local coal [18]. SAPO-34, a silicoaluminophosphate with the chabazite network topology, is used as the commercial catalyst in this process. Besides, significant research is being undertaken for process to convert methanol to propylene, gasoline and/or distillate products. The versatility of these processes derives from the feedstock flexibility of syngas production including coal [19], natural gas [20] and biomass [21, 22].

In our previous detailed study of the effect of the morphology and thickness of nanolayered zeolites [23] (Chapter 5), we found that an increase of the Al content in the gel used to synthesize nanolayered ZSM-5 to values below Si/Al = 40 led to an amorphous product. In general, it is desirable to be able to tune the acidity of ZSM-5 for specific

applications such as hydroconversion of *n*-alkanes. In an earlier report of Ryoo and co-workers [16], it was found that synthesis of ZSM-5 nanosheets with Si/Al = 20 did not result in a fully crystalline product. In the present work, we explored the synthesis of multi- and unilamellar nanolayered ZSM-5 zeolite with a target Si/Al ratio of 20. The starting point of our efforts was the realization by computational modeling that the end group of the diquateryary C_{22-6-6}^{2+} template is too bulky to allow for complete filling of all intersections of ZSM-5 nanolayers with quaternized ammonium compounds (Fig. 6.1). Accordingly, we surmised that a shorter end group (i.e., a propyl instead of hexyl) could potentially lead to increased crystallinity. The nanolayered zeolites were characterized by XRD, SEM, TEM, Ar physisorption, UV-Raman and NMR spectroscopy. Their acidic properties were investigated by ^{27}Al NMR spectroscopy and IR spectroscopy using CO, pyridine and 2,4,6-collidine as probe molecules,. The catalytic properties of the nanolayered zeolites are measured in the MTH reaction at 400 °C.

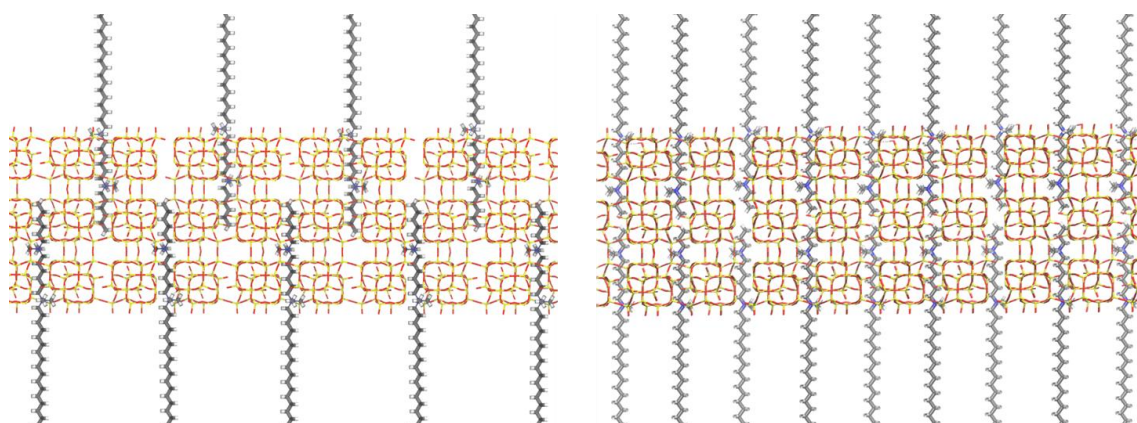


Figure 6.1: Filling of the micropores of nanolayered silicalite-1 with (left) $C_{16}H_{33}N^+(CH_3)_2-C_6H_{12}-N^+(CH_3)_2-C_6H_{13}$ and (right) $C_{16}H_{33}N^+(CH_3)_2-C_6H_{12}-N^+(CH_3)_2-C_3H_7$. In the modeling it was assumed that both quaternary ammonium groups interact with the silicalite-1 framework.

6.2 Experimental section

6.2.1 Synthesis of templates

$[C_{22}H_{45}-N^+(CH_3)_2-C_6H_{12}-N^+(CH_3)_2-C_6H_{13}]Br_2$ (denoted as $C_{22-6-6}Br_2$): For synthesis of $C_{22-6-6}Br_2$, we followed the procedure outlined before [15, 24, 25]. Briefly, N,N,N',N'-tetramethyl-1,6-diaminohexane was reacted with 1-bromo-undecane in order to obtain $C_{22-6}Br$. This intermediate was subsequently reacted with 1-bromohexane to obtain $C_{22-6-6}Br_2$.

$[C_{22}H_{45}-N^+(CH_3)_2-C_6H_{12}-N^+(CH_3)_2-C_3H_7]Br_2$ (denoted as $C_{22-6-3}Br_2$): Briefly, N,N,N',N'-tetramethyl-1,6-diaminohexane was reacted with 1-bromo-undecane in order to obtain $C_{22-6}Br$. This intermediate was subsequently reacted with 1-bromopropane to obtain $C_{22-6-3}Br_2$.

The hydroxyl form surfactant was obtained by ion-exchange of the bromide form of the surfactant with an anion-exchange resin (Amberlite, IRN-78) in a flask overnight.

6.2.2 Synthesis of materials

Synthesis of MFI zeolite nanosheets with Si/Al=50

An amount of 1.4 g of C₂₂₋₆₋₃ template (bromide form) was dissolved in 7.8 ml deionized water at 60 °C. 0.21 g of NaOH was added to the solution and the template solution was stirred at 50 °C for 4 h. A second solution was made by mixing 0.05 g Al(OH)₃, 10 ml deionized water and 5.54 ml TEOS for 1 h. The template solution was cooled to room temperature. This solution was added dropwise under vigorous stirring to the solution with the template. A white suspension formed. The suspension was stirred for 1 h in an open vessel at room temperature and subsequently transferred to a Teflon-lined stainless steel autoclave. The autoclave was heated under rotation at 150 °C for 5 days. The white product was recovered by filtration and washed with copious amounts of deionized water and ethanol. The product was dried over night at 110 °C.

Synthesis of MFI zeolite nanosheets with Si/Al=20

1.4 g of C₂₂₋₆₋₃ template (bromide form) was dissolved in 7.8 ml deionized water at 60 °C. This gives a clear solution. 0.21 g of NaOH was added to the solution and the template solution was stirred at 50 °C for 4 h. A second solution was made by mixing 0.13 g Al(OH)₃, 10 ml deionized water and 5.54 ml TEOS for 1 h. The template solution was cooled to room temperature. The silica solution was added dropwise under vigorous stirring to the template solution and a white suspension formed. The suspension was stirred for 1 h in an open vessel at room temperature. The resulting thick gel was subsequently transferred to a Teflon-lined stainless steel autoclave. The autoclave was heated under rotation at 150 or 170 °C for 5 days. The white product was recovered by filtration and washed with copious amounts of deionized water and ethanol. The product was dried over night at 110 °C. A similar procedure was followed using the hydroxyl form of C₂₂₋₆₋₃ with the exception that the crystallization time was extended to 11 days.

Post-treatment zeolites

The organic part of the zeolites was removed by calcination in air with a heating ramp of 1 °C/min to 550 °C followed by an isothermal period of 6 h. Their proton forms were obtained by triple ion exchange of the calcined zeolite with 1 M NH₄NO₃ at 80 °C for 2 h and calcination in static air at 550 °C for 4 h. The zeolites are denoted as follows: ZSM-5(x, y)-T

with x representing the template, y the Si/Al ratio and T the temperature of hydrothermal synthesis.

Table 6.1: Molar composition of synthesis gels and hydrothermal synthesis conditions for the preparation of nanostructured MFI zeolites (hydrothermal synthesis in Teflon-lined autoclaves was done under rotation at 60 rpm).

Zeolite	SDA	Gel composition (molar ratio)					T (°C)	Time (days)
		SDA	TEOS	Al(OH) ₃	NaOH	H ₂ O		
ZSM-5(C ₂₂₋₆₋₃ Br ₂ , 50, 150)	C ₂₂₋₆₋₃ Br ₂	8	100	2	22	4050	150	5
ZSM-5(C ₂₂₋₆₋₆ Br ₂ , 50, 150)	C ₂₂₋₆₋₆ Br ₂	8	100	2	22	4050	150	5
ZSM-5(C ₂₂₋₆₋₃ Br ₂ , 20, 150)	C ₂₂₋₆₋₃ Br ₂	8	100	7	22	4050	150	5
ZSM-5(C ₂₂₋₆₋₆ Br ₂ , 20, 150)	C ₂₂₋₆₋₆ Br ₂	8	100	7	22	4050	150	5
ZSM-5(C ₂₂₋₆₋₃ Br ₂ , 20, 170)	C ₂₂₋₆₋₃ Br ₂	8	100	7	22	4050	170	5
ZSM-5(C ₂₂₋₆₋₆ Br ₂ , 20, 170)	C ₂₂₋₆₋₆ Br ₂	8	100	7	22	4050	170	5
ZSM-5(C ₂₂₋₆₋₃ (OH) ₂ , 20, 170)	C ₂₂₋₆₋₃ (OH) ₂	15	100	7	0	4050	170	11

6.2.3 Physicochemical properties

Basic characterization

X-ray diffraction patterns were recorded on a Bruker D4 Endeavor diffractometer using Cu K α radiation in the 2θ range of 5-60 °. Elemental analyses were carried out by ICP-OES (Spectro Ciros CCD ICP optical emission spectrometer with axial plasma viewing). The zeolite crystals were crushed and then dissolved in 1.5 ml of an acid mixture of HF/HNO₃/H₂O. Argon physisorption experiments were carried out at 87.6 K in a Micromeritics ASAP 2020 instrument in static mode. The samples were outgassed at 350 °C for 8 h prior to the sorption measurements. The Brunauer-Emmett-Teller adsorption isotherm model was used to determine the total surface area (S_{BET}) in the p/p_0 range between 0.05-0.25. The mesopore volume (V_{meso}) and mesopore size distribution were calculated from the adsorption branch of the isotherm by the Barrett-Joyner-Halenda (BJH) method. The micropore volume was determined by the NLDFT method (Ar at 87 K on oxides as the model, assuming cylindrical pores, without regularization).

Electron microscopy

Scanning electron microscopy (SEM) pictures were taken on a FEI Quanta 200F scanning electron microscope at an accelerating voltage of 3-5 kV. The catalysts were coated with gold prior to measurements. Transmission electron microscopy (TEM) pictures were taken on a FEI Tecnai 20 at 200 kV. The zeolites were suspended in ethanol and dispersed over a carbon coated holey Cu grid with a film prior to measurements.

Vibrational spectroscopy

UV Raman spectra were recorded with a Jobin-Yvon T64000 triple stage spectrograph with spectral resolution of 2 cm^{-1} operating in double subtractive mode. The laser line at 325 nm of a Kimmon He-Cd laser was used as to excite the sample. The power of the laser on the sample was lower than 4 mW.

FTIR spectra were recorded in the range of $4000\text{-}400\text{ cm}^{-1}$ by a Bruker Vertex V70v instrument. The spectra were acquired at a 2 cm^{-1} resolution and averaged over 20 scans. Zeolites (typically 10 mg) were pressed into thin self-supporting wafers with a diameter of 13 mm and placed inside a controlled-environment infrared transmission cell, capable of heating and cooling, gas dosing and evacuation. For pretreatment, the zeolite wafer was first heated to $550\text{ }^{\circ}\text{C}$ at a rate of $2\text{ }^{\circ}\text{C}/\text{min}$ in an oxygen atmosphere. Then, the cell was outgassed at the final temperature until the residual pressure was below 5×10^{-5} mbar. For CO adsorption, the sample was cooled to 77 K and CO was introduced into the cell via a sample loop connected to a Valco six-port valve. For pyridine (Py) and 2,4,6-collidine (Coll) adsorption, Py and Coll were introduced from an ampoule at their vapor pressure at room temperature. The exposure time of 20 min was followed by desorption for 1 h at temperatures of 150, 300 and $500\text{ }^{\circ}\text{C}$. Spectra after evacuation treatments were recorded after cooling the sample to $150\text{ }^{\circ}\text{C}$. To quantify the total amount of Brønsted acid sites and Lewis acid sites, the molar extinction coefficient values of 0.73 and $1.11\text{ cm} \cdot \mu\text{mol}^{-1}$ of pyridine were employed, respectively [26]. To quantify the external Brønsted acid sites, the molar extinction coefficient of $10.1\text{ cm} \cdot \mu\text{mol}^{-1}$ of collidine was employed [27].

NMR spectroscopy

Nuclear Magnetic Resonance (NMR) spectra were recorded on a Bruker DMX500 NMR spectrometer. For the ^{27}Al Magic Angle Spinning (MAS) NMR, a standard Bruker MAS probehead was used with rotor diameter of 2.5 mm, operated at a spinning rate of 20 kHz. Quantitative ^{27}Al NMR spectra were recorded using a single excitation pulse of $1\text{ }\mu\text{s}$ and an interscan delay of 1 s. The tetrahedral and octahedral aluminum content in the various catalysts was estimated from spectral deconvolution and peak areas of the respective signal components using a commercial ZSM-5 sample with a known Al content (Akzo-Nobel) as an external reference. The ^{27}Al chemical shift is referred to a saturated $\text{Al}(\text{NO}_3)_3$ solution.

^1H and ^{29}Si MAS NMR spectra of the zeolites were recorded at $60\text{ }^{\circ}\text{C}$ and a sample rotation rate of 10 kHz using a double-channel 4-mm MAS probehead. These experimental NMR conditions represent a compromise between the ^1H NMR resolution required, on the

one hand, and effective ^1H - ^{29}Si cross-polarization to record ^{29}Si NMR spectra. Two-dimensional $^{29}\text{Si}\{^1\text{H}\}$ cross-polarization based HETeronuclear CORrelation (HETCOR) NMR spectra were recorded with a rectangular contact pulse of 3 ms with carefully matched amplitudes on both channels. Tetramethylsilane (TMS) was employed as an external reference for the chemical shift for ^1H and ^{29}Si NMR.

6.2.3 Catalytic activity measurements

The concentration of strong Brønsted acid sites in the aluminosilicates was evaluated from catalytic activity measurements in the hydroconversion of *n*-heptane of Pd-loaded aluminosilicates. To this end, a sieve fraction (177-420 μm) of the dried support was loaded with 0.4 wt% Pd via incipient wetness impregnation with a solution of appropriate concentration of $\text{Pd}(\text{NH}_3)_4(\text{NO}_3)_2$. The resulting materials were calcined at 573 K. Prior to testing, the catalysts were reduced at 713 K at 30 bar in flowing hydrogen. Hydroconversion of *n*-heptane was carried out at 30 bar at a H_2 /hydrocarbon ratio of 24 mol/mol. The reaction temperature was lowered from 713 K till 473 K at a rate of 0.2 K/min. The kinetics of bifunctional, aluminosilicate-catalyzed hydroconversion of *n*-alkanes is well understood [28, 29]. *n*-Heptane hydroconversion involves the dehydrogenation of *n*-heptane by the noble metal phase, isomerization or β -scission by strong Brønsted acid sites and hydrogenation of the *i*-olefins to *i*-paraffins. Meeting the requirement of sufficient hydrogenation activity is easily met if the metal loading is not too low [30]. In such case, the Brønsted-acid catalyzed conversion step of the intermediate olefins via carbenium-ion chemistry is rate limiting and the catalytic activity scales with the density of acid sites when their acidity is assumed to be constant. The activity of the catalyst is expressed as the temperature for which a hydrocarbon conversion of 40 % was achieved. Assuming first-order kinetics in the reactant hydrocarbon and a constant pre-exponential factor, we can relate the number of acid sites (N_{iso}) to the temperature required to obtain a conversion of *n*-heptane of 40 % (T_{40}) according to

$$\ln N_{\text{iso}} = C + \frac{E_{\text{act}}}{RT_{40}} \quad (3),$$

in which E_{act} (kJ mol^{-1}) is the activation energy, R ($\text{kJ mol}^{-1} \text{K}^{-1}$) the gas constant and C is a constant. The term E_{act}/RT_{40} scales with the number of active sites.

Catalytic activity measurements of methanol conversion were carried out in a quartz tubular fixed-bed reactor with 4 mm inner diameter. Firstly, the zeolites were pressed, crushed and sieved in a particle size fraction between 250 and 500 μm . Secondly, the shaped catalyst (50 mg) was placed in a reactor between two quartz-wool plugs. Prior to the reaction,

the catalyst was activated at 550 °C in artificial air (30 ml/min) for 2 h. The methanol-to-olefins reaction was performed at 400 °C. Methanol (Merck, 99%) was introduced to the reactor by flowing He through a saturator kept at 19 °C with the flow rate 30 ml/min. The weight hourly space velocity (WHSV) was kept at 6 g.g⁻¹.h⁻¹ and the effluent was analyzed online by gas chromatography (Compact GC Interscience equipped with TCD and FID detectors with RT-Q-Bond and Al₂O₃/KCl columns). The coke deposited after a reaction time of 48 h was measured by thermogravimetric analysis (TGA) on TGA/DSC 1 STAR system of Mettler Toledo. The temperature was increase to 850 °C at a rate of 5 °C/min under flowing air (50 ml/min).

6.3 Results and discussion

6.3.1 Structural properties

Fig. 6.2 depicts XRD patterns and transmission electron microscopy (TEM) images of two nanolayered ZSM-5 zeolites synthesized at 150 °C using C₂₂₋₆₋₆Br₂ and C₂₂₋₆₋₃Br₂. The Si/Al ratio in the synthesis gel was 50. Clearly, the crystallinity of these two ZSM-5 zeolites is very comparable. The patterns are also similar to those reported before by the Ryoo group [15] and by us [23] (Chapter 5). The TEM images point to formation of multilamellar ZSM-5 sheets. The sheets in the electron microscopy images of the zeolite synthesized with C₂₂₋₆₋₃Br₂ appear to be slightly better ordered than those of the zeolite sheets synthesized with C₂₂₋₆₋₆Br₂.

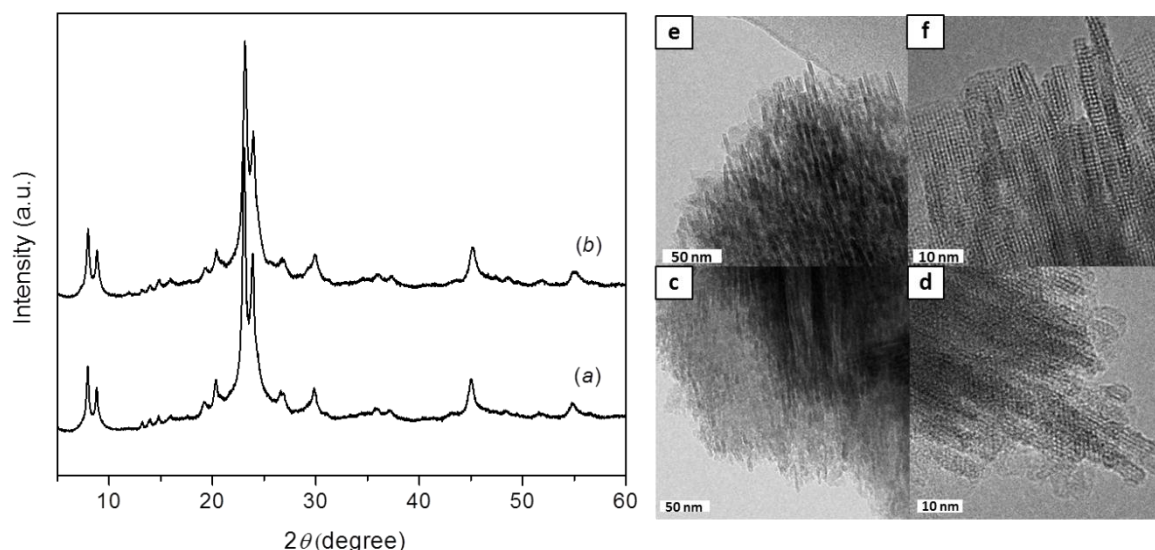


Figure 6.2: (a, b) XRD patterns and TEM images (c-f) of nanolayered ZSM-5 zeolites synthesized from a gel with Si/Al ratio of 50: (a, c, d) ZSM-5(C₂₂₋₆₋₃Br₂, 50, 150) and (b, e, f) ZSM-5(C₂₂₋₆₋₆Br₂, 50, 150).

Fig. 6.3 shows the XRD patterns of ZSM-5 zeolites with an initial gel Si/Al ratio of 20. At a hydrothermal synthesis temperature of 150 °C, it was not possible to obtain a significant amount of crystalline ZSM-5 zeolite using the C₂₂₋₆₋₆- or C₂₂₋₆₋₃-based templates in 5 days. An increase of the hydrothermal synthesis temperature to 170 °C substantially increased the crystallinity of the materials. ZSM-5(C₂₂₋₆₋₃Br₂, 20, 170) is significantly more crystalline than the zeolite prepared with C₂₂₋₆₋₆Br₂. The crystallinity of ZSM-5 crystallized in the presence of C₂₂₋₆₋₃(OH)₂ at 170 °C is similar to the zeolite crystallized with C₂₂₋₆₋₆Br₂ at the same temperature. Despite these improvements, the crystallinity of ZSM-5(C₂₂₋₆₋₃Br₂, 20, 170) is lower than those of the corresponding zeolite with a Si/Al of 50 crystallized at 150 °C.

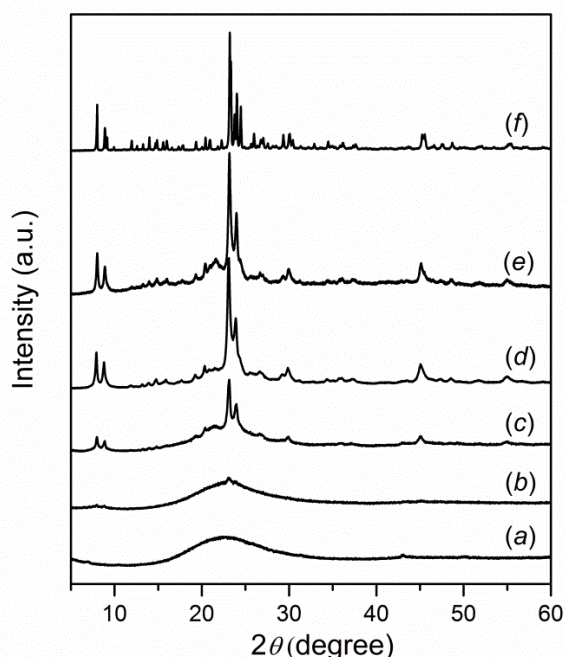


Figure 6.3: XRD patterns of (a) ZSM-5(C₂₂₋₆₋₆Br₂, 20, 150), (b) ZSM-5(C₂₂₋₆₋₃Br₂, 20, 150), (c) ZSM-5(C₂₂₋₆₋₆Br₂, 20, 170), (d) ZSM-5(C₂₂₋₆₋₃Br₂, 20, 170), (e) ZSM-5(C₂₂₋₆₋₃(OH)₂, 20, 170) and (f) bulk ZSM-5 with a Si/Al ratio of 20.

UV Raman spectra (325 nm laser excitation) of the zeolites synthesized at a Si/Al ratio of 20 are shown in Fig. 6.4. The spectrum of the bulk ZSM-5 reference zeolite shows several bands at 291, 380, 461 and 800 cm⁻¹, which are characteristic for the MFI framework [31, 32]. The most intense band around 380 cm⁻¹ is assigned to the double-five ring vibration in MFI zeolite. The weaker band at 800 cm⁻¹ is assigned to a symmetric stretching mode of the silicate framework [31, 33]. The intensity of these two bands is sensitive to the MFI crystallinity [34]. ZSM-5 zeolites synthesized at 170 °C exhibit a much stronger band at 380 cm⁻¹ than the ones synthesized at 150 °C. Another obvious difference to be noticed from Fig. 6.3 is the higher intensity of the 380 cm⁻¹ band for ZSM-5(C₂₂₋₆₋₃(OH)₂, 20, 170) and

ZSM-5($C_{22-6-3}Br_2$, 20, 170) as compared to ZSM-5($C_{22-6-6}Br_2$, 20, 170). This is consistent with the higher XRD crystallinity of the materials derived from C_{22-6-3}^{2+} . The spectra of the materials synthesized at 150 °C do not contain a clear band around 380 cm^{-1} , suggesting that the MFI structure has not been formed yet in line with their predominant amorphous nature derived from XRD.

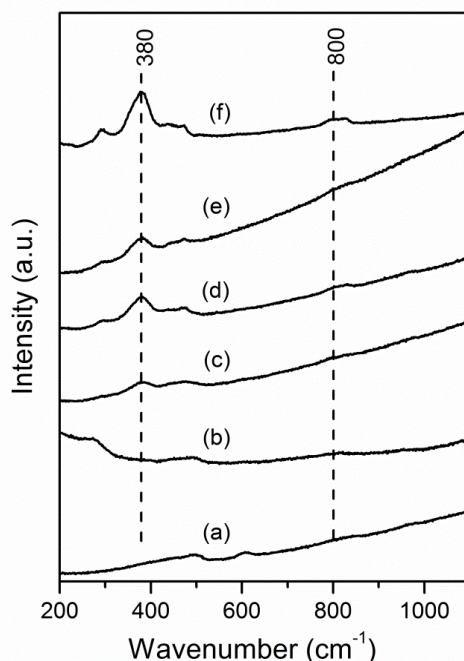


Figure 6.4: UV Raman spectra of ZSM-5($C_{22-6-6}Br_2$, 20, 150), (b) ZSM-5($C_{22-6-3}Br_2$, 20, 150), (c) ZSM-5($C_{22-6-6}Br_2$, 20, 170), (d) ZSM-5($C_{22-6-3}Br_2$, 20, 170), (e) ZSM-5($C_{22-6-3}(OH)_2$, 20, 170) and (f) bulk ZSM-5.

The electron microscopy images in Fig. 6.5 show significant differences in the morphology of the samples. The two materials synthesized at 150 °C display some ordering at the mesoscale, which is the result of the micellar properties of the amphiphilic C_{22-6-n}^{2+} templates. This clearly indicates that the crystallization process has not started yet and silica condensation predominates. It is well known that the rate of ZSM-5 crystallization increases with the Si/Al ratio. This explains the large difference in crystallinity for the ZSM-5($C_{22-6-6}Br_2$, R , 150) samples with $R = 20$ and 50. The finding that a meso-ordered silica phase forms prior to the start of crystallization is very similar to the observations made by Koekkoek et al. for an organosilane-modified Fe/ZSM-5 synthesis [32]. When the crystallization temperature is increased to 170 °C, the TEM images are dominated by nanolayers of ZSM-5. For the synthesis carried out in the presence of the Br-form of the template, the multilamellar morphology is evident both from TEM and SEM images in line with earlier reports [15, 23], whereas unilamellar nanolayers of ZSM-5 are apparent from the images for ZSM-5($C_{22-6-3}(OH)_2$, 20, 170).

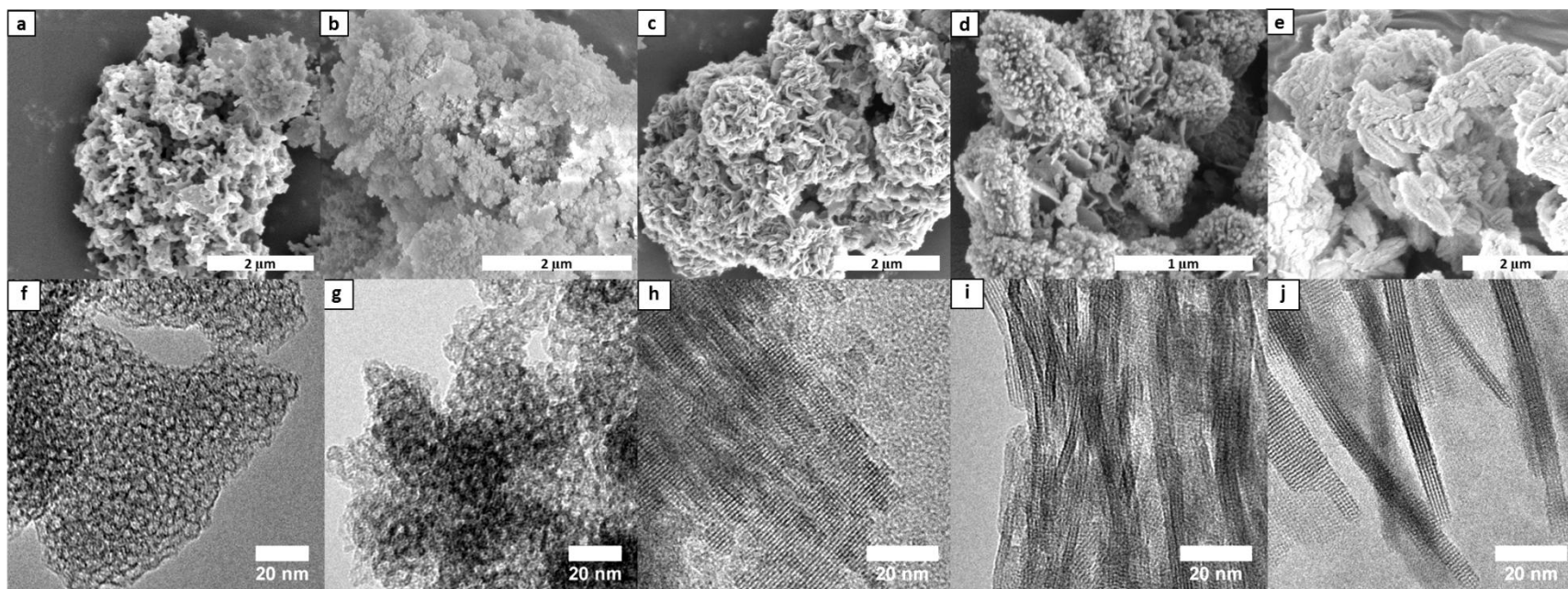


Figure 6.5: (top) SEM and (bottom) TEM images of (a,f) ZSM-5(C₂₂₋₆₋₆Br₂, 20, 150), (b,g) ZSM-5(C₂₂₋₆₋₃Br₂, 20, 150), (c, h) ZSM-5(C₂₂₋₆₋₆Br₂, 20, 170), (d, i) ZSM-5(C₂₂₋₆₋₃Br₂, 20, 170) and (e, j) ZSM-5(C₂₂₋₆₋₃(OH)₂, 20, 170).

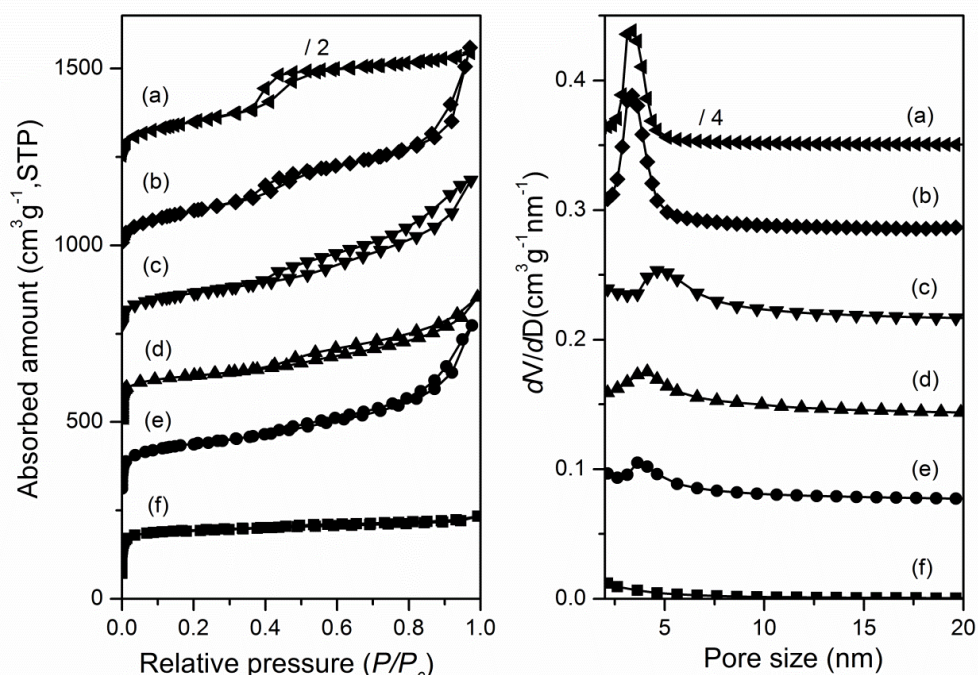


Figure 6.6: (left) Ar physisorption isotherms and (right) pore size distributions of calcined (a) ZSM-5($C_{22-6-6}Br_2$, 20, 150), (b) ZSM-5($C_{22-6-3}Br_2$, 20, 150), (c) ZSM-5($C_{22-6-6}Br_2$, 20, 170), (d) ZSM-5($C_{22-6-3}Br_2$, 20, 170), (e) ZSM-5($C_{22-6-3}(OH)_2$, 20, 170), and (f) bulk ZSM-5. The isotherms were vertically offset by equal intervals of $250 \text{ cm}^3 \text{ g}^{-1}$. The pore size distributions were calculated via BJH algorithm using the adsorption branch and vertically offset by equal intervals of $0.07 \text{ cm}^3 \text{ g}^{-1} \text{ nm}^{-1}$.

Table 6.2: Textural properties of ZSM-5 zeolites as determined by Ar physisorption.

Sample	S_{BET}^a ($\text{m}^2 \cdot \text{g}^{-1}$)	V_{tot}^b ($\text{cm}^3 \cdot \text{g}^{-1}$)	V_{meso}^c ($\text{cm}^3 \cdot \text{g}^{-1}$)	V_{micro}^d ($\text{cm}^3 \cdot \text{g}^{-1}$)	V_{super}^e ($\text{cm}^3 \cdot \text{g}^{-1}$)	S_{micro}^f ($\text{m}^2 \cdot \text{g}^{-1}$)	S_{ext}^g ($\text{m}^2 \cdot \text{g}^{-1}$)
ZSM-5($C_{22-6-6}Br_2$, 50, 150)	506	0.80	0.63	0.10	0	n.d.	n.d.
ZSM-5($C_{22-6-3}Br_2$, 50, 150)	527	0.80	0.65	0.10	0.04	n.d.	n.d.
ZSM-5($C_{22-6-6}Br_2$, 20, 150)	685	0.75	0.66	0	0.07	0	826
ZSM-5($C_{22-6-3}Br_2$, 20, 150)	342	0.72	0.67	0.01	0	0	429
ZSM-5($C_{22-6-6}Br_2$, 20, 170)	370	0.56	0.48	0.05	0.01	57	313
ZSM-5($C_{22-6-3}Br_2$, 20, 170)	415	0.48	0.37	0.12	0.04	177	261
ZSM-5($C_{22-6-3}(OH)_2$, 20, 170)	572	0.67	0.50	0.12	0.05	279	292
ZSM-5(20)	373	0.21	0.06	0.12	0.06	281	91

^a Brunauer-Emmett-Teller (BET) surface area ($p/p_0 = 0.1-0.3$); ^b total pore volume at $p/p_0 = 0.97$; ^c mesopore volume calculated by BJH method; ^d V_{micro} and ^e V_{super} are the micropore and supermicropore volumes from 0-0.50 nm and 0.50-2.0 nm, respectively, calculated from NLDFT (Ar at 87 K on oxides as the model, assuming cylindrical pores, without regularization); ^f micropore surface area calculated by the t -plot method; ^g external surface area calculated by t -plot method.

The Ar physisorption isotherms and pore size distributions (PSDs) of all materials are shown in Fig. 6.6. The textural properties are collected in Table 6.2. The isotherms of the zeolites synthesized at a Si/Al ratio of 50 are not shown. The isotherm of the reference bulk

ZSM-5 is of type I, consistent with its microporous nature. The isotherms of ZSM-5 ($C_{22-6-6}Br_2$, 20, 150) and ZSM-5($C_{22-6-3}Br_2$, 20, 150) are of type IV, consistent with the predominance of mesopores. The order at the mesoscale is evident from the PSD, which points to quite uniform mesopores with a size of ~ 3 nm. The t -plot analysis did not provide evidence for microporosity in ZSM-5($C_{22-6-6}Br_2$, 20, 150) and gave a micropore volume of $0.01 \text{ cm}^3 \cdot \text{g}^{-1}$ for ZSM-5($C_{22-6-3}Br_2$, 20, 150). From the isotherms of the zeolites synthesized at 170°C , it follows that both micro- and mesopores are present. The micropore volume of ZSM-5($C_{22-6-6}Br_2$, 20, 170) is substantially lower ($0.05 \text{ cm}^3 \cdot \text{g}^{-1}$) than the micropore volumes of the zeolites synthesized with C_{22-6-6}^{2+} under otherwise identical conditions. This difference together with the relatively large pore volume suggests that ZSM-5($C_{22-6-6}Br_2$, 20, 170) contains some amorphous silica material. From the comparable micropore volumes of ZSM-5($C_{22-6-3}Br_2$, 20, 170), ZSM-5($C_{22-6-3}(OH)_2$, 20, 170) and bulk ZSM-5, we infer that the nanolayered zeolites contain little amorphous silica material. The mesopore volume of the unilamellar zeolite is higher than that of the multilamellar one, consistent with earlier reports.

One-dimensional ^1H MAS NMR spectra of ZSM-5($C_{22-6-3}Br_2$, 20, 170) and ZSM-5($C_{22-6-6}Br_2$, 20, 170) are dominated by the narrow signal of CH_2 moieties in the C_{22} tails of the template molecules (Fig. 6.7a). In addition, a small narrow signal from the C_{22} methyl moieties is visible at 0.9 ppm, as well as a broader minor signal at 2.2 ppm, assigned to the C_{22} CH_2 moiety at the β position with respect to the nearest N atom. The relatively small widths of these three resonances are consistent with high mobility of the C_{22} tails at the NMR measurement temperature of 60°C . At large magnification, the broad signal of the $\text{N-CH}_{2,3}$ protons shows up at 3.2 ppm (Fig. 6.7b). Its linewidth indicates that the N centers of the template molecules are strongly immobilized. To probe which parts of the template molecules are actually embedded within the MFI nanolayers, two-dimensional $^{29}\text{Si}\{^1\text{H}\}$ HETCOR was carried out (Fig. 6.7d). This dipole-coupling based NMR technique shows the correlations of ^{29}Si and ^1H spins that are close together in space ($< 5 \text{ \AA}$).

In comparison to the 1D ^1H MAS NMR spectra (Fig. 6.7a), the $\text{N-CH}_{2,3}$ signal at 3.2 ppm contributes relatively strongly to the ^1H NMR projections (Fig. 6.7c) of the 2D HETCOR spectra. The other broad signal at 1 ppm in the ^1H NMR projection can result from immobilized CH_2 moieties in the C_6 and C_3 fragments of the template molecules. Both observations confirm that the ammonium centers are located inside aluminosilicate structures formed. Closer inspection of the 2D spectra allows rough differentiation between Si atoms with different coordination along the (direct) ^{29}Si NMR frequency axis (drawn vertically in

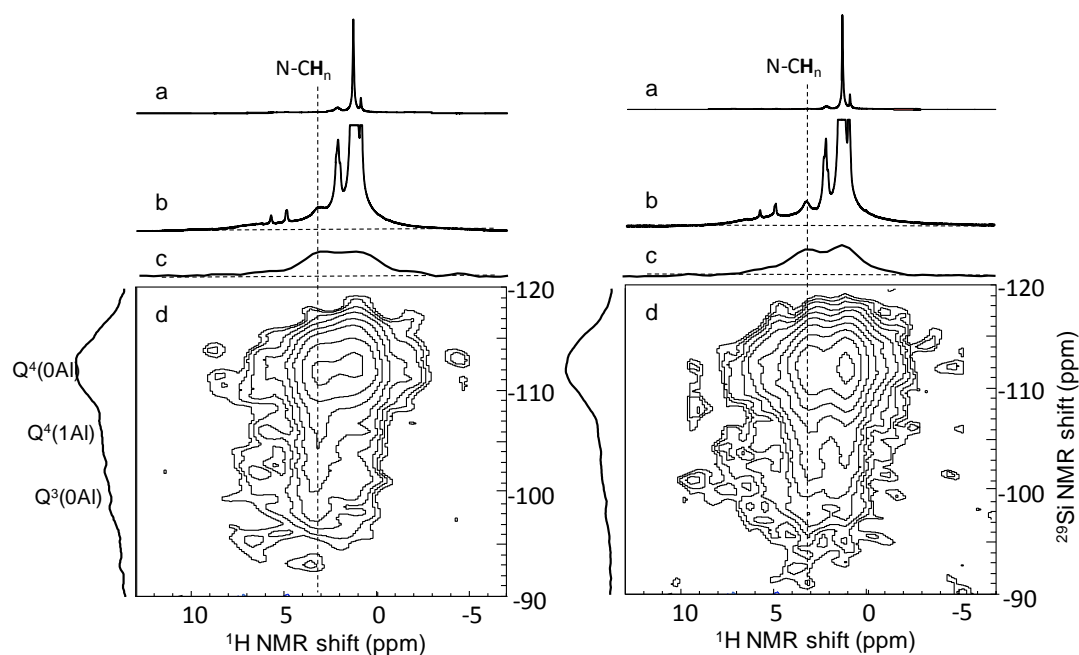


Figure 6.7: ^1H MAS NMR and $^{29}\text{Si}\{-^1\text{H}\}$ HETCOR of (left) ZSM-5($\text{C}_{22-6-3}\text{Br}_2$, 20, 170) and (right) ZSM-5($\text{C}_{22-6-6}\text{Br}_2$, 20, 170). (a) ^1H NMR spectra, (b) magnified ^1H NMR spectra; (c) ^1H NMR projection spectra of (d) the 2D HETCOR spectra. ^{29}Si NMR projection spectra are plotted along the direct frequency axis, plotted here in vertical direction. Positions of the overlapping signals of differently coordinated Si atoms are indicated along the ^{29}Si NMR projection spectrum. (10 kHz MAS; 60 °C NMR measuring temperature).

Fig. 6.7d): $\text{Q}^4(0\text{Si}) = \text{Si}(\text{OSi})_4$ at -112 ppm, $\text{Q}^4(1\text{Al}) = \text{Si}(\text{OSi})_3(\text{OAl})$ at -107 ppm, and $\text{Q}^3(0\text{Al}) = \text{Si}(\text{OSi})_3\text{OH}$ at -102 ppm. The detailed 2D NMR lineshapes in Fig. 6.7d suggest that the N centers of the template molecules tend to be located close to the $\text{Q}^4(1\text{Al})$ silicon positions in the aluminosilicate lattice. This makes sense because of the negative charge associated with local Al substitutions into the silicate lattice. There are only two minor differences in the corresponding 1D ^1H NMR and 2D HETCOR spectra of ZSM-5($\text{C}_{22-6-3}\text{Br}_2$, 20, 170) and ZSM-5($\text{C}_{22-6-6}\text{Br}_2$, 20, 170). Firstly, for ZSM-5($\text{C}_{22-6-3}\text{Br}_2$, 20, 170), the $\text{Q}^4(1\text{Al})$ signal appears to be slightly more emphasized both in the 2D HETCOR spectrum and its ^1H NMR projection. A possible explanation is that the N centers of the template molecules with C_3 termini are less hindered to be localized close to the Al positions in the aluminosilicate structures, than template molecules with C_6 termini. Secondly, whereas the linewidth of the 3.2 ppm signal of the $\text{N-CH}_{2,3}$ moieties in ZSM-5($\text{C}_{22-6-3}\text{Br}_2$, 20, 170) (Fig. 6.7b, left) is closely similar to that in the ^1H NMR projection of the HETCOR spectrum (Fig. 6.7c, left), the resonance of the corresponding ^1H NMR signal of ZSM-5($\text{C}_{22-6-6}\text{Br}_2$, 20, 170) (Fig. 6.7b, right) is narrower than in the ^1H NMR projection (Fig. 6.7c, right). This suggests that the N centers of the template molecules in ZSM-5($\text{C}_{22-6-3}\text{Br}_2$, 20, 170) are completely and rigidly encapsulated within the aluminosilicate nanolayers, whereas the template N centers in

ZSM-5($C_{22-6-6}Br_2$, 20, 170) appear to be less perfectly embedded, at least at the relatively high Al content employed here. The less perfect structure of ZSM-5($C_{22-6-6}Br_2$, 20, 170) is consistent with its lower crystallinity reflected by XRD.

6.3.2 Acidity characterization

Fig. 6.8 shows ^{27}Al NMR spectra before and after ammonia adsorption. The spectra of the aluminosilicates are dominated by a signal around 55 ppm due to tetrahedrally coordinated framework Al (FAI) and a weaker one around 0 ppm due to octahedrally coordinated extraframework Al (EFAI). The concentrations of the respective species are obtained by integration of the corresponding spectral features and are given in Table 6.3. The amorphous aluminosilicates (Fig. 6.8a, b) contain a larger proportion of octahedral Al than the crystalline ones (Fig. 6.8c-e). Ammonia treatment results in a significant increase of the tetrahedral Al signal at the expense of the octahedral signal for ZSM-5($C_{22-6-6}Br_2$, 20, 150). It can be seen that the total resonant area increases, which implies that some initially, likely tetrahedral Al species become visible. The flexibility of the Al coordination is typically observed for Al species that are not bound into a segregated alumina or amorphous silica-alumina phase [30, 35-37].

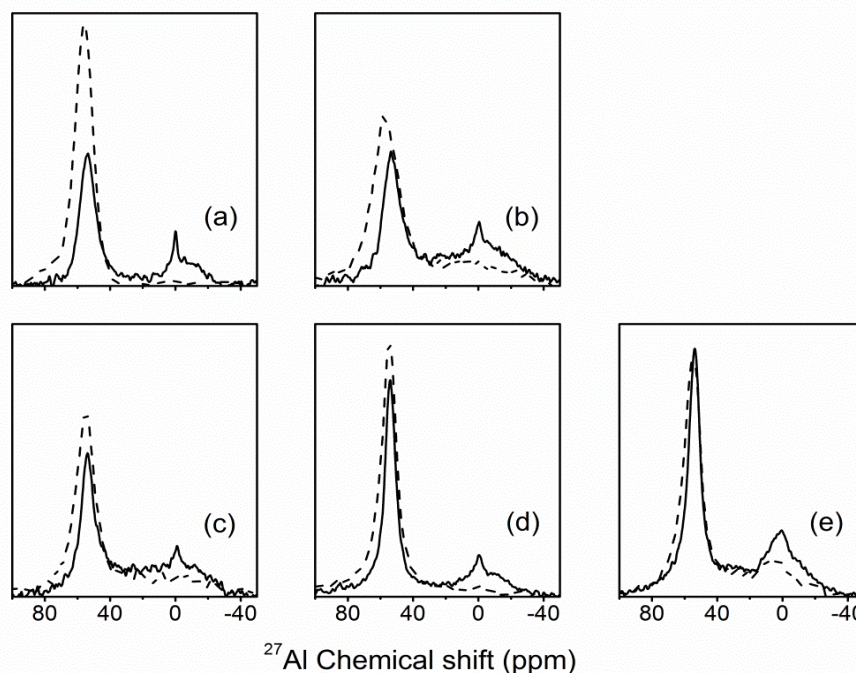


Figure 6.8: ^{27}Al MAS NMR spectra before (solid line) and after ammonia exposure (dashed line) of (a) ZSM-5($C_{22-6-6}Br_2$, 20, 150), (b) ZSM-5($C_{22-6-3}Br_2$, 20, 150), (c) ZSM-5($C_{22-6-6}Br_2$, 20, 170), (d) ZSM-5($C_{22-6-3}Br_2$, 20, 170) and (e) ZSM-5($C_{22-6-3}(OH)_2$, 20, 170).

Table 6.3: The Si/Al ratio, the concentration of Al ([Al]), framework Al ([FAI]) and extraframework Al ([EFAI]) in nanolayered and bulk ZSM-5 zeolites as determined from ICP and ^{27}Al NMR, compared to the concentration of Brønsted Acid Sites ([BAS]), Lewis Acid Sites ([LAS]) and external Brønsted acid sites ([extBAS]) from IR measurements of adsorbed pyridine and 2,4,6-collidine.

Sample	Si/Al ratio ^a	[Al] ^a (mmol g ⁻¹)	^{27}Al NMR			Pyridine IR		collidine IR
			[FAI] ^b (mmol g ⁻¹)	[EFAI] ^c (mmol g ⁻¹)	[FAI] _{NH₃} ^d (mmol g ⁻¹)	[BAS] ^e (mmol g ⁻¹)	[LAS] ^e (mmol g ⁻¹)	[extBAS] ^e (mmol g ⁻¹)
ZSM-5(C ₂₂₋₆₋₆ Br ₂ , 50, 150)	45	0.36	0.24	0.13	0.38	0.20	0.09	0.06
ZSM-5(C ₂₂₋₆₋₆ Br ₂ , 20, 150)	20	0.79	0.18	0.09	0.40	n.d. ^f	n.d. ^f	n.d. ^f
ZSM-5(C ₂₂₋₆₋₃ Br ₂ , 20, 150)	18	0.88	0.23	0.20	0.39	0.10	0.16	0.13
ZSM-5(C ₂₂₋₆₋₆ Br ₂ , 20, 170)	23	0.69	0.22	0.16	0.33	0.15	0.12	0.10
ZSM-5(C ₂₂₋₆₋₃ Br ₂ , 20, 170)	27	0.60	0.25	0.10	0.38	0.28	0.16	0.05
ZSM-5(C ₂₂₋₆₋₃ (OH) ₂ , 20, 170)	20	0.79	0.33	0.19	0.39	0.16	0.14	0.05
ZSM-5(20)	19.4	0.83	0.56	0.07	n.d. ^f	0.81	0.05	0.01
ZSM-5(27)	27	0.60	0.51	0.09	0.60	0.53	0.11	0.02

^a determined by ICP analysis; ^b NMR peak area integrated from 100 to 30 ppm; ^c NMR peak area integrated from 30 to -50 ppm; ^d based on ^{27}Al NMR spectra of dehydrated zeolites after NH₃ adsorption; ^e determined after evacuation at 150 °C; ^f not determined.

It is indicative of its high dispersion close to a silica network [30]. The observation that these changes are less pronounced for ZSM-5($C_{22-6-3}Br_2$, 20, 150) indicates that part of the Al may have segregated into an aluminium oxide phase in this sample. Indeed, after ammonia adsorption on ZSM-5($C_{22-6-6}Br_2$, 20, 150), the octahedral signal has nearly vanished. Although the changes are less drastic for the three crystalline zeolites, in all three samples a decrease of the octahedral signal is observed together with an increase of the tetrahedral signal. In all these zeolites, part of the Al remains in octahedral coordination, suggesting that some Al has segregated into a separate phase. Before ammonia adsorption, more than 43% aluminum species are tetrahedral coordinated.

Fig. 6.9 and 6.10 display the FTIR spectra of dehydrated zeolites with CO adsorption in hydroxyl stretch region and in carbonyl stretch regions, respectively. Except for the two zeolites crystallized at 150 °C, all zeolites show a perturbed OH band around approximately 3310 cm^{-1} with a shoulder around 3415 cm^{-1} . The strong band around 3310 cm^{-1} is characteristic for strongly acidic bridging hydroxyl groups perturbed by CO. They are associated with the negative feature of the unperturbed bridging OH groups around 3610 cm^{-1} , which is evident in Fig. 6.9c-f. The red shift of $\sim 300\text{ cm}^{-1}$ implies that the acid sites are similar in strength for these materials. The band around 3415 cm^{-1} appearing at higher CO coverage represents sites of lower acidity, consistent with their lower red shift upon CO perturbation. This band is most likely due to the presence of amorphous silica-alumina [23, 38]. The feature around 3415 cm^{-1} is strongest for the two ZSM-5($C_{22-6-n}Br_2$, 20, 150) samples, consistent with the predominant amorphous nature of these materials. The Brønsted acid sites in these materials are much weaker than the bridging hydroxyl groups of crystalline ZSM-5 as follows from their much lower red shift of 200 cm^{-1} . In the carbonyl stretching region, bands at 2175 cm^{-1} and 2138 cm^{-1} belongs to CO adsorption on strong Brønsted acidic sites and physisorbed CO, respectively. Compared to ZSM-5, the concentration of Brønsted acidic sites of ZSM-5($C_{22-6-6}Br_2$, 20, 170), ZSM-5($C_{22-6-3}Br_2$, 20, 170) and ZSM-5($C_{22-6-3}(OH)_2$, 20, 170) is lower.

The trends for the bands at 3304 and 2175 cm^{-1} are similar. From this, it follows that the acidity decreases in the order bulk HZSM-5 > ZSM-5($C_{22-6-3}Br_2$, 20, 170) > ZSM-5($C_{22-6-3}(OH)_2$, 20, 170) > ZSM-5($C_{22-6-6}Br_2$, 20, 170). The two amorphous materials exhibit a clear band at 2174 cm^{-1} , emphasizing further that this band should not be used exclusively as an indicator of strong Brønsted acidity. Importantly, all the three zeolites crystallized at 170 °C contain a band at 2230 cm^{-1} , which points to the presence of strong Lewis acidic sites. This band is absent for bulk HZSM-5. This difference indicates that part

of the Al ions are present as highlight dispersed extraframework Al species, possibly at cation-exchange positions.

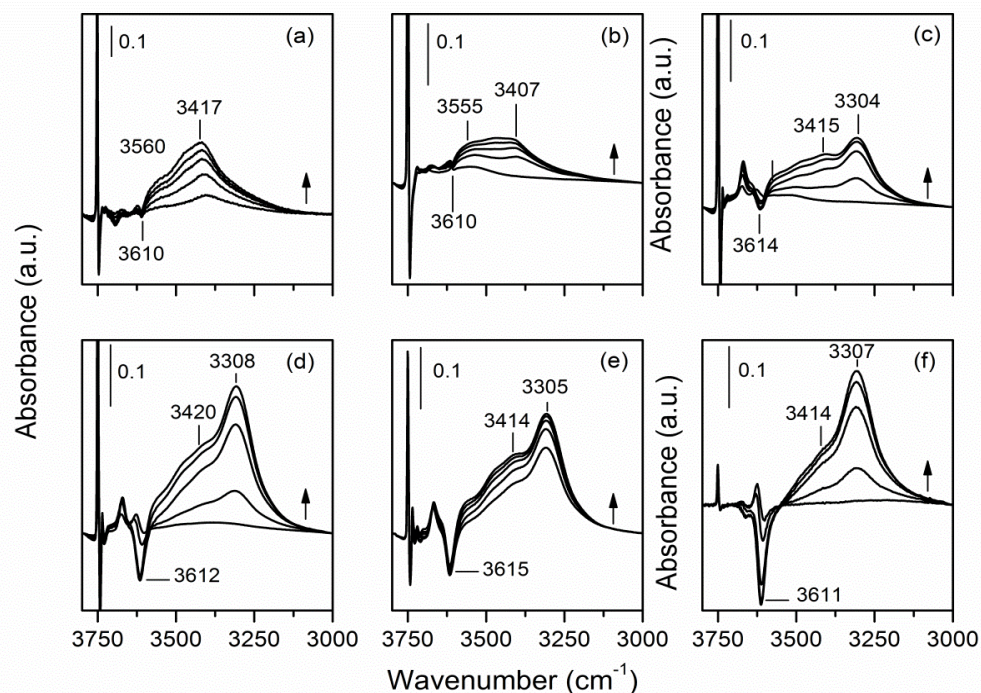


Figure 6.9: Hydroxyl stretch regions of FTIR spectra of (a) ZSM-5($C_{22-6-6}Br_2$, 20, 150), (b) ZSM-5($C_{22-6-3}Br_2$, 20, 150), (c) ZSM-5($C_{22-6-6}Br_2$, 20, 170), (d) ZSM-5($C_{22-6-3}Br_2$, 20, 170), (e) ZSM-5($C_{22-6-3}(OH)_2$, 20, 170), and (f) bulk ZSM-5 at 80 K as a function of the CO coverage. (The spectra normalized by weight and referenced to spectrum of dehydrated zeolite).

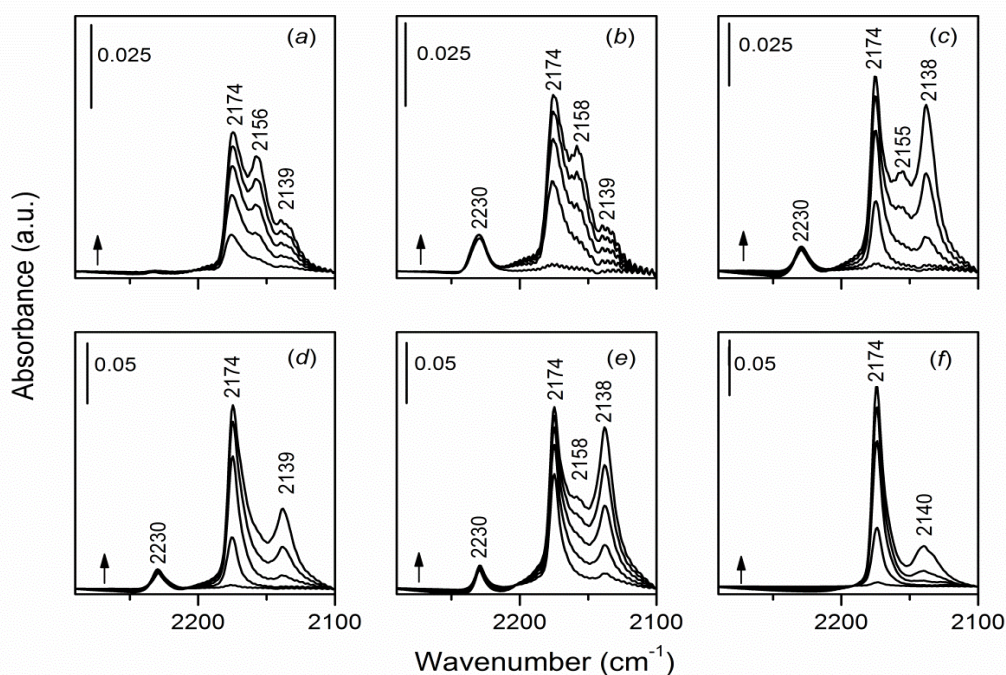


Figure 6.10: CO stretch regions of FTIR spectra of (a) ZSM-5($C_{22-6-6}Br_2$, 20, 150), (b) ZSM-5($C_{22-6-3}Br_2$, 20, 150), (c) ZSM-5($C_{22-6-6}Br_2$, 20, 170), (d) ZSM-5($C_{22-6-3}Br_2$, 20, 170), (e) ZSM-5($C_{22-6-3}(OH)_2$, 20, 170), and (f) bulk ZSM-5 at 80 K as a function of the CO coverage. (The spectra normalized by weight and referenced to spectrum of dehydrated zeolite).

Fig. 6.11(top) shows the FTIR spectra of adsorbed pyridine after evacuation at 150, 300 and 500 °C. Table 6.4 lists the concentration of Brønsted and Lewis acid sites as a function of the evacuation temperature. Pyridine adsorption on nanolayered ZSM-5 zeolite has been discussed in detail in our previous work ([23], Chapter 5). The IR bands at 1545 and 1455 cm^{-1} after pyridine adsorption are assigned to pyridine associated with Brønsted and Lewis acid sites, respectively.

Table 6.4: Concentration of Brønsted and Lewis acid sites determined by IR spectra of adsorbed pyridine.

Sample	[BAS]-150 (mmol/g) ¹	[BAS]-300 (mmol/g) ²	[BAS]-500 (mmol/g) ³	[LAS]-150 (mmol/g) ¹	[LAS]-300 (mmol/g) ²	[LAS]-500 (mmol/g) ³
ZSM-5(C ₂₂₋₆₋₃ Br ₂ , 20, 150)	0.10	0.04	0	0.16	0.12	0.07
ZSM-5(C ₂₂₋₆₋₆ Br ₂ , 20, 170)	0.15	0.11	0.06	0.12	0.09	0.08
ZSM-5(C ₂₂₋₆₋₃ Br ₂ , 20, 170)	0.28	0.23	0.13	0.16	0.11	0.07
ZSM-5(C ₂₂₋₆₋₃ (OH) ₂ , 20, 170)	0.16	0.11	0.06	0.14	0.08	0.05
ZSM-5(20)	0.81	0.78	0.46	0.05	0.03	0.02

¹ determined after evacuation at 150 °C; ² determined after evacuation at 300 °C; ³ determined after evacuation at 500 °C.

Clearly, all nanolayered zeolites have a significantly lower density of Brønsted acid sites than their bulk counterpart, despite nearly similar bulk Al content. The trend in Brønsted acidity is consistent with the CO_{ads} IR results. The higher crystallinity of the C₂₂₋₆₋₃Br₂-templated zeolites vs. the C₂₂₋₆₋₆Br₂-templated one goes together with a higher concentration of Brønsted acid sites. ZSM-5(C₂₂₋₆₋₃(OH)₂, 20, 170) has a lower Brønsted acidity than its C₂₂₋₆₋₃Br₂-templated counterpart. It is also seen from Table 6.4 that the nanolayered ZSM-5 zeolites contain more Lewis acid sites than the bulk reference, which should be due to a high portion of Al being at extraframework positions in the former samples.

The presence of Brønsted acid sites on the external zeolite surface (including the mesopore surface area of the nanolayered zeolites) has been probed by IR spectroscopy of adsorbed 2, 4, 6-collidine. The respective IR spectra are also given in Fig 6.11 and quantitative results are summarized in Table 6.5. The peak at 1637 cm^{-1} , due to coordination of the probe to Brønsted acid sites, is used to determine the concentration of external acid sites. The concentration of external Brønsted acid sites for the bulk zeolite is negligible. The nanolayered zeolites exhibit a higher concentration of external Brønsted acid sites. Notably, the largely amorphous ZSM-5(C₂₂₋₆₋₃Br₂, 20, 150) contains a reasonable amount of Brønsted acid

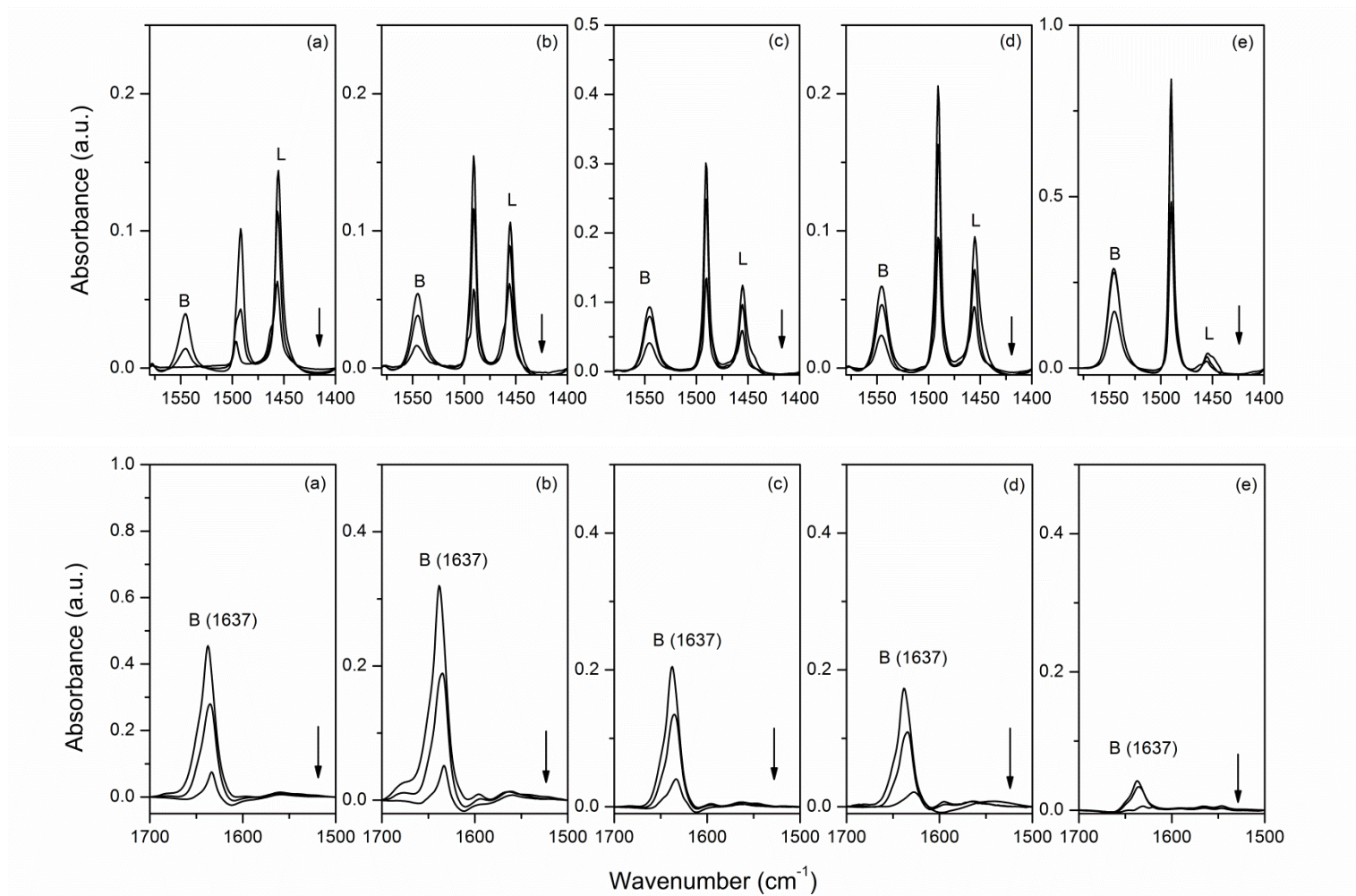


Figure 6.11: IR spectra of (top) pyridine and (bottom) 2,4,6-collidine adsorbed on (a) ZSM-5($C_{22-6-3}Br_2$, 20, 150), (b) ZSM-5($C_{22-6-6}Br_2$, 20, 170), (c) ZSM-5($C_{22-6-3}Br_2$, 20, 170), (d) ZSM-5($C_{22-6-3}(OH)_2$, 20, 170), and (e) bulk ZSM-5 after evacuation at 150, 300 and 500 °C (arrow indicates increasing temperature).

sites, suggesting that its mesopore surface contains a significant number of bridging hydroxyl groups. For purposes of comparison, the values of Brønsted acid sites probed by pyridine and 2,4,6-collidine after evacuation at 150 °C are also given in Table 6.3

Table 6.5: Concentration of external Brønsted acid sites (extBAS) determined by IR spectra of adsorbed 2, 4, 6-collidine.

Sample	[extBAS]-150 (mmol/g) ¹	[extBAS]-300 (mmol/g) ²	[extBAS]-500 (mmol/g) ³
ZSM-5(C ₂₂₋₆₋₃ Br ₂ , 20, 150)	0.13	0.07	0.01
ZSM-5(C ₂₂₋₆₋₆ Br ₂ , 20, 170)	0.10	0.05	0.01
ZSM-5(C ₂₂₋₆₋₃ Br ₂ , 20, 170)	0.05	0.03	0.01
ZSM-5(C ₂₂₋₆₋₃ (OH) ₂ , 20, 170)	0.05	0.03	0.01
ZSM-5(20)	0.01	0.01	0

¹ determined after evacuation at 150 °C; ² determined after evacuation at 300 °C; ³ determined after evacuation at 500 °C.

Summarizing, the acidity characterization clearly shows that the nanolayered zeolites synthesized at 150 °C with a gel Si/Al ratio of 20 contain very few Brønsted acid sites of zeolitic strength. This is most likely due to their amorphous nature as followed from XRD. The absence of strong Brønsted acid sites in these materials follows from the absence of a strongly perturbed band around 3300 cm⁻¹ in the IR spectrum upon CO adsorption. Care should be taken with interpretation of CO_{ads} IR data, since in the perturbed CO spectrum a band around 2174 cm⁻¹ is observed. This band likely relates to CO perturbing hydroxyl groups of weaker acidity. IR spectroscopy of adsorbed pyridine also probes these non-zeolitic Brønsted acid sites, suggesting that this technique should be used with great care in amorphous aluminosilicas. The lower acidity of these hydroxyl groups follows from the erosion of the band due to the pyridinium-ion after evacuation at 500 °C. The nanolayered zeolites crystallized at 170 °C with a gel Si/Al ratio of 20 show significant strong Brønsted acidity, similar in strength to a bulk HZSM-5 zeolite. However, the concentration of such sites is much lower for all three nanolayered zeolites. In contrast to bulk HZSM-5, they contain an appreciable amount of Lewis acid sites, most likely present in highly dispersed form (CO_{ads} IR). The relatively low concentration of Brønsted acid sites likely has two causes. Firstly, the use of diquaternary ammonium-type structure directing agents in the crystallization of ZSM-5 at a Si/Al ratio of 20 does not result in efficient insertion of Al³⁺ in the framework. The reason is that the crystallization decreases with increasing Al content [ref needed]. Consequently, the framework Si/Al ratio will be higher than the gel Si/Al ratio. The

results in Table 6.3 ([FAI] content vs. [Al] content) are consistent with this view. The second cause is related to the first one: the EFAl ions may act as charge-compensating species for the negative charge induced by the Al framework substitutions. Such sites will impart Lewis instead of Brønsted acidity to the final zeolite. However this may be, the proposed approach to use of $C_{22-6-3}Br_2$ instead of $C_{22-6-6}Br_2$ results in increased zeolite crystallinity and increased Brønsted acid site density. When $C_{22-6-3}(OH)_2$ is used as the template, the acidity is somewhat lower, but this seems to be mainly due to the increased density of EFAl species.

6.3.3 Catalytic activity measurements

Table 6.6 shows the catalytic activities of Pd-loaded ZSM-5 zeolites for the hydroconversion of *n*-heptane. Assuming uniform strength of the strong acid sites involved in the isomerization of alkene intermediates and the Brønsted acid-catalyzed isomerization being rate-limiting [30], the relative density of Brønsted acid sites (N_{BAS}) is compared on the basis of the temperature to reach a reactant conversion of 40 %. Under these conditions, the dominant products from *n*-heptane are monobranched isomers, mainly 2-methylhexane and 3-methylhexane. Compared to bulk HZSM-5 reference, all nanolayered zeolites contain less Brønsted acid sites. The two zeolites synthesized at 150 °C, ZSM-5($C_{22-6-6}Br_2$, 50, 150) and ZSM-5($C_{22-6-3}Br_2$, 50, 150), have comparable acidity, which is lower than that of HZSM-5, mainly due to the lower Al content. Nevertheless, it can already be seen that the activity is lower than is to be expected on the basis of the Al content, stressing again that also at Si/Al = 50 not all Al atoms give rise to strong Brønsted acid sites. When the Al content is increased to Si/Al = 20 in ZSM-5($C_{22-6-3}Br_2$, 20, 150), the activity in alkane hydroconversion is very low. This result is consistent with its amorphous nature and the absence of Brønsted acid sites that are of zeolitic strength and strong enough to isomerize the alkene intermediates. When the crystallization is done at 170 °C, the materials become crystalline and significant Brønsted acidity is imparted. The catalytic performance of ZSM-5($C_{22-6-3}Br_2$, 20, 170) is substantially higher than that of ZSM-5($C_{22-6-6}Br_2$, 20, 170). ZSM-5($C_{22-6-3}(OH)_2$, 20, 170) exhibits intermediate acidity. The trends in the acidity of the three nanolayered zeolites synthesized at 170 °C cohere with those from the acidity characterization.

Fig. 6.12 shows the methanol conversion as a function of the reaction time for bulk and nanolayered ZSM-5 zeolites. For the determination of conversion and selectivity, dimethyl ether (DME) is considered as an unconverted species. Further details about the production distribution after 1 h time on stream and the coke content as determined by TGA analysis of spent samples are listed in Table 6.7. Bulk HZSM-5 zeolite initially nearly completely

Table 6.6: Catalytic activities of *n*-heptane hydroconversion of Pd-loaded ZSM-5 zeolites (N_{iso} is proportional to the number of Brønsted acid sites and defined as unity for ZSM-5(20)).

Sample	Si/Al ratio	[Al] (mmol g ⁻¹)	T_{40} (K)	E_{act} (kJ/mol)	N_{BAS}
ZSM-5(C ₂₂₋₆₋₆ Br ₂ , 50, 150)	45	0.36	517	165	0.27
ZSM-5(C ₂₂₋₆₋₃ Br ₂ , 50, 150)	46	0.35	522	170	0.19
ZSM-5(C ₂₂₋₆₋₃ Br ₂ , 20, 150)	18	0.88	631	136	0.001
ZSM-5(C ₂₂₋₆₋₆ Br ₂ , 20, 170)	23	0.69	536	174	0.06
ZSM-5(C ₂₂₋₆₋₃ Br ₂ , 20, 170)	27	0.60	508	163	0.54
ZSM-5(C ₂₂₋₆₋₃ (OH) ₂ , 20, 170)	20	0.83	517	171	0.27
ZSM-5(20)	19.4	0.83	498	140	1

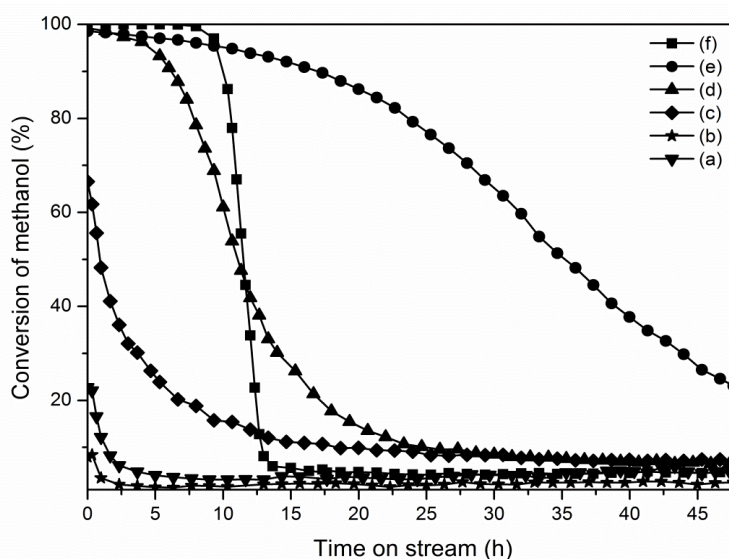


Figure 6.12: Methanol conversion of (a) ZSM-5(C₂₂₋₆₋₆Br₂, 20, 150), (b) ZSM-5(C₂₂₋₆₋₃Br₂, 20, 150), (c) ZSM-5(C₂₂₋₆₋₆Br₂, 20, 170), (d) ZSM-5(C₂₂₋₆₋₃Br₂, 20, 170), (e) ZSM-5(C₂₂₋₆₋₃(OH)₂, 20, 170), and (f) bulk ZSM-5.

converts methanol to products with at least one carbon-carbon bond. The product mixture containing ethylene, propylene and a significant number of longer products is typical for methanol conversion over ZSM-5 zeolite [39]. This zeolite starts to deactivate after about 10 h on stream and the lifetime defined as the time at which the methanol conversion is 50 % is 11 h. The initial methanol conversion of ZSM-5(C₂₂₋₆₋₃Br₂, 20, 170) and ZSM-5(C₂₂₋₆₋₃(OH)₂, 20, 170) is also close to 100%. Deactivation of ZSM-5(C₂₂₋₆₋₃Br₂, 20, 170) is more pronounced than for ZSM-5(C₂₂₋₆₋₃(OH)₂, 20, 170). This difference is consistent with our earlier findings for uni- and lamellar nanolayered ZSM-5 zeolites [23] (Chapter 5). Note that the lifetimes of these three zeolites are substantially shorter than their counterparts with a higher Si/Al ratio. The significantly lower acidity of ZSM-5(C₂₂₋₆₋₆Br₂, 20, 170), which was also apparent from alkane hydroconversion, results in partial conversion of methanol already at the start of the reaction. Comparison of the product mixtures of the three nanolayered

Table 6.7: Lifetime, product distribution, and coke content of nanosheets MFI zeolite catalysts for the MTO reaction (WHSV = 6 g.g⁻¹.h⁻¹; T = 400 °C) after 1 h time on stream.

Zeolite	TON _{product} ^a	TON _{total} ^b	Lifetime ^c (h)	C ₁ (%)	C ₂ ⁼ (%)	C ₂ ⁻ (%)	C ₃ ⁼ (%)	C ₃ ⁻ (%)	C ₄ (%)	C ₅₊ (%)	Coke Content (%) ^d
ZSM-5(C ₂₂₋₆₋₆ Br ₂ , 20, 150)	n.d. ^e	n.d.	n.d.	n.d.	n.d.	n.d.	n.d.	n.d.	n.d.	n.d.	11
ZSM-5(C ₂₂₋₆₋₃ Br ₂ , 20, 150)	2.0 × 10 ³	3.4 × 10 ⁴	n.d.	n.d.	n.d.	n.d.	n.d.	n.d.	n.d.	n.d.	8
ZSM-5(C ₂₂₋₆₋₆ Br ₂ , 20, 170)	7.4 × 10 ³	4.7 × 10 ⁴	1	1.4	2.8	0.1	38.8	0.6	39.6	18.4	5
ZSM-5(C ₂₂₋₆₋₃ Br ₂ , 20, 170)	9.0 × 10 ³	2.7 × 10 ⁴	11	1.6	7.7	0.1	33.6	2.6	42.3	13.5	11
ZSM-5(C ₂₂₋₆₋₃ (OH) ₂ , 20, 170)	>4.1 × 10 ⁴	>5.1 × 10 ⁴	35	0.4	4.6	0.1	37.5	1.7	39.8	19.7	5
ZSM-5	3.0 × 10 ³	8.9 × 10 ³	11	0.7	14.8	0.2	26.7	7.2	40.1	15.6	10

^a turnover number: number of moles of methanol converted into products other than dimethyl ether in 48 h per BAS; the concentration of BAS is the value from pyridine IR after evacuation at 150 °C; ^b turnover number: number of moles of total methanol converted into products in 48 h per BAS; the concentration of BAS is the value from pyridine IR after evacuation at 150 °C; ^c Catalyst lifetime defined as the time passed to reach 50% of the initial conversion; ^d Determined by TGA analysis after a reaction time of 48 h; ^e not determined.

zeolites with bulk HZSM-5 shows that the former produce less ethylene. This would be consistent with ethylene being a secondary product from oligomerization and cracking of olefins longer than ethylene and an indication that the reaction mainly proceeds via homologation of propylene with methanol as proposed by the Olsbye group [40, 41]. The two materials synthesized at 150 °C, ZSM-5($C_{22-6-3}Br_2$, 20, 150) and ZSM-5($C_{22-6-6}Br_2$, 20, 150), exhibit very low activity in methanol conversion and mainly produce an equilibrium mixture of methanol and DME. The product mixtures after a reaction time of 1 h for these materials are not given because of the low conversion. After complete deactivation the coke content of the zeolites is about 10-11 %, comparable to values reported before by us for nanolayered ZSM-5. The coke content of ZSM-5($C_{22-6-3}(OH)_2$, 20, 170) is lower, because this sample has not fully deactivated after 48 h.

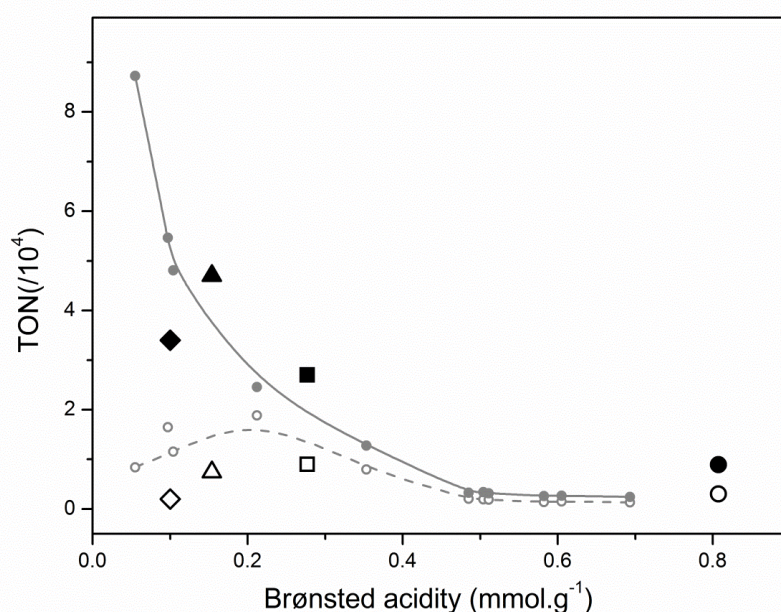


Figure 6.13: (Solid symbols) TON_{total} and (open symbols) $TON_{product}$ as a function of the concentration of Brønsted acid sites: (●) bulk HZSM-5, (■) ZSM-5($C_{22-6-3}Br_2$, 20, 170), (▲) ZSM-5($C_{22-6-6}Br_2$, 20, 170) and (◆) ZSM-5($C_{22-6-3}Br_2$, 20, 150). The data in grey is for a set of steamed HZSM-5 zeolites measured in the methanol-to-hydrocarbons reaction at 350 °C at similar WHSV [39].

Finally, we plot in Fig. 6.13 the total methanol conversion capacity expressed as a turnover numbers (TON). We define two capacities, namely the number of moles of methanol converted (TON_{total} , including DME formation) and the number of moles of methanol converted into products with C-C bonds ($TON_{product}$) per mole of BAS (pyridine IR values in Table 6.3) [39]. The trends for TON_{total} and $TON_{product}$ with the Brønsted acidity are again very similar to previous data. Briefly, zeolites with a high density of Brønsted acid sites deactivate rapidly because of the high rate of consecutive reactions of products into coke. The

decreasing Brønsted acidity of nanolayered ZSM-5 zeolites results in an increased amount of methanol converted per BAS because of the lower coke formation rate. As a result, the total amount of methanol converted per BAS increases strongly with decreasing BAS density. However, it also causes carbon-carbon bond forming reactions to become slower, so that DME becomes a more predominant product. Similar to a set of HZSM-5 zeolites steamed at various temperatures this results in optimum performance in terms of $\text{TON}_{\text{product}}$ at intermediate Brønsted acidity. Note that similar to our previous study [23] (Chapter 5), the unilamellar ZSM-5($\text{C}_{22-6-3}(\text{OH})_2$, 20, 170) zeolite shows a significantly higher $\text{TON}_{\text{product}}$ than the other zeolites.

6.4 Conclusions

Nanolayered ZSM-5 zeolites are promising for a variety of acid-catalyzed reactions. However, their synthesis at relatively high Al content has not been achieved yet. Based on the hypothesis that the hexyl group in $\text{R-N}^+(\text{CH}_3)_2\text{-C}_6\text{H}_{12}\text{-N}^+(\text{CH}_3)_2\text{-C}_6\text{H}_{13}$ with R is a long alkyl chain does not allow for complete filling of the micropores of the nanolayered zeolites by quaternary ammonium ions, we explored the use of a similar template with a propyl end group, $\text{R-N}^+(\text{CH}_3)_2\text{-C}_6\text{H}_{12}\text{-N}^+(\text{CH}_3)_2\text{-C}_3\text{H}_7$. Whilst at a crystallization temperature of 150 °C nanolayered ZSM-5 zeolite can be synthesized at a Si/Al ratio of 50, increasing the Al content to Si/Al = 20 results in X-ray amorphous materials with very low Brønsted acidity. The crystallization rate can be improved when the hydrothermal synthesis is carried out at 170 °C. This materials synthesized with a propyl-terminated template gave zeolites with higher crystallinity than the hexyl-terminated ones. Also, the total Brønsted acidity is higher for the more crystalline sample. Nevertheless, the total acidity is significantly lower than that of bulk HZSM-5 at comparable Si/Al ratio. The reason is the difficulty of building a significant amount of tetrahedral Al in the thin zeolite nanolayers. Another aspect is that the Al atoms that do not end up in the zeolite framework decrease the Brønsted acidity, because they act as charge-compensating species instead of protons. The catalytic performance in *n*-heptane hydroconversion trends well with the Brønsted acidity as probed by CO_{ads} and Py_{ads} IR. In the methanol-to-hydrocarbons reaction optimum methanol conversion capacity is observed for samples with intermediate Brønsted acidity.

References

- [1] A. Corma, *Chem. Rev.* 95 (1995) 559-614.
- [2] G. Busca, *Chem. Rev.* 107 (2007) 5366-5410.
- [3] W.E. Farneth, and R.J. Gorte, *Chem. Rev.* 95 (1995) 615-635.
- [4] A. Corma, *Curr. Opin. Solid State Mater. Sci.* 2 (1997) 63-75.
- [5] L. Tosheva, and V.P. Valtchev, *Chem. Mater.* 17 (2005) 2494-2513.
- [6] A. Chica, U. Diaz, V. Fornes, and A. Corma, *Catal. Today* 147 (2009) 179-185.
- [7] A. Corma, M.J. Diaz-Cabanas, F. Rey, S. Nicolououlas, and K. Boulahya, *Chem. Commun.* (2004) 1356-1357.
- [8] J.X. Jiang, J.H. Yu, and A. Corma, *Angew. Chem. Int. Ed.* 49 (2010) 3120-3145.
- [9] J.L. Paillaud, B. Harbuzaru, J. Patarin, and N. Bats, *Science* 304 (2004) 990-992.
- [10] K. Egeblad, C.H. Christensen, M. Kustova, and C.H. Christensen, *Chem. Mater.* 20 (2008) 946-960.
- [11] J. Perez-Ramirez, C.H. Christensen, K. Egeblad, and J.C. Groen, *Chem. Soc. Rev.* 37 (2008) 2530-2542.
- [12] R. Chal, C. Gérardin, M. Bulut, and S. van Donk, *ChemCatChem* 3 (2011) 67-81.
- [13] L.-H. Chen, X.-Y. Li, J.C. Rooke, Y.-H. Zhang, X.-Y. Yang, Y. Tang, F.-S. Xiao, and B.-L. Su, *J. Mater. Chem.* 22 (2012) 17381-17403.
- [14] K. Moller, and T. Bein, *Chem. Soc. Rev.* 42 (2013) 3689-3707.
- [15] M. Choi, K. Na, J. Kim, Y. Sakamoto, O. Terasaki, and R. Ryoo, *Nature* 461 (2009) 246-250.
- [16] K. Na, M. Choi, W. Park, Y. Sakamoto, O. Terasaki, and R. Ryoo, *J. Am. Chem. Soc.* 132 (2010) 4169-4177.
- [17] P.M.M. Blauwhoff, J.W. Gosselink, E.P. Kiffer, S.T. Sie, and W.H.J. Stork. 1999. *Catalysis and Zeolites*. J. Weitkamp, and L. Puppe, editors. Springer.
- [18] Q.-L. Chen, W.-M. Yang, and J.-W. Teng, *Chin. J. Catal.* 34 (2013) 217-224.
- [19] N.M. Laurendeau, *Prog. Energy Combust. Sci.* 4 (1978) 221-270.
- [20] D.A. Hickman, and L.D. Schmidt, *Science* 259 (1993) 343-346.
- [21] D. Sutton, B. Kelleher, and J.R.H. Ross, *Fuel Process. Technol.* 73 (2001) 155-173.
- [22] M. Asadullah, S. Ito, K. Kunimori, M. Yamada, and K. Tomishige, *J. Catal.* 208 (2002) 255-259.
- [23] L. Wu, P.C.M.M. Magusin, V. Degirmenci, M. Li, S.M.T. Almutairi, X. Zhu, B. Mezari, and E.J.M. Hensen, *Microporous Mesoporous Mater.* (2013) In press.
- [24] L. Wu, V. Degirmenci, P.C.M.M. Magusin, N.J.H.G.M. Lousberg, and E.J.M. Hensen, *J. Catal.* 298 (2013) 27-40.
- [25] L.L. Wu, V. Degirmenci, P. Magusin, B.M. Szyja, and E.J.M. Hensen, *Chem. Commun.* 48 (2012) 9492-9494.
- [26] J. Datka, A.M. Turek, J.M. Jehng, and I.E. Wachs, *J. Catal.* 135 (1992) 186-199.
- [27] N.S. Nesterenko, F. Thibault-Starzyk, V. Montouilliout, V.V. Yushchenko, C. Fernandez, J.P. Gilson, F. Fajula, and Ivanova, II, *Kinet. Catal.* 47 (2006) 40-48.
- [28] G.E. Giannetto, G.R. Perot, and M.R. Guisnet, *Ind. Eng. Chem. Prod. Res. Dev.* 25 (1986) 481-490.

- [29] J.W. Thybaut, C.S.L. Narasimhan, J.F. Denayer, G.V. Baron, P.A. Jacobs, J.A. Martens, and G.B. Marin, *Ind. Eng. Chem. Res.* 44 (2005) 5159-5169.
- [30] E.J.M. Hensen, D.G. Poduval, P.C.M.M. Magusin, A.E. Coumans, and J.A.R. van Veen, *J. Catal.* 269 (2010) 201-218.
- [31] P.K. Dutta, and M. Puri, *J. Phys. Chem.* 91 (1987) 4329-4333.
- [32] A.J.J. Koekkoek, C.H.L. Tempelman, V. Degirmenci, M.L. Guo, Z.C. Feng, C. Li, and E.J.M. Hensen, *Catal. Today* 168 (2011) 96-111.
- [33] P.K. Dutta, K.M. Rao, and J.Y. Park, *J. Phys. Chem.* 95 (1991) 6654-6656.
- [34] S. Mintova, B. Mihailova, V. Valtchev, and L. Konstantinov, *J. Chem. Soc.-Chem. Commun.* (1994) 1791-1792.
- [35] E. Bourgeat-Lami, P. Massiani, F. Drenzo, P. Espiau, F. Fajula, and T.D. Courieres, *Appl. Catal.* 72 (1991) 139-152.
- [36] A. Omegna, J.A. van Bokhoven, and R. Prins, *J. Phys. Chem. B* 107 (2003) 8854-8860.
- [37] M.F. Williams, B. Fonfe, C. Sievers, A. Abraham, J.A. van Bokhoven, A. Jentys, J.A.R. van Veen, and J.A. Lercher, *J. Catal.* 251 (2007) 485-496.
- [38] E.J.M. Hensen, D.G. Poduval, V. Degirmenci, D. Ligthart, W.B. Chen, F. Mauge, M.S. Rigutto, and J.A.R. van Veen, *J. Phys. Chem. C* 116 (2012) 21416-21429.
- [39] S.M.T. Almutairi, B. Mezari, E.A. Pidko, P.C.M.M. Magusin, and E.J.M. Hensen, *J. Catal.* 307 (2013) 194-203.
- [40] S. Svelle, F. Joensen, J. Nerlov, U. Olsbye, K.P. Lillerud, S. Kolboe, and M. Bjorgen, *J. Am. Chem. Soc.* 128 (2006) 14770-14771.
- [41] M. Bjorgen, S. Svelle, F. Joensen, J. Nerlov, S. Kolboe, F. Bonino, L. Palumbo, S. Bordiga, and U. Olsbye, *J. Catal.* 249 (2007) 195-207.

Summary

Mesoporous CHA and MFI Zeolite Catalysts for Methanol Conversion Reactions

Zeolites are microporous crystalline aluminosilicates, which are widely used in the petrochemical industry for acid-catalyzed reactions. Zeolites are usually synthesized in the form of relatively large crystals, which may lead to mass transport limitations during catalytic reactions. The generation of mesoporosity in zeolite crystals has become a very important research topic in the last decade [1, 2]. Among the many strategies explored, the use of two templates involving a conventional structure directing agent that directs formation of a microporous crystalline framework with a mesoporegen to give in a one-pot synthesis a hierarchical zeolite containing interconnected micro- and mesopores is the most desirable, but also the most challenging.

In this thesis, the synthesis of hierarchical acidic chabazite (CHA) and ZSM-5 (MFI) zeolites is explored with the aim to improve their catalytic properties. The focus is on the development of more stable catalysts for the methanol conversion reaction. Methanol is an increasingly important chemical intermediate, which can be manufactured from syngas derived from sources such as coal, gas or biomass. The zeolites explored in this study are aluminosilicate and silicoaluminophosphate variants with the chabazite topology, SSZ-13 and SAPO-34, as well as the aluminosilicate ZSM-5. In chapter 2 and 3, the design, synthesis, characterization and catalytic performance of hierarchical SSZ-13 zeolites are investigated. Chapter 4 explores a number of approaches to further increase the stability of chabazite zeolites and efforts are made to understand the effect of mesopore generation in SAPO-34. In chapter 5 and 6, similar approaches are explored for nanolayered ZSM-5.

Chapter 2 explores the use of several mesoporegen in the synthesis of SSZ-13 with a Si/Al ratio of 20. Computational modeling is used to predict the goodness of fit of several

proposed templates in the chabazite structure. These mesoporegen contain a polar head group, which interacts with the growing zeolite surface sufficiently strong, and an apolar hydrocarbon tail, which blocks the zeolite growth in the direction perpendicular to the zeolite surface. This study is the first to report the successful synthesis of a hierarchical zeolite by combining two templates based on non-covalent interactions with silicates, one directing formation of micropores and the other mesopores [3]. It was shown that by combination of N,N,N-trimethyl-1-adamantanammonium hydroxide (TMAdOH) as a structure-directing agent (SDA) with $C_{22-4-4}Br_2$ - $(C_{22}H_{45}-N^+(CH_3)_2-C_6H_{12}-N^+(CH_3)_2-C_6H_{13})Br_2$ - highly mesoporous SSZ-13 can be obtained. A set of hierarchical SSZ-13 zeolites was prepared by combining N,N,N-trimethyl-1-adamantanammonium hydroxide (TMAdOH) as a structure-directing agent (SDA) with several mesoporegens ($C_{22-4-4}Br_2$, $C_{22-4}Br$, $C_{22-6-6}Br_2$ and TPOAC) [4]. Their structural and textural properties were characterized in detail. The use of the diquatery ammonium-type surfactant $C_{22-4-4}Br_2$ next to TMAdOH induces considerable mesoporosity without impeding the microporosity. In contrast, a mesoporegen with only one quatery ammonium center ($C_{22-4}Br$) does not generate mesoporosity, because its interaction with the zeolite is not strong enough. The predicted mismatch of $C_{22-6-6}Br_2$ results in low crystallinity of the product. Focusing on $C_{22-4-4}Br_2$, the mesopore volume increases with the mesoporegen/SDA ratio. This approach presents a generally applicable strategy for the synthesis of hierarchical zeolites, because it requires only replacing a small part of the conventional SDA by a usually more expensive mesoporegen. It is also shown that the new approach results in better ordered materials than the use of organosilanes. The generality of our approach of combining two different templates for zeolite structure direction and crystal growth inhibition has been recently shown by the Ryoo group [5]. Thus, a novel promising method has been developed with clear cost advantage over approaches involving the sole use of an expensive template, which combines zeolite directing and mesoporegen functions.

In chapter 3, the acidic and catalytic properties of the hierarchical SSZ-13 zeolites synthesized in chapter 2 are studied. The reaction of choice is the methanol-to-olefins reaction. Conventional SSZ-13 and mesoporous SSZ-13 exhibit comparable Brønsted acidity. A larger portion of these acid sites are at the external surface in the hierarchical zeolites. Comparatively, the use of other templates does not give zeolites with such favorable

properties. The use of the organosilane TPOAC does not result in the exclusive introduction of Al^{3+} in the zeolite framework. Besides, the formation of ZSM-5 as a competing phase is undesirable for the application of these zeolites to convert methanol to light olefins. Hierarchical SSZ-13 zeolites display a much longer lifetime as catalysts in the methanol-to-olefins reaction than conventional SSZ-13. The light olefins yields of such zeolites are very similar with more than 90 % selectivity to ethylene and propylene. The increased lifetime is due to better utilization of the micropore space. There are two competing effects of the introduction of mesoporosity: (i) increased accessibility of the micropore space and, accordingly, better utilization of the micropore space and (ii) increased rate of coke formation with increasing external surface (increasing mesopore volume). Maximum catalyst lifetime is obtained at a relatively low $\text{C}_{22-44}\text{Br}_2/\text{SDA}$ ratio. These hierarchical SSZ-13 zeolite catalysts can be regenerated without loss of activity. From a commercial point of view, such robust hierarchical SSZ-13 zeolites may have potential in practice. Currently, the methanol-to-olefins process has been commercialized in China. A first unit (annual capacity 1800 k ton methanol) has been successfully commissioned in Shenhua's Baotou plant. Several other plants are under construction. The process is carried out in a configuration close to the FCC process, with a turbulent fluidized bed reactor and a regeneration section. The commercial catalyst is SAPO-34 based. Although a more acidic zeolite such as SSZ-13 may allow reactor operation at lower temperature, its rate of coke formation is significantly larger compared to SAPO-34. Besides energy savings, a longer lifetime of the catalyst in the reaction section may result in smaller regenerator sections, which would improve the economics of the overall process.

The main objective of chapter 4 was to improve the stability of CHA type zeolite catalysts for the methanol-to-olefins reaction. Two methods have been explored. Firstly, the best mesoporous SSZ-13(20) zeolite catalyst from chapters 2 and 3 were silylated, resulting in a relatively minor improvement of the lifetime. It evidences that the external zeolite surface contributes to the formation of coke. Secondly, SSZ-13 zeolite with a Si/Al ratio of 50 was synthesized. Lower acidity resulted in a lower rate of deactivation compared to SSZ-13 with a Si/Al ratio of 20. The lifetimes of microporous SSZ-13 with Si/Al ratios of 20 and 50 were 2.8 and 7 h, respectively. Introducing mesoporosity in SSZ-13(50) by use of the

organosilane TPOAC only resulted in a minor improvement of the lifetime. This is because the lower rate of coke formation for SSZ-13(50) as compared to SSZ-13(20) already resulted in much better utilization of the micropore space. It was not possible to synthesize mesoporous SSZ-13 at high Si/Al ratios by use of $C_{22-4-4}Br_2$. Instead, it led to formation of ZSM-5 zeolite. Attempts to synthesize SAPO-34 by use of $C_{22-4-4}Br_2$ as mesoporegen were also not successful and competing AIPO-phases were obtained. However, by addition of TPOAC a mesoporous SAPO-34 was synthesized. In this case the intracrystalline mesoporosity did not lower the deactivation rate as was observed for SSZ-13 zeolites. The total methanol conversion capacity per acid site for microporous and mesoporous SAPO-34 was comparable. These findings bring the complete utilization of the micropore of SAPO-34 in the methanol-to-olefins reaction to the fore. The notable difference with SSZ-13, whose micropore space is underutilized, relates to the much lower acidity of silicoaluminophosphates. Accordingly, there is no benefit of introduction of mesoporosity in SAPO-34. Consistent with this, it is found that the deactivation for micro- and mesoporous SAPO-34 zeolites proceeds in a very similar manner with time on stream in the MTO reaction.

In chapter 5, a set of nanolayered ZSM-5 zeolites synthesized using multiquaternary ammonium surfactants are studied in-depth. Although the zeolites are close to the materials reported by Ryoo et al. [6] with regards to structure and morphology, accurate control of thickness of the constituent nanosheets as recently shown by the Ryoo group [7] was not achieved. A detailed study of the acidity of such nanolayered zeolites is currently lacking. In our study, acidity characterization of nanolayered ZSM-5 zeolites reveals that the Brønsted acid sites (BAS) are similar in strength to those in bulk HZSM-5. Nanolayered zeolites contain a higher amount of BAS at their external (mesopore) surface. Unilamellar zeolites have a higher concentration of external BA and silanol sites than multilamellar ones. The number of BAS in the nanolayered zeolites is considerably lower than the tetrahedral Al content, the difference increasing with nanolayer thickness. Except for one particular sample (nanolayered ZSM-5 synthesized from $C_{22-6-6}(OH)_2$), the total turnover of methanol normalized per BAS trends inversely with the concentration of BAS. There is no correlation with the concentration of external BAS. Catalyst deactivation due to coke mainly depends on

the BAS concentration. A unilamellar ZSM-5 zeolite prepared using $C_{22-6-6}(OH)_2$ displayed substantially improved performance in terms of a much lower rate of coke deactivation in line with earlier data Choi et al. [6]. Since the acidic and textural properties of this zeolite did not differ significantly from the others, it remains to be determined why this zeolite performs so much better.

In chapter 6, the synthesis, acidity and catalytic properties of nanolayered ZSM-5 zeolites with a Si/Al content of 20 are explored. Whilst at a crystallization temperature of 150 °C nanolayered ZSM-5 zeolite can be synthesized at a Si/Al ratio of 50, increasing the Al content to a Si/Al ratio of 20 resulted in X-ray amorphous materials with very low Brønsted acidity. The crystallization rate can be improved when the hydrothermal synthesis is carried out at 170 °C. The crystallinity of the nanolayered zeolites can be improved by tailoring the originally proposed $R-N^+(CH_3)_2-C_6H_{12}-N^+(CH_3)_2-C_6H_{13}$ (R = long alkyl chain). By replacing the hexyl end group by a propyl end group, in principle all intersections of the nanolayered ZSM-5 zeolite can be occupied by quaternary ammonium ions. The zeolite synthesized with a propyl-terminated template exhibited higher crystallinity than the hexyl-terminated ones. This also led to higher Brønsted acidity. Nevertheless, the total acidity is significantly lower than that of bulk HZSM-5 at comparable Si/Al ratio. The reason is the difficulty of building a significant amount of tetrahedral Al in the thin zeolite nanolayers. Another aspect is that the Al atoms that do not end up in the zeolite framework may act to replace protons and, accordingly, decrease Brønsted acidity. The catalytic performance in *n*-heptane hydroconversion trends well with the Brønsted acidity as probed by CO_{ads} and Py_{ads} IR. In the methanol-to-hydrocarbons reaction optimum methanol conversion capacity is observed for samples with intermediate Brønsted acidity.

Reference

- [1] J. Perez-Ramirez, C.H. Christensen, K. Egeblad, and J.C. Groen, *Chem. Soc. Rev.* 37 (2008) 2530-2542.
- [2] S. van Donk, A.H. Janssen, J.H. Bitter, and K.P. de Jong, *Catal. Rev. Sci. Eng.* 45 (2003) 297-319.
- [3] L. Wu, V. Degirmenci, P. Magusin, B.M. Szyja, and E.J.M. Hensen, *Chem. Commun.* 48 (2012) 9492-9494.
- [4] L. Wu, V. Degirmenci, P.C.M.M. Magusin, N.J.H.G.M. Lousberg, and E.J.M. Hensen, *J. Catal.* 298 (2013) 27-40.
- [5] C. Jo, J. Jung, H.S. Shin, J. Kim, and R. Ryoo, *Angew. Chem. Int. Ed.* 52 (2013) 10014-10017.
- [6] M. Choi, K. Na, J. Kim, Y. Sakamoto, O. Terasaki, and R. Ryoo, *Nature* 461 (2009) 246-250.
- [7] W. Park, D. Yu, K. Na, K.E. Jelfs, B. Slater, Y. Sakamoto, and R. Ryoo, *Chem. Mater.* 23 (2011) 5131-5137.

Acknowledgements

My PhD work turned out to be like a marathon. It took longer than expected and the end seemed always far away. But once I was getting near to the finishing line, I became greatly excited and overflowed with deep gratitude.

Firstly, my deep gratefulness to my supervisor: Prof. Dr. Emiel Hensen, who gave me the opportunity to do my PhD project in his group. Emiel, you have always supported me to grow as a scientist with guidance, assistance and encouragement. Thank you very much for your timely suggestion for my experiments, inspiring discussions and intensive and illuminating modification for my manuscripts. It was my great honor to be part of your group.

I would also like to thank Dr. Pieter Magusin for being my co-promoter. NMR turned out to be one of the most important characterization methods in my work. You have made great efforts to help me to optimize the optimum conditions for NMR measurements and to interpret the data. Also many thanks in the thesis writing process.

I also acknowledge to the financial support provided by the Technology Foundation STW and the useful discussions from the user committee members, Dr. Marcello Rigutto of Shell, Dr. Thomas Davidian of Dow and Dr. Eelco Vogt of Albemarle.

I would also like to thank the other members of my defense committee: Prof. Dr. Rutger van Santen, Dr. Xander Nijhuis and Prof. Dr. Freek Kapteijn for spending time on reviewing my concept thesis and offering valuable comments.

My special thanks go to Dr. Volkan Degirmenci, who worked several years with me on the STW VIDI project. You have set up the in-situ Raman experiments in our lab and also were instrumental in setting up equipment to do in-situ NMR. You also taught me how to determine the acidity of my samples and get started with the catalytic tests. I appreciate that you were always able to keep a positive attitude to my experimental results, even if it did not

correspond to expectation. Besides, you are a good friend. Many thanks for your assistance, discussion and support. I wish you all the best in Belfast.

I would like to extend my thanks to Arjan, Bartek, Xiaochun, Sami and Evgeny. Arjan, many thanks for making my start in the field of zeolite synthesis more easy at the initial stages of my project. You gave me a lot of valuable advices and assistance in my whole PhD period, even when you were already working on Floor 4. Bartek, thanks for your support and useful insights from your theoretical modeling efforts. Xiaochun, thank you for helping with the Raman measurements and completing the last few but very essential experiments that completed my thesis. Sami, thank you likewise for helping out with the NH_3 -adsorbed ^{27}Al NMR measurements and your assistance with IR. Evgeny, thank you for your suggestions and comments on my project.

Also my gratitude goes to others who provided help with experiments: Nick, thank you for the FIB-SEM measurement! Yi and Nicolay, thank you for help with SEM. Xianyang, it has been an enjoyable experience to learn together with you TEM. Christiaan, Georgy, Chaochao, Alessandro, William, Peng, Michel and Yanmei, thanks very much for your help in various parts of my research.

Many thanks to the technical supporting team: Johan Velzen, Brahim Mezari, Adelheid Elemans-Mehring, Tiny Verhoeven, and Ad Wonders for their help with the experiments. Johan, thank you very much for taking my favorite SEM picture which is on the cover.

To our beautiful and energetic secretary: Emma Eltink. IMC group is now like a family, and you are the parent. You have organized so many wonderful group activities, and these moments will always stay in my heart. You also talked with me, supported me and encouraged me when my project went not very well. Thank you.

To my officemates for the memorable time: Michel, we shared the office for 4.5 years, and we went to visit conferences in Salamanca and Munich together. Thank you a lot for your advice about work, life and your jokes. William, I really enjoy our discussions on scientific and non-scientific issues. Thank you, Pieter, thanks for your continuously updated weather

forecast. Weiyu, especially thank you for your help with my thesis printing.

To my lunch partners: Yi Zhang, Tianwei, Guanna, Shuxia, Alessandro and Xianyang, I very much enjoyed the time spent together. Many thanks for being good friends supporting me and concerning about me.

I would like to thank all the other colleagues in IMC group for the wonderful time we spent: Burcu and Alex, thanks for your delicious cookies. Aysegul, Christiaan, Xianyang and Chaochao, I really enjoy the conference trip to Caen with you guys. Thomas, Robert, Abdul, Lennart, Tamas, Yi Ma, Xuefang, Lingqian, Wei, Xiaoming, Kaituo, Quanbao, Ivo, Anton, Cristina, Eric.....Thank you all.

I also would like to express my sincere gratitude to Prf. Dr. Peng Wu (East China Normal University, China), who was the supervisor in my Master period. Thank you for opening a door for me to the world of zeolite.

在这里我还要感谢所有的中国朋友们。这些年来的无数次聚餐，打牌，出游让枯燥的实验生活中多了很多色彩。艳梅，当时我到了荷兰遇到的第一个朋友。你的乐观，热情，和积极也带着我更快的适应这里的生活。你就快要当妈妈了，祝福你们一家三口永远幸福。桃子和高路，感谢你们在那个下雪的深夜去接我和艳梅，还弄粥给我们吃。桃子，你是个能把家庭，事业和兴趣爱好都经营的有声有色的人，我很佩服你。祝福你跟小荷兰，还有 Roos 永远快乐开心。高路，我太喜欢小兔兔了，特别感谢你们在朱敏住院的时候给我们提供吃的喝的，刘荣你把豆芽菜都一个一个的择干净，你太敬业了。关师兄，你在实验室的时候，每天我都会问你咨询很多问题，从实验到生活，感谢你不厌其烦的帮助。祝你和杨杰还有你们的宝宝在上海生活一切如意。张奕，我们是同一根绳上的蚂蚱（你懂的），所以我们有太多的感同身受的苦衷和会心一笑，未来的某天你的事业和爱情一定会双双而来。朱小伟，我们共同分享了很多八卦和好吃的，希望你每天都吃的好玩的好。冠娜，你跟鹏鹏终于团聚了，祝你们早日得偿所愿。超超，我的嫡亲师弟，谢谢你每次跟我耐心讨论分子筛的种种，也感谢你跟谢伟烧菜给我跟朱敏吃，祝你早日毕业工作，一家三口和和美美。小春，你善于思考，做事细心，跟你的讨论我也获益良多，祝你们一家早日团聚。刘鹏，美琴，亮亮你们三个我都很佩服，一个在实验室里成

果累累，一个家里外头打点的妥妥贴贴，还有一个聪明又适应力强。我们两家做了四年的邻居，感谢你们以实际行动告诉我模范家庭的样子。卫余，你非常有想法，做事情特别靠谱，特别感谢你帮我处理打印论文的一些问题，提前祝你新婚愉快，百年好合。学庆和丽萍，你们两个特别热心，Eric 很可爱，感谢你们很多的帮助，祝你们全家一直开心。其实还有更多的朋友我要感谢：宋立国，康博，唐老师，许炜，张志军，马艺，汤栋林，郭强，李晓波，郭美玲，王培远……感谢你们的陪伴和帮助。

我还要感谢我的家人，感谢你们对我的爱和支持。爷爷奶奶，姥姥姥爷，感谢你们对我从小的爱护。亲爱的爸爸妈妈，感谢你们的养育之恩，我的每一点成绩都有你们的心血。公公婆婆，感谢你们每次都烧好多菜给我吃，感谢你们对我的支持和理解。最后，特别感谢我的丈夫朱敏：是你给了我勇气，陪伴我来到陌生荷兰开始一段并不轻松的旅程，谢谢你爱我懂我包容我安慰我开导我照顾我鼓励我支持我欣赏我。我永远爱你。

List of Publications

Related to the thesis:

L. Wu, V. Degirmenci, P. C.M.M. Magusin, B.M. Szyja and E.J.M. Hensen, Dual template synthesis of a highly mesoporous SSZ-13 zeolite with improved stability in the methanol-to-olefins reaction, *Chem. Comm.*, 48 (2012) 9492-9494. (Chapter 2-3)

L. Wu, V. Degirmenci, P.C.M.M. Magusin, N.J.H.G.M. Lousberg and E.J.M. Hensen, Mesoporous SSZ-13 zeolite prepared by a dual template method with improved performance in the methanol to olefins reaction, *J. Catal.*, 298 (2013) 27-40. (Chapter 2-3)

L. Wu, V. Degirmenci, P.C.M.M. Magusin and E.J.M. Hensen, Mesoporous SAPO-34 and high-silica SSZ-13 as catalysts for the methanol-to-olefins reaction, submitted (Chapter 4)

L. Wu, P.C.M.M. Magusin, V. Degirmenci, M. Li, S.M.T. Almutairi, X. Zhu, B. Mezari and E.J.M. Hensen, Acidic properties of nanolayered ZSM-5 zeolites, *Microporous Mesoporous Mater.*, (2013) in press (Chapter 5)

L. Wu, A.J.J. Koekkoek, X. Zhu, P.C.M.M. Magusin, S.M.T. Almutairi V. Degirmenci and E.J.M. Hensen, Synthesis, acidity and catalytic properties of nanolayered HZSM-5 zeolite with high aluminum content, in preparation (Chapter 6)

Others:

S.K. Schnell, L. Wu, A.J.J. Koekkoek, S. Kjelstrup, E.J.M. Hensen and T.J.H. Vlugt, Adsorption of argon on MFI-nanosheets: experiments and simulations, *J. Phys. Chem. C*, (2013) in press

Y. Zhang, X.Y. Quek, L. Wu, Y. Guan and E.J.M. Hensen, Palladium nanoparticles entrapped in polymeric ionic liquid microgels as recyclable hydrogenation catalysts. *J. Mol. Catal. A: Chemical*, 379 (2013) 53-58.

J. Ruan, P. Wu, B. Slater, Z. Zhao, L. Wu and O. Terasaki, Structural characterization of interlayer expanded zeolite prepared from Ferrierite lamellar precursor. *Chem. Mater.*, 21 (2009) 2904–2911.

L. Wu, Y. Liu, P. Wu, M. He, Hydrothermal synthesis and characterization of CDS-1 type

titanosilicate, *Acta Chimica Sinica*, 66 (2008) 141-144.

P. Wu, J. Ruan, L. Wang, L. Wu, Y. Wang, Y. Liu, W. Fan, M. He, O. Terasaki, and T. Tatsumi, Methodology for synthesizing crystalline metallosilicates with expanded pore windows through molecular alkoxylation of zeolitic lamellar precursors. *J. Am. Chem. Soc.*, 130 (2008) 8178-8187.

Curriculum Vitae

Leilei Wu was born on April 15th 1982 in Rizhao, China. After she obtained her bachelor's degree in 2004 at Qufu Normal University in Shandong province, she continued her master's studies at East China Normal University in Shanghai, China. Her research topic was "post-modification and characterization of the structures of lamellar zeolites" under the guidance of Prof. Peng Wu. In June 2007 she defended her thesis and got her master's degree. Since July 2007, she worked in Shanghai Jiao Tong University as a research assistant. In January 2009, she started a PhD project under supervision of Prof. Emiel J.M. Hensen at the Eindhoven University of Technology. In her research, she focused on the development and application of mesoporous CHA and MFI zeolite catalysts for methanol conversion reactions.

